

# Determination of the transport levels in thin films of organic semiconductors

Dissertation zur Erlangung des  
naturwissenschaftlichen Doktorgrades  
der Bayerischen Julius - Maximilians - Universität Würzburg

vorgelegt von  
Stefan Krause  
aus Jena

Würzburg 2009

Eingereicht am: 29.6.2009

bei der Fakultät für Physik und Astronomie

1. Gutachter: Prof. Dr. E. Umbach

2. Gutachter: Prof. Dr. J. Pflaum

der Dissertation.

1. Prüfer: Prof. Dr. E. Umbach

2. Prüfer: Prof. Dr. J. Pflaum

3. Prüfer: Prof. Dr. C. Honerkamp

im Promotionskolloquium

Tag des Promotionskolloquiums: 27.7.2009

Doktorurkunde ausgehändigt am:

# Eidesstattliche Erklärung

Ich versichere hiermit an Eides statt, dass ich die vorliegende Dissertation eigenständig, d. h. insbesondere selbständig und ohne Hilfe eines kommerziellen Promotionsberaters angefertigt und keine anderen als die angegebenen Quellen und Hilfsmittel verwendet habe.

Stefan Krause, Las Vegas, den 23.6.2009

# Contents

Eidesstattliche Erklärung	III
List of Figures	VII
List of Tables	XIII
List of Abbreviations	XIV
1. Introduction	1
2. Influences on the energetic position of the transport levels	3
2.1. Polarization . . . . .	3
2.1.1. Gas phase vs. solid state . . . . .	8
2.1.2. Differences between surface and bulk . . . . .	10
2.1.3. Conclusions on polarization induced intermolecular screening . . . . .	12
2.2. Film morphology and thickness . . . . .	13
2.2.1. Morphology information from spectroscopic data . . . . .	14
2.2.2. Growth mode of PTCDA . . . . .	16
2.2.3. Growth mode of Alq3 . . . . .	18
2.2.4. Growth mode of CuPc . . . . .	19
2.2.5. Growth mode of DIP . . . . .	20
2.2.6. Growth mode of PBI-H4 . . . . .	25
2.2.7. Conclusions on growth modes . . . . .	26
2.3. Band alignment . . . . .	27
2.3.1. Vacuum level vs. Fermi level alignment . . . . .	27
2.3.2. Interface dipoles . . . . .	29
2.3.3. Experimental results . . . . .	31

2.4.	Band bending . . . . .	31
2.4.1.	Theory of band bending . . . . .	32
2.4.2.	Experimental results . . . . .	33
2.5.	Diindenoperylene - Different geometric film structures for one molecule . . . . .	38
2.5.1.	Dependence of geometric structure on sample preparation . . . . .	38
2.6.	How geometric structure influences the UPS/IPS - spectrum: Diindenoperylene . . . . .	61
2.6.1.	DFT calculations . . . . .	61
2.6.2.	The DIP-metal interface (monolayer investigation) . . . . .	66
2.6.3.	Comparison of the multilayer phases . . . . .	71
2.6.4.	How structural changes cause IP changes . . . . .	77
2.6.5.	Multilayer phase transition in the UPS . . . . .	79
2.6.6.	HREELS of the different phases . . . . .	80
2.6.7.	Summary and Conclusions . . . . .	85
2.7.	Summary and Conclusions . . . . .	87
3.	Peak broadening mechanisms . . . . .	89
3.1.	Lifetime . . . . .	90
3.2.	Experimental resolution . . . . .	91
3.3.	Band dispersion and bending . . . . .	92
3.4.	Structural inhomogeneities . . . . .	94
3.5.	Vibration and phonon coupling . . . . .	96
3.6.	Static and dynamic screening . . . . .	98
3.7.	Summary and conclusions . . . . .	100
4.	Determination of the transport levels and their gap . . . . .	102
4.1.	Inorganic semiconductors . . . . .	102
4.1.1.	Si(001) and its preparation . . . . .	103
4.1.2.	Positioning in the Brillouin zone . . . . .	104
4.1.3.	Influence of surface states . . . . .	108
4.1.4.	Position of the transport levels in the spectrum . . . . .	116
4.2.	Organic semiconductors . . . . .	119
4.2.1.	Position of the transport levels in the spectrum . . . . .	120
4.2.2.	Determination of exciton binding energies . . . . .	125

4.3. Summary and Conclusions . . . . .	128
5. Summary	130
6. Zusammenfassung	133
Bibliography	137
A. IPS radiation damage for organic semiconductors	150
B. Most intense infrared active modes	152

# List of Figures

2.1. Relaxation during the process of photoemission. . . . .	4
2.2. Polaron formation . . . . .	6
2.3. Comparison of ionization potentials for solid state and gas phase of naphthalene determined by UPS . . . . .	8
2.4. Comparison of the UPS of PTCDA in gas phase and of a multilayer film on Ag(111) . . . . .	9
2.5. Sketch of the different surroundings of molecules at the surface and in the bulk of a polarizable medium . . . . .	10
2.6. Comparison of the HOMO of Anthracene in gas phase and the two angles ( $20^\circ$ and $80^\circ$ ) of the solid state sample . . . . .	12
2.7. Attenuation behavior of the substrate XPS signal with growing film thickness for the three growth modes . . . . .	15
2.8. Chemical structure of Perylene - 3,4,9,10 - Tetracarboxylic Dianhydride. . . . .	16
2.9. Chemical structure of Aluminum Tris(8-Hydroxyquinoline). . . . .	17
2.10. Thickness dependent attenuation of the Ag 3d intensity for Alq <sub>3</sub> . . . . .	18
2.11. Chemical structure of (29H, 31H-Phthalocyaninato(2-)-N29, N30, N31, N32)Copper. . . . .	19
2.12. Attenuation of the silver substrate with increasing CuPc coverage for $T_{Substrate} < 200K$ . . . . .	19
2.13. Chemical structure of Diindeno-Perylene. . . . .	20
2.14. Thickness dependent attenuation of the Ag 3d intensity for DIP prepared at substrate temperatures below 150K. . . . .	21
2.15. Photograph of the Ag(111) crystal . . . . .	22
2.16. Thickness dependent attenuation of the Ag 3d intensity for DIP prepared at substrate temperatures of about 210K. . . . .	22
2.17. Growth mode for DIP on Ag(111) at $T_{Substrate} = 210K$ . . . . .	23

2.18. Photograph of a DIP film prepared at 210K and the same film after 30 minutes at 350K . . . . .	24
2.19. Thickness dependent attenuation of the Ag 3d intensity for DIP prepared at substrate temperatures above 350K. . . . .	24
2.20. Growth behavior for DIP at $T_{Substrate} = 350K$ if the layers are prepared in more than one step. . . . .	25
2.21. Chemical structure of N,N' - Di(2,2,3,3,4,4,4 - Heptafluorobutyl) - 3,4,9,10. . . . .	25
2.22. Sketch of the two possible types of band alignment between metal substrate and organic semiconductors. . . . .	28
2.23. Overview about the mechanisms that form and influence the interface dipole between metal and organic film. . . . .	29
2.24. Overview of the possible types of a band bending with growing film thickness in thin films of organic semiconductors. . . . .	33
2.25. Thickness dependent position of the frontier orbitals and the vacuum level for PTCDA . . . . .	35
2.26. Thickness dependent position of the frontier orbitals and the vacuum level for CuPc . . . . .	35
2.27. Thickness dependent position of the frontier orbitals and the vacuum level for Alq <sub>3</sub> . . . . .	36
2.28. Thickness dependent position of the frontier orbitals and the vacuum level for DIP grown below 150K substrate temperature	36
2.29. Thickness dependent position of the frontier orbitals and the vacuum level for DIP grown at 210K substrate temperature .	37
2.30. Thickness dependent position of the frontier orbitals and the vacuum level for DIP grown above 350K substrate temperature	37
2.31. Series of LEED patterns of the DIP monolayer on Ag(111) . .	40
2.32. SPALEED diffractogram of a monolayer DIP on Ag(111) . . .	40
2.33. Series of diffractograms showing the monolayer of DIP on Ag(111) for different temperatures . . . . .	41
2.34. Series of SPALEED line scans (300 K to 370 K) for a monolayer DIP on Ag(111) . . . . .	42
2.35. Diffractogram of the monolayer DIP on Ag(111) . . . . .	43
2.36. Line scan through the (0,0) - spot of the monolayer DIP and one scan perpendicular to the first . . . . .	44



2.37. Model of the arrangement of the DIP molecules on the silver surface . . . . .	45
2.38. LEED pattern of a 5 - 6 layer thick DIP film on Ag(111). The substrate temperature during deposition was 125 K. $E_{kin} = 26$ eV . . . . .	46
2.39. SPALEED Pattern for a DIP multilayer (5 - 6 layers) grown at 117 K. $E_{kin} = 35$ eV . . . . .	46
2.40. A series of SPALEED diffractograms for two preparation temperatures and different electron energies ( $T_{Sub} < 150$ K). . . . .	47
2.41. SPALEED diffractograms of DIP multilayer films grown at 150 K (a) and 115 K (b) . . . . .	48
2.42. Line scan through the (0,0) - spot of the diffraction pattern. The angles are defined in the same way as in Figure 2.36. $E_{kin} = 35$ eV . . . . .	49
2.43. LEED pattern of a 5 - 6 layers thin DIP film prepared at $T_{Substrate} = 420$ K. $E_{kin} = 30$ eV . . . . .	51
2.44. SPALEED diffractogram of a DIP film grown at 400 K substrate temperature. The thickness is about 5 - 6 layers. $E_{kin} = 35$ eV . . . . .	51
2.45. Combined calculated and measured SPALEED pattern for DIP grown at 400 K. The red spots are calculated and the blue line represent the unit cell vectors, starting in the (0,0)-spot in the upper right corner. . . . .	52
2.46. Line scans through the (0,0)-spot for DIP grown at 400 K. The scans are parallel to the unit cell vectors. . . . .	53
2.47. A series of SPALEED diffractograms at different energies of DIP films prepared at $T_{Substrate} = 210$ K. (a) shows the complete diffraction pattern at 23 eV, (b) at 45 eV, and (d) at 35 eV. (c) is a detail of diffractogram (d), marked by the red box. . . . .	54
2.48. The calculated diffraction patterns for two rectangular unit cells and the oblique one ( $T_{Sub} = 210$ K) . . . . .	55
2.49. Line diffractogram through the (0,0) - spot along the $\mathbf{a}'$ - vector. . . . .	55
2.50. Structural transition from low temperature phase to high temperature phase by heating of the sample in several steps. . . . .	57

2.51. Structural phase diagram of DIP on Ag(111) depending on coverage $\Theta$ and temperature T. . . . .	60
2.52. Calculated Diindenoperylene geometry. The calculation was conducted with the B3LYP DFT functional and the 6-311G+(d,p) basis set in Gaussian03. . . . .	62
2.53. Calculated FTIRRA spectrum for the single DIP molecule . . .	63
2.54. XPS spectrum of clean silver and after annealing of a multilayer film at 450 K for 30 minutes. . . . .	67
2.55. (a) UPS spectrum of directly deposited 1.7 layers of DIP at 150 K. (b) UPS spectrum of the annealed monolayer ( $T > 450$ K) deposited at room temperature. (c) and (d) are spectra (a) and (b) from which a Fermi function and a quadratic background were subtracted. . . . .	68
2.56. Specular and off - specular HREELS spectrum of the monolayer DIP on Ag(111). $E = 2.3$ eV, $\Delta E = \text{ca. } 2.5 - 3.0$ meV. . .	69
2.57. UPS spectra and SPALEED pattern for all preparation conditions. . . . .	71
2.58. The IPS spectra that correspond to the films in Figure 2.57. . .	73
2.59. Angle dependent UPS spectra for a DIP film prepared at 136 K. . . . .	74
2.60. Series of UPS spectra of a DIP film prepared at 420 K substrate temperature. . . . .	76
2.61. ARUPS series of a 210 K DIP film. . . . .	77
2.62. Dependence of of the intensity ratio of HOMO to HOMO-1 on the emission angle. . . . .	78
2.63. Comparison of the UPS spectra of DIP grown at 210 K and 420 K . . . . .	79
2.64. The IPS spectra that correspond to the films in Figure 2.63. . .	80
2.65. On the left hand side are the Ag 3d - XPS spectra for clean silver and the two preparations. On the right hand side the corresponding C 1s spectra are shown. . . . .	81
2.66. Sketch of the energy levels of lying and standing DIP molecules with respect to the silver substrate. . . . .	81
2.67. Series of UPS spectra corresponding to a structural phase transition of the multilayer. . . . .	82

2.68.	To Figure 2.67 corresponding XPS spectra of the Ag 3d substrate peak for the freshly deposited film and after the subsequent annealing cycles. . . . .	83
2.69.	Comparison of the HREELS spectra for all DIP structural phases and calculated IR spectrum. . . . .	84
2.70.	Models for the different structures related to the substrate temperatures during the growth of the film. . . . .	86
3.1.	IPS spectra for Alq <sub>3</sub> (a), PTCDA (b) and CuPc (c). The red lines represent the fit result after deconvolution of the experimental broadening. . . . .	91
3.2.	Band dispersion of silicon in its $\overline{\Gamma X}$ -direction. . . . .	93
3.3.	Sketch of inhomogeneous peak broadening. . . . .	94
3.4.	Franck-Condon principle . . . . .	97
3.5.	Sketch of dynamic charge delocalization. . . . .	99
4.1.	LEED pattern of the 2x1 reconstructed Si(001) surface . . . .	103
4.2.	Model of the 2x1 reconstructed Si(001) surface . . . . .	105
4.3.	FCC Brillouin zone . . . . .	105
4.4.	Electron escape cone . . . . .	106
4.5.	$\Gamma$ KLUX emission plane with the emission cones . . . . .	108
4.6.	Calculated bandstructure of silicon between the $\Gamma$ and X point	109
4.7.	Calculation of the overall contribution of the first layer of Si(001) to the PES spectrum assuming an exponential attenuation of the signal of lower lying layers . . . . .	110
4.8.	Valence and conduction level spectra of Si(001) 2x1 . . . . .	111
4.9.	Fit results for two UPS spectra and one IPS spectrum of Si(001) 2x1 . . . . .	112
4.10.	Comparison of valence and conduction level spectra of the Si(001) 2x1 and H:Si(001) 1x1 surface . . . . .	113
4.11.	XPS spectra for a silicon (001) surface after etching and subsequent annealing . . . . .	115
4.12.	Band gap of silicon measured with UPS and IPS . . . . .	117
4.13.	Combined UPS and IPS data for all molecules investigated in this work . . . . .	121

4.14. Combined UPS and IPS spectra for the three phases found for DIP on Ag(111). . . . .	122
4.15. UPS and IPS spectra of P3HT/ITO. . . . .	124
4.16. Combined UPS and IPS spectrum of a monolayer PTCDA on Ag(111). . . . .	125
4.17. IPS spectra for the clean Ag(111) (top, measured in this work) the PTCDA monolayer on Ag(111) at 15° (middle) and 0° (bottom) angle of electron incidence. . . . .	126
A.1. IPS spectra of a monolayer PTCDA (left) and of a 6.9 nm thick film (right) on Ag(111). Every spectrum shows the sum of ten scans after different exposure times. . . . .	150
B.1. Pictures of the five out - of - plane modes at their strongest dislocation. Dislocation is exaggerated for better visibility. . .	152
B.2. Part one of the in - plane infrared active modes. . . . .	153
B.3. Part two of the in - plane infrared active modes. . . . .	154
B.4. Part three of the in - plane infrared active modes. . . . .	155

# List of Tables

2.1.	Calculated polarization energies of polyacene crystals . . . . .	7
2.2.	Values for the IMFP for different kinetic energies of the electrons in PTCDA on Ag(111) . . . . .	17
2.3.	Experimentally determined values for the interface dipole strength for several combinations of molecules and substrates. . . . .	30
2.4.	Results for interface dipole ( $\Delta$ ) induced shift of the vacuum level for different molecules. . . . .	31
2.5.	Results for the length of the unit cell vectors of the monolayer DIP on Ag(111) superstructure for various temperatures and for two different methods to determine them . . . . .	45
2.6.	Results for the length of the unit cell vectors of the DIP multilayer on Ag(111) superstructure for various temperatures below 160 K and for two different methods to determine them. . . . .	50
2.7.	Results for the length of the unit cell vectors of the DIP multilayer on Ag(111) superstructure grown at $T_{Substrate} > 350$ K. . . . .	52
2.8.	Results of the length of the unit cell vectors for the three superstructures of DIP grown at $T_{Substrate} = 210$ K. . . . .	56
2.9.	Calculated vibrational modes with their energies in $\text{cm}^{-1}$ . . . . .	63
2.10.	Calculated energy positions of the orbitals in DIP gas phase with respect to the vacuum level. . . . .	66
2.11.	Fit results of the DIP monolayer UPS spectrum for the directly prepared 1.7 ML film and the annealed monolayer. . . . .	69
3.1.	FWHM of HOMO and LUMO for all molecules investigated. . . . .	90
4.1.	Exciton binding energies of all investigated organic materials. . . . .	127

# List of Abbreviations

<b>2PPE</b>	Two-Photon Photoemission
<b>Alq<sub>3</sub></b>	Aluminum Tris(8-Hydroxyquinoline)
<b>AR(I)PES</b>	Angle Resolved (Inverse) Photoelectron Spectroscopy
<b>BZ</b>	Brillouin Zone
<b>CuPc</b>	(29H,31H-Phthalocyaninato(2-)-N29,N30,N31,N32)Copper
<b>DiMe-PTCDI</b>	N,N'-dimethyl-3,4,9,10-perylenetetracarboxylic dimide
<b>DIP</b>	Diindeno[1,2,3-cd:1',2',3'-lm]Perylene
<b>EA</b>	Electron Affinity
<b>H<sub>2</sub>Pc</b>	Phthalocyanine
<b>HOMO</b>	Highest Occupied Molecular Orbital
<b>HOPG</b>	Highly Ordered Pyrolytic Graphite
<b>HREELS</b>	High Resolution Electron Energy Loss Spectroscopy
<b>IMFP</b>	Inelastic Mean Free Path
<b>IP</b>	Ionization Potential
<b>IPES/IPS</b>	Inverse Photoelectron Spectroscopy
<b>ITO</b>	Indium Tin Oxide
<b>LASER</b>	Light Amplification by Stimulated Emission of Radiation
<b>LUMO</b>	Lowest Unoccupied Molecular Orbital
<b>NEXAFS</b>	Near Edge Absorption Fine Structure
<b>P3HT</b>	Poly(3-Hexylthiophene-2,5-Diyl)
<b>PBI-H<sub>4</sub></b>	N,N' - Di(2,2,3,3,4,4,4 - Heptafluorobutyl) - 3,4,9,10 Tetracarboxylic Acid Bisimide

<b>PES</b>	Photoelectron Spectroscopy
<b>PTCDA</b>	Perylene - 3,4,9,10 - Tetracarboxylic Dianhydride
<b>QMS</b>	Quadrupole Mass Spectrometer
<b>SBZ</b>	Surface Brillouin Zone
<b>SCLS</b>	Surface Core Level Shift
<b>(SPA)LEED</b>	(Spot Profile Analysis)Low Energy Electron Diffraction
<b>UPS</b>	Ultraviolet Photoelectron Spectroscopy
<b>XPS</b>	X-ray Photoelectron Spectroscopy





# 1. Introduction

The field of organic semiconductors has experienced a tremendous development over the past 50 years. Particularly, in the past two decades thin films of these materials have reached charge carrier mobilities that are comparable with hydrated amorphous silicon (a-Si:H) used in modern TFT displays ([DM02], [HC02]). Although organic materials have been studied for years and are successfully used in commercial applications, there is a lack of comprehensive understanding of fundamental properties such as geometric structure or electronic properties as well as of the dependence of charge injection [IHI<sup>+</sup>04] and charge transport [Kar03] on these properties.

For a systematic tailoring of the molecules and device architectures, it is important to establish a consistent method to measure the energetic position of transport levels. The early investigators treated organic semiconductors like their inorganic counterparts and measured the gap between the transport levels by optical absorption ([DDL<sup>+</sup>91], [FKS84], [HCH<sup>+</sup>94]). The groups of A. Kahn [WHSK97] and K. Seki [TSM<sup>+</sup>92] pioneered the use of (inverse) photoelectron spectroscopy for this purpose, which is also the subject of this work.

However, it is not straightforward to define the term transport level in organic semiconductors since it depends on the mechanism of charge transport. In the case of coherent band-like transport (as it would be in inorganic semiconductors), the levels are delocalized wave function derived from the former HOMO and LUMO. If hopping transport dominates, which occurs on the time scale of  $10^{-14}$  s [SC94], the transport state corresponds to a relaxed ionic state (RIS) in which all relaxation processes within that time scale took place. A major goal of this work is to correlate the spectroscopic results to localized or delocalized charge states. The question for the exciton binding energies is strongly connected to this matter, since it is in both transport mechanisms necessary to create electron-hole pairs and to separate them in order to have free charge carriers. The only direct method to measure this quantity is to compare the transport level gap to the optical gap, which is the energetically lowest optical transition excitable and, hence, the lowest excitonic state. Depending on the definition of the transport level position, the exciton binding energies in the literature vary between 0 and 1.5 eV even for the same molecular species ([BCH96], [HMK00]).

The identification of the transport levels in the spectra is only one aspect of this work. Of course it is a very important one, since it also concerns the fundamental intermolecular interaction. It will be shown that the exciton binding energies have much lower values than commonly assumed ([KCSU08], [HKSP00], [ZGG06]). The variety of effects that influence the "measured" position of these levels is also important. Therefore the first Chapter as introduction into the physical models will address the effects often discussed in this context, e.g., the polarizability of the molecules and its impact on the

## 1. Introduction

---

PES spectrum, the alignment at interfaces, and the bending of the electronic levels. They all will be discussed in the light of new publications as well as own experimental data. Additionally, a new aspect is introduced to the discussion on the example of the system Diindenoperylene on Ag(111) - the influence of geometric film structure on the electronic structure. This molecule forms a wide variety of different film geometries, which were investigated by SPALEED. This structural data is related to changes in the valence level and HREELS data in order to understand the observed phenomena.

Chapter 3 will then address the processes responsible for the peak widths in valence level PES spectra. This will again be done by a combination of literature review and own experimental data in order to give a complete overview and to quantify each contribution.

Finally, under consideration of all aspects discussed in the previous chapters the determination of the transport levels in the PES spectrum is discussed. Since inorganic semiconductors are better understood regarding their basic properties as electronic structure, exciton binding energies and charge transport, this will be done first for the silicon (001) face. Based on these results, a way for determining the transport levels as well as exciton binding energies for thin films of organic semiconductors is proposed with strong consequences for the picture of the interaction of the molecules in their condensates.

## 2. Influences on the energetic position of the transport levels and shape of the photoelectron spectrum of organic semiconductors

Since the overall goal of this work is to establish a method to determine the transport levels in thin films of organic semiconductors with the combination of UPS and IPS, it is necessary to consider the various influences on the measured energetic position of these levels. These shifts can origin either from the investigation method itself or from processes at the interface between film and substrate or within the thin film.

This Chapter will therefore start to focus on the investigation method itself and in particular on the screening of the photoinduced charge during the process of photoemission. In the discussion of the transport level determination, the polarizability of large organic molecules is often an issue, especially the difference between bulk and surface. Subsequently, the morphology of the films and its relevance for the PES measurements will be addressed. The energy level alignment at the interface as well as the subsequent shift with increasing distance from the interface is an additional aspect which influences the position of the levels in the spectrum and which justifies the careful observation of the growth mode. Finally, the importance of structural aspects can be shown using Diindenoperylene on Ag(111). Therefore this system will be introduced in detail. A combination of structural measurements with SPALEED and intermolecular interaction sensitive measurement with HREELS will be utilized to monitor the changes in the geometric structure, which will then be related to the observed changes in the UPS and IPS spectra.

The results will then be summarized and their importance for the determination of the energy positions will be discussed. This discussion can be summarized in a recommendation, which data received for a certain combination of molecule and substrate is specific for the system and which is of general importance.

### 2.1. Polarization

The molecules that form the class of organic semiconductors mainly consist of large benzene-like  $\pi$ -electron systems. In these systems the valence electrons are strongly delocalized across the molecule and therefore they are easily influenced by electric fields. This fact is the source of the discussion about the influence of polarization on the energetic

## 2. Influences on the energetic position of the transport levels

---

position of the transport levels in thin films of these materials. An overview about theoretical considerations as well as experiments that try to quantify the influence of polarization will be given in this Section. Special attention will be on the measurement of binding energies in photoelectron spectroscopy and the consequences for charge carriers.

### Relaxation and correlation effects during the photoemission process

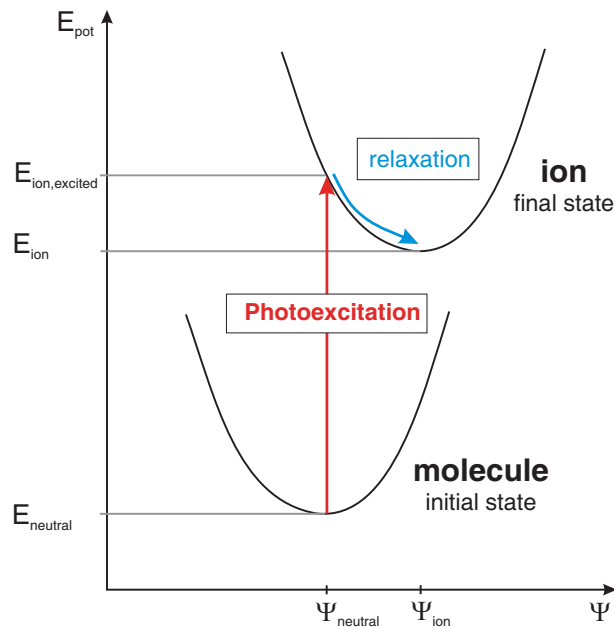


Figure 2.1.: Sketch of the photoinduced transition from a neutral molecule into an excited state of the ion. The y axis is the total potential energy of the system and the x axis is a geometric relaxation coordinate.

A crucial question in photoelectron spectroscopy is which energies one really probes. The most general answer is that one measures the difference between the total energies of the initial state  $E_i^N$  with  $N$  electrons and the final state  $E_f^{N-1}$  with  $N-1$  electrons. However, these energies are not easily accessible and therefore approximations are needed, such as **Koopmans' approximation**. It assumes that the photoemission process is instantaneous and the system has therefore no time to react to the hole generated. This corresponds to the vertical arrow in Figure 2.1 and is therefore called a "vertical transition". The measured energies should therefore be the negative energy of the orbital from which the emitted electron originates. This is of course not true because it assumes

that the creation of a hole in one orbital has no influence on other orbitals. Relaxation contributions are **not** taken into account in this approximation.

Of course, one has to correct for the relaxation energy. One part is also sketched in Figure 2.1 in which the y axis represents the total potential energy. The parameter  $\Psi$  on the x axis corresponds to a geometric relaxation coordinate, which could for instance be the distance between the hydrogen atoms in a  $\text{H}_2$  molecule but is more complex in other cases. The **intramolecular relaxation** is related to a change in the orbital energies and a rearrangement of the electronic system, which is symbolized by the curved arrow in Figure 2.1 and the change in  $E_{pot}$  and  $\Psi$ . The larger the molecule the smaller is the change of the interatomic distances and the more important is the change in the orbital energies. The second relaxation mechanism, which is not included in this sketch, originates from the charge flow from the surrounding molecules towards the ion - the **extramolecular relaxation**. This can be either a transport of charge or via the polarizability of the vicinity, which is the driving mechanism that rearranges the electron densities of the surrounding molecules by inducing dipoles. In the next paragraph this will be discussed in more detail for the case of charge carriers in a polarizable medium.

The size of the relaxation effects depends on the strength of the polarizability in the vicinity of the photoinduced hole and on the localization of the orbital from which the electron is excited. The latter is represented by the **correlation energy**, which originates from two types of interactions between the electrons. One is the Coulomb interaction the other one the Pauli repulsion, which is due to the Pauli principle that says that two electrons in an atom must have at least one different quantum number. The correlation energy is defined as the difference between the non-relativistic Hartree-Fock limit  $E_{HF-limit}^{NR}$  and the non-relativistic exact energy  $E_{exact}^{NR}$ .

$$E_{cor} = E_{HF-limit}^{NR} - E_{exact}^{NR} \quad (2.1)$$

If one electron is removed from the system this additional energy has to be provided. The size of it depends on the localization of the electronic system. The more delocalized it is the smaller is the effect of the removed electron on the remaining ones.

This has a tremendous effect on the photoemission spectrum. Even if the investigated system is highly polarizable, the photoelectron spectroscopy might not be sensitive to it because of the delocalized nature of the orbital in which the excitation took place.

## The electronic polaron

The term polaron is often used in the context of charge transport in organic molecular crystals. Hopping transport is the dominating channel at room temperature. Therefore, charge carriers remain long enough on one molecule for the vicinity to react to its presence. In this context polaron describes a charge carrier in a medium of high polarizability. However, this is not the original definition of this term. One can find this definition e.g. in the book of Ashcroft and Mermin [AM76], which describes a polaron as a charge in an ionic crystal that leads to a distortion of the lattice - the charge couples to a phonon. Later this definition was expanded for molecular crystals. The coupling to

## 2. Influences on the energetic position of the transport levels

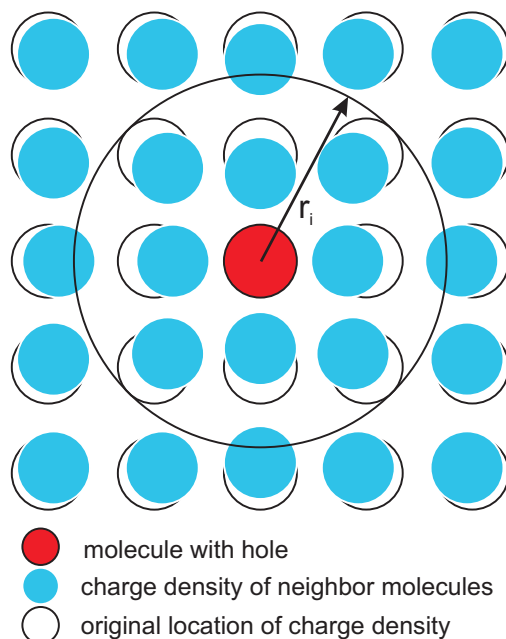


Figure 2.2.: Sketch of the formation of an electronic polarization "cloud" around a localized charge.  $r_i$  is the distance from the charge located in a hypothetical crystal.

dipole active vibrational modes of molecules (see Section 3.5 for more information; small molecular polaron) and the coupling to a cloud of virtual excitons (electronic polaron), which represent the intermolecular screening, were added. A sketch of an electronic polaron can be found in Figure 2.2. It illustrates the dislocation of the electrons of the  $\pi$  - ring systems of the surrounding molecules due to induced dipole interaction with the charge carrier. The energy of interaction is the polarization energy which is proportional to  $r_i^{-4}$ . Silinsh and Čàpek give a complete overview about the methods used to compute such polarization energies in their book [SC94]. In the following a short summary of their picture to describe the effect of polarization is given. This part will be needed later where the peak broadening due to the excitation of vibrationally excited final states during photoemission is discussed (3.5). They define the *total effective polarization energy*  $W_{eff}$  for positive charge carriers:

$$W_{eff}^+ = P_{eff}^+ + E_b \quad (2.2)$$

and for negative charge carriers:

$$W_{eff}^- = P_{eff}^- + E_b \quad (2.3)$$

$E_b$  is the energy of molecular (vibronic) polarization - the small molecular polaron. The experimental access to  $E_b$  is the difference between the optical  $E_{g,opt}$  and the adiabatic

energy gap  $E_{g,ad}$ :

$$E_b = \frac{E_{g,opt} - E_{g,ad}}{2} \quad (2.4)$$

In this context, adiabatic means that the ionized molecule already reacted on the removal of the charge, and the whole system is relaxed. The optical gap Silinsh and Čàpek refer to is determined from electromodulation spectra and the adiabatic gap from intrinsic photogeneration. From this ansatz they extract values of 0.1 to 0.2 eV for  $E_b$ . The fraction of  $P_{eff}^+$  and  $P_{eff}^-$  that originates from the induced dipole interaction ( $P_{id}$ ) is extracted from comparative measurements of the vertical ionization potential and electron affinity between gas phase and solid state.

$$P_{eff}^{+-} = P_{id}^{+-} + W_{Q_0}^{+-} \quad (2.5)$$

"Vertical" means in this case that the system did not have time to relax and that the molecules in ground state and excited state still have the same geometry. These measurements will be discussed in detail in Section 2.1.1. The second term,  $W_{Q_0}$ , which is the interaction energy with the permanent quadrupole moment, can either be positive or negative and has to be calculated. Table 2.1 contains the calculated values from ref. [SC94] to show the range of these energies.

Table 2.1.: Calculated values for all energies depending on the polarization in polyacene crystals. The values are taken from ref. [SC94] and given in eV.

Crystal	$P_{id}$	$W_{Q_0}^+$	$P_{eff}^+$	$W_{Q_0}^-$	$P_{eff}^-$
Benzene	-1.16	-0.04	-1.19	+0.04	-1.12
Naphthalene	-1.21	-0.16	-1.38	+0.16	-1.05
Anthracene	-1.19	-0.18	-1.38	+0.18	-1.01
Tetracene	-1.14	-0.22	-1.36	+0.22	-0.93
Pentacene	-1.08	-0.22	-1.29	+0.22	-0.86

## Experiments to quantify the influence of polarization

In the following an overview about experiments trying to quantify the polarizability as well as its influence on the photoelectron spectrum is given. The first part reviews the results and interpretations of UPS measurements, which compare the spectra of organic molecules in their gas phase with the ones in solid state. In the past the focus was on the differences of the ionization potential but recently also the shape of the spectra became part of the interpretation. The second part discusses the influence that polarizability would have in the case of a surface sensitive investigation method like PES and compares a key experiment to recent results.

## 2.1.1. Gas phase vs. solid state

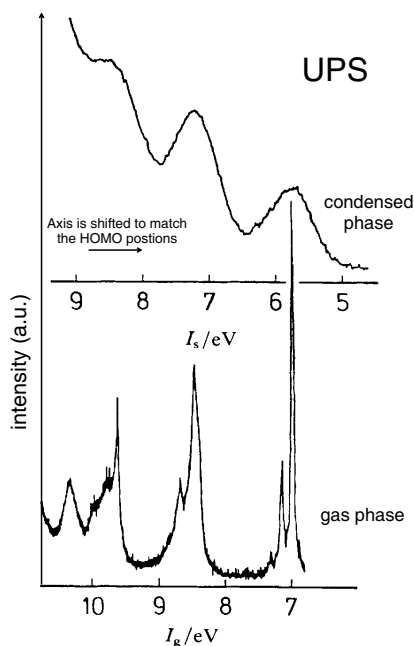


Figure 2.3.: Comparison of ionization potentials for solid state (top) and gas phase (bottom) of naphthalene determined by UPS, from N. Sato et al. [SSI81]. Independent of the shift in this graph, the IP for the solid state has been determined as the onset of the HOMO.

Theoretical calculations of the electron binding energies in organic molecules are quite difficult due to the high number of atoms in such a molecule. These calculations are usually done with density functional theory (DFT), which in principle needs no approximations. However, there is no analytical solution for the part of the potential that treats the electron correlation (the exchange correlation potential) and the development of good approximations is one of the major tasks in this field. Therefore, these calculations are always done for free molecules that do not interact with neighbors. In order to validate the calculations, one needs valence level spectra of the gas phase of the molecules, in which their interaction is negligible. An early attempt to do this can be found in the paper R. Boschi et al. [BMS72] from 1972. This matter is still topical because the approximations for the exchange correlation potential have become much better, but theory is still unable to fully reproduce the valence level energies in UPS. A recent study from N. Dori et al. [DMK<sup>+</sup>06] compares different ways to calculate these energies and compares the results, which clearly show that none of the methods exactly reproduces the spectra.

The groups of W.R. Salaneck [Sal78] and N. Sato ([SSI81], [SIS<sup>+</sup>82], [ISS87]) were the first who tried to quantify the influence of polarization in organic molecular crystals by comparison of the gas phase ionization potential, which was gained from photoemission data, with that of the solid state. The results of their measurement are shown in Figure 2.3, in which the solid state UPS (upper spectrum) is compared. They attributed the whole shift of the ionization potential to screening of the photon generated hole by the



surrounding molecules in the solid state - the Polarization shift  $P^+$  (corresponding to  $P_{id}$  in equation (2.5)). This interpretation is based on the assumption that the molecule does not interact with the surrounding ones and can be treated as a free molecule in a polarizable medium. In this way they determined  $P^+$  for a large number of different molecules and derived values between 0.9 and 3.0 eV. However, the crucial point that the molecules keep their electronic structure no matter if they are in the gas phase or the solid state, needs to be revised. Also the measurement of the ionization potential in the solid state is not straight forward and can depend on the **geometric structure** (see for details 2.6).

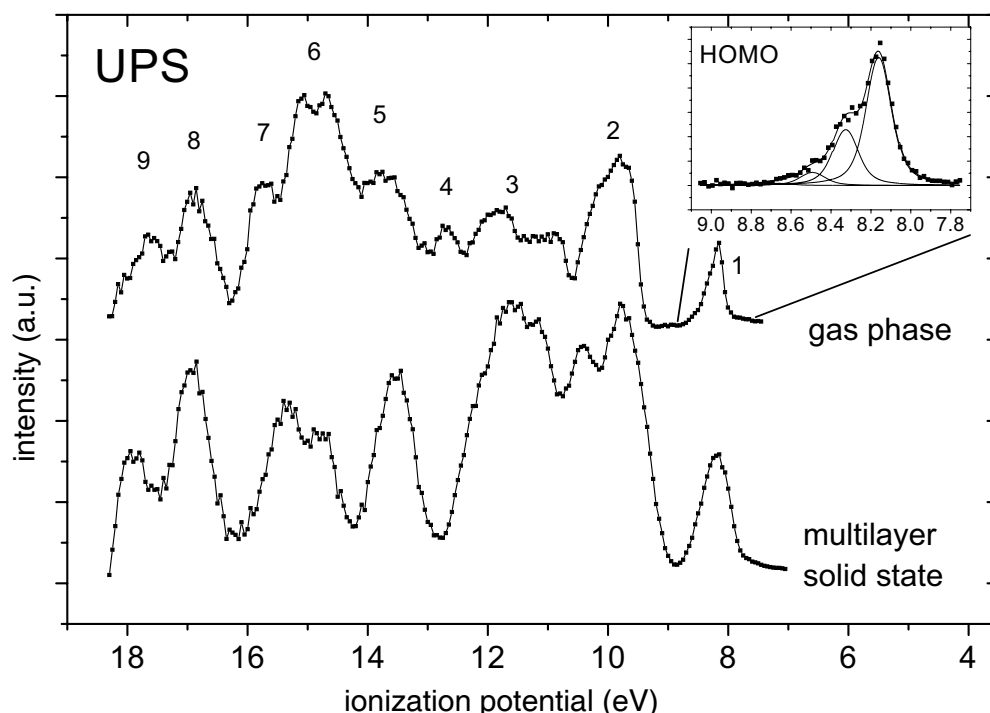


Figure 2.4.: Comparison of the UPS of PTCDA in gas phase and of a multilayer film on Ag(111), modified from [Kil02].

L. Kilian [Kil02] investigated not only the ionization potentials of the molecules but did also compare the shape of the spectrum and searched for shifts in the electronic levels. Figure 2.4 shows the spectra of a ten layer thick PTCDA film grown on a Ag(111) crystal at 300K and of PTCDA in gas phase. Additionally the solid state spectrum is shifted by 6.10 eV in order to match the ionization potential of the gas phase. The most significant difference is the absence of structure 4 and 7 in the solid state spectrum. Other structures shift in energy, e.g., structure 5 to smaller binding energies and structure 6 to higher ones, or they become broader (2) or smaller (3). Angle resolved measurements on the solid state film showed that the differences were not due to angular effects, e.g., because of the symmetry of the transition matrix element. These significant changes are a strong hint that the molecules in the solid state strongly interact with each other resulting in changes

## 2. Influences on the energetic position of the transport levels

of their electronic structure. Recent NEXAFS measurement by F. Holch et al. [HHF<sup>+</sup>] compare gas phase and solid state spectra of PTCDA and corroborate this finding. They also looked for shifts of the energies that indicate electronic interaction. In NEXAFS an electron is excited resonantly from a core level into an unoccupied level. Therefore it is possible to distinguish at which of the atoms in a molecule the excitation took place. This fact made it possible for them to attribute the electronic shifts to the  $\pi$  electron system. A substantial  $\pi$  -  $\pi$  interaction of PTCDA in the solid state was found. Publications from Y. Zou [Zou03], H. Yamane [YKO<sup>+</sup>03], [YKY<sup>+</sup>08] and G. Gavrila [GMK<sup>+</sup>04] show that even a small dispersion (a few 100 meV) of the HOMO for PTCDA (Zou, Yamane), NTCDA (Zou), pentacene (Yamane), and DiMe-PTCDI (Gavrila) exist. These high resolution ARUPS measurements support the assumption that in an organic semiconductor crystal the molecules interact strong enough to change the electronic structure of an individual molecule.

All the findings of L. Kilian, F. Holch, H. Yamane, and G. Gavrila indicate that the picture of the solid state of organic molecules needs to be revised. The picture of a molecule that keeps the electronic structure of the gas phase embedded into a highly polarizable medium is proved to be wrong. It is still true that in the gas phase the molecule has no extramolecular relaxation channels for the hole produced in the photoemission process and therefore one measures orbital energies which are closer to the ones of the excited ion. However, the difference to the solid state is not only the extramolecular relaxation but also the increased degree of delocalization of the frontier orbitals. As discussed in the previous Section, this work suggests that the UPS spectra are less influenced by the missing electron and therefore are very close to the energy levels of the neutral molecule.

### 2.1.2. Differences between surface and bulk

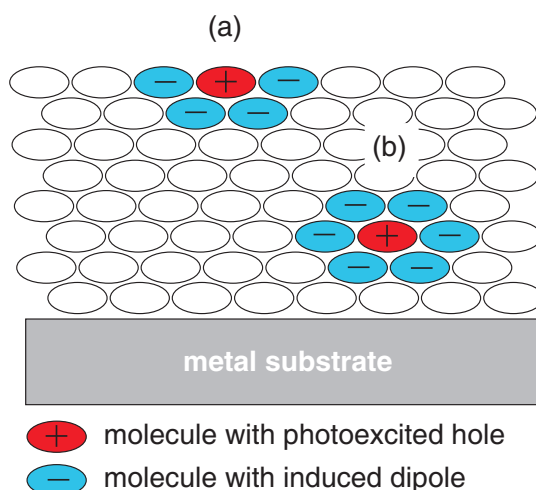


Figure 2.5.: Sketch of the different surroundings of molecules at the surface (a) and in the bulk (b) of a polarizable medium. This picture is based on the assumption of strong polarization effects.

Photoelectron spectroscopy is a very surface sensitive investigation method. If the incident photons have energies in the regime 30-60 eV, the escape depths of the electrons are up to 10 Å. A consequence of the effect of polarization being considered for organic semiconductors is that it strongly depends on the surroundings which is different at the surface and in the bulk. A molecule that is located directly at the surface (a) has only about half as many neighboring molecules as one located in the bulk (b), which is sketched in Figure 2.5.

Tsipser et al. [TSGK02] treated this matter theoretically as well as experimentally in 2002. They investigated films of PTCDA on Ag(111) and Au(111) with increasing thickness and traced the position of the HOMO and the LUMO. A clear increase of the distance between these levels was found with increasing film thickness from monolayer and to a thickness of 64 Å. This change of about 450 meV was completely attributed to different polarizability of the molecules in the monolayer with no other molecules above and below and the surface molecules of a thick film. They already mentioned that the gap decreases near metal surfaces due to a screening induced band bending (see Section 2.4), but argued that this only decreases the effect of the surface to bulk screening difference. In addition, theoretical calculations of the polarization screening of a pile of layers with corresponding image layers at an interface were done. Their results fitted the experimental data and suggest a surface to bulk polarization difference of 410 meV. However, the behavior of HOMO and LUMO still fits a screening induced band bending model very well and does not need additional effects to be explained.

W.R. Salaneck investigated this effect in his paper from 1978 [Sal78]. A multilayer film of Anthracene was prepared and investigated by ARUPS. He could identify two components in the HOMO varying their relative intensities with the change of angle. The corresponding measurement shows Figure 2.6, in which he attributed shifts of 1.2 eV and 1.5 eV to these components. The difference of 0.3 eV was attributed to the surface to bulk shift of the polarization screening. This is a key experiment and most of the literature that deals with surface to bulk polarization shifts relates to this article. However, polarization is not the only possible explanation for this behavior. One could also think of structural reasons for the observed angle dependence such as, e.g., Davydov splitting. If the unit cell of an organic crystal contains more than one molecule, the different angular behavior due to matrix element effects will also lead to two components in the spectrum. Another possible explanation is an effect similar to the one described in 2.6. For Diindenoperylene one has, depending on the substrate temperature during preparation, the case that two different crystalline structures coexist. If these two structures are grown on top of the other, one will see a superposition of both phases for normal emission and only one component for grazing emission due to the surface sensitivity of PES.

Nevertheless, tools are available to check if the angular change of intensity in the HOMO is due to a surface and a bulk component. L. Kilian [Kil02] measured the HOMO of PTCDA for a variety of angles and fitted the peak with two components. He investigated the relative intensities of the two components and calculated how they should behave if surface to bulk shift exists. These calculations were done very carefully and even accounted for refraction of the electrons at the interface. His result showed that one can exclude the two components to simply originate from a bulk and a surface

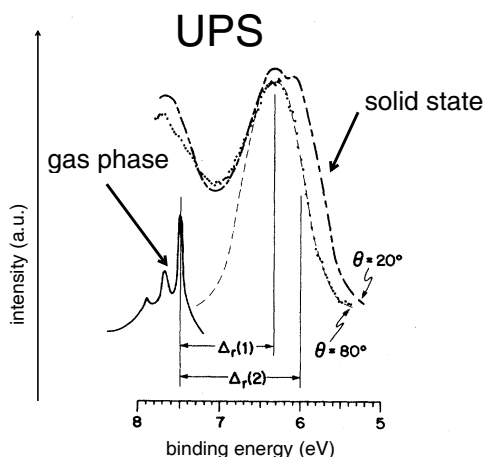


Figure 2.6.: Comparison of the HOMO of Anthracene in gas phase and two angles ( $20^\circ$  and  $80^\circ$ ) of the solid state sample. The author identifies a component shifted by 1.2 eV ( $\Delta_r(1)$ ) and one by 1.5 eV  $\Delta_r(2)$ . The picture originates from [Sal78] and was altered.

component.

As was shown in the previous Section, the valence levels might be too delocalized to be sensitive for intermolecular relaxation such as polarization. An archetype of a localized orbitals is the core level of an atom of the molecule. Its binding energy is changed due to chemical bondings but it will not split into bonding and antibonding orbitals. Therefore the core levels have been investigated by M. B. Casu et al. [CZK<sup>+</sup>07],[Cas08] with high resolution XPS. They investigated the C 1s level of multilayer films of PTCDA, coronene and H<sub>2</sub>Pc with synchrotron radiation with an energy of 700 eV and 335 eV. Additionally, the angle was varied between normal emission and up to  $75^\circ$  off normal in order to increase the surface sensitivity. The corresponding spectra gave no indication of a splitting between surface and bulk species, what they should have done as shown by simulations if a shift of 400 meV was present as found by Tsiper et al. [TSGK02]. Due to the energy resolution M.B. Casu et al. gave an upper limit of of **100 meV**. This method to detect surface core level shifts (SCLS) was already successfully applied before by, e.g., C. Heske et al. [HWH<sup>+</sup>97] on polar Cd(Zn)Te(100) where they found shifts in the order of 0.7 to 0.9 eV depending on the surface termination. Even measurements on the often compared noble gas crystals show SCLS of 0.15 - 0.25 eV ([MW84], [MUW83], [Nef95] and [Buc01]).

### 2.1.3. Conclusions on polarization induced intermolecular screening

The previous Sections gave an overview about the literature and in particular about recent results on the influence of polarization in organic thin films. In addition to the aspects relevant for PES also the basics of the influence of polarization on charge carriers was given. The question if a major contribution to the binding energy of a polaron can be measured by a comparison of gas and condensed phase UPS spectra was discussed. The

important key experiments by the groups of N. Sato and W. R. Salaneck were revised with the help of additional aspects from the work of L. Kilian and F. Holch. This revision demands for a reexamination of the current concept for the intermolecular interaction in organic thin films. It also puts the conclusion of polarization being the only reason for the IP shift into question because stronger interaction leads to a higher amount of delocalization in the valence levels. If this delocalization is stronger than assumed in the past, **photoelectron spectroscopy probes** energy levels that are close to the ones of **the neutral molecule**, and polarization effects are less important.

A second aspect that PES is influenced by polarization is the reaction of the neighborhood on a charge, in particular, if the charge is located at the surface or in the bulk. This contribution is crucial for the determination of the position of the transport levels in organic semiconductor films. The early measurements by W. R. Salaneck still being the basis of this theory have also been revised. L. Kilian clearly showed that the angle dependent changes in the HOMO of PTCDA can not be described by a bulk and a surface component. This was not only shown for valence levels but also for core levels which are very sensitive for relaxation effects due to their strongly localized nature. M. B. Casu et al. could assign an **upper limit for a surface to bulk shift of 100 meV** limited by the experimental resolution.

**In summary**, it has been shown that polarization either plays only a minor role for the condensed phase of organic semiconductors and that therefore polaron binding energies are very small or that photoelectron spectroscopy is not sensitive to it.

## 2.2. Film morphology and thickness

In this work, the determination of transport levels is done via PES. This method is integrating over a large area compared to the lattice constants of the organic crystals and is surface sensitive - most of the signal in UPS originates from the topmost 10 Å.

Thus the values to be determined may heavily depend on the morphology of the surface. One example is the work function: the rougher a surface is the lower the work function becomes. K. Besocke et al. [BKW77] showed that the work function of metal surfaces depends on the step density of the investigated crystalline face, which can be attributed to a surface roughness. Since there is often no Fermi level alignment between the organic adsorbate and the metallic substrate (will be shown in 2.3), a change in the morphology connected with a change in the work function can shift the energetic position of the thin film level against the substrate Fermi level.

Furthermore, the interface between the film and the substrate is important for the position of the energy levels. If the molecules are covalently bound to the substrate, they will form common orbitals with energies different from the original ones. This can even result in changes of the second or third layer orbitals. Therefore one needs a sufficient thickness for measuring the properties of the film without influences of the interface. Simultaneously, the thickness has to be uniform in order to avoid holes in the film or thinner areas through which the signal from the interface superimposes the film signal.

The goal here for all cases was the preparation of as smooth films as possible with-

## 2. Influences on the energetic position of the transport levels

---

out hindering the formation of large uniform crystals. However, these are two aims that sometimes are not compatible, and compromises have to be made. Morphology is affected by many parameters of the film preparation, such as substrate treatment and temperature, the chemical composition of the substrate, the deposition rate, and the purity of the deposited material. This results in a large phase space in which many local minima coexist.

In the following, the method to measure the film thickness and morphology with XPS is briefly explained followed by the experimental results for all molecules that were investigated in this dissertation.

### 2.2.1. Morphology information from spectroscopic data

In order to gain morphology information one needs to determine the thickness of the adsorbate layer first. PES delivers this information through the attenuation behavior of the substrate core level intensities with increasing amount of material adsorbed. This has been investigated by M.P. Seah and W.A. Dench [SD79] in the late 1970s. Equation (2.6) shows how the intensity of a substrate XPS line drops with increasing thickness  $z$  of an adsorbate layer.

$$I(z) = I_0 \cdot e^{-\frac{z}{\lambda}} \quad (2.6)$$

$\lambda$  is the inelastic mean free path of the electrons which is the distance an electron travels through the film before it scatters inelastically. More recent publications ([BN79], [BN80], [BN82], [CS97], [PJ09]) also account for elastic scattering. However, these elastic effects have only little influence on the results for  $\lambda$  and, in particular, cancel out for comparative statements which are made in the following. They are therefore neglected. Equation (2.6) assumes that the overlayer grows layer by layer and that the film has a homogeneous thickness. However, that is not always the case and this is the point where morphology information comes into play. A crucial property of the PES measurement is that the major part of the substrate signal comes from the thinnest areas of the adsorbed film. Therefore this **thickness is a lower limit**.

Morphology information can be gained from the comparison of this thickness to the nominal one. The determination of the latter needs more effort, and it is defined as the thickness that the film would have if it grew layer by layer. By comparison of the nominal thickness to the attenuated substrate signal intensity one can derive a qualitative surface morphology. Three requirements have to be met in order to measure the nominal thickness:

- An investigation method in which the signal changes with increasing thickness ( $\rightarrow$  XPS),
- A very stable evaporator and a monitor that controls its output,
- A reference point for calibration.

In this thesis, the first point was realized with the standard evaporator design used in the EPII. It consists of a copper cylinder with four holes for the heating filaments and one

hole for a glass tube filled with the organic material. On top of it a plate with a pinhole is mounted connected with a thermocouple that measures the temperature. In addition, a shutter is installed with which the evaporation can be interrupted. This design results in an evaporator which is very stable in temperature and at the same time reacts fast at changes in the heating current. A quadrupole mass spectrometer mounted perpendicular to the evaporator (only ionization cage in molecular beam) is used to control its output.

The reference point used for the calibration of the XPS attenuation is the PTCDA monolayer on Ag(111). One can very easily prepare it and it has been intensively investigated in the past [STS<sup>+</sup>00], [TES<sup>+</sup>02a], [ZKS<sup>+</sup>06a], [KUS04], [KHT<sup>+</sup>08]. With the help of this monolayer one can determine how much it attenuates the substrate signal and extrapolate the thickness from the known interlayer distance. All thicknesses other than for PTCDA are measured in PTCDA monolayer equivalents and then are multiplied by 3.22 Å which is the distance of neighboring layers in the PTCDA crystal.

With the help of the reference point the evaporation rate of the evaporator can be calibrated by measuring the evaporation time needed to deposit an amount of material that attenuates the substrate as much as the PTCDA monolayer.

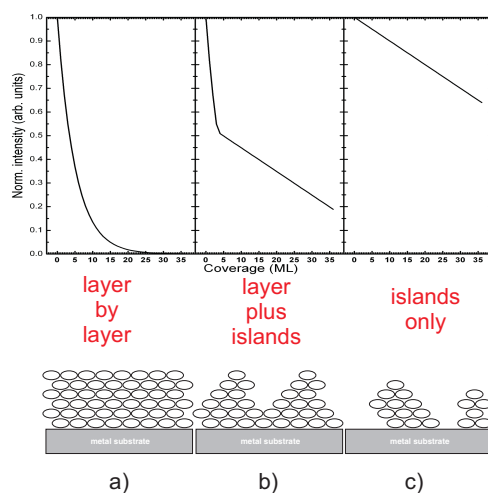


Figure 2.7.: Attenuation behavior of the substrate XPS signal with growing film thickness for the three growth modes: a) layer-by-layer, b) islands + layer and c) islands only.

Figure 2.7 shows the effect of different growth modes on the substrate signal attenuation in XPS. In this Figure and in the following ones the x axis represents the nominal thickness and the y axis the substrate signal intensity which is a measure of the number of closed layers. Figure 2.7 a) represents the ideal case of layer-by-layer or Frank-van-der-Merve growth. Part b) illustrates the layer + island or Stranski-Krastanov growth mode, in which the signal behaves like in part a) until islands start to grow. As soon as islands evolve signal decreases because much signal still originates from the area between the islands. This fact is also the reason for the even weaker attenuation of the substrate XPS signals for the islands only or Volmer-Weber growth in 2.7 c).

These growth modes and the surface roughness connected to them is in many cases not that distinct. The borderline between a rough layer-by-layer to a Stranski-Krastanov

## 2. Influences on the energetic position of the transport levels

---

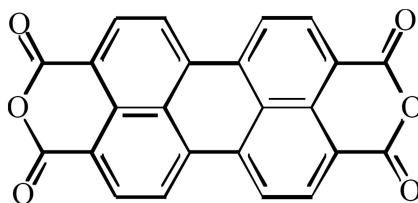


Figure 2.8.: Chemical structure of Perylene - 3,4,9,10 - Tetracarboxylic Dianhydride.

growth is diffuse. In order to obtain a further reference for a growth that is very close to van-der-Merve growth, the system PTCDA on Ag(111) was chosen which has the advantage of being investigated in detail with many experimental methods. T. Graber ([Gra09] and [Gra]) did a very careful investigation of this matter. With the help of these values one can now compare other molecules and their  $\lambda$  at a kinetic electron energy of 885 eV to the ones of PTCDA (in the following referred to as  $\lambda_{PTCDA} = 22.7 \text{ \AA}$ ) and the closer they are the smoother are the films. In the next Subsection experimental results will be presented for PTCDA, Alq<sub>3</sub>, CuPc, DIP (as a function of preparation) and PBI-H<sub>4</sub>. Only the x-axis in the data plots for all of these molecules has error bars, which reflects the evaporator stability of  $\pm 10\%$  between different preparation events and are therefore only a part of the overall error. The remaining error originates from the thickness calibration due to the attenuation of the PTCDA monolayer and affects the scaling of the x-axis. The intensity ratio between the clean silver and the actual film thickness can be determined very precisely and therefore no error bar is given for the y-axis. All deviations of the attenuation on this axis are due to growth effects, such as deviations from layer-by-layer growth. The error of  $\lambda$  therefore reflects how close the actual growth mode is to layer-by-layer growth - the larger the error the farther away.

### 2.2.2. Growth mode of PTCDA

For PTCDA (structure in Fig. 2.8) on Ag(111) much literature exists which contains the optimal preparation recipe to obtain very smooth and well long range ordered films ([Kil02], [KUS04], [MGS<sup>+</sup>06], [CSS<sup>+</sup>03], [For97]). In her PhD thesis, T. Graber prepared several series of films with increasing thickness and monitored the decrease of the intensity of several silver substrate XPS lines. These measurements were done at the "Neue ESCA" in Würzburg with an unmonochromatized X-ray source and later repeated at BESSY in Berlin with several photon energies. The results for the silver substrate lines are given in Table 2.2.

Since these measurements were done in the same UHV chamber and under the same preparation conditions ( $T_{Substrate} \cong 210\text{K}$ , deposition rate about 1 ML / min), no further data will be shown in this work.



Table 2.2.: Values for the IMFP for different kinetic energies of the electrons in PTCDA on Ag(111). Values of electron escape depths for different silver lines are from T. Graber ([Gra] and [Gra09]).

$E_{kin}$ in eV	$\lambda$ in ML	$\lambda$ in Å	core level (excitation line)
1480	8.56	27.6	Ag 4d (Al $K\alpha$ )
1250	9.16	28.4	Ag 4d (Mg $K\alpha$ )
1115	7.14	22.2	Ag 3d (Al $K\alpha$ )
913	5.90	18.3	Ag $3p_{\frac{5}{2}}$ (Mg $K\alpha$ )
885	7.31	22.7	Ag 3d (Mg $K\alpha$ )
683	5.91	18.3	Ag $3p_{\frac{5}{2}}$ (Mg $K\alpha$ )
652	7.38	22.9	Ag $3p_{\frac{3}{2}}$ (Mg $K\alpha$ )
335	3.01	9.3	Ag - Auger $_{MVV}$ (Mg $K\alpha$ )

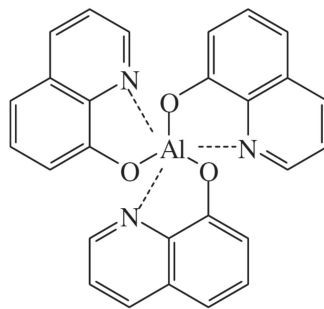


Figure 2.9.: Chemical structure of Aluminum Tris(8-Hydroxyquinoline).

### 2.2.3. Growth mode of Alq<sub>3</sub>

The geometric structure of the Alq<sub>3</sub>-molecule is very complex (chemical structure in Fig. 2.9), which hinders the formation of a simple crystalline structure. Nevertheless, M. Brinkmann et al. [BGM<sup>+</sup>00] found three different crystallographic phases in X-ray powder diffraction measurements of which two exhibit triclinic and one a trigonal structure. The hydroxyquinolines of two neighboring molecules align in these phases and have distances between 3.5 and 3.9 Å. M. Brinkmann et al. also investigated thin films of the molecule and could not find any diffraction signals for film thicknesses of up to 100 nm that were prepared at substrate temperatures up to 425 K. Therefore one can expect these films to be amorphous, which does not mean that they have no crystalline structure at all but that the order is constrained to the nearest neighbors. An advantage

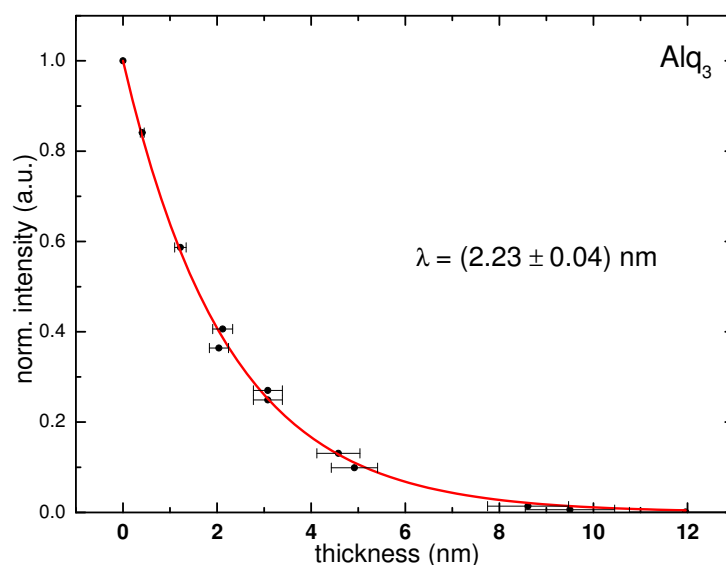


Figure 2.10.: Thickness dependent attenuation of the Ag 3d intensity for Alq<sub>3</sub>.

of this growth behavior is that one can exclude of Stranski-Krastanov and Volmer-Weber mode and assume these films to exhibit a low surface roughness, because no large Alq<sub>3</sub> crystallites are formed. Figure 2.10 shows the thickness dependent change of the Ag 3d peak intensity. This intensity can be found on the y axis and is normalized to the intensity of the clean silver substrate. The inset shows the result of a fit of equation (2.6) to the data points with  $\lambda_{Alq_3} = 22.3 \text{ \AA}$  for a kinetic electron energy of 880eV. This number is very close to the one of PTCDA measured by T. Graber and confirms the high quality of her films. All the films that appear as data points in Figure 2.10 were prepared at **substrate temperatures** between room temperature and 393K and **evaporator temperatures** between 544K and 554K.

In summary, Alq<sub>3</sub> forms very smooth films with a low degree of ordering. The fact that the fitted curve is for all points within the error bars, justifies the choice of  $\pm 10 \%$  for the relative error in film thickness and shows the high stability of the evaporator utilized.

## 2.2.4. Growth mode of CuPc

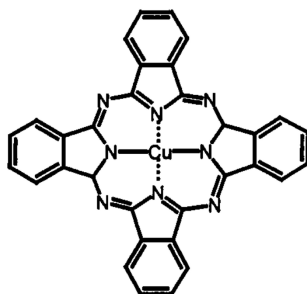


Figure 2.11.: Chemical structure of (29H, 31H-Phthalocyaninato(2-)-N29, N30, N31, N32)Copper.

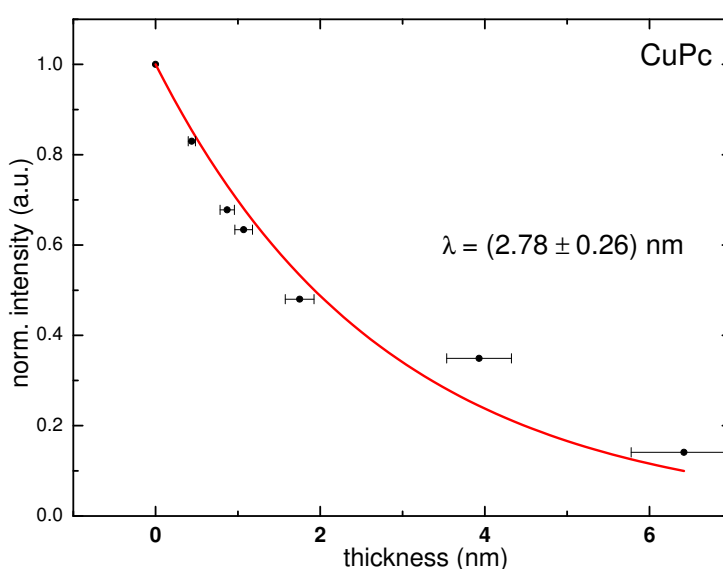


Figure 2.12.: Attenuation of the silver substrate with increasing CuPc coverage for  $T_{Substrate} < 200K$

Only little literature is available for multilayer films of CuPc (structure given in Fig. 2.11) on Ag(111). K. Manadhar et al. [MEP<sup>+</sup>07] investigated thin films (less than two layers) of this system with STM at room temperature and after annealing. As soon as a second layer was grown they found an ordered structure at the surface with the lattice constants of 12.3 Å and 15.3 Å and an angle of 86° between them.

However, there is no information on the crystalline structure at low temperatures given, and structural measurements have not been conducted in this work. Since smooth layers were the aim of this investigation, the films were prepared at very low temperatures (90 - 200K) and are assumed to consist of only small crystalline regions. The temperature

## 2. Influences on the energetic position of the transport levels

---

of the evaporator was about 670K. Figure 2.12 shows the data for CuPc. The exponential decrease and the  $\lambda_{CuPc}$  value of **27.3 Å** indicate a good film quality. However, a closer look to the fit reveals that the first four points are below the fitted curve and the last two above. Therefore two lines that intersect at 2 nm would also suit the growth behavior. Since no more points for thicker films have been measured for this molecule, it can be stated that the film growth is at least up to 2 nm (corresponding to about six layers) layer by layer like.

### 2.2.5. Growth mode of DIP

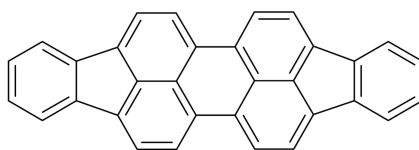


Figure 2.13.: Chemical structure of Diindeno-Perylene.

In the respective literature DIP (for structure see Fig. 2.13) is mainly grown on silicon oxide or gold. For these substrates it is possible to grow well ordered films which was checked with XRD measurements by A.C. Dürr et al., F. Schreiber et al. and S. Kowarik et al. ([Sch04], [Dür02], [KGS<sup>+</sup>06], [KGS08], [DNSF<sup>+</sup>06]). However, A.C. Dürr already found signs of competing growth modes of DIP films on silicon oxide. The substrate that was used in this work is Ag(111) and the growth of the DIP films strongly depended on the temperature of the sample during deposition. Three regions with different growth behavior depending on the substrate temperature could be identified:

- Below 150K
- About 210K
- Above 350K

This categorization is based on the different valence level UPS spectra and will be discussed in detail in the Sections 2.5 and 2.6. In the following, the growth modes for the different substrate temperature regions will be presented.

#### Below 150K

At low temperatures the mobility of the molecules decreases and the DIP films mainly grow in the crystalline phase that is induced by the first layer (see SPALEED data in Subsection 2.5.1). Due to their low mobility, the molecules are not able to form large crystals. However, the SPALEED data shows a clear diffraction pattern up to a thickness of at least five layers. The spots in this pattern are quite broad which is a sign for low coherence of the refracted electrons. The reason for this can be, e.g., the formation of very small crystals. Figure 2.14 shows the attenuation of the silver substrate signal with

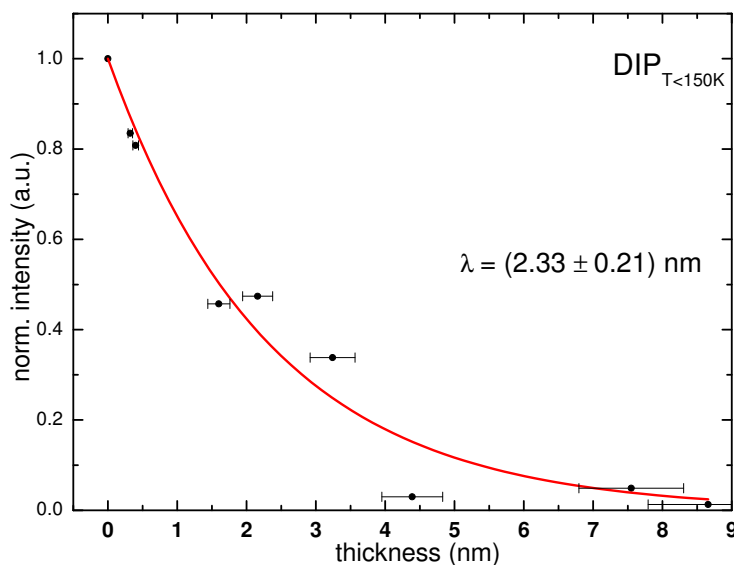


Figure 2.14.: Thickness dependent attenuation of the Ag 3d intensity for DIP prepared at substrate temperatures below 150K.

growing DIP thickness. The exponential decrease and the value for  $\lambda_{DIP,150K} = 23.3 \text{ \AA}$  resulting from the fit to the data indicate that the DIP films are very smooth, also compared to PTCDA. A drawback of this low temperature preparation is that the phase is not stable. As soon as the temperature rises the films started to reorganize which is even visible by eye. Figure 2.15 shows this effect. One can see the front part of the sample holder with the round Ag(111) crystal in the center of the picture. There are two regions visible on this crystal, a smaller round shaped marked as a), where the electron beam of the IPS setup hit the sample and the surrounding region b) with a greenish color. The beam damage during the IPS measurement has immobilized the molecules in region a) and it remained transparent, whereas the rest of the thin film could reorganize and become visible to the eye.

### About 210K

The SPALEED data (Section 2.5.1 shows that the crystals in this phase are relatively larger which results in smaller spot widths in the diffractogram. At the same time it showed a superposition of three different structures and in some case became diffuse. With the help of the ARUPS measurements (Section 2.6.3) this could be related to a change in the crystal phase for the topmost layers only.

This explains the slightly bigger  $\lambda_{DIP,210K} = 25.4 \text{ \AA}$  extracted from the fit in Figure 2.16. The morphology for this preparation temperature is only a little rougher than for 150K, which corroborates the ARUPS findings of a change in the topmost layers only. However, this changes if the films are not prepared in one step. As soon as one evaporates a second or third time on the same sample the layer starts to form islands. In Figure 2.17 an exponential decay was fitted to the data ( $\lambda'_{DIP,210K} = 46.9 \text{ \AA}$ ) but one could easily

## 2. Influences on the energetic position of the transport levels

---

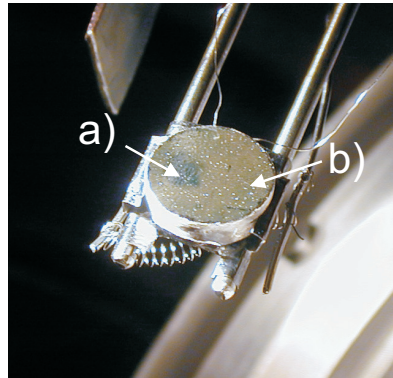


Figure 2.15.: Photograph of the Ag(111) crystal. The DIP film has been prepared at 150K and cooling was stopped. This picture was taken after seven hours of measurement at RT. Arrow a) points to the part destroyed by IPES and arrow b) to the intact part.

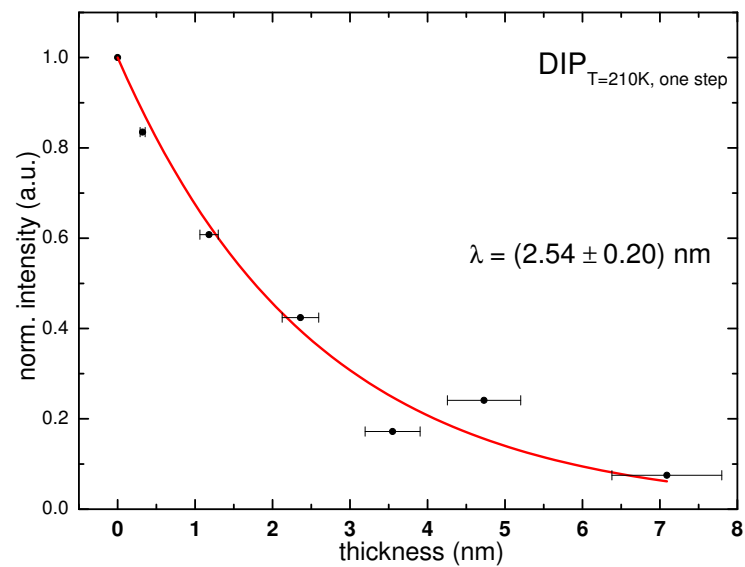


Figure 2.16.: Thickness dependent attenuation of the Ag 3d intensity for DIP prepared at substrate temperatures of about 210K.

insert two lines crossing at a thickness of 1.2 nm. This behavior can be explained with the rearrangement of the upper layers after the first deposition. The next time material is evaporated on this film there are regions with two different crystalline orientations which leads to the formation of islands and strong Stranski-Krastanov growth.

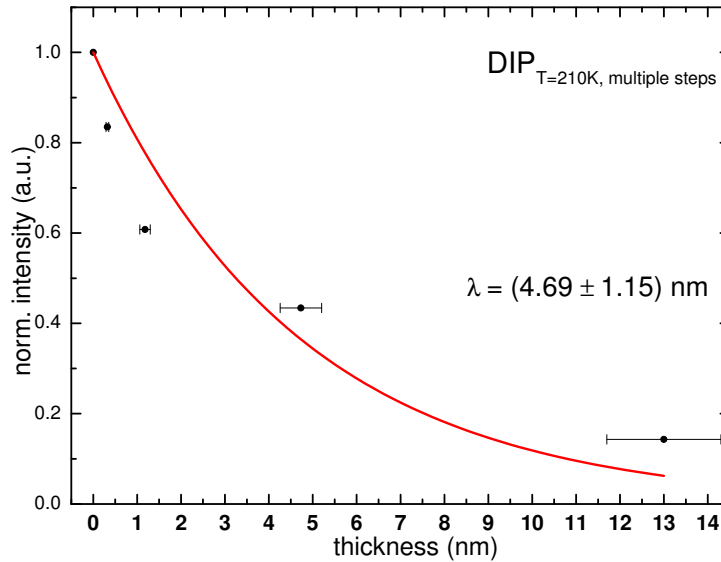


Figure 2.17.: Growth mode for DIP on Ag(111) at  $T_{Substrate} = 210\text{K}$ . The data points were all measured on the same day.

Figure 2.18 illustrates the instability of the crystalline phase(s) of the 210K preparation. No matter if the film is slowly annealed by simply turning off the cooling or if rapidly heated to 350K for a few minutes, the crystal starts to change color. At the same time the XPS signals of the substrate rise and the carbon signal decreases. Since there is no evaporation of material at 350K (see [Dür02]) and the film becomes visible. In the picture in Figure 2.18 the film seems to scatter the light diffuse which means that the structures the molecules form are in the order of  $\mu\text{m}$ . Interference effects of smaller structures would only lead to a change in color.

### Above 350K

At substrate temperatures above 350K we find a phase transition in the first layer. The interaction with the silver becomes weaker and the diffraction pattern in the SPALEED vanishes. Therefore the DIP grows in its preferred structure which is according to the size of the unit cell an upright standing crystalline phase (Subsection 2.5.1). Even though it has little contact with the substrate it still is very stable and even after cooling back to room temperature it will not change. Figure 2.19 shows the growth behavior if the films are prepared in one step. The larger  $\lambda_{DIP,350K}$  of  $30.7 \text{ \AA}$  indicates that these films are rougher and that they consist of a layer plus islands. This gets even more pronounced if one tries to grow a second layer on the first one. In Figure 2.20 one can see that after

## 2. Influences on the energetic position of the transport levels

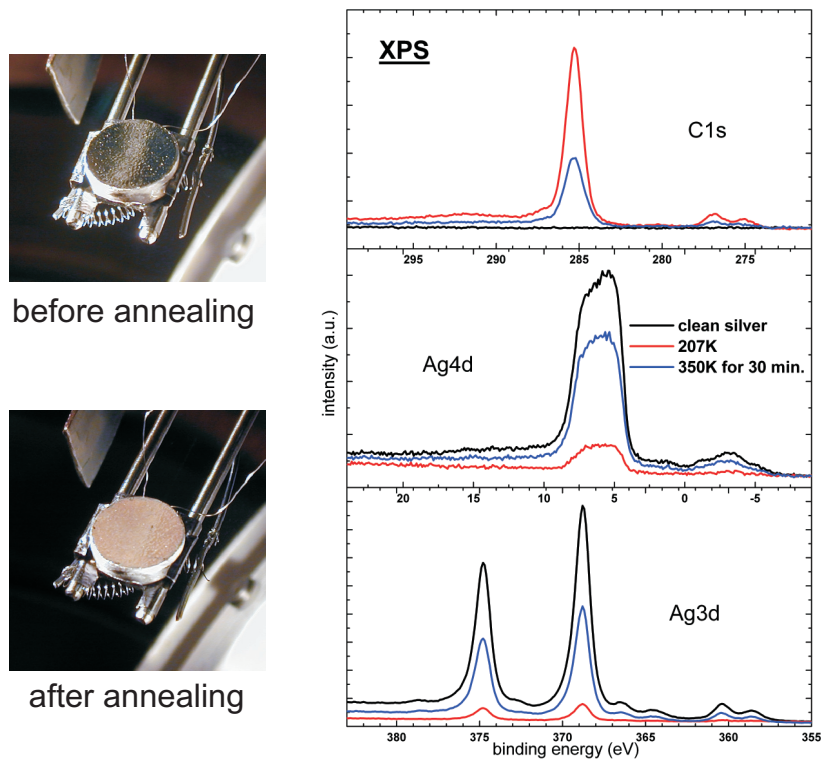


Figure 2.18.: On the left side one can see the photograph of a film prepared at 210K (top) and the same film after 30 minutes at 350K (bottom). The right side shows the corresponding XPS spectra for the C 1s, Ag 4d and Ag 3d.

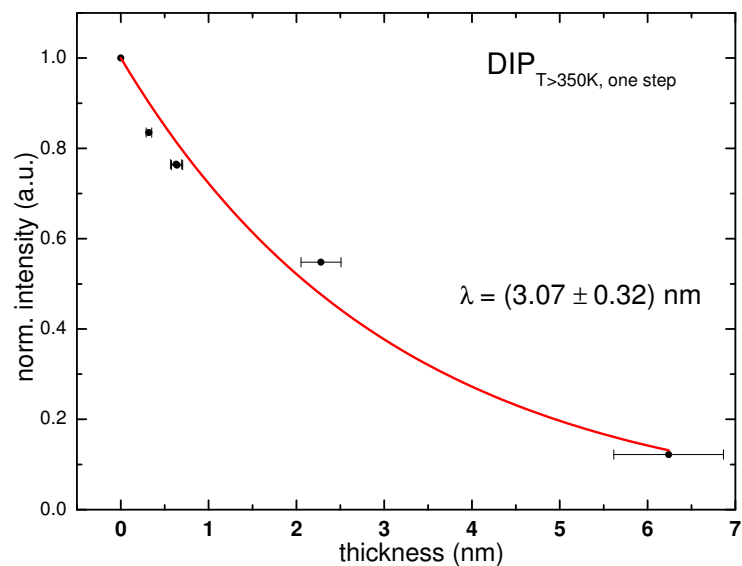


Figure 2.19.: Thickness dependent attenuation of the Ag 3d intensity for DIP prepared at substrate temperatures above 350K.



the first step at 0.5 nm the normalized intensity decreases very slowly. One can therefore conclude that the second evaporation mainly increases the crystallites in the direction perpendicular to the surface.

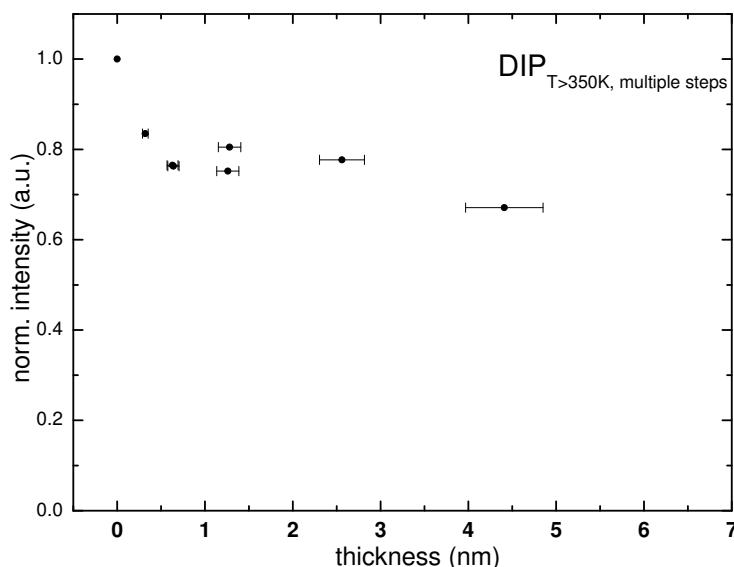


Figure 2.20.: Growth behavior for DIP at  $T_{\text{Substrate}} = 350\text{K}$  if the layers are prepared in more than one step.

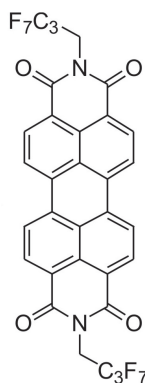


Figure 2.21.: Chemical structure of N,N' - Di(2,2,3,3,4,4,4 - Heptafluorobutyl) - 3,4,9,10.

### 2.2.6. Growth mode of PBI-H4

PBI-H<sub>4</sub> (structure in Figure 2.21) grows in a so-called slip-stacked face-to-face crystalline structure if one grows single crystals from a toluene solution which was investigated in the group of F. Würthner ([Che06], [OLB<sup>+</sup>07]). The distance between two neighboring perylene cores in these crystals was determined to 3.31 Å. However, the crystallinity of thin films has not been investigated so far and is therefore unknown.

## 2. Influences on the energetic position of the transport levels

---

Since the growth behavior of this molecule has been investigated in more detail in the diploma thesis of M. Scholz ([Sch08] and [SSK<sup>+</sup>09]), no data will be shown and the results from this thesis are presented. All thin films in this work were grown at room temperature. M. Scholz investigated the growth mode for PBI-H<sub>4</sub> on Ag(111) for  $T_{\text{Substrate}} = 150\text{K}$  and for  $T_{\text{Substrate}} = \text{RT}$ , and he found an IMFP of  $\lambda_{\text{PBI-H}_4,150\text{K}} = 20.2 \text{ \AA}$  and  $\lambda_{\text{PBI-H}_4,\text{RT}} = 25.9 \text{ \AA}$ . These findings indicate a slightly rougher film at room temperature and that the low temperature films are very close to layer-by-layer growth.

### 2.2.7. Conclusions on growth modes

The data for all five investigated molecules has shown that all of them can be grown in very smooth films if the substrate temperature is sufficiently low. It also demonstrates that one needs to perform the XPS measurements for various thicknesses in order to be sure of the quality of the films. If new molecules or new substrates are used for which no information about the thin film structure is available, it is also necessary to complement the growth mode measurements by structural experiments. This combination is a requirement for thin films of high quality for which the transport level measurements result in reliable data.

## 2.3. Band alignment

The position of the frontier orbitals of the first layer of an organic adsorbate with respect to the metal substrate as well as their evolution with growing film thickness (subject of the next Section) depends on the interface. Thus it is strongly influenced by the substrate used and the type of interaction of the molecular film with it. In nearly all cases the vacuum level of adsorbate and substrate are shifted with respect to each other which is related to an interface dipole.

The following Section will present the two basic types of band alignment and the different interaction possibilities that determine the strength and sign of the interface dipole.

### 2.3.1. Vacuum level vs. Fermi level alignment

The two basic reference levels are the Fermi level, which determines the maximum energy to which electronic states are occupied, and the vacuum level at which electrons are not influenced by the solid from which they originate. The latter would be accomplished by a free electron at infinite distance from the surface but the electrons can be regarded as nearly free at a few hundred nanometers above the surface of a solid. However, in photoelectron spectroscopy the term vacuum level is used for an electron at rest just outside the solid where it still is affected by the surface potential and therefore is different from the "real" vacuum level. It is therefore important to specify the term "vacuum level alignment", since the only way to reach an alignment of the vacuum levels would be to place metal and organic at infinite distance from each other. A very good review on this aspect can be found in the paper of H. Ishii et al. [ISIS99] in which the authors defined the vacuum level above the surface as  $VL(s)$  and introduced the alignment of these (virtual) vacuum levels. The term "virtual" accounts for the fact that at an interface no vacuum level exists, since there is no vacuum any more. Additional to this alignment, H. Ishii et al. also introduced the existence of a dipole layer in between the metal and the organic which serves as a kind of bias voltage shifting the  $VL(s)$ 's with respect to each other. The origin of this dipole layer will be treated in more detail in the next Section.

Figure 2.22 illustrates the band schemes for the two different types of alignment. Note, that both types are similar at the interface and only differ in the evolution of the bands for growing thickness. In the case of vacuum level alignment no band bending will occur and the position of the orbitals with respect to the substrate Fermi level will be constant even for thick films. Since the interface dipole and the attributed shift of the vacuum levels depend on the substrate chosen, the measurement will provide different positions of the Fermi level between HOMO and LUMO for different substrates. In the case of Fermi level alignment (b) the bands will evolve such that within a thickness  $W$  the interface dipole is screened and the Fermi levels of substrate and adsorbate align. This means that the relative positions of HOMO and LUMO with respect to the substrate Fermi level do not depend on the substrate and should converge to a common value for sufficient thickness of the films. This thickness  $W$  should be much smaller for organic

## 2. Influences on the energetic position of the transport levels

than for inorganic semiconductors where the screening is done by free charge carriers moving to the interface in order to screen the interface dipole. The molecules can screen the interface dipole much more efficient by displacing their electron cloud. The model

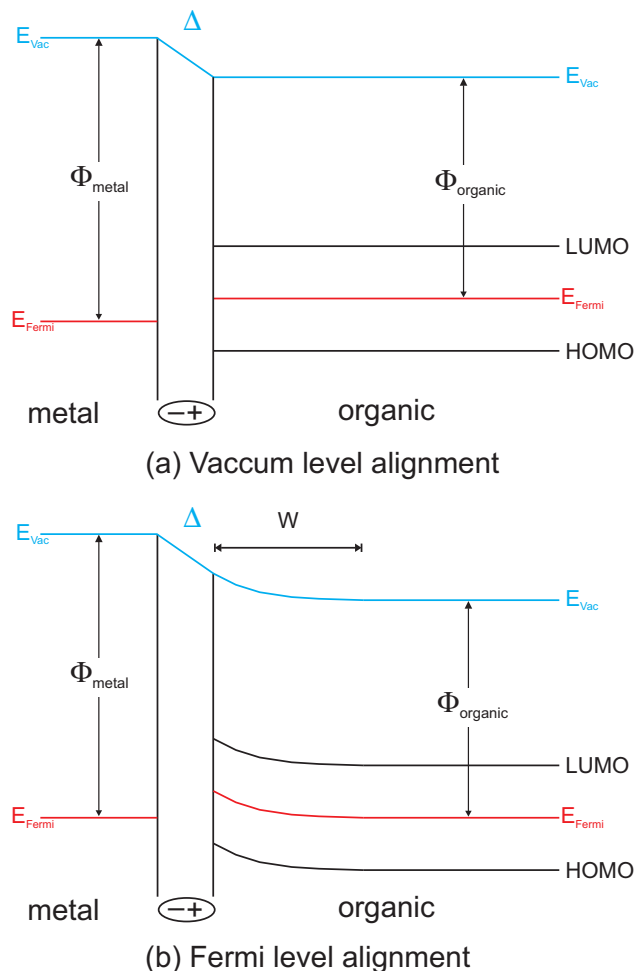


Figure 2.22.: Sketch of the two possible types of band alignment between metal substrate and organic semiconductors: (a) Alignment of the vacuum levels with a shift due to an interface dipole  $\Delta$ . (b) Alignment of the Fermi level after cancellation of the interface dipole within the diffusion layer of thickness  $W$ .

to describe the Fermi level alignment is inspired by the Schottky contact model for a inorganic semiconductor-metal contact.

The two types can be distinguished only by the evolution of the relative positions of HOMO and LUMO with respect to the substrate Fermi level with growing film thickness at different substrates. In the band schemes the position of the Fermi level in the organic thin film was chosen to be in the middle between HOMO and LUMO where it is expected to be a priori. If the molecules in the film share a common Fermi level, it can be shifted by contaminants that act like a dopant. In addition, the molecule itself can act like a doped semiconductor by being rather electron drawing or injecting. Since this discussion

is quite complex and beyond the scope of this work, it will not be treated in detail. Ishii et al. [IHI<sup>+</sup>04] utilized Kelvin probe measurements to detect Fermi level alignment for C<sub>60</sub>, TPD and Alq<sub>3</sub> on different substrates and for growing thicknesses. Kelvin probe measures the work function and thus the position of the vacuum level and it does not suffer the limitation of sample charging that PES has, which limits the maximum thickness that can be investigated to about 100 nm. Ishii et al. found Fermi level alignment only for the case of C<sub>60</sub> for which the work function on different substrates converged to 4.44 eV at thickness of about 500 nm.

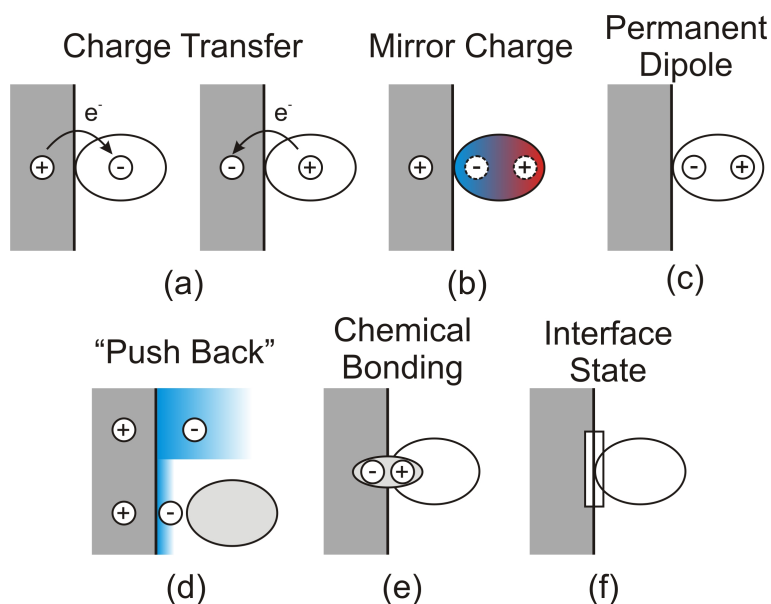


Figure 2.23.: Overview about the mechanisms that form and influence the interface dipole between metal and organic film. (a) Transfer of charge across the interface, (b) concentrated charge in the molecule can be screened by the metal through a mirror charge, (c) a permanent dipole of a molecule influences depending on the orientation of the molecules, (d) a rearrangement of the electron cloud over the metal surface, (e) a chemical bonding resulting in shared orbitals and an connected charge rearrangement and (f) the formation of an interface state serving as a buffer for charge.

### 2.3.2. Interface dipoles

Ishii et al. [ISIS99] investigated the interface dipole shift for various molecules on several substrates and found two trends:

- The deposition of an organic molecule on a metal mostly lowers the work function of the metal resulting in a negative sign for the interface dipole  $\Delta$ .
- $\Delta$  is mostly a monotonic function of the metal work function except for some cases - the higher the metal work function the more negative the  $\Delta$ .

## 2. Influences on the energetic position of the transport levels

Furthermore, Ishii et al. review the respective literature and provide six different ways such a dipole layer at the interface could be formed. Figure 2.23 shows a series of sketches that picture the different mechanisms. Picture (a) illustrates the effect of charge transfer in which depending on the respective molecule either charge is transferred to the molecule or from the molecule to the metal leading to the formation of an ion. If in the adsorbate the electrons become concentrated the metal will screen this charge and a positive charge remains at the vacuum side (b). The simplest case of a dipole layer would be molecules with a permanent dipole moment as sketched in (c). (d) illustrates the probably most common way of lowering the metal work function by a back pushing of the charge density above the metal surface. Picture (e) shows the formation of shared electronic states via the formation of a chemical bond accompanied by an exchange of charge. Finally, the data of Ishii et al. indicate the existence of an interfacial state that serves as a buffer for charge and is able to influence the size of  $\Delta$  - see (f).

The effect described as "interface dipole" corrects the simple picture of vacuum level alignment and includes the interaction between organic adsorbate and metal substrate. It is a crucial quantity since it determines the relative position of HOMO and LUMO with respect to the metal Fermi level in the case that no Fermi level alignment occurs. Table 2.3 summarizes values found in the literature and shows the experimental values for several combinations of molecules and substrates. The methods used to determine them are Kelvin probe and UPS measurements. It exemplifies the large variety of interface dipole values that can occur for a single molecule as well as the trends stated above.

Table 2.3.: Experimentally determined values for the interface dipole strength for several combinations of molecules and substrates. The values are extracted from two papers by H. Ishii et al.<sup>a</sup> ([ISIS99] and [IHI<sup>+</sup>04]) and one paper by I. G. Hill et al.<sup>b</sup> [HRKH98].

Organic <sup>a</sup>	Sub.	$\Delta$ /eV	Organic <sup>a</sup>	Sub.	$\Delta$ /eV	Organic <sup>b</sup>	Sub.	$\Delta$ /eV
TPD			DP-NTCI			PTCDA		
	ITO	-0.3		Al	0.4		Mg	1.3
	Ca	-0.6		Au	-0.7		In	0.5
	Mg	-0.6	TCNQ				Sn	0.4
	Ag	-1.0		Au	0.2		Au	-0.1
	Cu	-1.2	H <sub>2</sub> TPP			Alq <sub>3</sub>		
	Au	-1.1		Mg	-0.3		Mg	-0.2
C <sub>60</sub>				Al	-0.6		Ag	-0.6
	Cu	0.3		Au	-1.0		Au	-0.5
Alq <sub>3</sub>			H <sub>2</sub> T(4-Py)P			$\alpha$ -NPD		
	Al	-1.0		Mg	-0.1		Mg	-0.3
	Au	-0.9		Al	-0.4		Au	-1.0

Continued on next page...

Organic <sup>a</sup>	Sub.	$\Delta/eV$	Organic <sup>a</sup>	Sub.	$\Delta/eV$	Organic <sup>b</sup>	Sub.	$\Delta/eV$
ZnTPP				Au	-0.6	CBP		
	Mg	-0.7	TTC				Mg	-0.4
	Al	-0.7		Mg	-0.3		Ag	-0.5
	Au	-0.6		Al	-0.5		Au	-0.5
TTN				Au	-0.7			
	Au	-0.4						

### 2.3.3. Experimental results

The size of the interface dipole and therefore the starting point of the band alignment can be measured with the help of UPS. Since the secondary electron cutoff defines the position of the vacuum level in a UPS spectrum, the size of  $\Delta$  is defined as the shift between the clean metal sample and a monolayer of organic molecules. The films should not be much thicker because the size of  $\Delta$  would then also depend on a possible band bending with growing thickness or an increased surface roughness. The results for the molecules on Ag(111) investigated in this work are shown in Table 2.4.

Table 2.4.: Results for interface dipole ( $\Delta$ ) induced shift of the vacuum level for different molecules. The values are determined by the shift of the secondary electron cutoff between clean Ag(111) and the multilayer film.

molecule	$\Delta/eV$
Alq3	-0.82
PTCDA	-0.10
CuPc	-0.44
TiOPc	-0.37
PBI-H4	+0.70
DIP < 150K	-0.18
DIP - 210K	-0.16
DIP > 350K	-0.22

## 2.4. Band bending

It was shown in the previous Section that the interface is very important for the position of the frontier orbitals relative to the substrate Fermi level. Once the second layer is formed

## 2. Influences on the energetic position of the transport levels

---

an additional shift of these levels can occur. There are several mechanisms driving this so-called "band bending". This concept of a bending of the bands with growing distance from an interface for organic semiconductors is influenced by the picture of a metal-inorganic semiconductor interface (Schottky contact) for which such observations were made.

In order to provide a complete picture, the theoretical considerations about bending and the experimental results of H. Ishii et al ([ISIS99] and [IHI<sup>+</sup>04]) will be reviewed first, followed by the experimental results of this work.

### 2.4.1. Theory of band bending in inorganic and organic semiconductors

In order to motivate this Section, the "classical" picture of a Schottky contact will be discussed first. Similar to the interface dipole described before, the metal and the semiconductor will arrange such that the vacuum levels align shifted by an interface dipole. This interface dipole can only be screened by the accumulation of charge carriers near the interface which happens on a short length scale on the metal side. The inorganic semiconductor has only few free charge carriers to screen the dipole. The length scale on which the screening takes place is typically a few hundred nanometers. Figure 2.24 (a) sketches this case for a n-doped inorganic semiconductor for which the Fermi level is located between the impurity level and the conduction band (the doped semiconductor was chosen, because of its higher amount of free charge carriers compared to the undoped case). This gradual screening causes a bending of the bands back to their original position with respect to the Fermi level and leads to the formation of a so-called space charge region in between metal and semiconductor.

Figure 2.24 (b) applies this model to an organic-metal contact. In addition to the screening of the interface dipole by charge carrier accumulation, organic molecules can rearrange their charge distribution such that they efficiently screen within a few molecular layers. The case of no band bending is shown in Figure 2.24 (c). In this "Flat band" case, the molecules are not able to screen the interface dipole which can be due to three reasons:

- The concentration of free charge carriers is too low to allow accumulation at the interface (high purity of the material).
- The polarizability of the molecules is too low.
- No common Fermi level in the molecular film exists which would drive an alignment through band bending.

A special case of band bending has been observed for Alq<sub>3</sub> and is sketched in Figure 2.24 (d). Alq<sub>3</sub> has a permanent dipole moment and if its thin films are grown without a light source present, these dipoles can align. This leads to a gradually growing electric field which steadily bends the bands. One of first who reported a gradual change of the HOMO of Alq<sub>3</sub> with growing thickness was I. G. Hill et al. [HMK00]. It was later investigated



in detail with Kelvin probe measurements and for much thicker films by H. Ishii et al. [IHI<sup>+</sup>04] who found out that this molecular dipole induced shift could be prevented by illumination of the sample with a 30W flashlight during the growth process. The shift of the Vacuum level was determined to be  $-0.05$  eV/nm. Finally, another special case of band bending needs to be mentioned. If the position of the frontier orbitals is determined with a charge producing method such as UPS or IPS, this charge can be screened by the metal near the interface within the process of photoemission. This effect should weaken proportional the distance of the interface and point in opposite directions for HOMO and LUMO, which is sketched in Figure 2.24 (e).

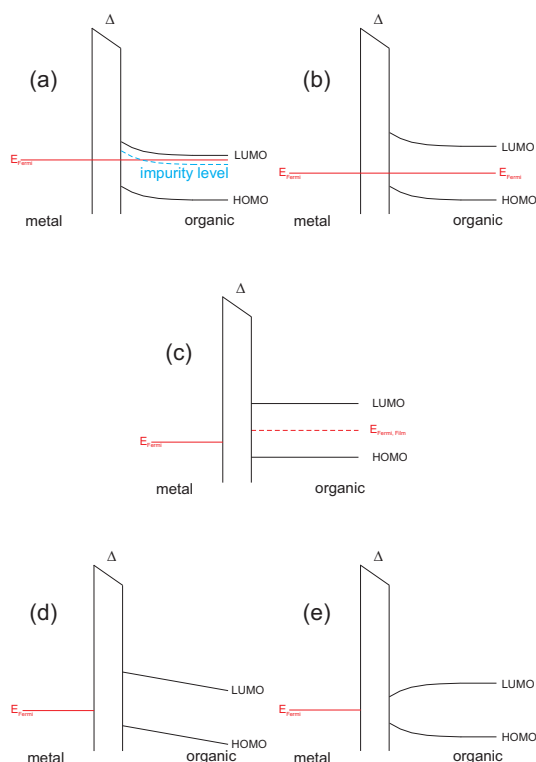


Figure 2.24.: Overview of the possible types of a band bending with growing film thickness in thin films of organic semiconductors. (a) Classical model from inorganic semiconductors of a charge carrier displacement induced bending. (b) Polarization induced screening of the interface dipole in the organic layer. (c) "Flat band" case due to the absence of a common Fermi level in the organic film or poor coupling of metal and adsorbate. (d) Special case bending for molecules with permanent dipole moment (e.g., Alq<sub>3</sub>). (e) Bending at the interface due to screening of the photoinduced charge near the metal surface.

### 2.4.2. Experimental results

H. Ishii et al. utilized Kelvin probe measurements to determine band bending for thin films of organic semiconductors, which only allow the determination of the work function

## 2. Influences on the energetic position of the transport levels

---

of the samples, but not the actual position of the orbitals. This could only be achieved by a combination of UPS and IPS, which provide the energetic position of HOMO, LUMO and the vacuum level on the same sample. The drawback of the latter method is that with increasing thickness charging becomes an issue, which has to be considered. The films presented in the following were therefore usually prepared with a thickness below 10 nm. Therefore the information is limited to the first 20 - 30 molecular layers. All peaks were evaluated at their onsets and the position of HOMO, LUMO and vacuum level is given with respect to the substrate (Ag(111)) Fermi level.

Note that the data was not intended to provide this information but in the process of evaluation it became clear that it can be extracted from the numerous data sets. The data sets for the molecules are therefore not complete and are especially lacking of IPS information for very thin films. However, the UPS data provides enough information to identify the different types of band bending unambiguously. In addition, some of the data points for the same molecule were recorded in different periods of time with up to two years in between (e.g., Alq<sub>3</sub>) and the good agreement of these measurements speaks for the quality of the data.

Only two types of band bending could be seen in the data - the "Flat band" case and the bending due to alignment of the permanent molecular dipoles induced. The latter could be observed in the case of Alq<sub>3</sub> for VL, HOMO and LUMO. The slope of the linear shift with increasing thickness is 0.05 eV/nm for all energy levels, which is in perfect agreement with the value reported by H. Ishii et al. [IHI<sup>+</sup>04]. All other molecules showed no shift of the VL or the LUMO with increasing thickness, except for the last two films in the data for DIP prepared at  $T_{Sub} < 150\text{K}$  in Figure 2.28. However, these two data sets are too few to identify a possible shift of these levels greater than the statistic fluctuation of the measurement.

For the small thicknesses of PTCDA (Fig. 2.25), DIP below 150 K (Fig. 2.28) and DIP at 210 K (Fig. 2.16) a gradual shift of the HOMO towards the Fermi level is observed with decreasing thickness. This is due to the chemisorptive interaction of the first organic layer and the silver substrate which leads to the formation of hybrid orbitals. In the case of PTCDA, the overlapping signals of the monolayer and the subsequent layers were separated by a fit of the peaks which increases the error in determination of the energetic position. A shift due to the screening of the photoinduced charge by the substrate can be excluded since it would also influence the position of the measured vacuum level, which remained constant.

In summary, the investigated molecules do not tend to a Fermi level alignment through a bending of the bands as was observed for the case of C<sub>60</sub> by H. Ishii et al. [IHI<sup>+</sup>04]. At least they do not within the thickness accessible by UPS (e.g., C<sub>60</sub> needs 500 nm). This fact is crucial if the energetic position of the frontier orbitals is determined, because it shows that the substrate used determines the position relative to its Fermi level by the interface dipole. Band bending plays therefore only a minor role in the thickness regime accessible by PES.

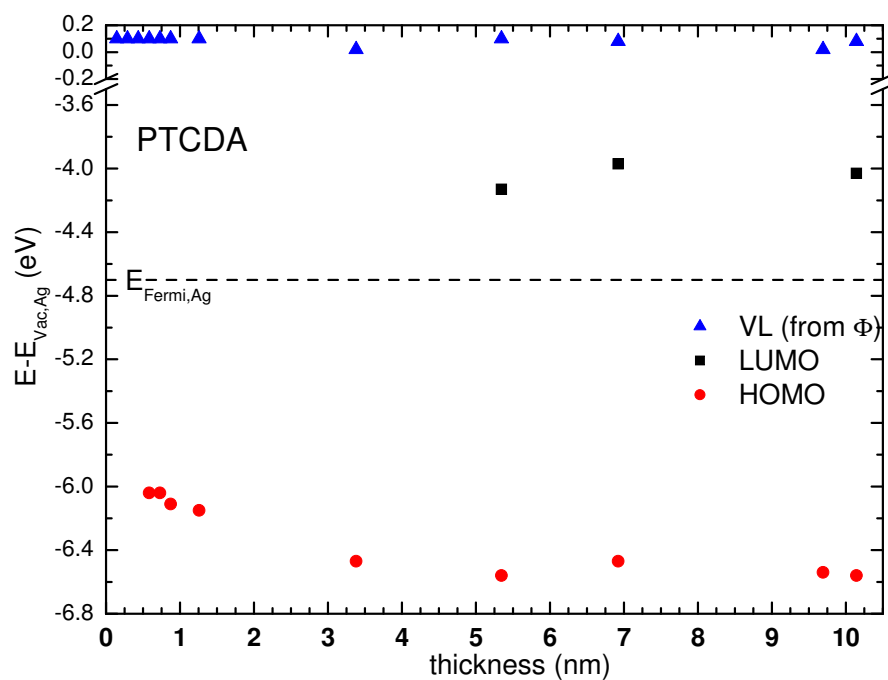


Figure 2.25.: Thickness dependent position of the frontier orbitals and the vacuum level for PTCDA

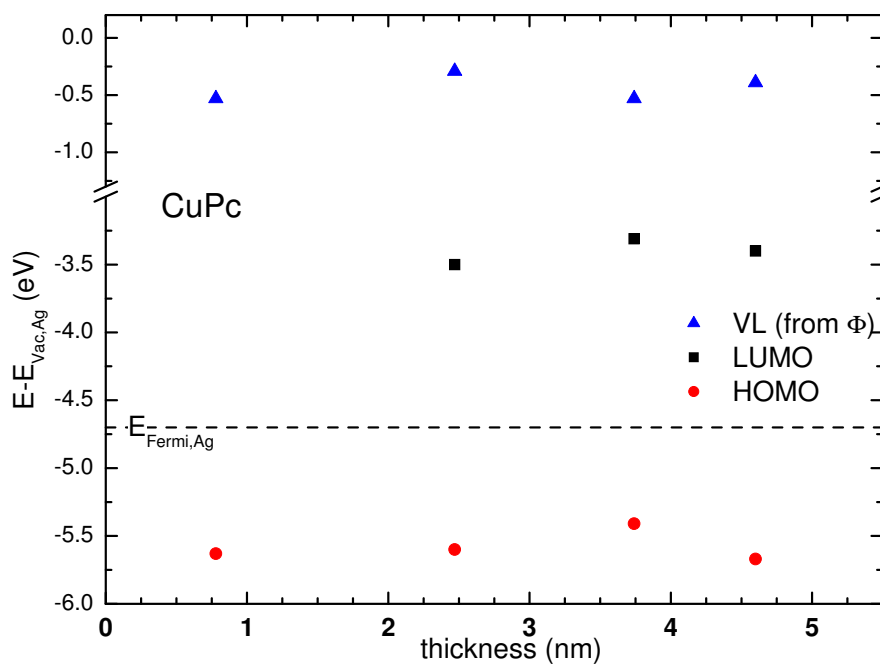


Figure 2.26.: Thickness dependent position of the frontier orbitals and the vacuum level for CuPc

## 2. Influences on the energetic position of the transport levels

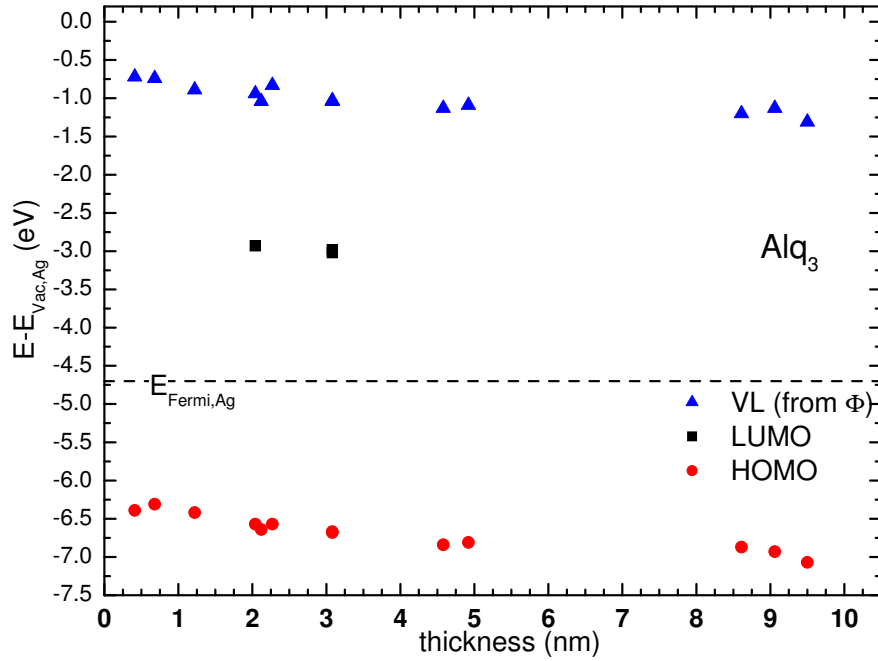


Figure 2.27.: Thickness dependent position of the frontier orbitals and the vacuum level for Alq<sub>3</sub>

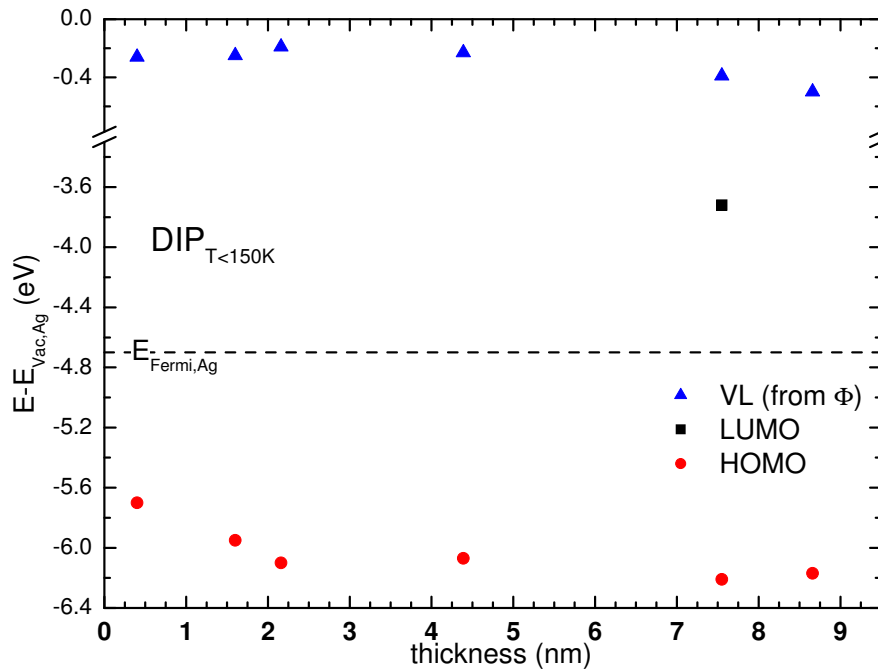


Figure 2.28.: Thickness dependent position of the frontier orbitals and the vacuum level for DIP grown below 150K substrate temperature

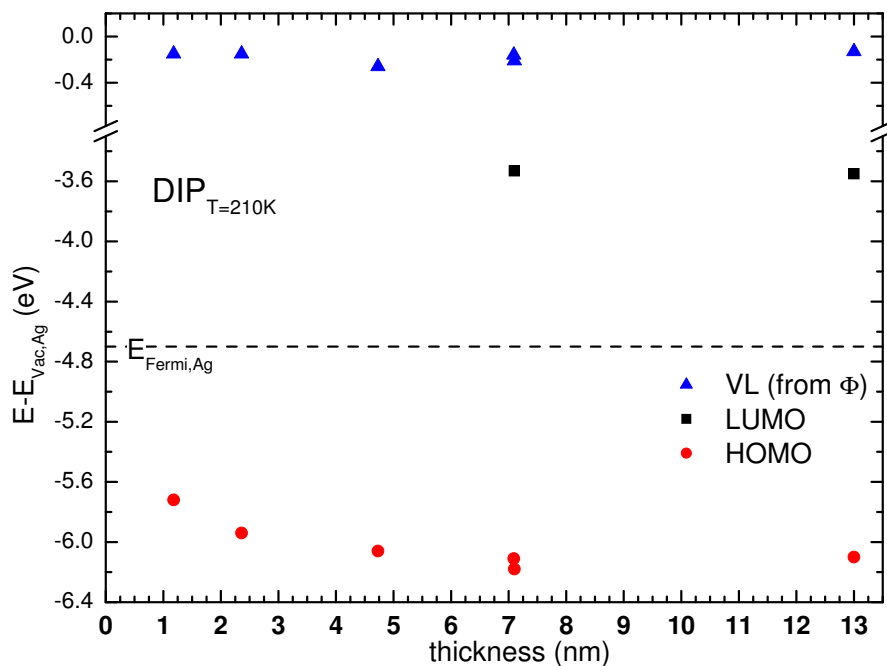


Figure 2.29.: Thickness dependent position of the frontier orbitals and the vacuum level for DIP grown at 210K substrate temperature

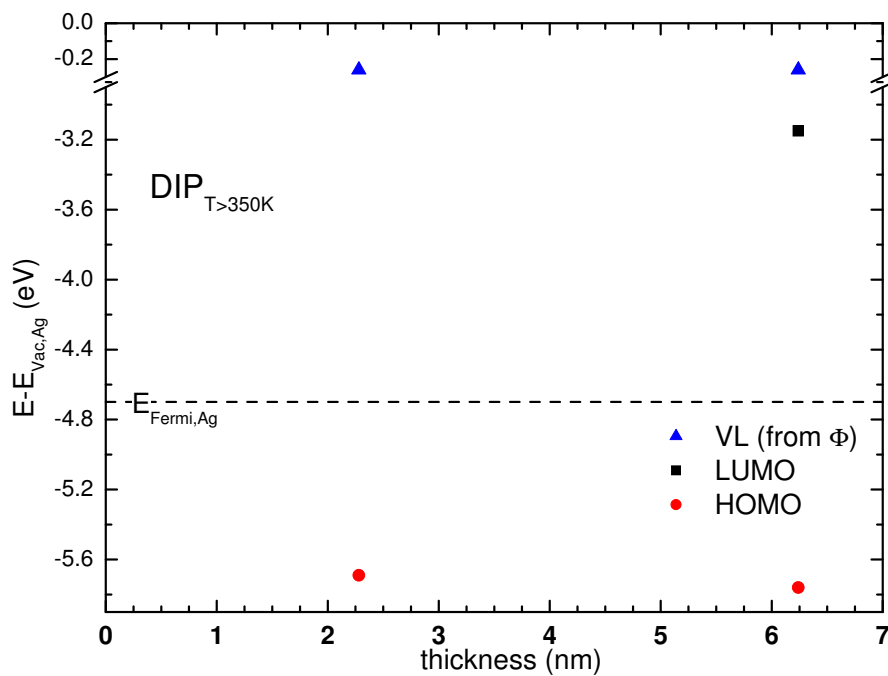


Figure 2.30.: Thickness dependent position of the frontier orbitals and the vacuum level for DIP grown above 350K substrate temperature

### 2.5. Diindenoperylene - an example of different geometric film structures for one molecule

The growth of organic molecular thin films is quite complex. Since the molecules are believed to form no covalent bonds in their crystals, it is assumed that weaker forces like van-der-Waals or electrostatic forces drive the relative arrangement of the molecules. In reality, there is a mixing of the forces and a broad transition region between full covalent and full van-der-Waals force exist. Therefore favor dipole or quadrupole moments as well as the geometry of the molecules certain arrangements of the molecules and obstruct others. If these conformations are regarded under a thermodynamic point of view, many shallow minima in the total energy of the system exist and transitions between them are possible with the help of energy input. This energy input can be provided by a heating of the sample during the deposition of the molecules or afterwards. On the other hand, a cooling of the sample decreases the mobility of the molecules during the deposition and inhibit the formation of the energetically optimized conformation. This results in microcrystalline or even amorphous films.

The second important factor is the interaction with the substrate which governs the structure of the first layer - the interface. The interplay between the first layer and the subsequent layers influences the growth mode of the films. As described in Section 2.2, the films can grow in three different modes depending on the misfit between the first layer and the natural structure of the single crystal corresponding to this molecule. The better both structures fit the more layer-by-layer like the films grow.

The influence of the structure on the measurement of the transport levels is one of the major topics in this work and it is therefore crucial to conduct structural measurements that can be correlated to the spectroscopic ones. Diindenoperylene proved to be an adequate candidate due to its rich set of multilayer structures. In the next two Sections, SPALEED as well as HREELS measurements for different substrate temperatures during preparation are shown.

#### 2.5.1. Dependence of geometric structure on sample preparation - (SPA)LEED - measurements

Spot profile analysis low electron energy diffraction (SPALEED) is able to measure surface unit cells in the sub-Ångström regime. It is therefore very suitable to measure the arrangement of two dimensional systems like monolayers of organic molecules on various substrates. The diffraction pattern also contains information about the symmetry of the molecules in this unit cell. The annihilation of certain sets of points allows the identification of symmetry elements like mirror planes, inversion centers, screw axes or glide planes. With the knowledge about them it is possible to develop models of the arrangement of the molecules in the surface unit cell.

If the thin films are homogeneous, SPALEED is also applicable to multilayer samples. In this case the development of a model is not trivial due to the third dimension - film thickness. For the measurement of the inter - plane distance perpendicular to the surface

a method like, e. g., XRD is necessary to complete the set of information needed for model development. Information about the surface unit cell and their change can still be detected on a very sensitive length scale. Such XRD measurements of DIP on gold, SiO<sub>2</sub> and Al<sub>2</sub>O<sub>3</sub> have been conducted by various groups and in the following their results will be used to interpret the data on silver.

The SPALEED data will be presented in the following way. First, the results for the monolayer are shown, which forms the basis of the multilayer films. Second, the results are presented for layers prepared below 150 K and above 350 K which both provide diffractograms explainable by a single superstructure, followed by the data for films prepared at 210 K that turned out to be a mixing of three phases.

The error bar of the graphic method of determining the superstructure matrices from the SPALEED diffraction pattern was discussed in the Diploma thesis of I. Kröger [Krö07] who also described the method in detail. The superstructure matrix entries have an error of  $\pm 0.04$ , which corresponds to a unit cell vector length uncertainty of  $\pm 0.13$  Å and an angle error of  $\pm 0.8^\circ$ . The unit cell area therefore has an error of  $\pm 3$  Å<sup>2</sup>.

### Monolayer DIP on Ag(111)

The first layer of an organic adsorbate is very important for the growth and structure of the next ones. It forms the interface to the metal surface and can be bound to it with forces anywhere between weak van-der-Waals forces and a covalent bond with the formation of new common orbitals. In order to explain the behavior of the multilayer DIP on Ag(111) with varying temperature during deposition, the change in the structure of the monolayer was investigated.

Since the SPALEED and PES measurements were performed in different vacuum chambers, the LEED diffraction patterns of the PES system will be shown first and will then be compared to the SPALEED diffractogram to ensure that the data can be correlated.

The preparation of the monolayer is fairly easy for DIP. A.C. Dürr [Dür02] investigated the desorption behavior of DIP on silicon oxide with X-ray diffraction and found out that the molecules start to desorb in a layer-by-layer process from the surface at temperatures above 420 K. In this work the silver crystal was heated up to 610 K in order to desorb the multilayer and a diffraction pattern representing the monolayer still appeared in the SPALEED. Usually a temperature between 470 and 490 K was chosen for the monolayer preparation.

Figure 2.31 (a) shows a photograph of the LEED screen in the PES system. One can clearly see six sets of spots which clearly contain a substructure. The arrangement of the six sets reflects the three fold symmetry of the (111) - plane of the silver substrate. Picture (b) shows a film of 5 - 6 ML thickness that has been annealed for 50 min. The sample already showed a change in color of the surface as described in Section 2.2.5 which means that the film already rearranged. Since the multilayer phase transition results in a different LEED pattern (see 2.5.1), the pattern in Figure 2.31 (b) is attributed to the underlying first layer. The diffraction pattern shows essentially the structure of (a) with much sharper spots which might be (partly) due to the fact that they were recorded at different temperatures (compare Fig. 2.33).

## 2. Influences on the energetic position of the transport levels

---

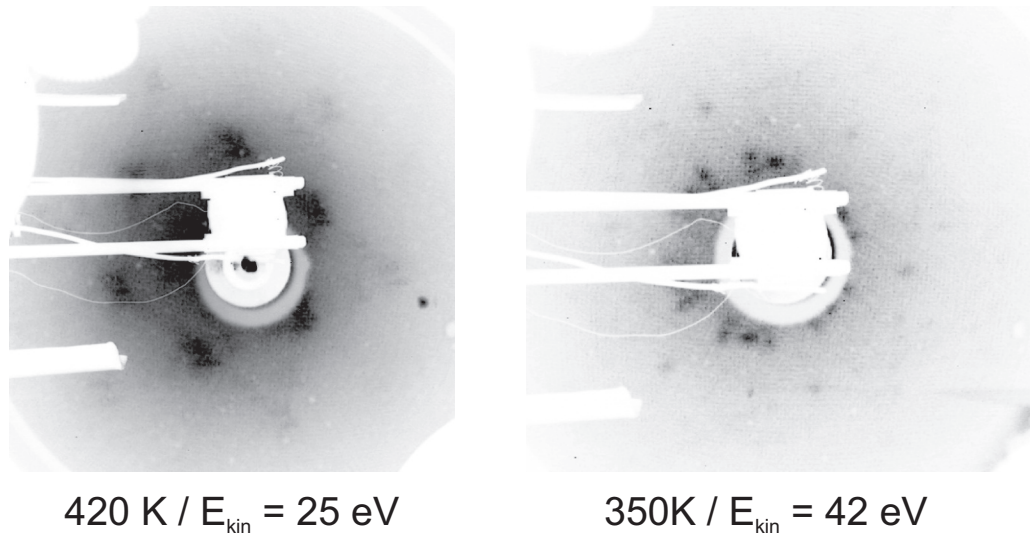


Figure 2.31.: (a) LEED pattern of a monolayer DIP on Ag(111). The monolayer was prepared by heating of a multilayer film to 420 K for 30 min. (b) Prepared by annealing a 5 - 6 ML thin film at 350 K for 50 min. It exhibits a structure close to the SPALEED monolayer structure.

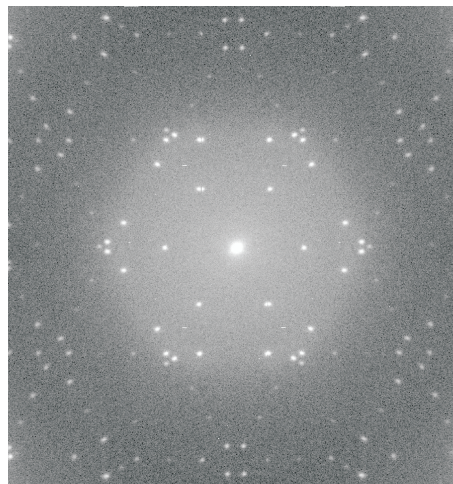


Figure 2.32.: SPALEED diffractogram of a monolayer DIP on Ag(111), prepared with a programmed temperature ramp to 480 K with a slope of 0.5 K/s. ( $E_{kin} = 35$  eV)



Figure 2.32 shows the complete SPALEED diffractogram of the DIP monolayer for better comparability to the LEED data, even though only a quarter of this diffractogram was actually measured. Previous measurements of this work of the whole pattern had revealed that it is possible to measure only a quarter and construct the diffractogram by mirroring of this quarter. The resolution of the complete pattern was quadrupled by this technique. The pattern is quite complex, and finding a solution for the unit cell of the superstructure is not trivial. However, later in this Section a unit cell will be presented that explains all spots.

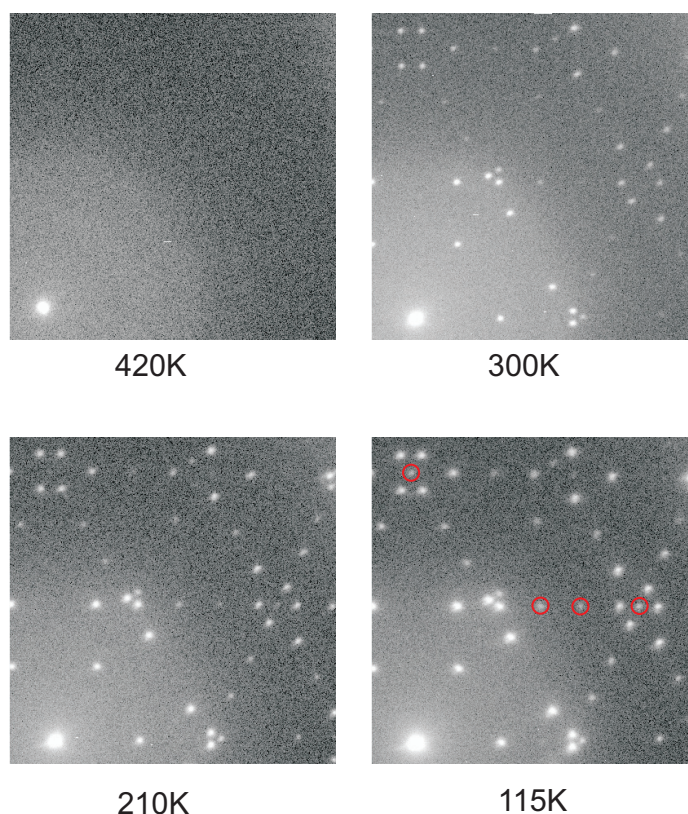


Figure 2.33.: This series of diffractograms shows the monolayer of DIP on Ag(111) for different temperatures. This monolayer was prepared by annealing of a multilayer film up to 480 K. Between each diffractogram the sample was cooled by liquid nitrogen at a rate of  $-0.5$  K/s. A vanishing of the structure can be observed for 420 K. The circles at 115 K mark spots that gradually appear with decreasing temperature. ( $E_{kin} = 35$  eV)

**Temperature dependent behavior** The diffraction pattern of the DIP monolayer shows a rich variation in its structure with varying temperature. Figure 2.33 shows a temperature series of diffractograms. The first diffractogram was recorded at 420 K, there no pattern visible except for a bright circle around the (0,0) - spot. With decreasing temperature (300 K) gradually the monolayer spots become visible and the circle gets weaker in intensity. In the pattern at 115 K some of the spots are marked with circles

## 2. Influences on the energetic position of the transport levels

that become more intense with decreasing temperature. Since the unit cell size does not change with temperature (next Section) and the intensity of these spots also varies with the kinetic energy of the incident electrons, this is attributed to the temperature dependence of the SPALEED measurement itself. Based on this series, a structural phase transition of second order has been found. It is second order because a broad transition region exists in which both phases coexist.

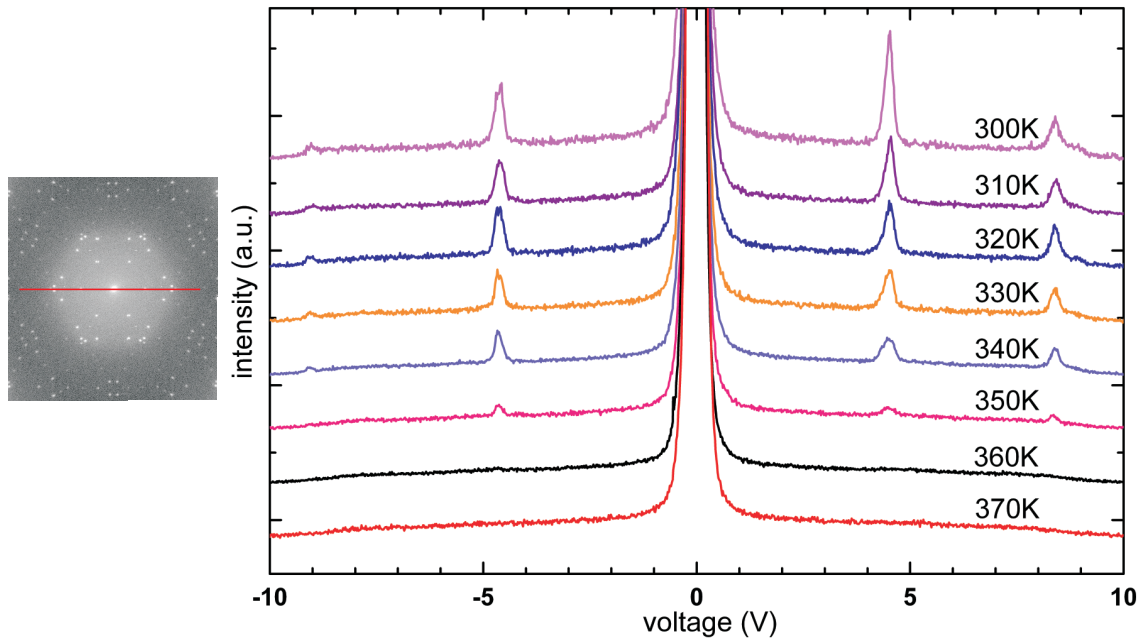


Figure 2.34.: Series of SPALEED line scans (300 K to 370 K) for a monolayer DIP on Ag(111). Between each scan the temperature was changed by 10K, and 20 min, were waited in order to give the system the time to reach equilibrium. On the left side, the position of the line scan in the diffractogram is marked with a line. ( $E_{kin} = 35$  eV)

**Phase transition** In order to investigate this phase transition in more detail a series of line scans through the (0,0) - spot was recorded, which is presented in Figure 2.34. For this measurement the temperature was changed in steps of 10 K and the sample was hold at this temperature for 20 min. It is therefore assumed that the system had enough time to reach thermal equilibrium. The position of the (0,0) - spot was corrected before every diffractogram in order to compensate temperature dependent changes of the geometry that would result in changes of the spot intensities. The gradual decrease of the superstructure spot intensities can be observed up to a temperature of 350 K and a complete absence at  $T \geq 360$  K.

## 2.5. Diindenoperylene - Different geometric film structures for one molecule

The line scan for  $T \geq 360$  K still shows the disk structure visible in Figure 2.33 with a radius of 7.4 Å. Since there are no rings but a disk, the molecules seem to have no preferred distance but a minimum distance of 7.4 Å. It can therefore be concluded that the molecules form a disordered phase in which either their intermolecular interaction, the molecule-substrate interaction or a combination of both is repulsive. Such a repulsive interaction of organic molecules is quite rare but has recently been observed for phthalocyanines on Ag(111) by C. Stadler et al. [CHK<sup>+</sup>09].

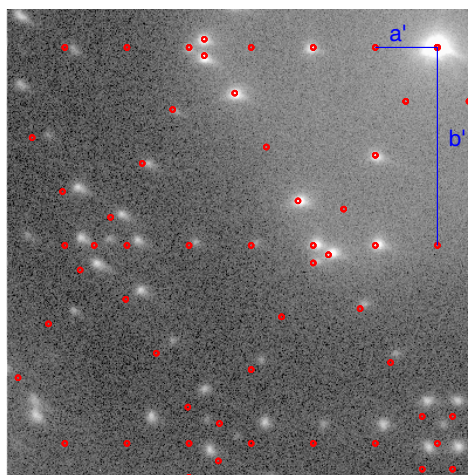


Figure 2.35.: Diffractogram of the monolayer DIP on Ag(111). The spots are the calculated positions of the reflexes and the lines show the reciprocal unit cell vectors  $a'$  and  $b'$ . ( $E_{kin} = 35$  eV)

**Unit cell of monolayer** SPALEED allows the determination of the unit cell parallel to the surface but it provides no information about the angle between the molecules and the surface as well as the distance between two adjacent molecular layers. Figure 2.35 shows the diffractogram of the DIP monolayer. The red spots mark the calculated diffraction pattern, and the blue lines represent the corresponding unit cell vectors. The farther away from the (0,0) - spot the less the calculation agrees with the measurement which originates from the imperfection of the electric field in the SPALEED and is hence an experimental artifact. Taking this into account, the pattern is reproduced very well.

In the direction of  $a'$  every second spot that has been calculated is not visible in the LEED pattern. This is a hint for a glide plane or a  $2_1$  screw axis in this direction which are not distinguishable due to the equivalence of the symmetry operations. It will therefore be referred to as an  $2_1$  screw axis in the following. This also seems to be the case for  $b'$  for which every second spot does not appear. Contrary to  $a'$  the missing spots of  $b'$  faintly appear for electron energies of 23 eV. The screw axis in this direction is therefore not completely perfect.

The length of the two vectors can be extracted in two ways. Either from the line scans in Figure 2.36 or from the calculations in Figure 2.35 - the angle between them is in both

## 2. Influences on the energetic position of the transport levels

cases is  $90^\circ$ . Table 2.5 shows the results of both methods for different temperatures. The resulting superstructure matrix is:

$$\begin{pmatrix} 10.3 & 0 \\ 1.9 & 3.8 \end{pmatrix}$$

The averaged value for **a** is **29.6 Å** and **9.5 Å** for **b**. Since the size and the shape of

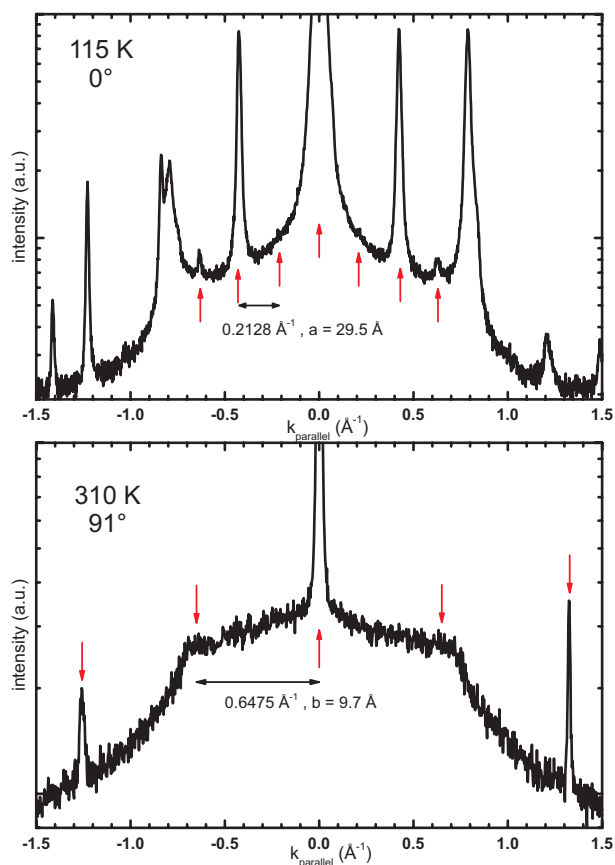


Figure 2.36.: Line scan through the (0,0) - spot of the monolayer DIP (top, line positioned as in 2.34) and one scan perpendicular to the first (bottom). The arrows indicate the position of the lattice vectors which have a length of 30.2 Å and 9.7 Å in real space. ( $E_{kin} = 35$  eV (top) and 50 eV (bottom))

the unit cell as well as the fact that there are two screw axes are now known, a model for the arrangement of the molecules on the surface can be constructed. Figure 2.37 shows this model for two molecules in the unit cell and two screw axes perpendicular to one another.

### Multilayer, below 150K

Organic thin films that were prepared at very low substrate temperatures are in general believed to have a low degree of order. The molecules are less mobile and therefore do

## 2.5. Diindenoperylene - Different geometric film structures for one molecule

Table 2.5.: Results for the length of the unit cell vectors of the monolayer DIP on Ag(111) superstructure for various temperatures and for two different methods to determine them.  $a$  is parallel to a substrate vector and the angle between the superstructure vectors is  $90^\circ$ .

method	T in K	a in Å	b in Å
line scan	115	29.5	-
line scan	320	-	9.7
fit	115	29.9	9.4
fit	210	29.5	9.4
fit	310	29.5	9.4

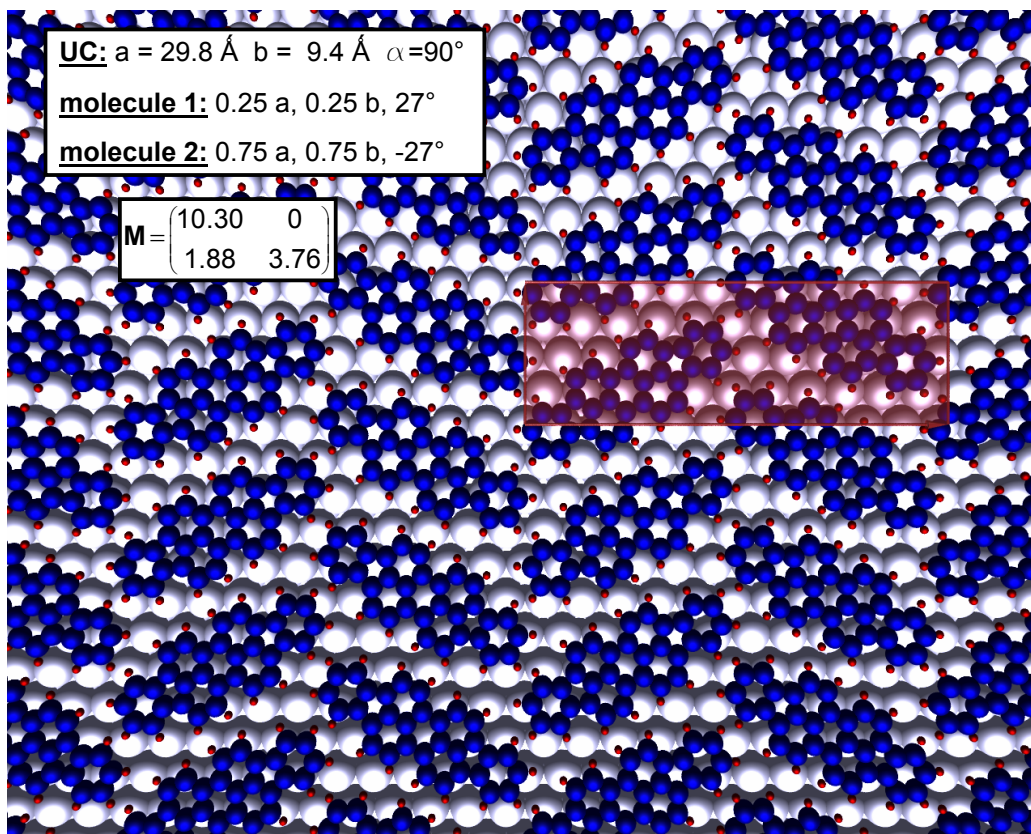


Figure 2.37.: Arrangement of the DIP molecules at the silver surface. In this model, two molecules per unit cell were derived that lie flat on the surface. The positions within the UC are given in the inset. This conformation accounts for the existence of two  $2_1$  screw axes (or two glide planes) that are needed due to the missing spots in the diffractogram.

## 2. Influences on the energetic position of the transport levels

---

not move far away from the place where they hit the surface. This results in a lack of crystalline order because the molecules are not able to reach the arrangement that represents the minimal free energy. However, DIP shows a clear LEED pattern even for deposition temperatures below 150 K and a thickness of 5 - 6 layers.

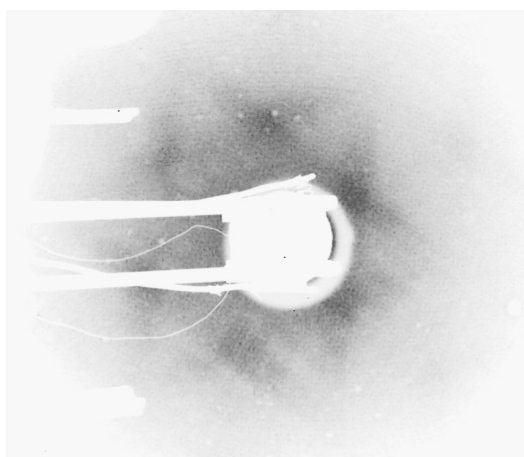


Figure 2.38.: LEED pattern of a 5 - 6 layer thick DIP film on Ag(111). The substrate temperature during deposition was 125 K.  $E_{kin} = 26$  eV

**LEED - Experimental results** Figure 2.38 shows the picture of the LEED screen for a DIP film prepared at 115 K substrate temperature in the PES chamber. The diffraction pattern has a star-like shape and the spots are quite blurry. The pattern resembles the one in Figure 2.31 (a) and was taken before the film was heated to 350 K which resulted in the pattern of 2.31 (b).

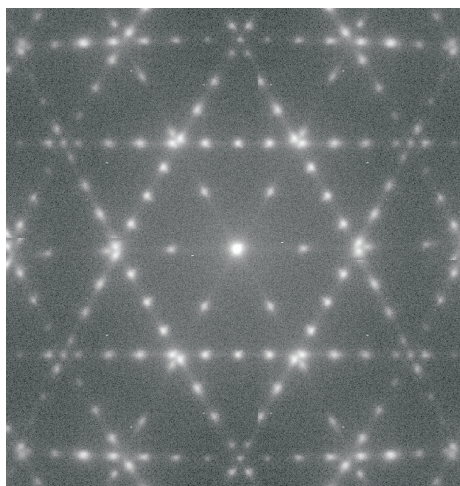


Figure 2.39.: SPALEED Pattern for a DIP multilayer (5 - 6 layers) grown at 117 K.  $E_{kin} = 35$  eV

**SPALEED - Experimental results** Figure 2.39 shows the SPALEED diffraction pattern of a DIP thin film prepared at 117 K substrate temperature, in which the star-like shape form the LEED pattern can be clearly identified. Nevertheless, the growth of the DIP molecule seems to be very sensitive to the substrate temperature in the region between 110 and 150 K. Figure 2.40 shows the comparison of the pattern of the film grown at 110 K and one film grown at 150 K substrate temperature. The width of the spots varies significantly and the unit cell changes. In the case of 150 K the pattern resembles the monolayer DIP with very sharp spots which indicates a long terrace width but the unit cell vector  $\mathbf{a}'$  is about two third of that of the monolayer. This is different for 110 K where the spots are considerably broader but the pattern itself is the same as for the monolayer.

L. Kilian [Kil02] described the change of spot widths in SPALEED with different preparation temperatures in his PhD thesis, in which he investigated the roughness and average terrace width for films of PTCDA on Ag(111) grown at temperatures between 160 and 320 K. For this investigation L. Kilian measured line scans through the (0,0) - spot and measured the Henzler rings which represent the (0,0) - spots from slightly tilted areas of the surface and which are a good measure for the roughness of a surface.

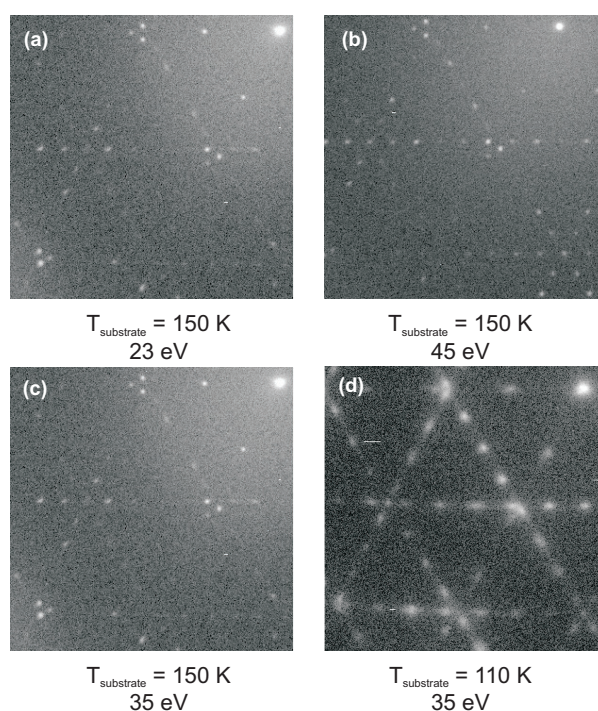


Figure 2.40.: A series of SPALEED diffractograms for two preparation temperatures and different electron energies. FWHM of (0,0) - spot is  $0.0101 \text{ \AA}^{-1}$  for (a) and  $0.0188 \text{ \AA}^{-1}$  for (d).

Since the measurements on the DIP films were not intended to provide this information, the electron energy was chosen in order to provide the best contrast for the spots which was the case for 35 eV. Nevertheless, the electron energies chosen for (a), (b) and (c) are very close to the in-phase energy (34 eV) and the out-of-phase energy (23 eV) that

## 2. Influences on the energetic position of the transport levels

---

L. Kilian chose in his investigation. No significant changes in the width of the diffraction pattern spots can be observed. This corroborates the assumption that the films grown at substrate temperatures of 150 K exhibit a long range order with small surface roughness. The increasing spot size for 110 K points towards a beginning surface roughness or micro-crystallinity due to the lowered mobility of the molecules. M. Münch [Mün01] did X-ray diffraction measurements on DIP films grown at SiO<sub>2</sub> at 140 K. His measurements showed that the films are amorphous under these preparation conditions. This could explain the beginning broadening of the diffraction pattern spots for films at 115 K. However, only further measurements can clarify this.

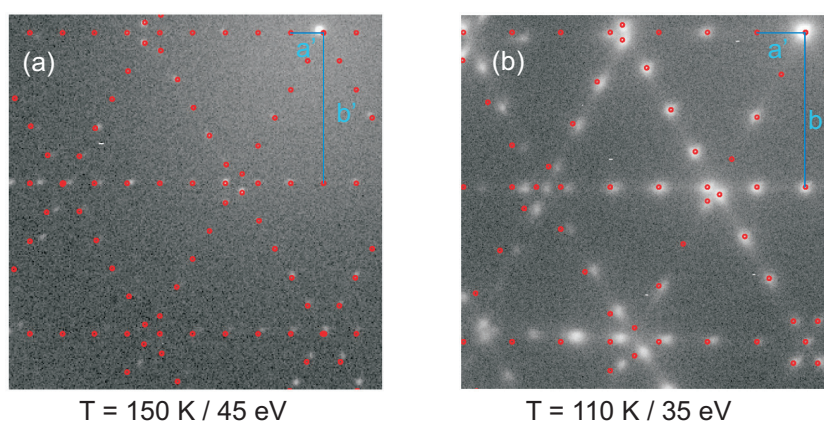


Figure 2.41.: SPALEED diffractograms of DIP multilayer films grown at 150 K (a) and 115 K (b). The red spots mark the calculated diffraction pattern for the blue unit cell vectors.

**Unit cell at below 150K** A small change of the substrate temperature of about 40 K has a strong influence. Not only the spot width changes but also the pattern itself. In Figure 2.41 (a) the measured diffractogram is superimposed by the calculated one. The unit cell vector **b** stayed constant but the length of **a** increased by a factor of about 1.5. The results for the unit cell vectors can be found in Table 2.6. For the 110 K film also line scans through the (0,0) - spot were recorded which are shown in Figure 2.42 and from which the vector length could be determined quite accurately.

A closer look at the diffraction pattern of the DIP film at 150 K reveals that the difference to the monolayer structure is a change in the screw axis. It changes from a 2<sub>1</sub> - to a 3<sub>1</sub> - axis which means that the unit cell now contains three molecules that are rotated along the **a** axis with distances of 1/3 of **a** and rotated by 120° to each other. Since the diffraction pattern in Figure 2.41 (b) is the same as for the monolayer, it is concluded that the molecules are too immobile to form the structure of 2.41 (a) and keep growing in the structure given by the substrate interaction of the first layer. The growth



mode experiments showed that all films prepared at substrate temperatures at or below 210 K are not stable and rearrange if the temperature is increased to about 300 K. This

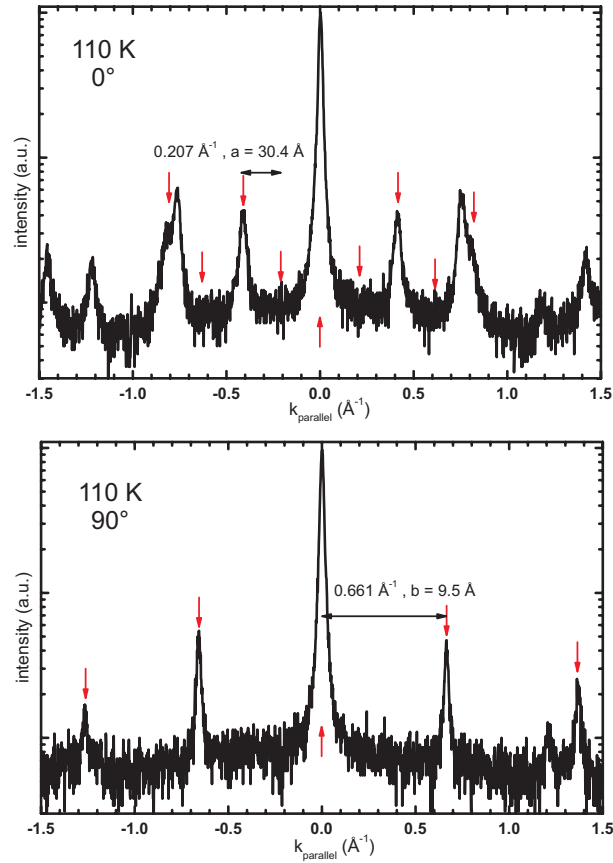


Figure 2.42.: Line scan through the (0,0) - spot of the diffraction pattern. The angles are defined in the same way as in Figure 2.36.  $E_{kin} = 35$  eV

is a hint that the crystalline structures at 110 and 150 K are metastable and might be strained. The superstructure matrices correlated to these unit cells are for 150 K

$$\begin{pmatrix} 15.1 & 0 \\ 1.9 & 3.8 \end{pmatrix}$$

and for 115 K.

$$\begin{pmatrix} 10.5 & 0 \\ 1.9 & 3.8 \end{pmatrix}$$

### Multilayer, above 350K

Measurements of DIP on polycrystalline gold by A. C. Dürr [Dür02] revealed that annealing the sample at 420 K diminishes the surface roughness. On gold the molecules stand upright on the substrate with an interlayer distance of 16.6 Å. Therefore the DIP

## 2. Influences on the energetic position of the transport levels

---

Table 2.6.: Results for the length of the unit cell vectors of the DIP multilayer on Ag(111) superstructure for various temperatures below 160 K and for two different methods to determine them.  $a$  is parallel to a substrate vector, and the angle between the superstructure vectors is  $90^\circ$ .

method	T in K	a in Å	b in Å
line scan	110	30.4	9.5
fit	115	30.3	9.5
fit	150	43.8	9.5

films on Ag(111) were also annealed, and it was checked whether this enhances the film quality and changes the morphology.

Depending on the preparation temperature of the film, this leads to different results. For films prepared at temperatures below 150 K, a structural phase transition happened which is described in Section 2.5.1 and the morphology stays constant. DIP films prepared at 210 K underwent a different structural change, in which the film morphology completely changes. The silver signal in XPS increases and the surface of the sample changes color (described in Section 2.2.5), which implies that the molecules rather cluster to islands.

Based on the phase transition of the monolayer at 350 K and the knowledge that DIP multilayers desorb at temperatures of 430 K, the preparation on a heated substrate (380 - 420 K) was tried and the results will be shown in the following.

**LEED - Experimental results** Figure 2.43 shows the LEED pattern of a DIP film that was prepared at  $T_{Substrate} = 420$  K. It is clearly visible that this pattern differs from the previous ones of the monolayer and films prepared at  $T_{Substrate} < 150$  K. A circular structure with twelve spots around the (0,0) - spot can be observed and further away a six spot structure that resembles the LEED pattern of clean Ag(111) but with completely different unit cell vectors. The latter can also be attributed to the DIP since the substrate pattern is out of the screen at these electron energies due to the smaller unit cell.

**SPALEED - Experimental results** Based on the LEED measurements and the preparation conditions described before, the same diffraction pattern could be produced in the SPALEED machine. Figure 2.44 shows the diffractogram in which the twelve circular spots as well as the six spot pattern from the LEED could be found. The small spot width is a hint for the good crystallinity of this structural phase. It was possible to record this pattern for fairly thick multilayer films of 8 - 9 layers thickness.

**Unit cell at above 350K** Similar to the monolayer and the very low temperature films, the unit cell vectors for this phase were determined with the help of the line scans in Figure 2.46 and by calculation of a diffraction pattern with the unit cell vectors used in Figure 2.45 and the results for the unit cell size for both methods is shown in Table

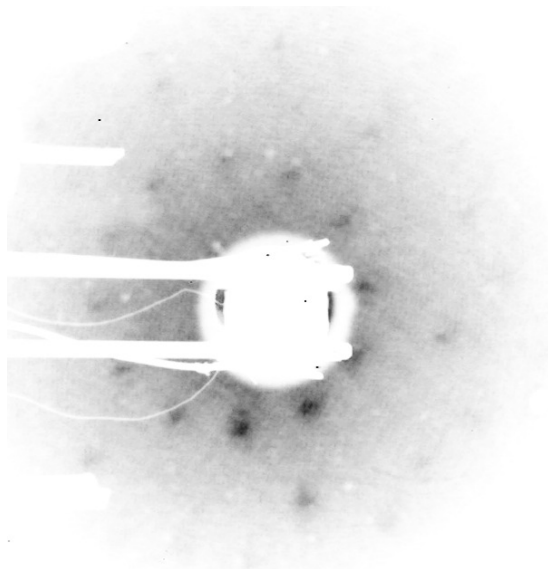


Figure 2.43.: LEED pattern of a 5 - 6 layers thin DIP film prepared at  $T_{Substrate} = 420$  K.  $E_{kin} = 30$  eV

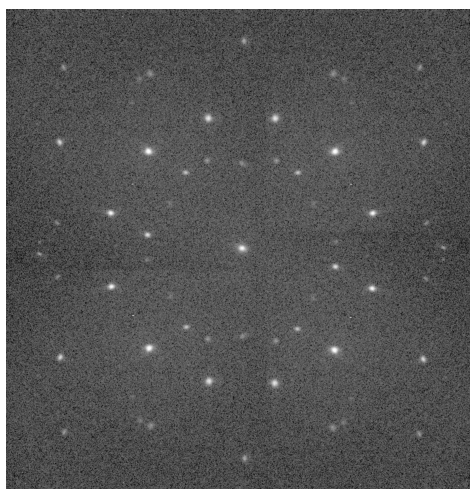


Figure 2.44.: SPALEED diffractogram of a DIP film grown at 400 K substrate temperature. The thickness is about 5 - 6 layers.  $E_{kin} = 35$  eV

## 2. Influences on the energetic position of the transport levels

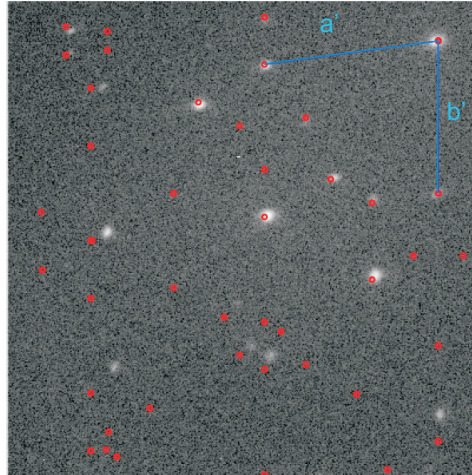


Figure 2.45.: Combined calculated and measured SPALEED pattern for DIP grown at 400 K. The red spots are calculated and the blue line represent the unit cell vectors, starting in the (0,0)-spot in the upper right corner.

2.7. The unit cell for  $T_{Substrate} > 350$  K is not rectangular but oblique with an angle of  $98^\circ$  and the vectors  $\mathbf{a} = 12.4 \text{ \AA}$  and  $\mathbf{b} = 11.3 \text{ \AA}$  resulting in the following superstructure matrix:

$$\begin{pmatrix} 3.8 & 0 \\ 3.1 & 5.0 \end{pmatrix}$$

If this unit cell is compared to the unit cell found for DIP on  $\text{SiO}_2$  and  $\text{Al}_2\text{O}_3$ , some similarities can be observed. The unit cell described in [DKK<sup>+</sup>03] has the vectors  $\mathbf{a} = 8.55 \text{ \AA}$  and  $\mathbf{b} = 7.09 \text{ \AA}$  with an angle of about  $90^\circ$  between them. It is assumed to contain two upright standing molecules. If a third molecule is placed in this unit cell and the length of the vectors is multiplied with 1.5, one receives approximately the vector length of the high temperature phase on silver ( $\mathbf{a} \cdot 1.5 = 12.8 \text{ \AA}$  and  $\mathbf{b} \cdot 1.5 = 10.6 \text{ \AA}$ ). However, the angle differs between the both and without knowledge of all three unit cell vectors of the high temperature phase, it remains a speculation.

Table 2.7.: Results for the length of the unit cell vectors of the DIP multilayer on Ag(111) superstructure grown at  $T_{Substrate} > 350$  K.  $\mathbf{a}$  is parallel to a substrate vector and the angle between the superstructure vectors is  $98^\circ$ .

method	T in K	a in $\text{\AA}$	b in $\text{\AA}$
line scan	400	12.4	11.3
fit	400	12.7	11.0

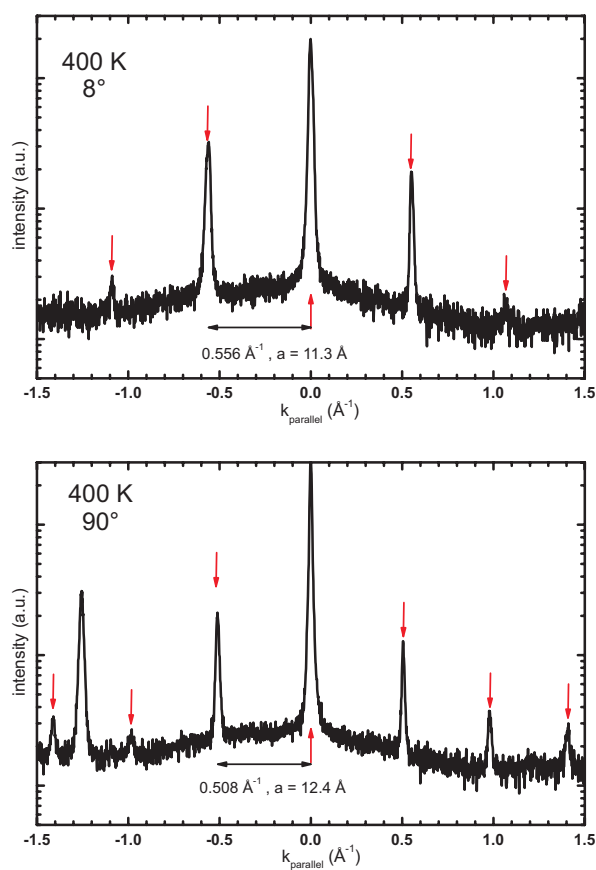


Figure 2.46.: Line scans through the (0,0)-spot for DIP grown at 400 K. The scans are parallel to the unit cell vectors.

### Multilayer, about 210K

The DIP films prepared at 210 K show very clear UPS spectra with small peaks and the growth mode determined with XPS was close to layer-by-layer growth. However, this is different for the structure determined by SPALEED.

Since no LEED diffractograms could be recorded before, no information about this structure was available, and it was uncertain if any structure exists. The difficulties with the measurement of a clear diffractogram continued in the SPALEED chamber. Most of the preparations delivered a SPALEED pattern but some did not, which is another hint towards the instability of this phase.

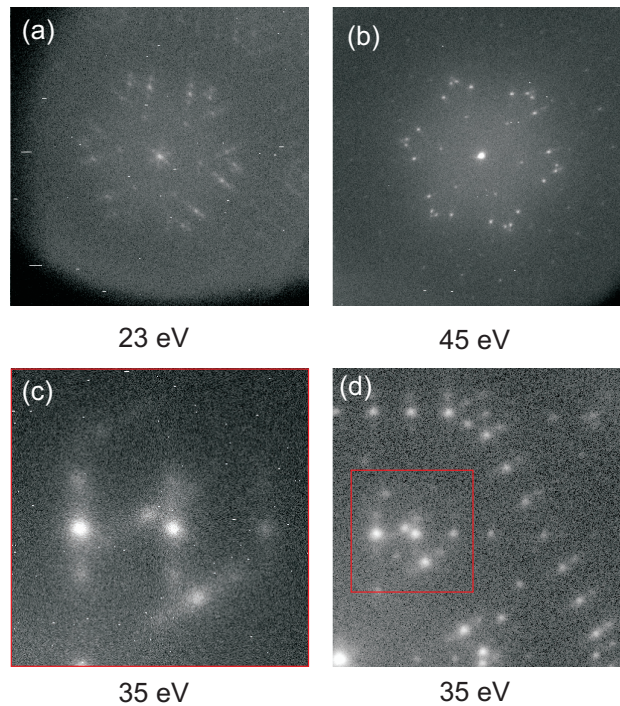


Figure 2.47.: A series of SPALEED diffractograms at different energies of DIP films prepared at  $T_{\text{Substrate}} = 210$  K. (a) shows the complete diffraction pattern at 23 eV, (b) at 45 eV, and (d) at 35 eV. (c) is a detail of diffractogram (d), marked by the red box.

**SPALEED - Experimental results** The series of diffractograms in Figure 2.47 reveals that the structure of the DIP films is quite complex at this growth temperature. Depending on the electron energy, different subpatterns become stronger in intensity. Nevertheless, the diffraction pattern of the monolayer is visible at all energies and seems to dominate.

In the previous Section for  $T_{\text{Substrate}} < 150$  K, a significant structural difference could be observed for small changes of the preparation temperature. Since this temperature has only been increased by another 60 K, it is remarkable that the difference in the pattern of the multilayer film is again strong.

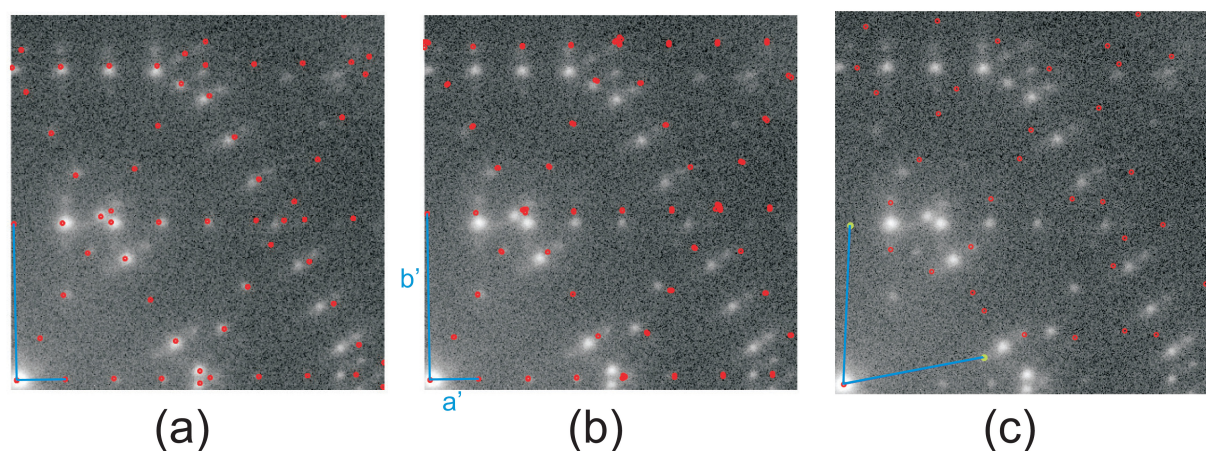


Figure 2.48.: The calculated diffraction patterns for two rectangular unit cells and the oblique one. Two of them have the same vector  $\mathbf{a} = 30.6 \text{ \AA}$  and an angle of  $90^\circ$  between the unit cell vectors. The length of  $\mathbf{b}$  is varied to fit all points in the measured diffractogram. The oblique unit cell resembles the unit cell at  $T_{\text{Substrate}} > 350 \text{ K}$  but has a smaller area (about  $3/4$ ) and an angle of  $103^\circ$ .

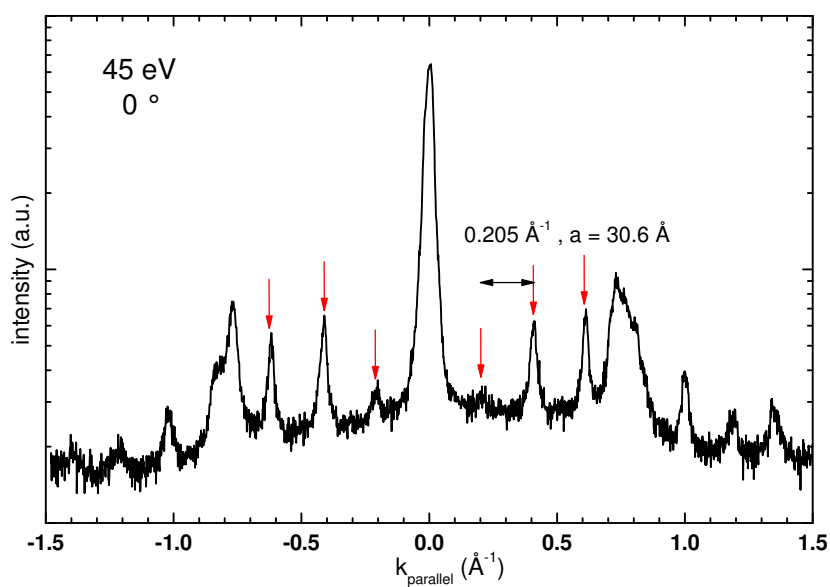


Figure 2.49.: Line diffractogram through the (0,0) - spot along the  $\mathbf{a}'$  - vector.

## 2. Influences on the energetic position of the transport levels

---

**Unit cell at about 210K** It was possible to extract three different unit cells from the diffractogram, which are shown with the diffractogram in Figure 2.48. The diffraction pattern is very complex and without knowledge of the monolayer structure the single patterns are not identifiable. Two of the patterns resemble the monolayer diffraction pattern and the third one has not been observed at other temperatures and resembles the high temperature phase. Table 2.8 contains the results of the graphically determined unit cells for all substructures and the result of the line scan in Figure 2.49. The superstructure matrices for the three unit cells are

$$\begin{pmatrix} 10.6 & 0 \\ 1.9 & 3.8 \end{pmatrix}$$

for (a) and

$$\begin{pmatrix} 10.6 & 0 \\ 1.8 & 3.6 \end{pmatrix}$$

for (b) and

$$\begin{pmatrix} 3.6 & -0.3 \\ 1.4 & 3.9 \end{pmatrix}$$

for (c).

In order to develop a model of this structural phase, it is necessary to include the

Table 2.8.: Results of the length of the unit cell vectors for the three superstructures of DIP grown at  $T_{Substrate} = 210$  K.  $\mathbf{a}$  is parallel to a substrate vector, and the angle between the vectors is  $90^\circ$  for (a) and (b), and it is  $103^\circ$  for (c).

method	T in K	a in Å	b in Å
line scan	210	30.6	-
fit (a)	210	30.6	9.5
fit (b)	210	30.6	8.2
fit (c)	210	10.9	9.8

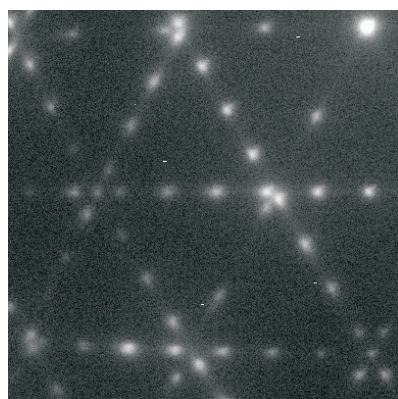
ARPES results (see Section 2.6.3). A strong change in the relative intensities of the orbitals was found for angles off the normal axis. The resulting UPS spectrum resembles the high temperature phase; it is therefore assumed that this effect is due to the decrease of the bulk sensitivity through the variation of the angle and the increase of surface contribution to the spectrum. Applying this to the SPALEED measurements, one possible interpretation is that the different unit cells found in the diffractogram are arranged on top of each other. On the bottom, the structure of the monolayer exists that seems to be slightly distorted in the direction of unit cell vector  $\mathbf{b}$ . This distortion might originate from the top lying structure which is a also distorted version of the high temperature unit cell. An alternative interpretation is that regions coexist on the surface with different structures of which the high temperature resembling phase forms crystallites and



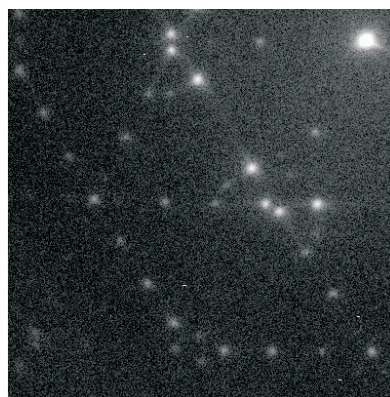
## 2.5. Diindenoperylene - Different geometric film structures for one molecule

---

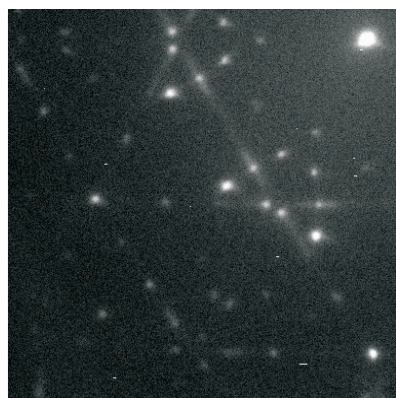
therefore dominates the UPS spectrum at high emission angles.



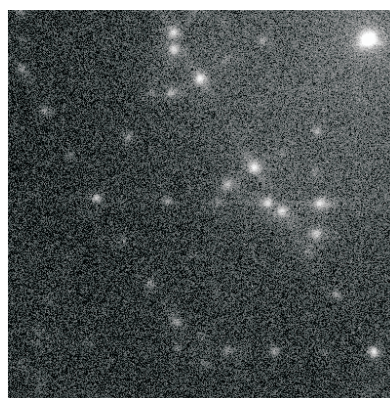
1. grown at 115 K



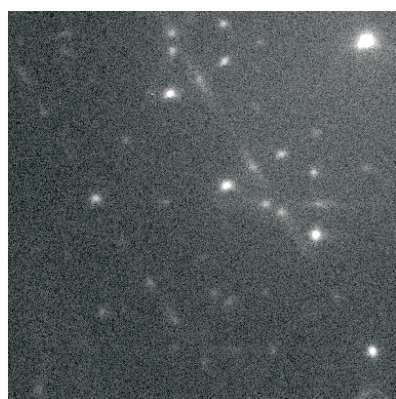
2. return to RT over night



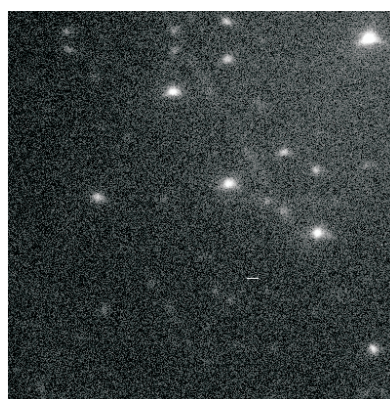
3. 30 min @ 380 K



4. 60 min @ 320 K



5. 60 min @ 380 K



6. 165 min @ 400 K

Figure 2.50.: Structural transition from low temperature phase to high temperature phase by heating of the sample in several steps.

### Phase transition in the multilayer

The UPS experiments in Section 2.6 showed that the low temperature phases are unstable and that a phase change can be induced by a slow return to room temperature or by an annealing at higher temperatures ( $T > 350$  K). The latter can either result in closed films that essentially keep their thickness as measured by XPS if the preparation temperature was below 150 K or, if this temperature was higher, it results in the thin-layer-plus-island morphology. Films for which the cooling was simply stopped always rearranged themselves in the thin-layer-plus-islands phase.

Therefore this phase transition was investigated by SPALEED, too. Figure 2.50 shows the structural change for a film prepared at 115 K (1.) which remained in the chamber over night and reached a substrate temperature of 278 K (2.) in this time. A change in the relative intensities can be observed with every annealing step (3. - 6.). It transits from a combination of a monolayer and a faint high temperature phase to a domination of the high temperature phase.

Two arrangements of the molecules are possible. Either regions with different structures exist and their proportion changes or more and more of the closed layers near the substrate change their orientation and only the first layer remains visible in the diffractogram. The XPS measurements in the growth mode Section (Figure 2.18) point towards the latter model. The substrate signal significantly increases after annealing at 350 K. Since DIP starts evaporating at temperatures above 420 K, the molecules could only move into the islands.

The second phase transition, found in the UPS data for films prepared at  $T < 150$  K and subsequently annealed for 15 min at 420 K, was not investigated in the SPALEED and will be discussed later (Section 2.6.5).

### Summary and conclusions of the SPALEED measurements

By the example of DIP it was shown that the structure and morphology of thin films on the same substrate can change significantly if the preparation conditions are slightly altered. An overview of all structural phases known so far can be found in Figure 2.51. In this diagram the x - axis represents the nominal coverage  $\Theta$  in monolayers and the y - axis the substrate temperature  $T$  at which the film, corresponding to the diffractogram, was prepared.

The diffraction pattern of the monolayer shows only little variation in the temperature regime of 115 K to 300 K. Only the intensity of some points changes which cannot be attributed to a change in symmetry. This intensity effect seems to originate from the fact that the monolayer pattern is a mixture of the LEED picture at 115 K and above 350 K where it only consists of a disk around the (0,0) - spot. This phase transition of second order, which is completed at 350 K, delivers the basis for the explanation of the multilayer behavior.

All of the multilayer phases found are variations of the two basic structures:

- monolayer structure

- high temperature phase ( $T_{Substrate} > 350$  K)

The diffractogram at 115 K shows mainly the broadened monolayer structure which seems to originate from a microcrystalline or amorphous film which is corroborated by measurements of M. Münch [Mün01]. His XRD measurements of DIP films grown on SiO<sub>2</sub> at 140 K revealed that the films are amorphous. At slightly higher temperatures of 150 K, Diindenoperylene arranges in a even larger unit cell in which three molecules fit. The visibility of only every third spot in the direction of  $\mathbf{a}'$  points towards a more complex structure with a  $3_1$  - screw axis.

The diffractogram at 210 K was interpreted as a mixture of three unit cells which are either arranged on top of each other or laterally coexisting. This interpretation accounts for the fact that ARPES measurements on this system show a strong variation with angle, and for the largest off-normal angle with the smallest electron escape depth the measurements delivered a spectrum that resembles the high temperature phase. The three unit cells could be identified as the monolayer unit cell and a slightly modified version of it and a modified version of the high temperature phase.

The films prepared at temperatures above 350 K showed a smaller unit cell compared to that of the monolayer. It resembles the so-called  $\sigma$  - phase of DIP on gold [KGS<sup>+</sup>06], in which the molecules stand upright. The altered ionization potential in this phase (see Section 2.6.3) corroborates this model since the IP change demands for a significant change in the structure of the thin films.

The results of the investigation of the phase transition for the multilayer films allow statements about the stability of the single phases at room temperature. The combination of the different monolayer and multilayer structures preferred by the molecules at this temperature leads to the observed strong Stranski-Krastanov behavior for low temperature films. The monolayer prefers its ordered structure for  $T < 350$  K and the subsequent layers prefer the  $T > 350$  K multilayer structure. The result is a strong strain between them and a rearrangement of the layers.

A closer look at the superstructures of the different phases allows conclusions about the interaction of the molecules and the silver substrate. D. E. Hooks et al. [HFW01] investigated this matter and summarized the possible superstructures found for the growth of molecules on solid substrates in their "grammar of epitaxy". All of the superstructures found for DIP on Ag(111) belong to the "Coincidence-II" group except for the two additional superstructures for  $T_{Substrate} = 210$  K which are assumed to grow on the DIP and not on the substrate. The "Coincidence-II" group is a special case of a point-on-line (POL) structure in which one superstructure vector is parallel to a unit cell vector of the substrate. In contrast to the standard POL structure the superstructure vector in the "Coincidence-II" does not end on a atom of the substrate. Therefore, the DIP superstructures belong to the rather weak interacting group. More information on this topic can be found in [HIKK94], [KUS06], [MF04] and [MF05].

In summary, all phases that were found during the UPS measurements in Section 2.6 and their correlated LEED diffractograms could be reproduced in the SPALEED machine. It was possible, to explain the arrangement of the molecules and the transitions between them. A weak but measurable interaction between the DIP and silver could be observed.

## 2. Influences on the energetic position of the transport levels

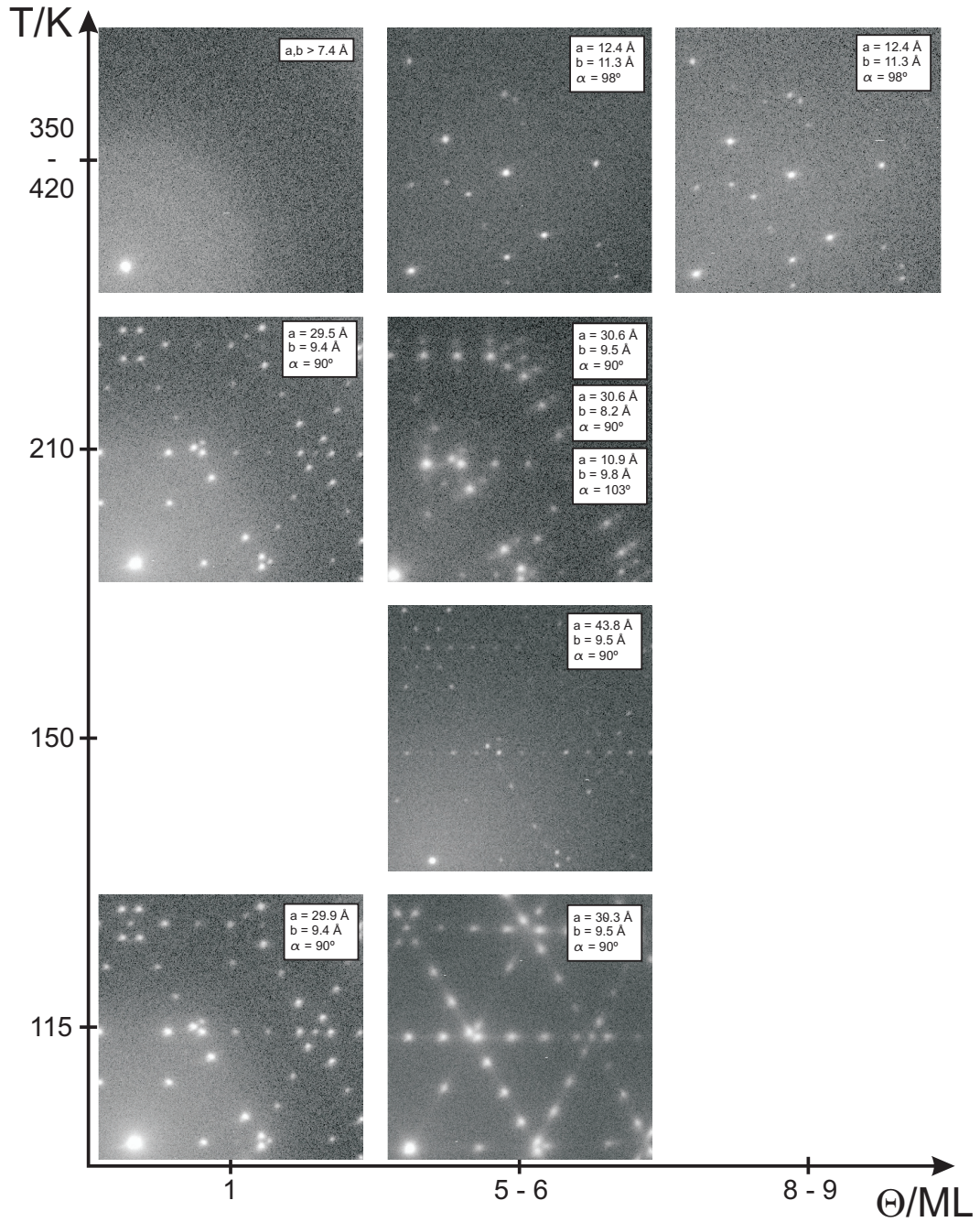


Figure 2.51.: Structural phase diagram of DIP on Ag(111) depending on coverage  $\Theta$  and temperature  $T$ .

## 2.6. How geometric structure influences the UPS/IPS - spectrum: Diindenoperylene

The last Section showed that organic thin film preparation has a huge number of parameters and that small changes of the conditions during growth can result in significantly different structures. In a temperature range as small as 100 K, four different geometric film structures were found. This circumstance is not considered for the determination of the transport levels in the respective literature. It is therefore even more important to specify the film preparation conditions for every measurement published because it is just one point in the parameter space.

The following Section will show the influence that different structures have on the measured shape and position of the frontier orbitals. In order to do this, UPS as well as IPS measurements will be presented for DIP on Ag(111) and for the temperature regions below 150 K, at about 210 K, and above 350 K. The SPALEED measurements revealed that these regions correspond to the three major structural categories being amorphous (or at least low degree of order), poly-structural, and single-structural film. Additionally to the PES data, High Resolution Electron Energy Loss Spectroscopy (HREELS) data will be shown in each Subsection. This data provides information about the vibrational modes in the different samples which are very sensitive to changes in the intermolecular interaction. In order to evaluate the HREELS spectra correctly, the vibrational frequencies of the free molecule were calculated with DFT. This provides not only the frequencies where signal is expected but also information about the direction and amplitude of such a vibration which helps to interpret frequency shifts.

The results of the DFT calculations will be shown first, followed by data for the monolayer DIP on Ag(111) which represents the interface between metal and organic thin film. Then, the results for the three different multilayer structures (the preparation at 150 K substrate temperature was not specifically investigated in PES) will be discussed and, finally, the results for all measurements will be summarized in order to present a consistent picture of the processes and the structural arrangements.

### 2.6.1. DFT calculations

The calculation of the vibrational modes is crucial for the interpretation of the HREELS spectra. Shifts in the frequencies between different structural or thermodynamic phases are indicators for a change in the intermolecular interaction between neighboring molecules. Commercial quantum chemical programs, such as Gaussian03 [FTS<sup>+</sup>04], make these calculations accessible for non - experts. In this work, the method of density functional theory (DFT) was chosen because of the good agreement with experimental values and its moderate demand of computing time. In this thesis, the Becke 3 - parameter Lee - Yang -Parr (B3LYP) hybrid functional was used for which P.J. Stephens et al. [SDCF94] showed the feasibility for this purpose. Due to the significant increase in accuracy compared to the 6-31G(d) basis set, this functional was combined with the triple -  $\zeta$  basis set 6-311G+(d,p) which is associated with only a small increase in computing time [AU05].

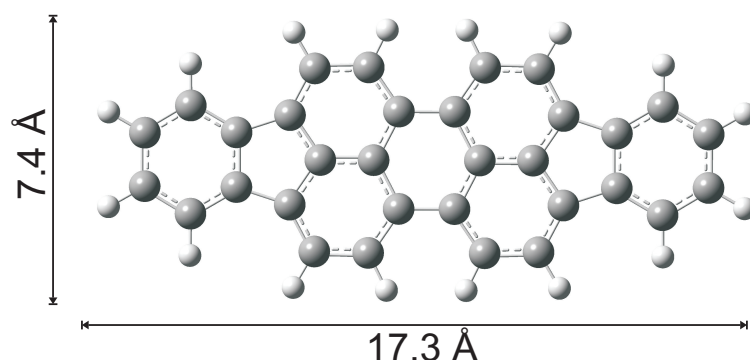


Figure 2.52.: Calculated Diindenoperylene geometry. The calculation was conducted with the B3LYP DFT functional and the 6-311G+(d,p) basis set in Gaussian03.

Before the actual frequencies can be calculated, the molecular geometry was modeled with the help of GaussView [IKM<sup>+</sup>03]. After fixing the symmetry of it to  $D_{2h}$ , the geometry was optimized in Gaussian03. The result of this optimization can be found in Figure 2.52 and complements the estimate for the dimensions of the diindenoperylene molecule that is given in the PhD thesis of M. Münch [Mün01] (length = 18.4 Å and width = 7 Å). This estimate bases on the crystallographic data of fluoranthene and perylene (Cambridge Crystallographic Database).

Besides of the actual frequencies of the vibrations, Gaussian03 also allows the calculation of the IR activity of the modes and the FTIRRA spectrum (Figure 2.53). V. Shklover et al. [TSS<sup>+</sup>00] showed that for the PTCDA molecule the relative intensities of the vibrations in the FTIRRA spectrum are comparable to the ones in the HREELS spectrum. However, the calculations assume a free molecule and harmonic oscillations. The first assumption ignores the interaction with neighbors in the thin film which leads to shifts of the energy of the peaks. The second assumption ignores the anharmonicity of the vibrational potential and can be corrected by a linear scaling factor. This factor is determined by the comparison of calculated and experimental frequencies. For the particular combination of B3LYP and 6-311G+(d,p) this factor is 0.9679 which was determined by M. P. Anderson et al. [AU05]. A third crucial information that the calculations provide is to which irreducible representation of the  $D_{2h}$  point group the vibration belongs. The results for the frequencies, the IR activity, and the irreducible representation of the various frequencies can be found in Table 2.9. The coordinate system to which the representations refer to is shown in the inset of Figure 2.53. A closer look at the results in Table 2.9 reveals that the IR active modes all refer to either  $B_{1u}$ ,  $B_{2u}$ , or  $B_{3u}$  symmetry. The  $B_{1u}$  and  $B_{2u}$  have a mirror plane in the  $xy$  - ( $B_{1u}$ ) and the  $xz$  - plane ( $B_{2u}$ ) which are both perpendicular to the molecular plane - whereas the  $B_{3u}$  representation has its mirror plane in the  $yz$  - plane. Therefore the  $B_{1u}$  and  $B_{2u}$  vibrations are in-plane and

## 2.6. How geometric structure influences the UPS/IPS - spectrum: Diindenoperylene

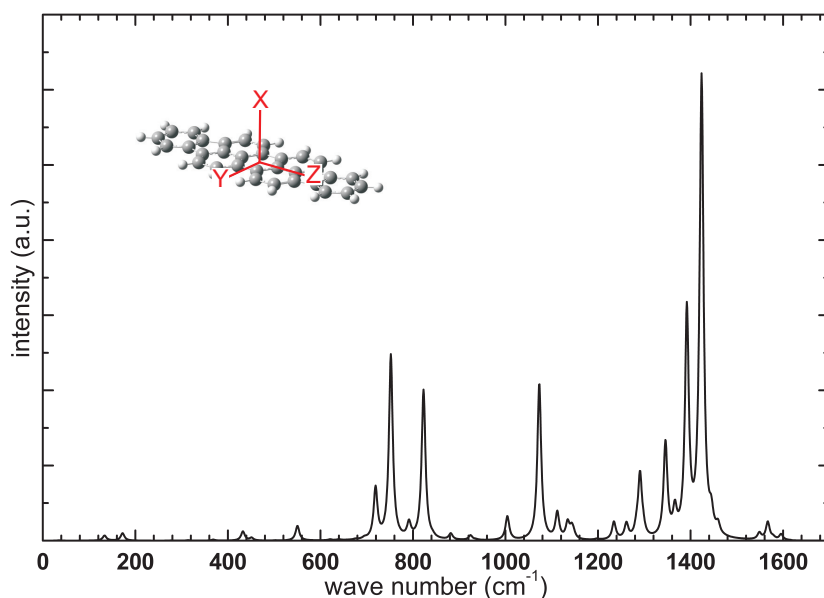


Figure 2.53.: Calculated FTIRRA spectrum for the single DIP molecule. The IR intensities are calculated with DFT: B3LYP/6-311G+(d,p). The inset shows the defined coordinate system to which the irreducible representations refer to.

the  $B_{3u}$  vibrations are out-of-plane. This fact will be used later in the interpretation of the HREELS data.

Table 2.9.: Calculated vibrational modes with their energy in  $\text{cm}^{-1}$  corrected by the factor 0.9679 (see text). The Table includes the irreducible representation (sym.) of the  $D_{2h}$  point group of the particular vibration and its infrared activity ( $I_{IR}$  in arbitrary units)

$E_{corr}/\text{cm}^{-1}$	sym.	$I_{IR}$	$E_{corr}/\text{cm}^{-1}$	sym.	$I_{IR}$
<b>34.85</b>	B3U	0.21	<b>58.92</b>	AU	0.00
<b>73.43</b>	B2G	0.00	<b>103.03</b>	B2U	0.05
<b>128.22</b>	B1G	0.00	<b>133.44</b>	B3U	3.34
<b>139.21</b>	AU	0.00	<b>146.90</b>	B2G	0.00
<b>172.50</b>	B3U	4.98	<b>181.72</b>	B3G	0.00
<b>212.52</b>	AG	0.00	<b>240.89</b>	B2G	0.00
<b>277.42</b>	B2U	0.13	<b>280.49</b>	B1G	0.00
<b>314.07</b>	B3U	0.30	<b>332.94</b>	AU	0.00
<b>368.36</b>	B1U	0.71	<b>371.35</b>	B3G	0.00
<b>377.51</b>	B2G	0.00	<b>431.40</b>	B3U	5.86
<b>431.44</b>	B2G	0.00	<b>435.23</b>	B1G	0.00

Continued on next page...

## 2. Influences on the energetic position of the transport levels

---

$E_{corr}/\text{cm}^{-1}$	sym.	$I_{IR}$	$E_{corr}/\text{cm}^{-1}$	sym.	$I_{IR}$
444.52	AG	0.00	450.39	B3U	1.87
456.42	B2G	0.00	468.75	B3G	0.00
495.36	AU	0.00	502.88	B2U	0.16
523.65	AG	0.00	550.35	B1U	9.86
559.52	B2U	0.00	559.58	B1G	0.00
567.73	B3G	0.00	581.53	AU	0.00
610.02	B3G	0.00	618.85	AG	0.00
620.92	B1U	0.65	630.52	B1G	0.00
634.20	B2G	0.00	636.10	B3U	0.28
646.81	AU	0.00	676.00	B2U	0.42
690.63	AG	0.00	695.25	B1U	0.95
696.80	B2G	0.00	709.37	B3U	20.93
739.49	B1G	0.00	740.99	AU	0.00
750.30	B2G	0.00	751.50	B3U	137.09
759.12	B3G	0.00	791.40	B1U	9.83
818.03	B2G	0.00	823.55	B3U	100.55
823.87	AG	0.00	824.20	B1G	0.00
824.85	AU	0.00	842.58	B2U	0.98
861.03	AU	0.00	861.21	B1G	0.00
881.69	B1U	4.00	922.84	AU	0.00
927.81	B3U	2.85	927.83	B2G	0.00
927.92	B2G	0.00	932.32	B1G	0.00
937.74	B3U	0.37	961.81	AU	0.00
961.81	B1G	0.00	961.97	B3G	0.00
982.85	AG	0.00	1003.97	B1U	14.70
1004.94	B2U	1.10	1011.32	AG	0.00
1027.80	B3G	0.00	1073.01	B1U	104.21
1073.41	B3G	0.00	1074.48	B2U	0.28
1078.82	AG	0.00	1111.96	B1U	17.65
1134.28	B2U	10.76	1135.96	B3G	0.00
1142.84	AG	0.00	1143.11	B1U	6.58
1146.94	B2U	3.15	1170.97	B3G	0.00
1196.12	AG	0.00	1196.95	B2U	0.68

Continued on next page...



## 2.6. How geometric structure influences the UPS/IPS - spectrum: Diindenoperylene

$E_{corr}/\text{cm}^{-1}$	sym.	$I_{IR}$	$E_{corr}/\text{cm}^{-1}$	sym.	$I_{IR}$
<b>1198.37</b>	B3G	0.00	<b>1234.37</b>	B1U	11.43
<b>1261.44</b>	B2U	9.99	<b>1262.48</b>	AG	0.00
<b>1275.50</b>	B3G	0.00	<b>1283.33</b>	B2U	5.83
<b>1290.69</b>	B1U	41.43	<b>1296.89</b>	AG	0.00
<b>1297.33</b>	B2U	5.33	<b>1301.82</b>	AG	0.00
<b>1324.36</b>	B3G	0.00	<b>1345.75</b>	B1U	63.11
<b>1366.17</b>	B1U	16.62	<b>1372.90</b>	AG	0.00
<b>1392.06</b>	B1U	150.19	<b>1408.01</b>	AG	0.00
<b>1417.36</b>	B3G	0.00	<b>1419.17</b>	B2U	13.90
<b>1423.90</b>	B1U	299.09	<b>1434.05</b>	AG	0.00
<b>1444.79</b>	B2U	12.36	<b>1446.18</b>	B3G	0.00
<b>1459.38</b>	B2U	6.54	<b>1470.33</b>	B3G	0.00
<b>1548.68</b>	B1U	4.36	<b>1549.04</b>	AG	0.00
<b>1566.80</b>	B2U	1.61	<b>1566.87</b>	B1U	10.20
<b>1566.90</b>	AG	0.00	<b>1575.95</b>	AG	0.00
<b>1578.33</b>	B3G	0.00	<b>1578.43</b>	B2U	1.48
<b>1581.03</b>	B3G	0.00	<b>1595.62</b>	B1U	3.82
<b>3045.20</b>	B3G	0.00	<b>3045.25</b>	B2U	2.26
<b>3049.37</b>	B1U	48.04	<b>3050.01</b>	B3G	0.00
<b>3050.63</b>	AG	0.00	<b>3051.64</b>	B1U	7.14
<b>3052.52</b>	B2U	12.50	<b>3053.05</b>	AG	0.00
<b>3060.87</b>	B3G	0.00	<b>3060.92</b>	B2U	44.54
<b>3067.10</b>	B3G	0.00	<b>3067.17</b>	B1U	0.10
<b>3072.18</b>	B1U	94.48	<b>3072.24</b>	AG	0.00
<b>3077.27</b>	B2U	44.95	<b>3077.41</b>	AG	0.00

Since the geometry of the molecule was already calculated, it needs only little effort to do a single point calculation in order to find the energy and electron densities of the molecular orbitals. The results of this calculation will be of importance in the discussion of the UPS spectra. A comparative study of the agreement of different calculational methods with experimental gas phase spectra of PTCDA by N. Dori et al. [DMK<sup>+</sup>06] showed that the chosen combination of hybrid functional and basis set does reproduce the gas phase data for the first few orbitals reasonably well but fails for higher binding energies. The energetic sequence of the calculated orbitals can vary from method to

## 2. Influences on the energetic position of the transport levels

---

method. The results of these calculations are given in Table 2.10, in which the HOMO and LUMO are highlighted by bold letters.

Table 2.10.: Calculated energetic positions of the orbitals in DIP gas phase with respect to the vacuum level. The irreducible representation of the  $D_{2h}$  point group associated with the orbitals and the type of orbital (unoccupied or occupied) are also given. The HOMO and LUMO are highlighted by a bold font.

E/eV	sym.	type	E/eV	sym.	type
-0.12	B2U	U	-6.76	B1G	O
-0.16	B1U	U	-7.04	B2G	O
-0.16	B1G	U	-7.23	B3U	O
-0.17	B2G	U	-7.38	AU	O
-0.28	AG	U	-7.95	B1G	O
-0.89	B2G	U	-8.03	B2G	O
-0.94	B3U	U	-8.95	B3G	O
-1.31	B3U	U	-9.03	B3U	O
-1.46	AU	U	-9.10	AG	O
<b>-2.98</b>	<b>B1G</b>	<b>U</b>	-9.22	AU	O
<b>-5.45</b>	<b>AU</b>	<b>O</b>	-9.36	B1U	O
-5.90	B2G	O	-9.48	B2U	O
-6.53	B3U	O	-9.56	AG	O

### 2.6.2. The DIP-metal interface (monolayer investigation)

The first layer of an organic thin film forms the interface between the metal substrate and the film. In general, one distinguishes between chemisorption and physisorption, depending on whether the molecules bind covalently to the substrate or via van-der-Waals interaction. However, the transition region between the two extreme cases is broad. Generally, a contact of the electronic systems of substrate and organic molecules associated with the formation of new electronic states is an unambiguous indicator of chemisorption. A prominent example of this process is the interface state of PTCDA on Ag(111) described by Y. Zou et al. [ZKS<sup>+</sup>06b]. Electronic states of this kind will be called former LUMO (F-LUMO) in this work. Since UPS probes the valence levels, it is a very feasible tool to quantify the strength of interaction by detecting new orbitals or relative shifts and splittings of the orbitals in the monolayer spectra compared to those of the multilayer. Prior to the discussion of the UPS data, this Section will focus on the XPS data of the monolayer.

In Section 2.2, XPS was already used to measure film thicknesses and the system PTCDA on Ag(111) provides the reference for this purpose. The monolayer of this system

## 2.6. How geometric structure influences the UPS/IPS - spectrum: Diindenoperylene

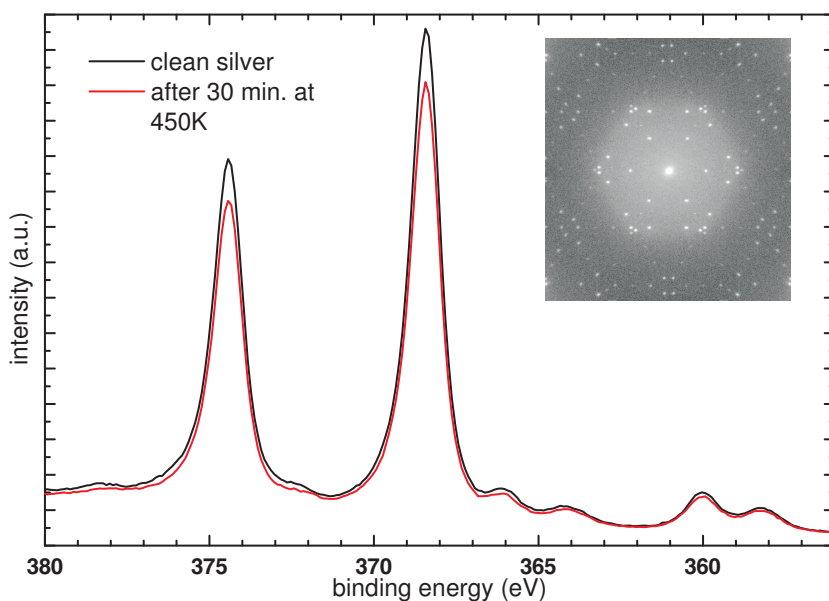


Figure 2.54.: XPS spectrum of clean silver and after annealing of a multilayer film at 450 K for 30 min. The remaining attenuation corresponds to the one of a film thickness of 0.90 ML of PTCDA. The inset shows the SPALEED diffractogram of a monolayer prepared in this way.

was investigated in great detail with a number of experimental methods. Glöckner et al. [GSS<sup>+</sup>98] used STM to determine the superstructure which the PTCDA monolayer forms on Ag(111) and found a unit cell with an area of  $239 \text{ \AA}^2$  containing two molecules. The unit cell of the DIP monolayer on Ag(111) has an area of  $281 \text{ \AA}^2$  and also contains two molecules. Since both molecules are nearly of the same size, one would expect that a monolayer DIP attenuates the XPS signal of the silver substrate by only 85 percent of the attenuation of the PTCDA monolayer. Figure 2.54 shows the XPS spectrum of the Ag 3d-peaks for clean silver and the DIP monolayer. The attenuation corresponds to the one of 0.90 ML PTCDA which is in very good agreement with this estimate and confirms that the DIP monolayer is formed by flat-lying molecules. A combination of flat-lying and standing molecules which could be interpreted from the phase transition of the monolayer found in the SPALEED is not likely since it would result in a significantly stronger attenuation (a film of standing molecule equals four to five layers of lying molecules).

### UPS

Figure 2.55 shows the UPS spectra of an annealed monolayer (b) and a film of 1.7 ML DIP which was prepared by direct evaporation of the molecules at  $T_{\text{Substrate}} = 150\text{K}$ . From the raw spectra (top) a Fermi function and a quadratic background were subtracted in order to identify possible peaks in particular at the Fermi edge where a F-LUMO would be expected to appear (bottom). After this procedure, four peaks could be observed in the spectrum which are all at positions (also relative positions) that differ from the multilayer spectrum. The positions of the maxima have been determined by a fitting of the spectrum with a series of Gaussian peaks and are given in Table 2.11. The existence

## 2. Influences on the energetic position of the transport levels

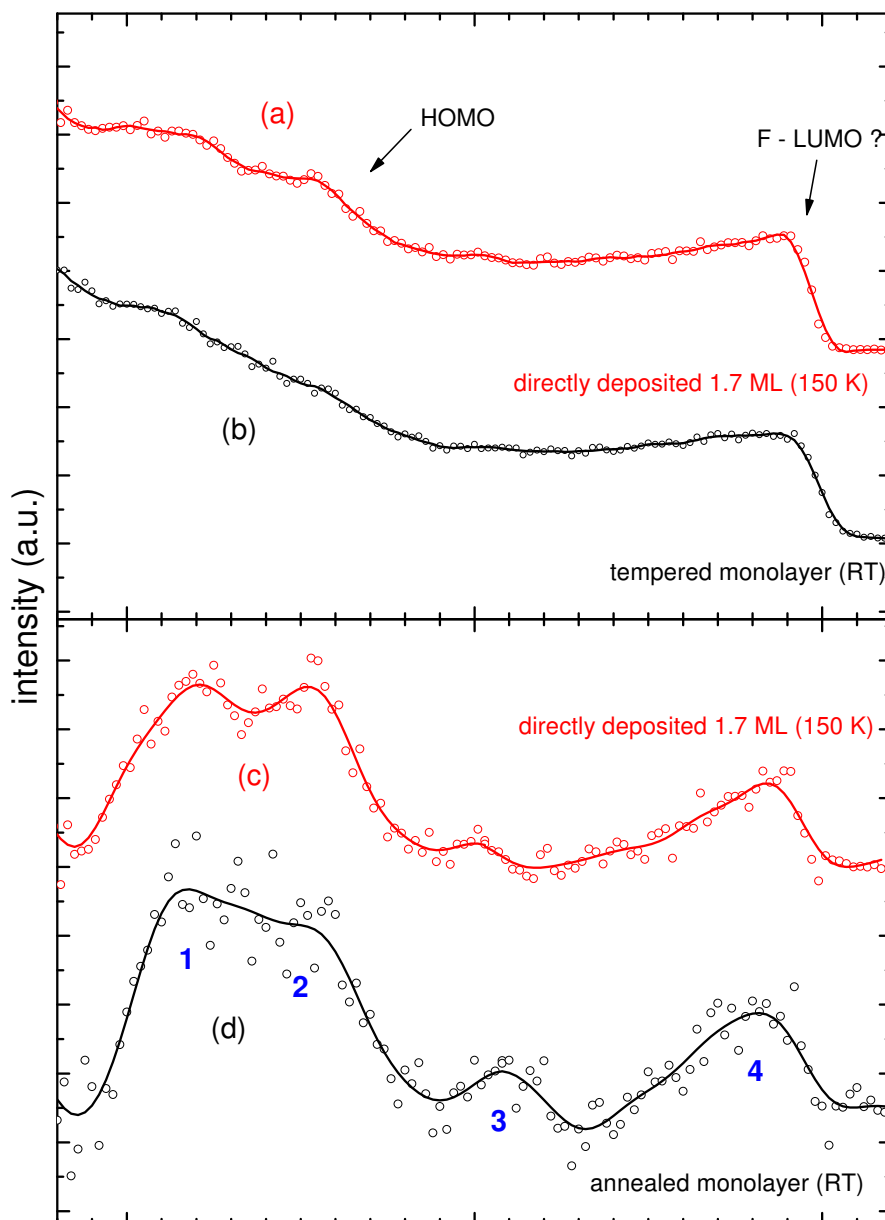


Figure 2.55.: (a) UPS spectrum of directly deposited 1.7 layers of DIP at 150 K. (b) UPS spectrum of the annealed monolayer ( $T > 450$  K) deposited at room temperature. (c) and (d) are spectra (a) and (b) from which a Fermi function and a quadratic background were subtracted.

## 2.6. How geometric structure influences the UPS/IPS - spectrum: Diindenoperylene

Table 2.11.: Fit results of the DIP monolayer UPS spectrum for the directly prepared 1.7 ML film and the annealed monolayer.

peak	direct	annealed
1	-1.81 eV	-1.83 eV
2	-1.45 eV	-1.46 eV
3	-1.05 eV	-0.95 eV
4	-0.15 eV	-0.18 eV

of a peak close to the Fermi edge and the different relative positions with respect to the multilayer are a clear hint towards a covalent interaction with the substrate.

### HREELS

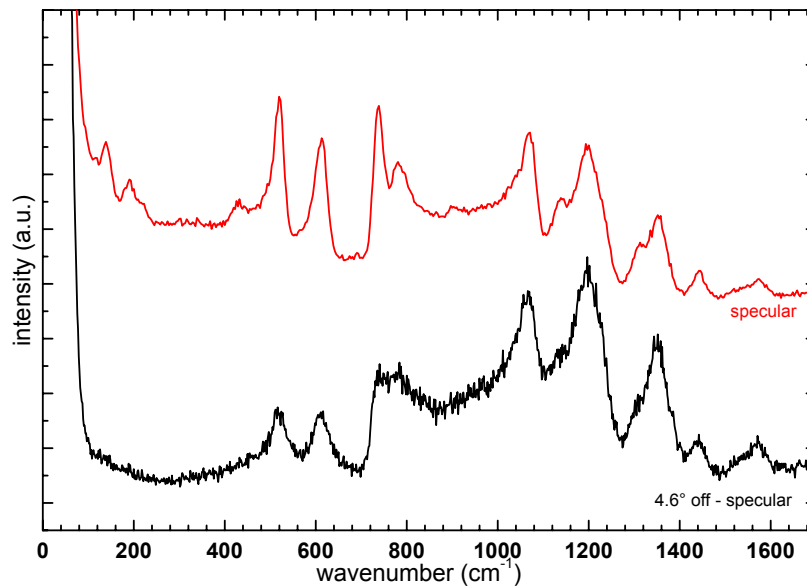


Figure 2.56.: Specular and off - specular HREELS spectrum of the monolayer DIP on Ag(111).  $E = 2.3$  eV,  $\Delta E = \text{ca. } 2.5 - 3.0$  meV.

In this investigation method, electrons with low kinetic energy and small energy spread  $\Delta E_{kin}$  are scattered on surfaces and a kinetic energy loss spectrum is recorded. These losses can be vibrations of molecules, phonons of crystals or, if the kinetic energies are sufficient, electronic transitions. The investigation of this work focuses on the vibrations of the adsorbed molecules, since they are sensitive to geometric film structure that can inhibit certain vibrations and to intermolecular interaction that can shift the frequencies or lead to new, lattice phonons. The information gained from these measurements complement the UPS measurement and can help to understand, if changes in the UPS

## 2. Influences on the energetic position of the transport levels

---

originate from geometric film structure changes or from changes in the interaction between molecules or between them and the substrate.

HREELS has a special selection rule for vibrations at metal surfaces which allows to gain additional information about the molecular orientation and the interaction of metal and adsorbate. Dipole active modes are affected by the metal screening. If the change in dipole moment due to the vibration is parallel to the surface the metal screening will cancel it out, but if the change is perpendicular to the surface the metal screening will enhance the signal. (see [BR96] and [SE84] for more information)

In order to check if changes between multilayer and monolayer are only due to the surface selection rule, it was measured in both geometries - specular as well as off - specular. The HREELS spectra can be found in Figure 2.56. The detailed discussion of the peaks will follow at the end of this Section, but some points should already be mentioned here. The specular and off - specular spectrum differ significantly from each other. All peaks belonging to the out-of-plane modes of the  $B_{3U}$  representation drastically loose intensity for the off-specular reflection whereas the in-plane modes of the  $B_{1U}$  and  $B_{2U}$  representations remain. This accounts for the fact that dipole active modes are suppressed in off-specular geometry and excitation via impact scattering plays a more important role. Since the peaks above  $1000\text{ cm}^{-1}$  and at  $518$  and  $611\text{ cm}^{-1}$  belong to in-plane vibrations, they should be suppressed due to the surface selection rule in specular geometry. Their appearance in both geometries can not be explained with an upright orientation or a deformation of the molecules, because the XPS data showed that the substrate attenuation corresponds to a closed film with a slightly lower density of molecules than for the PTCDA monolayer on Ag(111). An upright standing film would need more molecules to be closed, which would result in a significant higher attenuation of the substrate signal. In addition, the superstructure matrix in the SPALEED diffractogram is not commensurate but the weakest interacting point-on-line case which makes a forcing of the molecules into a superstructure via substrate interaction and a correlated deformation unlikely. Therefore, the reason for the enhancement of the in-plane modes has to be searched in the electronic interaction of metal and molecule.

In order to do so, the spectra are compared to measurements of PTCDA on silver by F. S. Tautz et al. [TSS<sup>+</sup>00] and similarities in the peak shapes can be found. The peaks above  $1000\text{ cm}^{-1}$  and at  $518$  and  $611\text{ cm}^{-1}$  in Figure 2.56 have a significant asymmetry towards lower wavenumbers and a characteristic dip on the high-wavenumber side. A similar observation for some peaks in the HREELS spectrum of PTCDA on Ag(111) was explained by the interaction with the substrate. In a subsequent paper F. S. Tautz et al. [TES<sup>+</sup>02b] treated this electron - phonon coupling theoretically and found out that the line shape could be reproduced with a function that resembles Fano line shape function.

F. S. Tautz [Tau07] described the corresponding model of interfacial dynamical charge transfer (IDCT) in his review of 2007. Depending on the strength of interaction and the corresponding distance of the molecules to the metal surface (limit  $\approx 3\text{ \AA}$ ), the vibrational energy relaxation via electron - hole - pair excitations can be highly mode - selective. If the latter is the case, the signal of modes that have their maximum amplitude in the region of the molecule where the bonding takes place is enhanced. The modes at  $518$  and  $611\text{ cm}^{-1}$  belong to the central modes at  $524$  and  $610\text{ cm}^{-1}$  which both have the

## 2.6. How geometric structure influences the UPS/IPS - spectrum: Diindenoperylene

maximum amplitude at the central benzene ring. The modes above  $1000\text{ cm}^{-1}$  belong to the calculated ones at  $1073$ ,  $1198$ , and  $1346\text{ cm}^{-1}$  that are mainly symmetric, in-plane stretching modes of the carbon atoms at the perylene core.

However, this model demands for a hybrid orbital like in the case of PTCDA on Ag(111) [ZKS<sup>+</sup>06a] in order to be applicable. The UPS data of the monolayer (see 2.3.3) points towards the existence of such an interface state which corroborates the assumption of a significant chemisorptive interaction of the first DIP layer to the silver surface. However, the data basis is too small and more temperature dependent experiments are necessary to fully understand the interaction between DIP monolayer and Ag(111) substrate. Additional X-ray standing wave (XSW) measurements could clarify if the distance between molecules and surface is small enough to enable covalent interaction.

### 2.6.3. Comparison of the multilayer phases

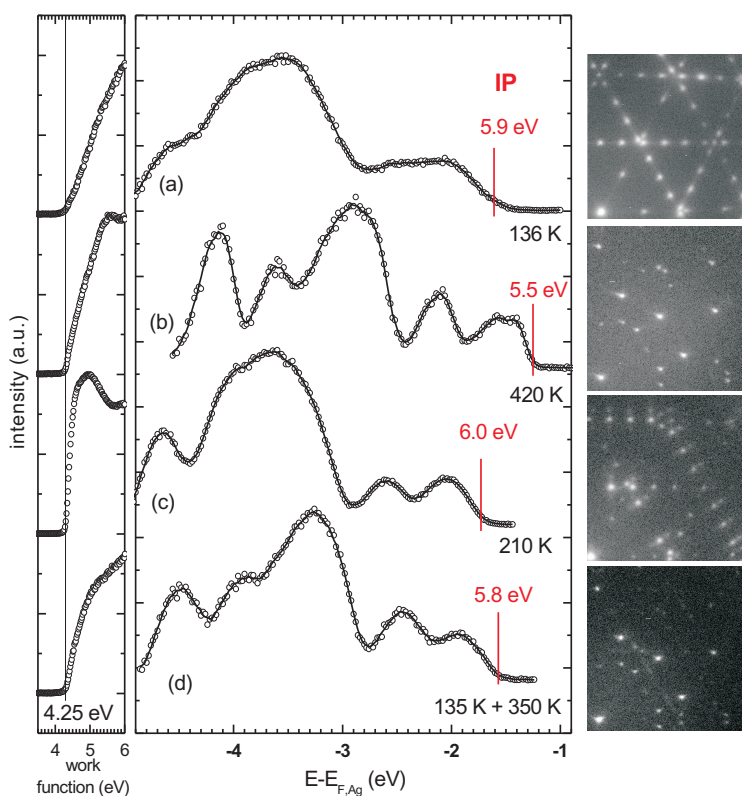


Figure 2.57.: Valence levels and secondary electron cut off as well as the corresponding SPALEED patterns for all preparation conditions. From top to bottom: below 150 K, above 350 K, 210 K and a film deposited at 136 K that was annealed at 350 K.

## 2. Influences on the energetic position of the transport levels

---

In the following, the different geometric structures of the thin films found in Section 2.5.1 are discussed with the help of (AR)PES data for the different preparations.

Figure 2.57 shows the UPS spectra (valence level region as well as secondary electron cut off) and the corresponding SPALEED diffraction patterns for all preparation conditions (a)-(c) and for the multilayer phase transition (d). In this plot of all spectra, the differences between the preparations are even more visible. The shifts of the valence level spectra (b) and (d) with respect to the other two as well as their different shape is striking. Particularly, the central peak series between -2.5 and -5.0 eV shows three separate peaks for (b) and (c) instead of two (a) and (c). Additionally, the intensity ration of the HOMO and HOMO-1 of about 1:1 for (a) and (c) changes for (b) and (d) to about 1:2.

The position of the secondary electron cut-off and the connected measured work function for all four preparations stayed constant. However, the rather big shift of the electronic levels (470 meV) in the high temperature phase (b) originates from the different work function of different crystal faces at the surface of the thin films. This results in a change of the IP (see [ZVZ<sup>+</sup>07] and Section 2.3) due to the absence of Fermi level alignment and will be discussed in detail in section 2.6.4. The direct phase transition by annealing the low temperature phase to 350 K (d) shows a smaller shift of 220 meV, which might also result in a change of the crystalline face at the surface. Since it has not been investigated in detail with SPALEED, it is only possible to speculate about the reason why this shift is smaller than the one of the high temperature phase.

Besides the shift of the spectra with respect to each other, the change of the peak width from 450 meV in (b), (c), and (d) to 600 meV in (a) is significant. This increased width is due to the decreased level of order in the thin films prepared below 150 K, which will be discussed in more detail in the peak broadening Chapter 3. Since the HOMO position for the determination of the ionization potential is determined at the onset of the peak, the difference between (a) and (c) can be fully attributed to the different peak widths.

An exceptional observation can be made for the high temperature phase (b). A new peak becomes visible on the low binding energy side of the HOMO ( $E_B = -1.4$  eV) with a very steep onset and a FWHM of about 180 meV. This component has no counterpart in the calculations and is only visible for films prepared this way. Since all films were grown from the same batch of DIP in the evaporator and the peak was neither visible in films before nor after such high substrate temperature preparations, a contamination with a dopant can be excluded. The DFT calculations predicted no peak near this position which is a small hint towards a structural origin regarding the quality of such calculations. Nevertheless, N. Dori et al. [DMK<sup>+</sup>06] showed that the results of the relative energy positions for the first two or three frontier orbitals around the Fermi energy are quite independent if one uses GW or the DFT with B3LYP functional. A structural cause could be a Davydov splitting due to two or more molecules in the unit cell of this particular crystalline structure. The ARUPS measurement of the Subsection 2.6.3 will investigate whether this peak is due to a surface effect.

The same observation of strong difference between the preparation can also be found for the IPS spectra in Figure 2.58. Similar to the UPS observations, the relative intensity



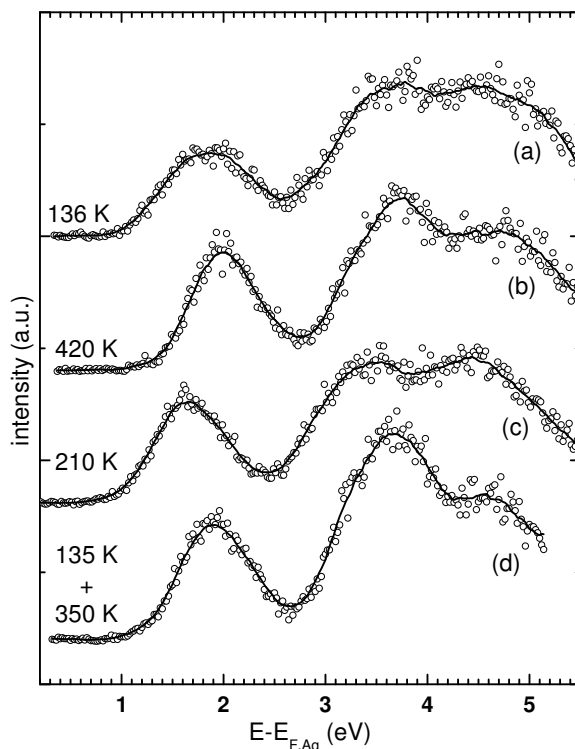


Figure 2.58.: The IPS spectra that correspond to the films in Figure 2.57.

ratio as well as the position of the electronic levels changes. The peak between 3 and 4 eV shows the strongest dependence of intensity on preparation and has the highest intensity for (b) and (c). The LUMO behavior is less simple, because it seems to have more than one component. The DFT calculation did not predict another electronic state near the LUMO (see Table 2.10), which leads to the assumption of an origin in the geometric structure of the thin films. The LUMO of the low temperature phase (a) appears very broad, which can also be attributed to inhomogeneous peak broadening. A closer look to the LUMO of the intermediate phase reveals a slight asymmetry to higher binding energies, which might be due to the mixing of several geometric structures in that phase.

The broadening of the low temperature spectrum (a) due to the inhomogeneity of the film does not shift the onset significantly. It seems more like there is an additional component on the high energy side of the LUMO of the 210 K phase, and the superposition of these two peaks form the low temperature LUMO. The 210 K LUMO itself also exhibits a slight asymmetry to the right which might be a result of its polycrystalline character. The IPS spectra (b) and (c) show a similar shift of their maxima as the corresponding UPS spectra. The smaller shift of the LUMOs of 360 meV for (b) and 270 meV for (d) with respect to (c) might also be the result of the superposition of two peaks in the LUMO of (c).

The position of the peak maxima shows the same trend as the UPS data. For the high temperature phase (b) and the annealed film (d), the peaks are shifted away from the

## 2. Influences on the energetic position of the transport levels

Fermi energy of the substrate. The shifts are 360 meV for (b) and 270 meV for (d) with respect to the intermediate phase (c). The discrepancy to the values for the UPS might be caused by the presence of a second peak in the LUMO of (c) that shifts the maximum position slightly.

### Low temperature phase ( $T < 150$ K)

The SPALEED measurements showed that films prepared at low temperature exhibit a lower degree of order but preserve the structure of the monolayer. In the PES investigation, films were grown between 125 and 150 K with no significant changes in the signature of the valence levels. Since the measurement of the temperatures in different UHV chambers can slightly differ (offsets of 20 K are not unusual), the highly ordered phase found in the SPALEED at 150 K growth temperature might not be achieved.

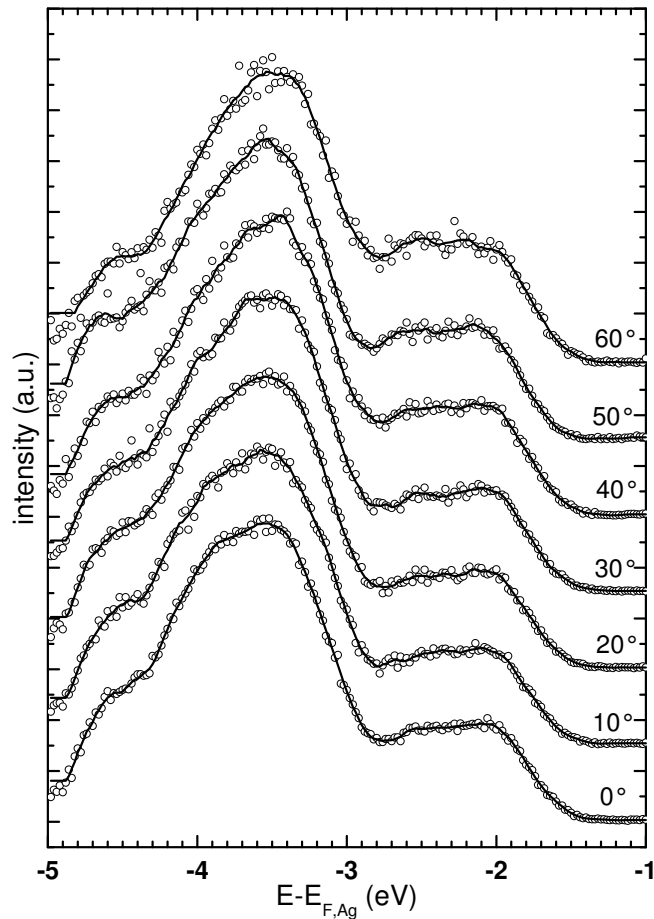


Figure 2.59.: Angle dependent UPS spectra for a DIP film prepared at 136 K.

**ARUPS** The change in the spectrum by variation of the angle shown in Figure 2.59 is quite small. A small change in intensity of the left shoulder of the central peak series can

## 2.6. How geometric structure influences the UPS/IPS - spectrum: Diindenoperylene

---

be detected. In general, the spectrum stays the same for all angles reflecting a low degree of order in the film and indicating that the surface shows no drastic change compared to the bulk.

### High temperature phase ( $T > 350$ K)

The photoelectron spectroscopy data in this Section originates from samples that were grown close to the desorption temperature of the DIP multilayer at 420 K. After the growth process the sample heating was stopped in order to avoid electromagnetic fields during the measurement. The SPALEED measurements of the previous Section showed that this does not influence the structure of the film which was additionally checked by the LEED installed at the PES chamber.

The SPALEED diffractogram for the high temperature preparation exhibited very sharp spots even for thicknesses of nine layers. The films are therefore expected to have a high degree of structural order.

**ARUPS** At a first glance, the ARUPS data in Figure 2.60 reveals no drastic changes in the shape of the spectrum. The broad peak at about -3 eV shows a variation on its right shoulder at which another peak varies its intensity with angle (maximum at  $40^\circ$ ). The peak at -2.2 eV shows a similar intensity variation, and it is very likely that the changes for both peaks are due to the altered geometry between incident dipole vector and the orbital symmetry with changing angle.

The angle dependent data shows no evidence that the new peak at -1.4 eV originates from a surface component. Its relative intensity has two maxima at  $0^\circ$  and  $40^\circ$  which is contrary to the expected behavior of a surface and a bulk component. In the latter case, the bulk component should have maximum intensity at normal emission and minimum intensity at  $70^\circ$ , the measurement is very surface sensitive (the surface component would behave the opposite way). The origin of this new and narrow peak is therefore neither a contaminant nor a surface effect and should be connected to the geometric structure of the thin film and the interaction of its molecules.

### Intermediate phase ( $T = 210$ K)

The SPALEED measurements have shown that at this preparation temperature the DIP molecules form polycrystalline films with three different structures. The samples were prepared at 210 K in the PES chamber without heating since the manipulator was cooled by pumping liquid nitrogen through it which could be controlled by a valve. The temperature could be stabilized in this way by  $\pm 5$  K. Further cooling of the sample resulted in no change of the measured UPS spectrum, which was important for the HREELS measurements.

**ARUPS** The angle dependent UPS data for this preparation temperature shows significant changes and can be seen in Fig. 2.61. First of all, the HOMO-1 at -2.6 eV increases in intensity. The central peak group at about 3.8 eV starts to split into two smaller

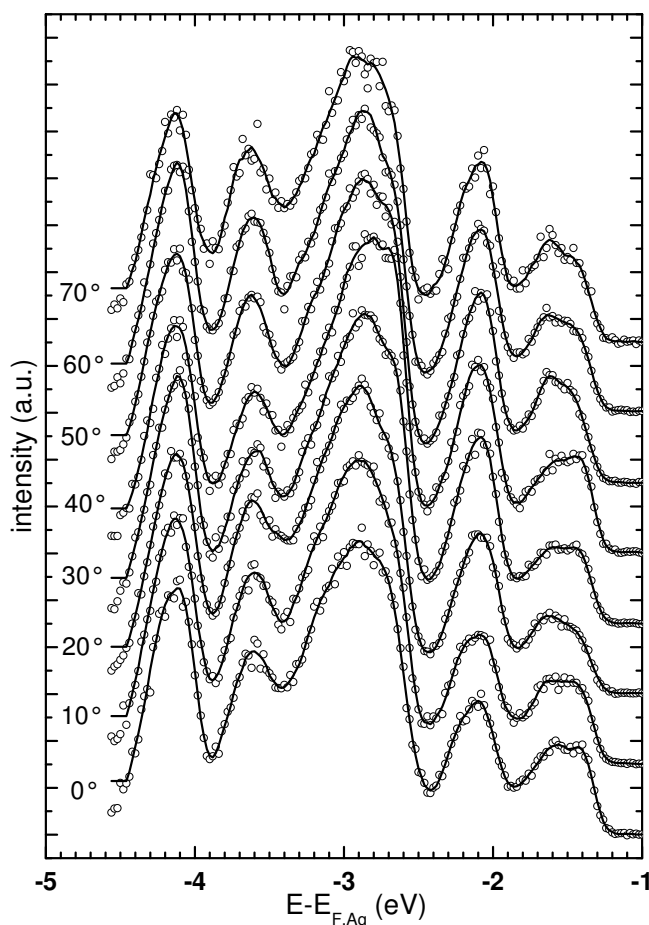


Figure 2.60.: Series of UPS spectra of a DIP film prepared at 420 K substrate temperature. Between each spectrum the angle was changed by  $10^\circ$ .

sub-peaks. The end positions at  $70^\circ$  are about 3.4 and 4.0 eV and in between there is a gradual shift of the two components. The final spectrum at  $70^\circ$  resembles the high temperature phase UPS without the sharp HOMO component and without being shifted (IP stays constant).

A closer look to the angle dependent intensity ratio between the HOMO and the HOMO-1 can be taken in Fig. 2.62. An obvious observation is that the intensity ratio does not follow continuous change expected for a surface and a bulk component, but rather alternates with a period of  $40^\circ$ . The DFT calculations assigned different irreducible representations to the HOMO and HOMO-1, which have different symmetries. If only one geometric structure would dominate in the thin films, the angle dependence of the dipole matrix element would be a possible explanation. This dependence should be different for different orbital symmetries. However, the SPALEED data showed the coexistence of three different phases and therefore the UPS spectrum of the film should be the superposition of the spectra of the single phases. The fact that the UPS spectrum at

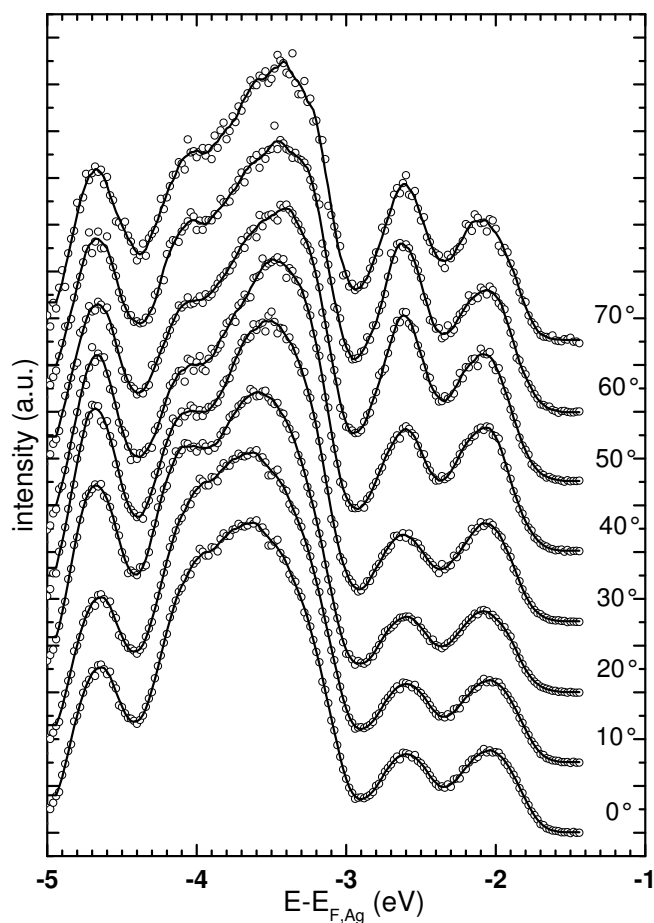


Figure 2.61.: ARUPS series of a 210 K DIP film.

70° resembles the high temperature/phase transition spectrum leads to the assumption that one of the structural phases dominates the spectrum at shallow angles. A film that shows such a behavior should therefore consist of different structural phases that are either arranged on top of each other or of which one of the geometries forms larger crystallites perpendicular to the surface. The variation in the HOMO to HOMO-1 ratio has therefore most likely multiple reasons and cannot be interpreted simply.

#### 2.6.4. How structural changes cause IP changes

The shift of the orbitals which was found in the previous Subsection is not a rigid shift of the entire spectrum as seen in Figs. 2.57 and 2.58. Moreover, the measured work function (= position of the secondary electron cut-off) stays constant. Figure 2.63 shows the frontier orbitals as well as the secondary electron cutoff for two differently prepared DIP films. The upper one was prepared at 210 K and the lower one at 420 K. By averaging separated peaks of the spectrum that do not change their relative position or undergo

## 2. Influences on the energetic position of the transport levels

---

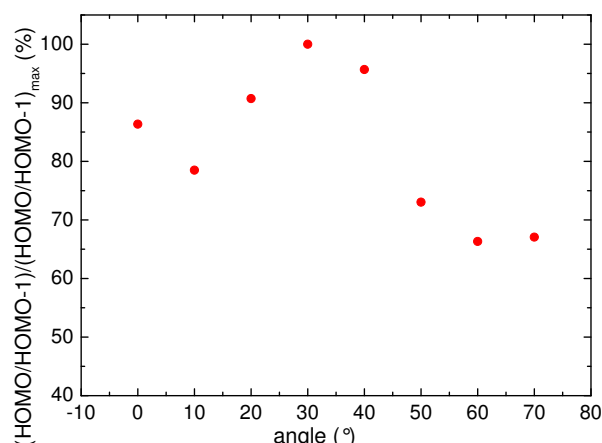


Figure 2.62.: Dependence of of the intensity ratio of HOMO to HOMO-1 on the emission angle.

strong changes in the intensity, the shift of the orbitals can be determined to about 480 meV. This finding is corroborated by the XPS results in Figure 2.65 which show a shift of the  $C_{1s}$  peak of 470 meV while the substrate peaks stay at the same position for both preparations. Together with the work function being constant, this can be related to a change in the ionization potential of the thin film. The IPS spectrum only shifts by 360 meV, which could be due to a superposition of the signals from different crystalline structures in the 210 K phase. The asymmetry of the LUMO in the 210K IPS spectrum corroborates the assumption of more than one component underneath.

However, changes like this have been reported before in the literature (e.g.: [FYK<sup>+</sup>06], [IKK<sup>+</sup>06], [IWN<sup>+</sup>03], [IHK<sup>+</sup>07], [INR07], [KGS<sup>+</sup>06]) and they were always attributed to a change in the orientation of the molecules with respect to the substrate. In the case of flat lying molecules the IP was in all cases higher than for molecules standing upright (change in IP up to 0.7 eV). S. Duhm et al. [DHS<sup>+</sup>08] suggested a simple model which explains this behavior. In their investigation DH6T was grown on Ag(111) and different ionization potentials were observed for the monolayer lying flat on the silver and the multilayer in which the molecules stand upright. A difference of 0.6 eV could also be seen in the XPS data, S. Duhm et al. performed DFT calculations on the electrostatic potential above the molecular film for different orientations of the molecules. A simpler example of the same mechanism is the change of work function for different faces of a metal single crystal. For such a system every crystal face has a different electrostatic potential through which an electron leaving the crystal has to travel. Transferred to the organic thin films, the lying and the standing molecules form different faces of an organic crystal with different work functions ( $\Phi_1$  and  $\Phi_2$ ). The important difference of the systems is the band alignment at the interface between substrate and adsorbed molecules. Since this band alignment is for most of the cases an alignment of the vacuum levels shifted by the interface dipole ( $\Delta$ , see Section 2.3), the vacuum level determined by the secondary electron cut-off in UPS stays at the same position because the interface does not change for the different orientations of the top molecules in the film. The Fermi

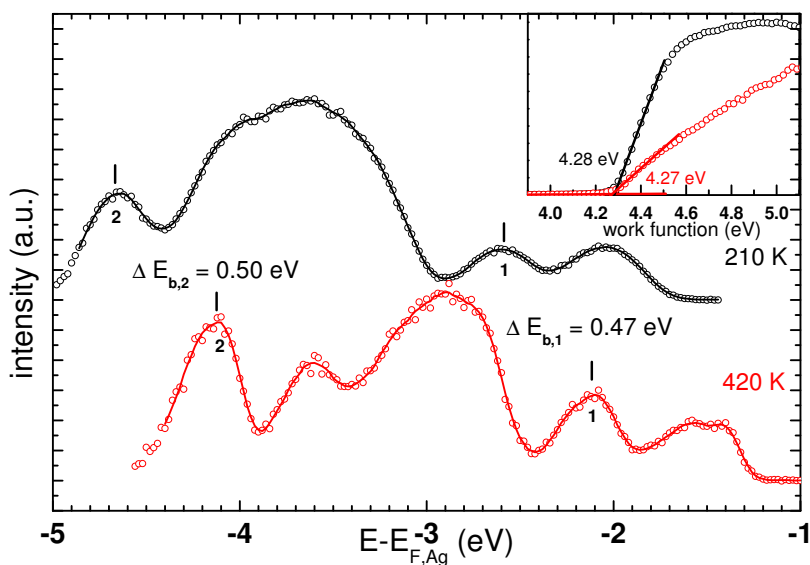


Figure 2.63.: Comparison of the UPS spectra of DIP grown at 210 K and 420 K respectively. The shift between them was determined using the sharp peaks labeled 1 and 2. The inset shows the work function for both films measured at the secondary electron cutoff.

levels do not align and a change in the work function of the film leads to a change in the ionization potentials. A sketch of this model can be found in Figure 2.66. As shown in Section 2.3, it is in most of the cases not possible to measure the position of the Fermi level within the molecular layer, which is why it was chosen in the middle between HOMO and LUMO in the sketch where it should be if no dopant is present.

From the fact that the interface dipole stays constant (no change in work function between the phases) and the observed change in the ionization potential, it can be concluded that the first layer of the high temperature phase lies flat on the substrate and the subsequent ones stand upright on top of it.

### 2.6.5. Multilayer phase transition in the UPS

One of the phase transitions described in the SPALEED Section was also investigated with UPS in Fig. 82. The preparation of a closed film was possible if the DIP was deposited at below 150 K and subsequently annealed, which is why this phase transition was also accessible to PES. Every time a film prepared at 210 K was annealed, the molecules rearranged in such a way that the substrate XPS signal significantly increased, the Fermi edge became visible in UPS even for very thick films and no usable valence level spectrum could be obtained. If the combination of preparation temperature and annealing temperature was chosen right, the film remained closed and the XPS did not show any increase of the substrate signal (see Figure 2.68).

Figure 2.67 shows the UPS spectra for a film prepared at 136 K which then annealed in three steps at 210, 280, and 350 K. The work function was lowered by 60 meV during

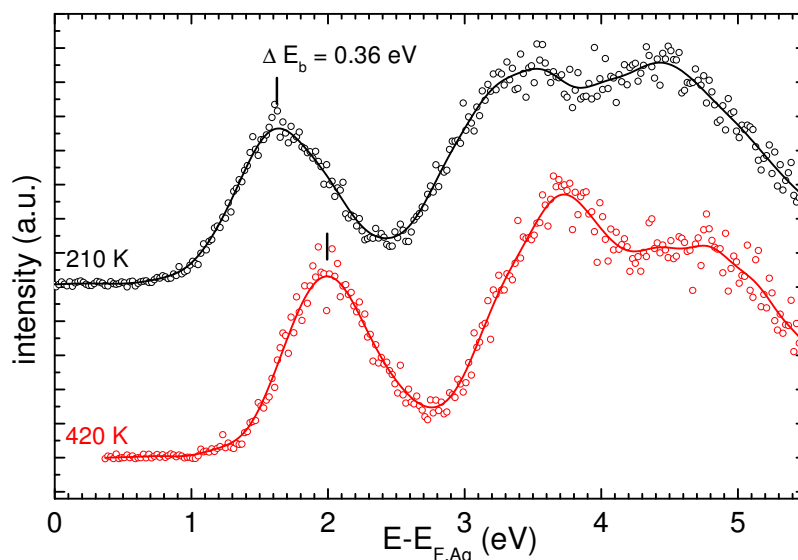


Figure 2.64.: The IPES spectra that correspond to the films used also for Figure 2.63. The shift was determined at the LUMO maximum.

the annealing process which is close to the detection limit of the apparatus. The shape of the spectrum did not change significantly by annealing the film at 210 or 280 K. After heating the substrate to 350 K the molecules had enough thermal energy to rearrange. The resulting spectrum resembles the high temperature phase and the 70° - spectrum of the ARUPS data for the 210 K preparation but is shifted by 220 meV with respect to the latter (including the work function shift).

### 2.6.6. HREELS of the different phases

The aim of the HREELS measurements was to acquire information about:

- Changes in the intermolecular interaction between different structural phases.
- The strength of interaction between molecules and substrate in the first layer.

Figure 2.69 displays a DFT calculated IR spectrum, all multilayer, and the monolayer HREELS spectra. The first information that can be extracted from this comparative plot is the difference between calculated IR spectrum and the different multilayer phases. Since HREELS in specular geometry and IR should provide quite similar results and since the IR spectrum was calculated for a free molecule, information about the difference between gas phase and solid state can be extracted.

Three regions in the spectra attract attention during comparison. One is the region between 100 and 250  $\text{cm}^{-1}$ , in which the calculation produces two weak peaks, but the measurements finds up to three. The third peak at 218  $\text{cm}^{-1}$  is only visible for 115 K and 210 K which could have two reasons. Either an residual gas condenses on the surface since both of the preparations were measured at 115 K (the equilibrium



## 2.6. How geometric structure influences the UPS/IPS - spectrum: Diindenoperylene

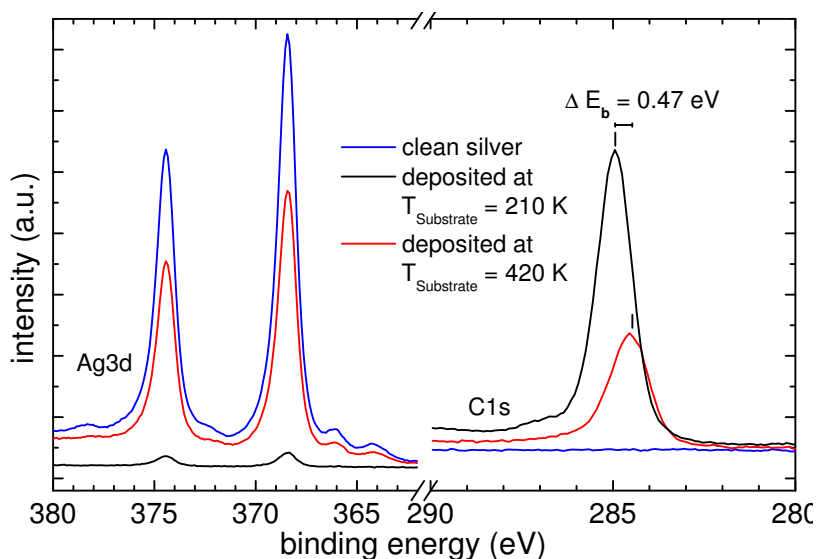


Figure 2.65.: On the left hand side are the Ag 3d - XPS spectra for clean silver and the two preparations. On the right hand side the corresponding C 1s spectra are shown.

temperature to which the sample cooled down without heating). Or, the cooling changed the intermolecular distances or the molecular structure in such a way that there is a shift of frequency, or a dipole inactive vibration is now excited. However, the residual gas origin is unlikely, since it would produce more than just one new peak, and the film structure seems to be responsible. A geometry change of the molecule for lower temperatures was suggested by M. Heinrich et al. [HPT<sup>+</sup>07] for the single crystal unit cell of DIP. They proposed a bending and torsional deformation of the DIP molecules in order to fit in their X-ray diffraction determined unit cell. This change breaks the  $D_{2h}$

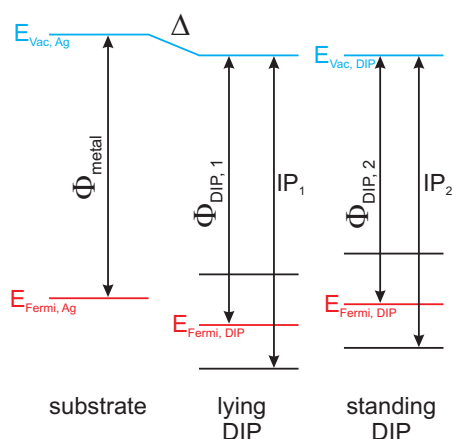


Figure 2.66.: Sketch of the energy levels of lying and standing DIP molecules with respect to the silver substrate.  $\Delta$  is the interface dipole which shifts the vacuum levels between substrate and adsorbate.

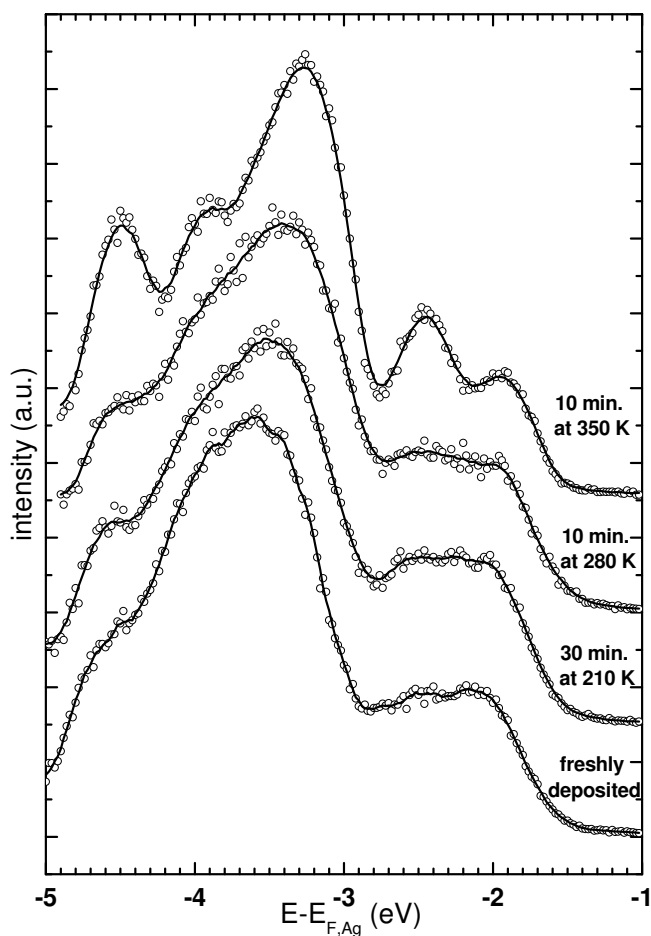


Figure 2.67.: Series of UPS spectra corresponding to a structural phase transition of the multilayer (see Section 2.5.1). This particular transition is only possible for films prepared below 150 K and annealed at  $\geq 350$  K.

symmetry of the molecule, but becomes irrelevant for higher temperatures because then the vibrations of the molecule have a higher amplitude than the actual bending. In that case the peak at  $218\text{ cm}^{-1}$  could originate from a former dipole inactive mode, which now has a significant excitation probability.

The second and third regions of attention are between  $500$  and  $650\text{ cm}^{-1}$  and from  $1000$  to  $1450\text{ cm}^{-1}$  where no peaks at  $518$ ,  $611$  and  $1200\text{ cm}^{-1}$  are found by the calculation, but in all measurements (very small but still visible for  $115\text{ K}$  and  $210\text{ K}$ ). The peak series around  $1400\text{ cm}^{-1}$  is strong in the calculation but weak in the experiment. These peaks become more intense with growing temperature. All of these peaks belong to in-plane bending modes of the hydrogen atoms or in-plane stretching modes of the carbon atoms. The mode at  $1424\text{ cm}^{-1}$ , e.g., belongs to a combination of a bending of the hydrogens and a stretching of the C-C bonds at the indeno-groups that could be suppressed by the arrangement of the molecules. The most intense dipole active modes are displayed at their maximum amplitude in Appendix B to visualize them.

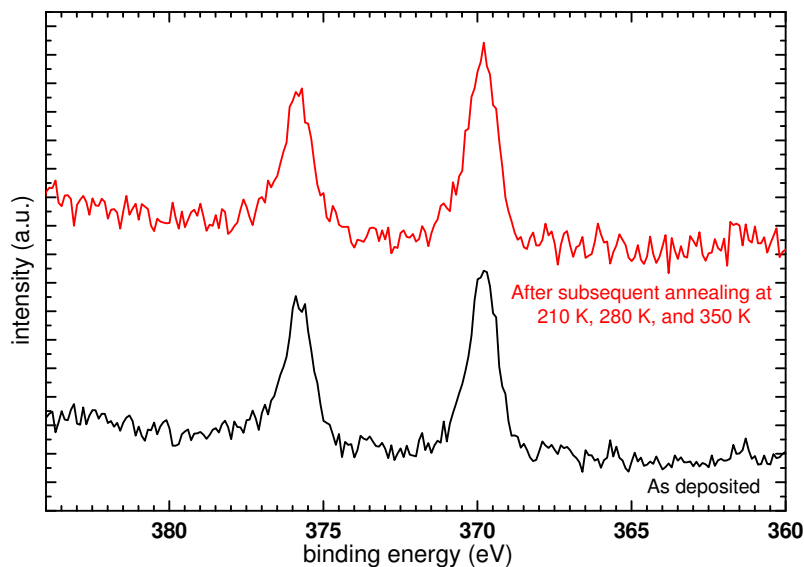


Figure 2.68.: To Figure 2.67 corresponding XPS spectra of the Ag 3d substrate peak for the freshly deposited film and after the subsequent annealing cycles.

The differences in position and intensity of calculated and measured spectra can have a variety of reasons. Modern DFT calculations are very precise in predicting these values (see, e.g., [AU05]), but they always predict them for a free molecule. Nevertheless, the calculated IR spectrum is quite close to the measured HREELS spectra and the observed differences for higher wavenumbers could either be a product of the intermolecular interaction and the arrangement of the molecules in the thin films or of the deformation of the molecules. The surface unit cell for the monolayer is big enough to arrange the molecules in it without a deformation. For all multilayer unit cells no data for the vector perpendicular to the surface is available and deformation as proposed by M. Heinrich et al. [HPT<sup>+</sup>07] can therefore not be excluded.

Significant changes between the structural phases could only be found for the low wavenumber vibrations below  $250\text{ cm}^{-1}$  and for the 210 K phase which consists of a mixture of three different structures, which was already mentioned in the comparison to the calculated IR spectrum. The small energetic shift (about  $10\text{ cm}^{-1}$ ) of some of the 210 K modes are likely to originate from the strained unit cell structure found in the SPALEED. The intensity changes for the  $B_{1U}$  and  $B_{2U}$  modes can be mostly attributed to the altered orientation of the molecules with respect to the substrate between 115 (flat) over 210 (mixture) to 400 K (standing). Considering the strong changes in the SPALEED data, the differences in HREELS are comparably small, which indicates a weaker intermolecular interaction in the case of DIP and explains the strong temperature dependent geometry changes for the molecule. This assumption is based on the large number of molecular arrangements and the obviously small energy differences between them.

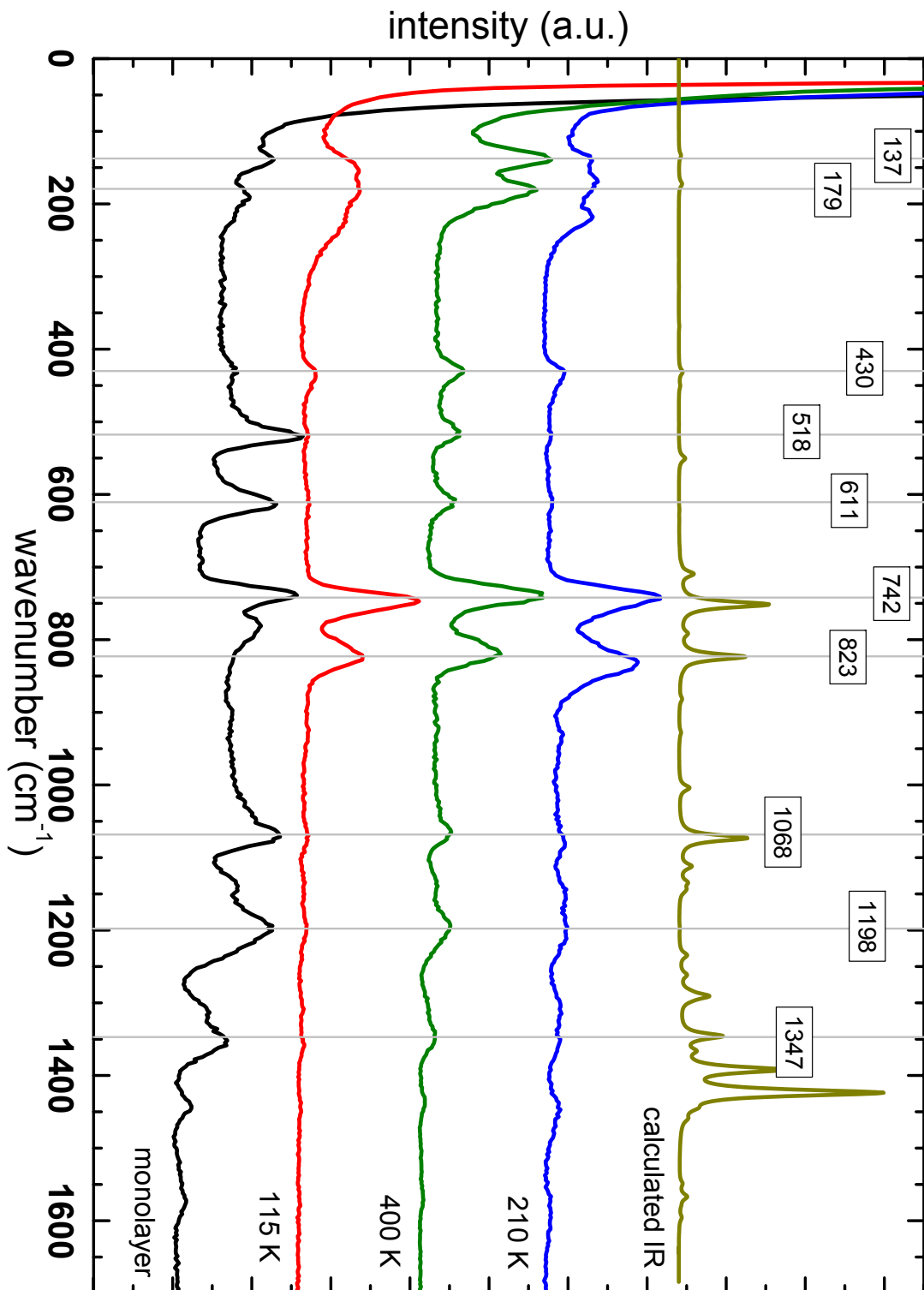


Figure 2.69.: Comparison of the HREELS spectra for all DIP structural phases. The gray lines indicate the peak positions at 400 K and are guidelines for the eye in order to recognize shifts.

## 2.6. How geometric structure influences the UPS/IPS - spectrum: Diindenoperylene

---

The interaction between monolayer and substrate was found to be significant because of the intensity of in-plane modes in the HREELS spectra. Since it was possible to determine the orientation of the molecules with respect to the silver surface to be flat lying, the strong intensity of the in-plane modes is likely to originate from the coupling of vibrations to electronic states of the substrate as described for PTCDA on Ag(111) by F. S. Tautz et al. [Tau07]. This kind of coupling demands for a chemisorptive bond, but could not be unambiguously verified in the UPS data of the monolayer due to the small data basis.

### 2.6.7. Summary and Conclusions

The variety of geometric structures in the previous SPALEED measurements found its counterpart in the PES spectra of the frontier orbitals. Every previously identified geometric structure could be related to a different combination of UPS, IPS, and HREELS spectra and allowed to study the effect of geometry to the electronic structure.

The basis for the attempt to model the different film geometries in the following was laid by the investigation of the monolayer, and therefore the interface between substrate and molecular thin film. UPS as well as HREELS measurements point towards a rather chemisorptive bond of the molecules to the substrate.

The differences of the PES spectra between the different multilayer phases could to a large extent be attributed to geometric effects, such as, e.g., the peak broadening due to a lower degree of order in the low temperature phase. Also the shift of the electronic levels between different structural phases could be related to a change of molecular geometry and, in particular, a change of the surface. The polycrystallinity of the intermediate temperature phase was visible in a significant angle dependence of the shape of the spectra, which lead to the assumption that different structural phases dominate the spectrum at different angles. Finally, the high temperature phase showed a new state in front of the HOMO, which does not originate from a contaminant. Also a surface effect could be excluded because the peak intensity showed no significant trend on the angle. Still possible are Davydov splitting of the electronic states or any kind of electronic intermolecular interaction.

The HREELS data for the multilayer films contains basically three main information. Firstly, there is a significant difference between calculated and measured intensities for the region above  $1000\text{ cm}^{-1}$  which has to be a solid state effect, since the calculations represent a free molecule. Secondly, the intensity from in-plane modes increases from low temperature over intermediate to high temperature phase, which indicates an increasing proportion of standing molecules with increasing preparation substrate temperature. Finally, an unidentified peak at  $218\text{ cm}^{-1}$  is visible at low temperatures and is connected to the geometric structure of the film or the molecules in it.

For a more comprehensive understanding of the structural effects of the different preparation methods, further investigation with, e.g., X-ray diffraction (XRD) or near edge absorption fine structure (NEXAFS) measurements would help to find the missing unit cell vector length perpendicular to the surface and the orientation of the molecules with respect to the substrate.

## 2. Influences on the energetic position of the transport levels

---

### Model of the film structures

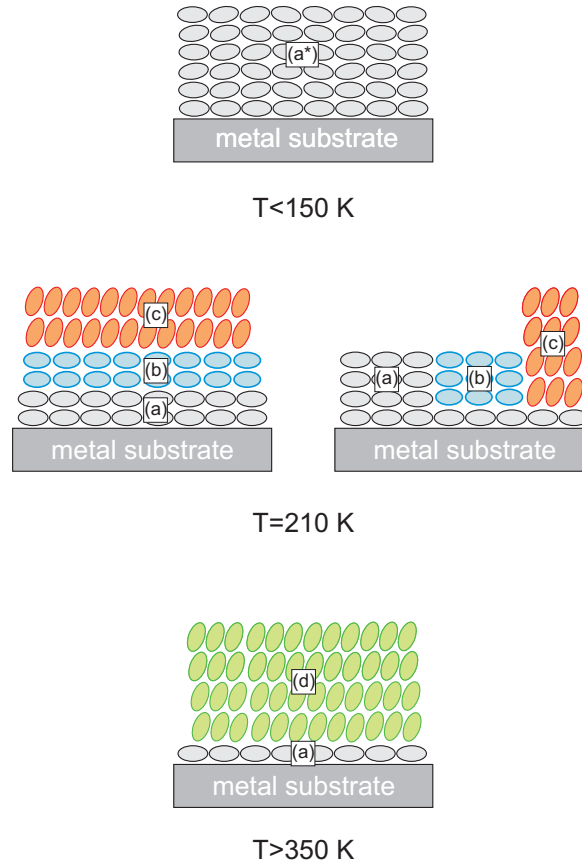


Figure 2.70.: Models for the different structures resulting from the substrate temperatures during the growth of the film. (a\*) represents the low order structure for  $T_{\text{Substrate}} < 150$  K. (a), (b) and (c) are the three structures found in the SPALEED pattern for 210 K and (d) represents the high temperature phase.

Based on the SPALEED, HREELS and ARUPS data, it was possible to develop a model for the film structures of the different phases. Figure 2.70 shows sketches for each preparation temperature region. In the region below 150 K the SPALEED data shows a slightly disordered variant of the monolayer structure (a) and was therefore named (a\*). The disappearance of the diffraction pattern for thicker films could originate from a gradual decrease of order with increasing distance from the metal surface.

The sketch of the 210 K phase shows two alternative models that are both consistent with the experimental data and could not be distinguished with the investigation methods used. Three different patterns were visible in the SPALEED diffractogram, and the ARUPS data showed that with increasing angle between the surface normal and the spectrometer a change in the shape of the UPS spectrum occurred. The intensity variations of the peaks in the angle-dependent spectra can be partly attributed to effects of the matrix element. The fact that the spectrum at  $70^\circ$  resembled strongly the high temperature

spectrum without the shift in binding energy indicates the domination of different geometric structures in the spectrum of normal and grazing emission. This angle dependent behavior can be explained with two different models. Either the molecular arrangement found as patterns in the diffractogram are arranged on top of each other with an altered version of the standing molecules of the high temperature phase (c) on the top and the monolayer structure (a) near the substrate, or regions of different geometric structure coexist on the sample. In the latter case, the change in the UPS spectra with the angle could be explained by an island growth of structure (c) which then overgrows the other islands (a) and (b) and therefore dominate the spectrum for higher angles. On the other hand, the spot sizes in the SPALEED are not significantly larger than the widths of the single domain patterns of the monolayer or the high temperature phase, which should be the case if the average domain size decreases due to the coexistence of three different ones. However, SPALEED is very surface sensitive and an arrangement on top of each other can therefore be excluded.

Finally, Figure 2.70 shows the structure model of the high temperature phase. The strong change in the ionization potential suggests that the molecules have an altered orientation to the substrate compared to the other phases which is very likely to be standing. The fact, that the measured work function stays constant in comparison to all other phases and that annealing of the multilayer results in a flat lying monolayer, suggests a lying monolayer of DIP molecules at the interface and standing molecules on top of them. The UPS spectrum resembles the 70° UPS for the 210 K phase, but the larger energy shift and the apparent differences in the spectrum lead to the assumption of a different structure (d) for the high temperature phase.

## 2.7. Summary and Conclusions

This Chapter tried to give a comprehensive overview about all influences to the positions of electronic levels in a PES and IPS experiment. Some of them are based on physical effects at interface to the substrate or within the thin films and others are directly connected to the processes during a photoemission experiment.

Transport gap determination discussion in the literature often mention the concept of polarization shift, which is related to the surface sensitivity of photoelectron spectroscopy. It was shown in this work and by the work of M. B. Casu et al. [CZK<sup>+</sup>07] that no shift between the surface and bulk of thin films could be observed, which could be expected if the surrounding for molecules in the bulk and at the surface is different. This discussion is closely connected to the one about the strength of intermolecular interaction, since an interaction stronger than pure van-der-Waals would open new delocalization channels for the charge produced in the photoemission process besides the polarization of the vicinity.

Since many of the effects that were described in this Chapter heavily depend on the thickness of the thin film, the aspect of film morphology was included in the discussion. Only films with a high homogeneity in thickness provide good thickness dependent information. It was shown, that this could be achieved for all the molecules if the proper growth conditions were chosen.

## 2. Influences on the energetic position of the transport levels

---

Energy level alignment at the interface and its further development with increasing film thickness was reviewed and complemented by own experimental results. It was shown that the major effect which determines the relative positions between molecule and metal substrate is the interface dipole. In the presented experimental data as well as in the reviewed literature no major shift of the adsorbate energy levels with respect to the substrate Fermi level could be observed with increasing film thickness. The only exception is  $\text{Alq}_3$  which represents a special case due to its permanent dipole moment which tends to align during the growth process under dark conditions. Therefore band bending plays only a minor role within the thickness range accessible by PES.

The focus of the experimental work of this Chapter is on the system DIP on Ag(111), which proved to be a reference system for the study of the influence of geometric structure to the electronic. For this purpose the growth temperature dependent film structures were investigated with SPALEED in order to lay a basis for the further assignment of structural changes to features of the valence level spectra. Particularly, the effect of low structural order and coexisting crystalline phases in the films could be observed. A structural reference point for all these observations was the high temperature phase that forms highly ordered thin films. Additionally, the molecules in this phase apparently have a different orientation with respect to the substrate than in the other phases, because they exhibit an altered work function. Due to the non-existence of Fermi level alignment, but an alignment of the "virtual" vacuum levels, this did not transfer to a shift of the secondary electron cut-off in the UPS spectrum. Therefore interface stayed the same, and a change of the surface shifted all electronic levels by about 450 meV resulting in an increase of the measured ionization potential.

In summary, the results of this Chapter demand for a stronger integration of structural aspects as well as substrate-adsorbate interaction into the discussion about the energy level position. It is not possible to determine the position of the Fermi level within the HOMO and LUMO of the organic thin films, since no Fermi level alignment within the first few hundred nanometers of film thickness has been observed so far. The more general approach to give the values of the positions for a specific system would therefore be the ionization potential and the electron affinity in combination with the value for the interface dipole. This information needs to be completed by the information about film structure, which could change these quantities.



### 3. Peak broadening mechanisms

This Chapter is the second important part for the definition of transport levels in valence spectra. After the influences to the peak position were shown, the mechanisms responsible for the width of these peaks will be in the focus of this Chapter. A further goal will be to quantify the size of each effect in order to identify the dominating effects during the process of photoemission. The inorganic semiconductors will be included in this discussion because they are regarded as a model system for the application of combined PES and IPS. However, comparative data has only been measured for the organic thin films, which have an important advantage: For many organic materials the HOMO and LUMO are peak energetically well separated from the rest of the spectrum (see Fig. 4.13). If there is only one electronic state per peak, which is corroborated by DFT calculations for PTCDA and DIP ([DMK<sup>+</sup>06] and Section 2.6.1), it is possible to determine the peak width of this single state. There is no guarantee for this, since solid state effects, such as Davydov splitting due to two or more molecules in the unit cell, can increase the number of states, but it is as close as possible to a single electronic state.

Since the experimental broadening in UPS is about one order of magnitude less than for IPS, the width of the HOMO of the molecules will be utilized for an estimate of the contribution of each effect. The shape of the HOMO can be fitted by a Gaussian peak for the multilayer from which a full width half maximum (FWHM) can be derived. All broadening contributions will also be approximated to be Gaussian peaks which are convoluted and together form the overall peak width. In this convolution the Gaussian widths  $\sigma$  add quadratically:

$$\sigma_{total}^2 = \sigma_1^2 + \sigma_2^2 + \sigma_3^2 \dots \quad (3.1)$$

$\sigma$  is connected to the FWHM via:

$$FWHM = 2\sqrt{2\ln 2} \cdot \sigma \quad (3.2)$$

These FWHM were determined for all molecules by a fit of a Gaussian function to the HOMO and LUMO and averaged over all investigated multilayer films. They are shown in Table 3.1. The values of the HOMO peak width are generally smaller than those of the LUMO, which will be discussed at the end of this Chapter. The HOMO values range between 0.44 and 0.76 eV. 0.45 eV was chosen as a lower limit, since inhomogeneous broadening and Davydov splitting have the smallest contribution (see Section 3.4). The contribution of all other effect will therefore be compared to this value and the missing contribution calculated with Eqn. (3.1).

The Sections of this Chapter address the six contributions responsible for the width of the peaks:

### 3. Peak broadening mechanisms

---

Table 3.1.: FWHM for HOMO and LUMO for multilayer films of the investigated molecules. Each HOMO/LUMO was fitted by a single Gaussian function (except for the DIP spectra for which the HOMO is not as separated and the HOMO-1 had to be included in the fit). The results of several samples were averaged with a standard deviation of  $\pm 0.03\text{eV}$ .

Molecule	FWHM <sub>HOMO</sub> / eV	FWHM <sub>LUMO</sub> / eV
PTCDA	0.55 $\pm$ 0.03	0.85 $\pm$ 0.03
CuPc	0.45 $\pm$ 0.03	0.92 $\pm$ 0.03
DIP (<150K)	0.61 $\pm$ 0.03	0.97 $\pm$ 0.03
DIP (=210K)	0.46 $\pm$ 0.03	0.79 $\pm$ 0.03
DIP (>350K)	0.44 $\pm$ 0.03	0.77 $\pm$ 0.03
Alq <sub>3</sub>	0.76 $\pm$ 0.03	1.03 $\pm$ 0.03
PBI <sub>4</sub>	0.54 $\pm$ 0.03	N/A

- lifetime
- experimental resolution
- energy band dispersion
- structural inhomogeneities
- vibration/phonon coupling
- static and dynamic screening effects (polarization and relaxation)

In the following it will be shown that from these contributions, only the last three have a significant contribution to the overall peak width. Additionally, these important contributions broaden the peak asymmetrically away from the Fermi energy, which is an important aspect for the discussion of the next Chapter.

#### 3.1. Lifetime

The lifetime of a state relates to an energy uncertainty of a measurement via the equation:

$$\delta E \cong \frac{2\hbar}{\tau} \quad (3.3)$$

The result is a Lorentz peak with width  $\delta E$ . All of the peaks investigated in this work did neither show a Lorentzian shape nor a convolution of a Lorentzian with a Gaussian peak, which results in a Voigt profile. The Lorentzian contribution to the peak width is therefore assumed to be very small. H. Yamane et al. [YNF<sup>+</sup>05] investigated a pentacene monolayer on highly ordered pyrolytic graphite (HOPG) with high resolution UPS. In

this publication they were able to resolve vibrational coupling and attributed Lorentzian widths of 50-90 meV to the 0-0 transition, which were partly attributed to the lifetime. This corroborates the assumption of a very small contribution.

## 3.2. Experimental resolution

The limited experimental resolution of the investigation methods additionally broadens the peaks in the spectrum. It can be experimentally determined from the broadening of the Fermi edge of a polycrystalline gold foil which is described in detail in the doctoral thesis of L. Weinhardt [Wei05]. In the case of UPS this resolution depends on the parameters of the electron energy analyzer such as radius, slit size, pass energy, and iris diameter. For the standard settings that were used to record the data for all molecules the

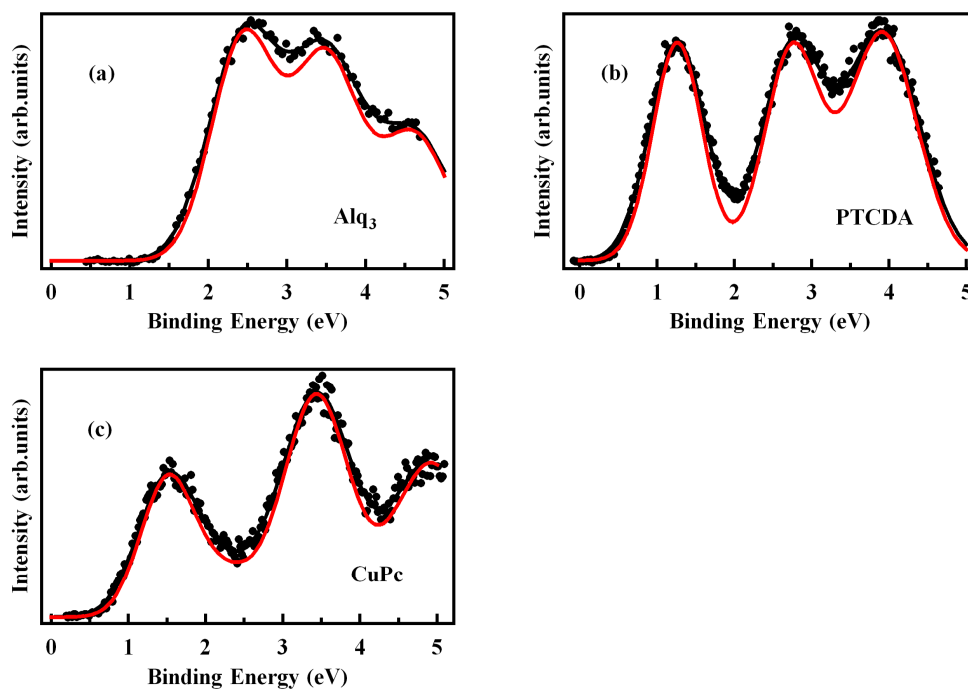


Figure 3.1.: UPS spectra for Alq<sub>3</sub> (a), PTCDA (b) and CuPc (c). The red lines represent the fit result after deconvolution of the experimental broadening.

experimental contribution resulted in an overall resolution of 50 meV. The UPS resolution was determined to 400meV and therefore is about one order of magnitude worse. It mainly depends on the window and the gas mixture chosen for the Geiger-Müller counting tube, which together form a photon band pass, as well as the energy spread of the electrons

### 3. Peak broadening mechanisms

---

emitted from the electron gun. It is possible to narrow the resolution by the use of a grating, which is accompanied by a tremendous reduction of the counting rate, and therefore is not applicable to organic thin films (see Appendix A). The contribution of UPS experimental broadening is very small, since the overall peak width reduces only by a few meV if it is deconvoluted using equation (3.1).

The results for IPS are shown in Figure 3.1. All spectra were fitted with a series of Gaussian peaks and a parabolic background. The red lines show these peaks after the 400 meV experimental contribution was deconvoluted, which results in only minor changes of the shape of the spectrum. Due to Eqn. (3.1) a peak of, say, 800 meV peak width becomes only slightly narrower (about 700 meV) after deconvolution:  $\sqrt{(800\text{meV})^2 - (400\text{meV})^2} = 693\text{meV}$ . Nevertheless, the experimental peak broadening shifts the LUMO onset by an average of about 50 meV, if not taken into account.

### 3.3. Band dispersion and bending

The electron analyzer used for this work has a limited angular resolution and therefore collects data from an angle range corresponding to a finite range of the k vector components parallel as well as perpendicular to the surface. The investigated part of the Brillouin zone is thus rather a volume than a point.

The valence levels of thin organic films have only a very weak **dispersion** because there is only a small overlap of the orbitals of neighboring molecules. The band dispersion was measured by Y.Zou [Zou03], H. Yamane et al. [YKO<sup>+</sup>03] and G. N. Gavrilina et al. [GMK<sup>+</sup>04] for different thin films of organic semiconductors and found to be in the order of a few hundred meV for these systems. However, the peak width of DiMe-PTCDA recorded with good angular resolution was reported as 600 meV by G.N. Gavrilina et al., which does not differ from the 550 meV for PTCDA reported in this work obtained from a three rotational domain film that averages over a larger fraction of the BZ.

Inorganic semiconductors have strongly dispersing bands and are therefore more sensitive to this effect. In the case of silicon described in Section 4.1, the analyzer acceptance angle was reduced to  $\pm 2^\circ$ . With the help of the following formula (from Section 4.1.2) it is possible to calculate the  $k_{parallel}$ -interval over which the measurement was thus averaged,

$$\Delta \left| \vec{k}_{parallel} \right| = \sqrt{\frac{2m}{\hbar^2} E_{kin}} \cdot (\sin\vartheta_1 - \sin\vartheta_2) \quad (3.4)$$

with  $E_{kin} = h\nu - E_{bind} - \Phi$  and  $\vartheta$  is the angle relative to the surface normal. If the free electron mass is taken for  $m$  and a kinetic energy of 6 eV is used (corresponding to electrons near the Fermi edge excited by ArI), one obtains a  $k_{parallel}$ -interval of  $8.8 \cdot 10^8 \text{ m}^{-1}$  corresponding to about 4% of the  $\overline{\Gamma X}$ -distance in the Brillouin zone. The size of the effect depends on the probed volume of the BZ. If it is at a maximum of a band, e.g., the VBM at  $\Gamma$ , 4% correspond to 10 meV. If the probed range of the BZ is not at an inflection point, 4% can be as much as 300 meV at  $0.5 \overline{\Gamma X}$  for the same electronic state.

Figure 3.2 illustrates this for the example of the dispersion of Si in the  $\overline{\Gamma X}$ -direction,

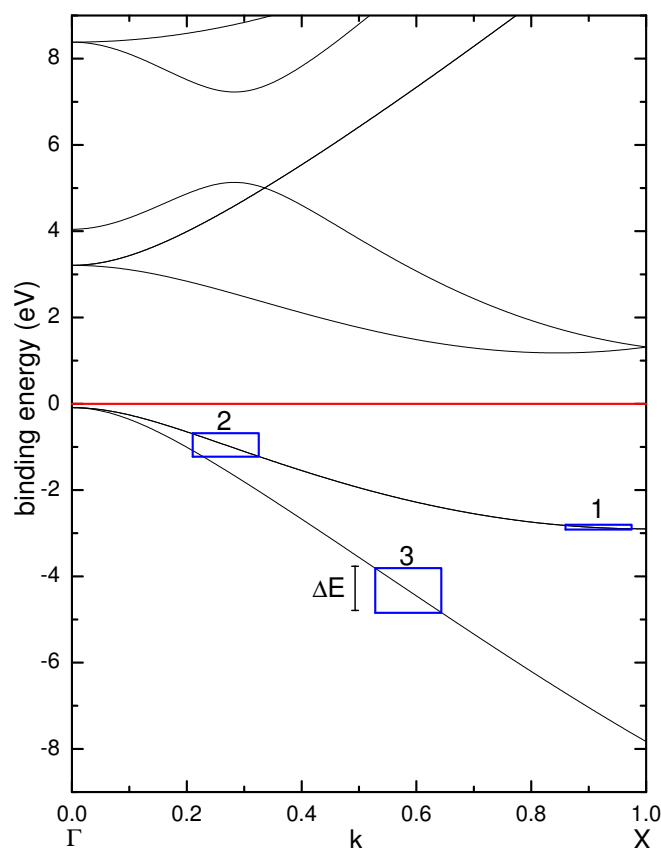


Figure 3.2.: Band dispersion of silicon in its  $\Gamma\bar{X}$ -direction. On the x axis is the k vector in units of the  $\Gamma\bar{X}$ -length and on the y axis the corresponding binding energy. The three blue squares illustrate the averaging for a given k interval at different positions of the Brillouin zone with different slopes of the dispersion relation.

which would be measured in a normal-emission PES experiment with variable photon energy on the Si(001) surface. Three regions are highlighted in which the effect of Brillouin zone averaging ( $\Delta k$  about 15%) is exaggerated for better visibility. The size of the effect increases from 1 to 3 and can be considerably large for the latter. The focus of this work is on the determination of the band extrema (corresponding to 1), where this effect is rather small. Depending on the mass of the hole (e.g. for the VBM) this contribution can vary, but for the measurement at an inflection point the size of this effect is very small. Besides, the VBM will be close to the onset of the peak because the dispersion only points away from the Fermi energy.

The **band bending** discussed in Section 2.4 can also have an influence to the width of the peaks. A photoemission experiment averages the peak positions over several molecular layers. If the position shifts with thickness as it was demonstrated for the  $\text{Alq}_3$  thin films, the peaks of the different layers superimpose and the sum is broader than the single peaks. However, the bending for  $\text{Alq}_3$  was about 50 meV/nm resulting in a very small additional contribution and could not be measured for other molecules.

### 3. Peak broadening mechanisms

---

Band bending is also known for inorganic semiconductors, e.g. due to surface states. The length scale (a few hundred nanometer, depending on the number of free charge carriers in the material) on which this bending occurs is again much larger than the information depth of the photoemission experiment and should therefore result in a very small (negligible) contribution only.

#### 3.4. Structural inhomogeneities

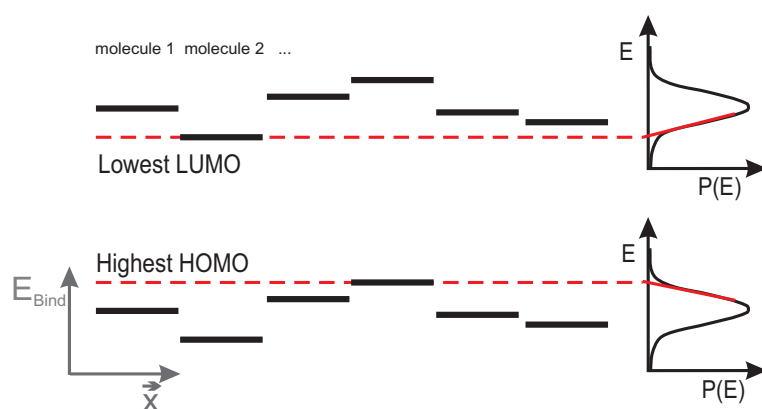


Figure 3.3.: Sketch of HOMO and LUMO levels, which are statistically distributed in energy. The distribution occurs due to the variation of the contribution of screening effects in a film with structural inhomogeneity. The two curves on the right represent the probability distribution for a certain vicinity and the related energetic position of the HOMO or LUMO.

Thin films of organic semiconductors are molecular crystals, in which the single molecules are not as strongly bound as the atoms in atomic crystals. Most of the molecules do not have spherical symmetry, and their orientation with respect to each other thus depends on local interactions. The higher the degree of order in the thin film, the more one orientation of the molecules with respect to each dominates. Some organic molecules, e.g., diindenoperylene, develop coexisting crystalline phases in thin films.

In a photoemission experiment, the molecule itself and its surrounding partners screen the charge produced, which alters the kinetic energy of the emitted electron. The size of this contribution depends on the relative orientation of the molecules with respect to each other [SW07]. Local STS measurements on tetracene on Ag(111) by S. Soubatch et al. [SWTT09] revealed that the screening contribution can shift by up 1 eV for the same molecule, which was attributed to site-specific polarization screening.

The effect of inhomogeneities to the local position of the energy levels is sketched in Figure 3.3. The x-axis represents a direction in space and the y-axis the binding energy

of the orbitals. The energetic position of the orbitals is distributed over a range due to the different arrangements of the molecules. The two curves on the right side represent the probability distribution of them. This distribution has a maximum at the most likely arrangement and is considered to be Gaussian if it is a statistical distribution. Other shapes could be a result of polymorphism when different crystalline structures produce a series of maxima with different heights superposing.

If this effect broadens the PES peak then the onsets of the peaks mark the lowest LUMO and the highest HOMO (see Fig. 3.3). These are the states, in which the photoinduced charges can easily leave the site of their production and experience the lowest relaxation effect contribution. Charge transport will most likely occur through such states. The onsets of the distribution  $P(E)$  (see Fig. 3.3) are therefore closer to the transport level than the maximum of the distribution, i.e. the peak maximum.

## Experimental results

In order to investigate the size of this effect, the HOMO peak widths of thin films of several organic semiconductors with different degree of inhomogeneity were compared. For PTCDA, CuPc and Alq<sub>3</sub> the geometric structures of the films were already discussed in Section 2.2 and the DIP geometric structures were discussed in detail in Section 2.5.1 of this work. The molecules can be categorized as well ordered in the case of PTCDA, CuPc and DIP prepared at  $T_{Substrate} > 350\text{K}$  and as poorly ordered for DIP ( $T_{Substrate} < 150\text{K}$ ) or amorphous for Alq<sub>3</sub>. A look at Table 3.1 reveals that except for PTCDA (FWHM=550meV) the well ordered films of DIP( $T > 350\text{K}$ ) and CuPc match very good with peak widths of about 450 meV. Note that this is also true for polycrystalline DIP ( $T = 210\text{K}$ ) phase indicating the absence of either strong variations of screening effects or changes of the intermolecular interaction between different geometric structures. The broader peak for PTCDA might be a result of a superposition of two components which was investigated by Y. Zou [Zou03] and L. Kilian [Kil02] in order to find the origin of these two components. The interpretation of surface and bulk components could be excluded by Kilian and Zou. The most probable origin is a Davydov splitting due to two molecules in the unit cell of the crystal. The films of less order show peak widths of 610 meV for DIP( $T < 150\text{K}$ ) and 760 meV for Alq<sub>3</sub>. If the full difference between 760 meV for the maximum and 450 meV for the minimum width is attributed to inhomogeneous broadening, a Gaussian peak width of 610 meV has to be convoluted with the minimum width to form a peak of 760 meV width. It is hence concluded that the peaks can be significantly broadened by this effect, but the peak onsets still mark The value 450 meV for well-ordered films appears to mark the lower limit of peak widths (without inhomogeneous broadening). Even the multilayer film of C<sub>60</sub> on Ag(111) shows a peak width of about 450-500 meV (graphically determined from Ref. [THH<sup>+</sup>97]), which is corroborated by the 420 meV that J.H. Weaver et al. [WMK<sup>+</sup>91] report for C<sub>60</sub> on GaAs(110) and InP(110). This molecule forms highly ordered films and it can be expected to be not sensitive to a change of the arrangement due to its spherical shape.

### 3.5. Vibration and phonon coupling

Electronic transitions of a photoemission experiment can couple to molecular vibrations or lattice phonons. Either the final state can couple to a vibration/phonon or the initial state. This process can be described in the "Frank-Condon" picture of Figure 3.4 that illustrates the example of a diatomic molecule. It shows two potential curves depending on  $R$  (the atomic distance of a diatomic molecule, or a more complex configurational coordinate otherwise) from which the lower one represents the initial and the upper the excited state. Initial as well as final state of a photoemission experiment can be vibrationally excited. The probability for such a transition from one vibrationally excited electronic state ( $\Psi(\nu_i)$ ) to another ( $\Psi(\nu_f)$ ) depends on the dipole matrix element and the Franck-Condon factors. The origin of the factors is the application of the Born-Oppenheimer approximation to the calculation of the probability amplitude of the complete transition (including electronic and vibrational excitation). This approximation allows to separate the wavefunction into a product of the vibrational ( $\Psi_v$ ), electronic ( $\Psi_e$ ) and spin ( $\Psi_s$ ) contribution, from which the following term for the Franck-Condon factors can be extracted:

$$FC(\nu_i, \nu_k) = \left| \int \Psi_{\nu_i} \Psi_{\nu_f} dR \right|^2, \quad (3.5)$$

$\Psi(\nu_i)$  the initial vibrational state and ( $\Psi(\nu_f)$  the final.

The intensities for the different vibrational transitions depend mainly on the separation  $R$  of the two potential curves, since vertical transitions are postulated by the Franck-Condon principle. Nevertheless, the ground to ground state transition has the lowest energy separation and thus the lowest binding energy.

After the discussion of the basic idea of the coupling of vibration to the electronic transition, experiments trying to measure the influence to the peak widths will be discussed. The vibrational ground state spectrum of thin films of organic molecules can be measured with, e.g., HREELS as it has been shown in Section 2.5. This provides a glimpse of the energies such vibrations can have. Additionally to the molecular vibrations, phonons of the molecular crystal as described in the paper of D. Hübner et al. [HSF<sup>+</sup>] can be observed in some cases. Hübner et al. investigated NTCDA multilayer films on Ag(111) with HREELS and found a series of peaks at low wavenumbers (52, 74, 112 cm<sup>-1</sup>) that could not be attributed to vibrations within the molecule, but originate from lattice phonons. This technique as well as IR-, Raman spectroscopy and neutron scattering were also applied to inorganic solids to measure their phonon spectra and dispersion relations, which usually have energies of up to 400 meV [Dem05].

As already mentioned at the beginning of this Section, the vibrations/phonons can influence the peak widths at two points during the photoexcitation process. The first one is the initial state. The higher the sample temperature at which the PES spectrum is recorded the more vibrational and phonon states are occupied. The measured energy of the electronic transitions is in this case reduced by the energy of the vibration leading to a broadening of the peak towards the Fermi energy. An experimental approach to determine the size of the initial state broadening effect was described in the publication



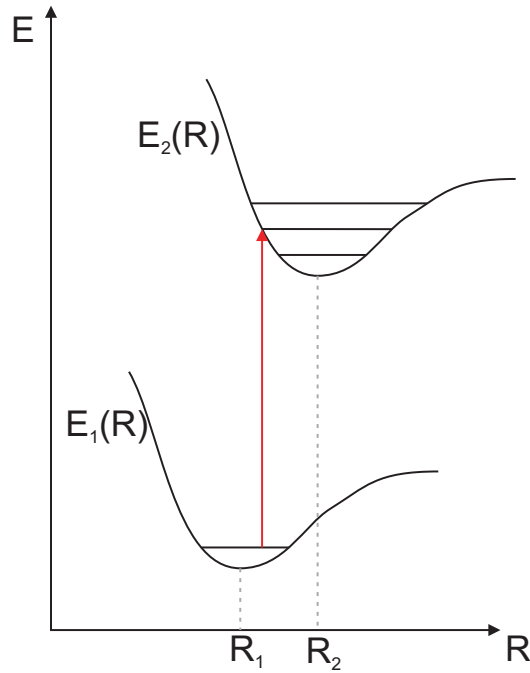


Figure 3.4.: This sketch illustrates an electronic transition in a diatomic molecule that couples to a vibronic transition in the Franck-Condon picture. The X axis represents the potential energy, the Y axis the distance of the atoms and the two potential curves represent the molecule before ( $E_1(R)$ ) and after ( $E_2(R)$ ) an absorption of a photon. Only vertical transitions (red arrow, no change in  $R$ ) are allowed since the cores are expected not to change their position during the absorption process.

of W. Salaneck et al. [SDE<sup>+</sup>80] from 1980. For this matter, the HOMO peak width of a multilayer film of isopropyl benzene was determined for a wide temperature range (15-150 K). Similar to the procedure described in the introduction of this Chapter, Salaneck et al. determined the additional broadening component by a quadratical addition of Gaussian peak widths depending on sample temperature. The following relation between the Gaussian peak width and the temperature was found:

$$\delta(T)^2 = \delta(0)^2 + c^2 \cdot T, \quad (3.6)$$

with  $c = 4.4(\pm 0.8) \cdot 10^{-2} eV K^{-\frac{1}{2}}$ .

However, this approach of the determination of the temperature dependent peak width has some drawbacks. Firstly, it is not obvious that the first peak in the spectrum originates from a single electronic state. Secondly, the approach does not take into account that other peak broadening effects also depend on the temperature. An example of this is the temperature dependence of the dynamic screening effect discussed in the next Section. It is therefore not straightforward to interpret the decrease of peak width with

### 3. Peak broadening mechanisms

---

decreasing temperature and attribute it completely to vibration/phonon broadening.

The second influence of vibration/phonon coupling is that of final state. Similar to the initial state, the final state to which the system changes by photoexcitation does not have to be the vibrational ground state. All vibrational modes of the molecule that are reachable by a vertical transition can be excited with the probability determined by the Franck-Condon factors. This effect is independent of the substrate temperature and broadens the peaks away from the Fermi energy.

Thus, there are two effects of which the initial state coupling broadens the peak towards the Fermi energy and the final state coupling away from it. Since most of molecules are in the vibrational ground state at room temperature, the excitation of a vibration/phonon dominates in PES experiments, and the peak broadening is preferably away from the Fermi energy.

The vibrations are not resolvable in valence level spectra of multilayer film, but in a recent publication by S. Kera and U. Ueno [KU05] the observation of such a measurement of the monolayer was reported. Several phthalocyanines on HOPG were investigated with high-resolution UPS and an asymmetric shape of the HOMO peak was observed. This was attributed to a hole-vibration coupling to a vibration with an energy 150 meV, because it was possible to fit the HOMO with a series of four peaks and this energy separation. This energy was equal for all phthalocyanines.

In summary, the excitation of vibrations/phonons dominates in the photoemission process, which leads to an asymmetric broadening of the peaks due to the fact that the ground to ground state transition leads to the lowest measured binding energy for the electronic state. The size of this effect is difficult to estimate, but other investigations indicate about 200 meV [HKSP00].

### 3.6. Static and dynamic screening

The effect of screening was already discussed in the Section 3.4. In the case of inhomogeneities the focus was on a local variation of the size of the screening contribution. There are two additional ways in which screening effects can broaden the peaks - static and dynamic effects.

Peak broadening due to static screening variations is based on different vicinities a charge may experience at the surface or in the bulk of a polarizable medium. Due to the integration of the signal of several molecular layers in the photoemission spectrum, a gradual change of the screening contribution to the measured binding energy results in a broader peak if the signal of several layers superimpose. However, in Section 2.1 it was shown that surface to bulk variations of peak binding energies could not be experimentally verified and are at most below 100 meV. This is corroborated by a publication of S. Kera and N. Ueno [KU05], in which these variations were found to be in the order of 50 meV. Peak broadening due to static polarization effects are therefore not considered to be of importance for organic materials.

Peak broadening due to dynamic screening effects assumes the screening process to fluctuate with time. This effect was introduced to give a further broadening mechanism

to explain the broad peaks in the case of inorganic semiconductors and the fact that peak onsets fit the position of the band extrema better. It is already mentioned in the paper of, e.g., T. Gleim et al. [GHU<sup>+</sup>03]. However, no mechanism was proposed so far to describe this effect and therefore this work will try to sketch it with a focus on thin films of organic semiconductors.

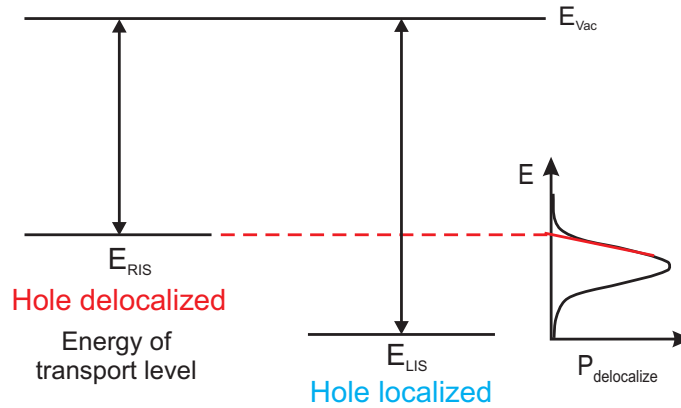


Figure 3.5.: Sketch of the peak broadening mechanism of dynamic charge delocalization. One of the two extremes that might occur during the process of photoemission is the hole being completely delocalized on the timescale of the emission process. Then the measured energy corresponds to the fully relaxed ionic state (RIS, left side) and is close to a neutral molecule. The second extreme is that the charge is still present and completely localized on the molecular orbital investigated. This corresponds to a localized ionic state to which only some polarization screening may contribute (LIS, middle). On the right hand side, a probability distribution of all intermediate degrees of delocalization is plotted each of them resulting in a different kinetic energy which broadens the measured peak. The red line indicates the position of the RIS at the low binding energy onset of the distribution.

The broadening due to dynamic screening effects accounts for the dynamics of a system at non-zero temperature. All bonding distances between the atoms as well as intermolecular distances change with time due to vibrations even at very low temperatures. The photoemission process happens on a very short time scale which is much shorter than that of the motion of the atoms. It probes therefore the energy and relaxation contribution of the actual arrangement which can be regarded as a snapshot picture. A PES experiment probes all possible arrangements which all deliver a slightly different value for the energy of the probed electronic state since they all differ in their screening contribution. The resulting peak in the spectrum is therefore a superposition of these energies and reflects their energetical distribution as well as the most likely arrangement (at the peak maximum). This model is sketched in Figure 3.5.

The sketch shows two possible extremes for the final state of a photoemission process despite the vibrational excitation. The energy of the emitted electron depends on

### 3. Peak broadening mechanisms

---

timescale of the events that happen while it is emitted. The sudden approximation for the photoemission process is of course not valid since one finds screening contribution to the measured kinetic energies. One of the extremes that can occur is that the hole (or electron for IPS) stays at its origin (molecule) and only polarization screening processes alter the kinetic energy of the photoemitted electron. This is referred to as the localized ionic state (LIS), because the energy of the probed electronic state is close to that of an ion. The second extreme is the complete delocalization of the hole which is the optimal screening (relaxed ionic state, RIS). The probed energy in this case is close to the neutral molecule. Of course, there are other cases for the which the hole is partly delocalized, i.e. redistributed within one molecule or redistributed over two, three, etc. molecules. The curve on the right hand side of Fig. 3.5 reflects the different energies connected to the distribution of the arrangements described above. In a first order approach these energies are arranged statistically around a most likely value resulting in a Gaussian shape. The energy distribution curve would directly lead to a broadening of the photoemission peak. The sketch in Figure 3.5 shows that the RIS value can be found at the low binding energy onset of the energy distribution and the LIS at the high binding energy onset. The screening contribution decreases therefore with distance from the Fermi energy, which results in a further asymmetric broadening mechanism.

Note that this effect also has a temperature dependence, since the screening channels depend on the size of intermolecular interaction. A good indicator for this size is the dominating charge transfer mechanism. N. Karl [Kar03] presented data for naphthalene which show a transition between hopping and band transport at about 50 K. This matter was also treated by M. Hutell and S. Strafröm [HS06] in a theoretic approach. Their calculations showed a transition from hopping to band transport for low temperatures and, additionally, indicated a broad transition temperature region in which both transport channels coexist. The contribution of screening depends on the localization of the charges and therefore the charge transport channel.

### 3.7. Summary and conclusions

This Chapter intends to give an overview of all broadening mechanisms which occur in the photoemission process with a focus on the valence states in organic as well as inorganic semiconductors. Note that the assumption of assigning a Gaussian peak width to each broadening mechanism is an oversimplification. The single contributions have probably their own spectral functions convoluted with each other. An example of this can be found in the literature for diatomic gases on different metal surfaces ([GS78], [Umb80], [Umb84]). The XPS line shape of these gases depends on the metal surface and the different transfer of screening charge. The substructure of the XPS peaks could be related to a charge transfer into an unoccupied molecular level from either a metal sp- or d- band resulting in different measured binding energies.

The peak broadening mechanisms of lifetime, experimental broadening, band dispersion, band bending and static screening effects have been shown to have negligible to the overall peak width. Although structural inhomogeneities have a high potential to

increase the peak width shown on the example of DIP, the minimum HOMO peak width is apparently not smaller than 450 meV for highly ordered thin films. Thus the major contribution to this value comes from coupling to vibrations and dynamic screening effects. The size of the effects is estimated as follows (a lifetime contribution was also added as Gaussian width for simplicity,  $W$ =FWHM):

$$W_{tot}^2 = W_{lt}^2 + W_{exp}^2 + W_{band}^2 + W_{inhom}^2 + W_{vib}^2 + W_{dyn}^2 \quad (3.7)$$

$$450meV^2 = 90meV^2 + 50meV^2 + 0meV^2 + 0meV^2 + 200meV^2 + 390meV^2 \quad (3.8)$$

From this estimate follows that a considerable part of the peak width remains unexplained if dynamic screening effects are not considered.

Furthermore, the Section of experimental broadening revealed that the peak width in IPS measurements is significantly larger than in UPS, which is not explainable by the worse resolution alone. A possible origin of the phenomenon are the radiation damage that is unavoidable during the IPS measurement (see Appendix A).

Finally, it was shown that all peak broadening mechanisms, except for the lifetime and the experimental broadening, broaden the peaks asymmetrically away from the Fermi edge. This leads to the important finding that the state of lowest energy which closest to a transport level is positioned near the low binding energy onset of the peak. This finding will be the basis for the discussion of the next Chapter.

## 4. Determination of the transport levels and their gap - From inorganic to organic systems

After the previous chapters discussed the various influences that determine the energetic position of the frontier orbitals as well as their peak width in photoemission, this chapter is intended to apply these findings to the transport level identification in a the spectrum. Although thin films of organic semiconductors are now studied for over 50 years (article from E.A. Silinsh: Studies Of Organic Semiconductors For 40 Years [Sil89]), the questions about the nature of the interaction of the molecules in crystals still is under debate. Generally, they are compared to van-der-Waals force bound crystals similar those of noble gases. However, recent experiments ([HHF<sup>+</sup>], [Kil02], [Cas08]) gave reason for doubts concerning this assumption.

The combination of UPS and IPS is only rarely used in literature because it is not fully established to determine band (transport) gaps. The approach in this work is to apply it to well-understood systems, such as inorganic semiconductors, first, identify the obstacles of the method and establish a way to treat them. This will be done by a combination of literature review and own experiments. Besides the sample preparation and the application of PES, this particularly addresses the question whether a transport level is determined by the peak maximum or by the onset.

This discussion will be then repeated for the thin films of organic semiconductors, applying the insights found for inorganic semiconductors where possible. With the transport gaps found, it is possible to determine the exciton binding energies for organic films and discuss the strength of intermolecular interaction.

### 4.1. Inorganic semiconductors

Even though the band gap determination with optical methods and band mapping via PES and IPS are well established for inorganic semiconductors, the extraction of the band gap from the latter data is not common and has only been reported for "surface" band gaps by H. Carstensen et al. [CCMS90].

This might originate from the obstacles one has to overcome in order to extract that quantity from (inverse) photoelectron spectroscopy data, which will be addressed in this Section. Inorganic semiconductors were chosen as a model system to perform the transport gap determination because they are much better understood than their organic counterparts. Their growth technology has evolved to a very high level over the last

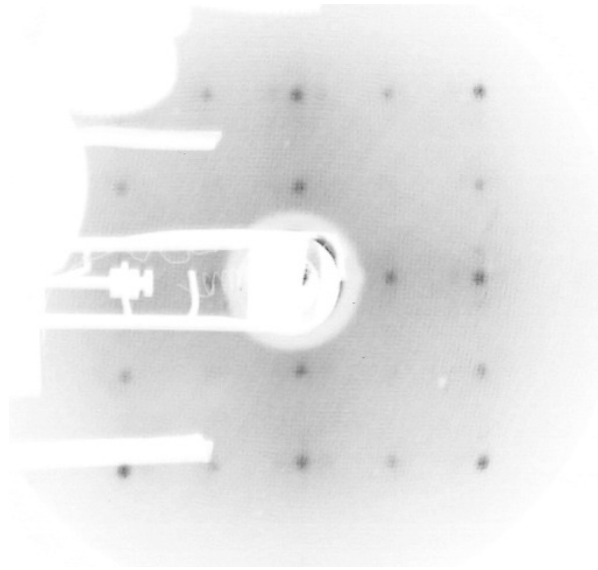


Figure 4.1.: LEED pattern of a Si(001) crystal after treatment with 5% HF and annealing to 900°C. A 2x2 reconstruction is visible resulting from two orthogonal 2x1 domains. The electron kinetic energy was 63 eV.

decades, which allows the production of large single crystals with low defect density and control of impurities on the dopant concentration level. Inorganic semiconductors form covalent bonds in these crystals and the evolution of calculations of the electronic structure allows a very precise prediction. This marks the first obstacle to overcome - to find the right position in the Brillouin zone of the single crystal and really measure the VBM and CBM of it.

The second obstacle originates from the surface sensitivity of the investigation method. The top layer of a semiconductor crystal may be different from that of the bulk concerning lattice constant, and the potential of the electron waves, which will be the topic of the second Subsection.

After considering this, the last part will propose a way to extract the position of the combined UPS and IPS spectrum based on the discussion of the previous two Chapters.

#### 4.1.1. The investigated material and its preparation: Si(001)

Silicon was chosen as a representative for inorganic semiconductors. It has an indirect band gap, which means that valence band maximum and conduction band minimum are at different points in the Brillouin zone. Si is widely used in the microelectronic industry for electronic devices. An advantage of this material is that it is an element semiconductor, which facilitates the preparation of its surface. In order to utilize PES, a defined surface is needed that ideally can be prepared in UHV and which has known properties in order to be able to distinguish surface from bulk signals. In contrast, many compound semiconductors exhibit a variety of surface reconstructions with a large phase space of

## 4. Determination of the transport levels and their gap

---

substrate temperature and the partial pressure of the two compound components, e.g., GaAs(001) surface [DH90]. The sample investigated here was a commercially available p-doped Si(001) wafer. In order to remove the silicon oxide layer, which forms due to the air exposure of the wafers after their production and during the transport, two methods can be applied. Either the sample is heated to 1150°C at a pressure better than  $5 \cdot 10^{-9}$  mbar for a few minutes (2-5 min., depending on the thickness of the oxide layer) and then is cooled down with a constant cooling rate of 1°C, or it is dipped in a 5% HF solution, blown dry with nitrogen and then heated in UHV to 900°C to remove the hydrogen. The second method provided a cleaner surface and was therefore preferred. The temperature was measured with a pyrometer through a viewport, which was set to the emissivity of polished silicon of 0.65 and corrected by the window absorption of 0.85 resulting in a corrected emissivity of 0.58.

The defined surface for this silicon face is the 2x1 reconstruction, which naturally forms during the cooling process after the removal of the oxide layer, and will be described in the following. This silicon crystal used did not have a miscut of 4° in the (010)-direction (as described in [JUH88]) and therefore had two 2x1 domains. This results in a 2x2 diffraction pattern in the LEED shown in Figure 4.1 as described in the paper of G.V. Hansson and R.I.G. Uhrberg [HU88]. A model sketch of the reconstructed silicon surface can be found in Figure 4.2. In literature it is referred to as the asymmetric dimer model, since the silicon atoms of the topmost layer recombine their "dangling" bonds by the formation of dimers. The two partners of this dimer are at different heights above the adjacent crystal plane (asymmetric) and form the 2x1 surface reconstruction (top view).

This surface was intensively investigated in the past and therefore provides a good basis for the application of PES and IPS for band gap determination.

### 4.1.2. Positioning in the Brillouin zone

The strong dependance of the energetic position of the valence bands on the k-vector of the photoexcited electron demands for a good knowledge of the position in the Brillouin zone during the measurement. In this Section, a simplified model for the final states in photoemission will be utilized to determine where the k-vector ends for certain excitation energies and if angle variation can help to reach the band extrema.

The investigated material in this work is silicon, which forms crystals of a face centered diamond cubic structure and has the same Brillouin zone shape as a face centered cubic crystal. Figure 4.3 illustrates the shape of it. The most important crystal directions in the BZ are indicated by so-called high symmetry points, which are the points in which the normal vector of a certain crystal face intersects the BZ. These are, e.g., the X point for the (001)-face or the L point for the (111)-face. The center of the BZ is the  $\Gamma$  point which is also the position of the valence band maximum.

In a PES experiment with fixed photon energy one can change the position within the BZ by variation of the angle between surface normal and electron energy analyzer, which changes the parallel as well as the perpendicular component of the k-vector with respect to the investigated crystal face. If the  $\Gamma$  point is not accessible with the photon energies available by the used experimental setup, it is possible to reach a neighboring



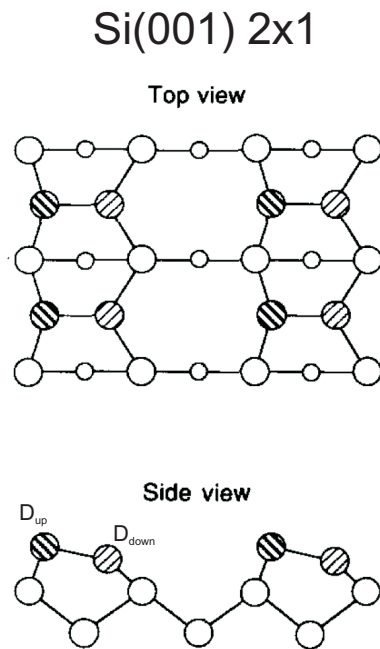


Figure 4.2.: Model of the 2x1 reconstructed Si(001) surface. The "dangling" bonds remaining from the cut through the surface saturate with each other and form a silicon dimer on the surface. The two silicon atoms in this dimer have different heights above the adjacent crystal layer and are marked as  $D_{up}$  and  $D_{down}$ . Modified from [HU88]

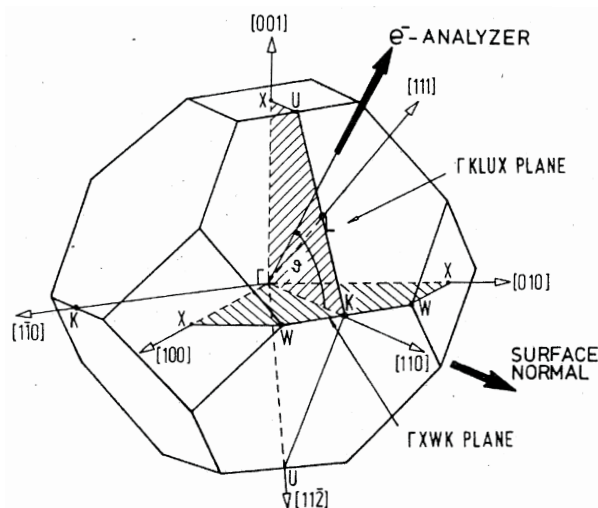


Figure 4.3.: Sketch of the 3D Brillouin zone of a FCC lattice. It illustrates the emission planes accessible in a PES experiment, in which the crystal is cut in the (110) plane and rotated in two directions perpendicular to each other. Picture modified from [Hüf95].

#### 4. Determination of the transport levels and their gap

BZ by choosing a feasible emission plane and angle. The planes are named after the high symmetry points that define them and two examples of them ( $\Gamma$ KLUX-(1 $\bar{1}$ 0) and  $\Gamma$ KWX-(001) emission plane) can also be found in Figure 4.3. If a tunable light source is available, the perpendicular component can be varied by changing the photon energy. It can be tuned such that the spectra at the  $\Gamma$  point can be recorded. The same applies for an IPES experiment with fixed electron energy and a photon detector that can vary the detected energy. However, such a detector has a very low signal due to its optical elements. None of these two options was available for the measurements in this work.

In order to determine the position of a PES measurement within the BZ, it is necessary to calculate the actual length of the k-vector of the excited photoelectron within the investigated material. A simplified model to describe the change of length and direction of the k-vector component perpendicular to the surface due to the transmission of the electron through the surface into vacuum as final step of the three step model is the free electron final state model (FEFS). It assumes that the final state to which an electron

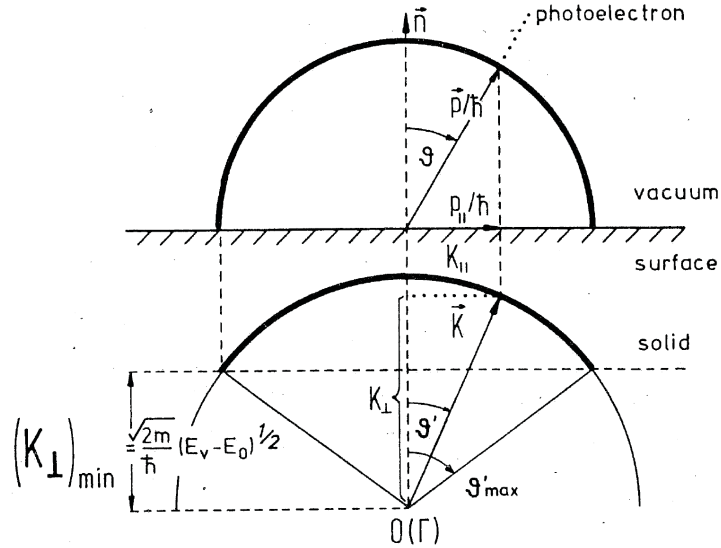


Figure 4.4.: This sketch pictures the relation between the k vector within the crystal and the measured outside. The component of  $\vec{k}$  perpendicular to the surface is not conserved (other than its parallel component). The thick lines represent the internal and external electron escape cones with the radii  $|\vec{k}| = \text{const}$  and  $|\vec{p}|/\hbar = \text{const}$ . The picture is modified from [Hüf95].

is excited is the k dispersion parabola of the free electron shifted by the so-called inner potential  $V_0$  ( $V_0 = |E_0| + \Phi$ ):

$$E_f = \left( \frac{\hbar^2}{2m^*} \right) (\vec{k} + \vec{G})^2 - |E_0|. \quad (4.1)$$

The inner potential for silicon was experimentally determined by several groups and its value ranges from 9.3 - 12.1 eV ([WSZT04], [WCLK97],[GMD<sup>+</sup>93] and [GS71]) of which

11.5 eV was chosen from the most recent publication.  $V_0$  can be considered as a surface potential barrier which the electrons have to overcome to leave the sample and at which electrons with insufficient energy are reflected. The electrons must satisfy the following condition to overcome the barrier:

$$\left(\frac{\hbar^2}{2m}\right) k_{\perp}^2 \geq E_V - E_0. \quad (4.2)$$

The parallel component of  $\vec{k}$  is preserved during the process. The emission angles of the photoelectrons within the crystal and in the vacuum therefore do not match, which is a refraction effect. Figure 4.4 illustrates this effect and the different escape cones of the electrons within the crystal and in vacuum.

In order to calculate the parallel and perpendicular components of  $\vec{k}$ , one starts with the basic energy conservation of photoemission:

$$E_f = E_{kin} + \Phi = -E_B + \hbar\omega. \quad (4.3)$$

The parallel component of  $\vec{k}$  can be easily determined by:

$$k_{\parallel} = \sqrt{\frac{2m^*}{\hbar^2} E_{kin}} \cdot \sin\vartheta. \quad (4.4)$$

In order to calculate  $k_{\perp}$ , one has to use both equations for the final state (eqn. (4.3) and (4.1)):

$$k_{\perp} = \sqrt{\frac{2m^*}{\hbar^2} (V_0 + E_{kin} \cdot \cos^2\vartheta)}. \quad (4.5)$$

The approximation of free electron final states is better for higher photon energies where more empty states to which an electron can be excited are available and which more resemble the free electron parabola. The photon energies utilized in this work are comparably low, which decreases the level of accuracy of the predictions of this model. Nevertheless, one can find out how close the experiment to the  $\Gamma$  point is and if one can reach a neighboring BZ by variation of the analyzer relatively to the sample. An elaborate article about the limits of this model was written by N. Nagelstraßer et al. [NDS<sup>+</sup>98]. Nevertheless, this model was successfully applied to the silicon (001)-face by P. Koke et al. [KGM<sup>+</sup>85].

The emission plane in which the closest neighboring  $\Gamma$  point lies is the  $\Gamma$ KLUX-(1 $\bar{1}$ 0) plane, which is illustrated in Figure 4.3. The accessible emission cones can be calculated with the formulas for  $k_{\parallel}$  and  $k_{\perp}$  and are shown in Figure 4.5. The black dots are the high symmetry points that define the plane whereas the green (IPES), blue (Ar I) and red (He I) points indicate the position of the electrons with highest kinetic energy excited with the corresponding source in steps of 5°. No adjacent  $\Gamma$  point can be reached by angle variation but the Ar I excitation at  $k_{\parallel} = 0$  is sufficiently close to the second BZ center, which is why this energy was chosen for the determination of the VBM in the following. The conduction band minimum is located at about 80% of the distance between  $\Gamma$  and

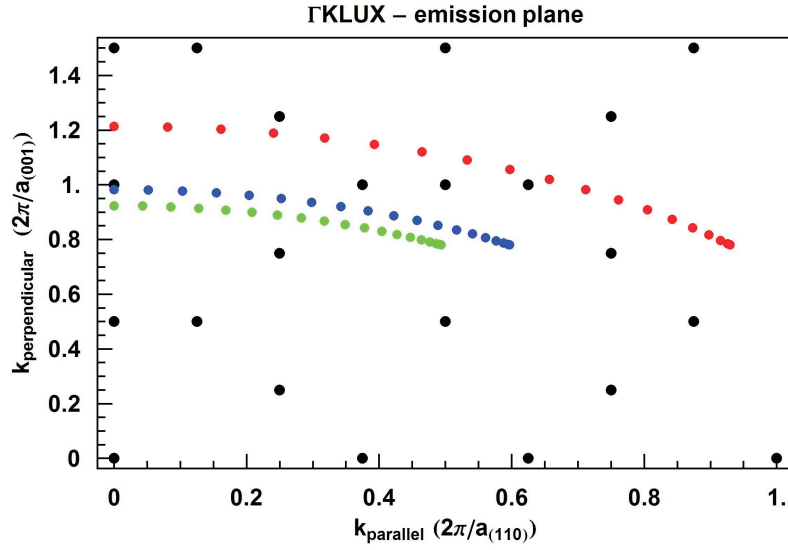


Figure 4.5.:  $\Gamma$ KLUX emission plane with the emission cones for the electron energies of 9.5 eV (IPES, green), 11.63 eV (Ar I, blue) and 21.22 eV (He I, red).

X, which can be seen in the calculated band structure in Figure 4.6.

### 4.1.3. Influence of surface states

The band gap is a bulk property and PES is surface sensitive, since it only probes the topmost about ten Å. Several effects described in the following can lead to new states in the gap, which are only present at the surface of a certain face of a semiconductor crystal. In order to determine a bulk band gap from this data, these states need to be identified and if possible eliminated from the spectrum. This Section will start with an estimate of the surface contribution to the spectrum in order to quantize the surface influence, describe the possible surface states and then show the experimental data for Si(001) and what was done to eliminate the surface states.

In his book on photoelectron spectroscopy, S. Hüfner [Hüf95] states that PES reproduces the calculated bulk band structure remarkably well despite its surface sensitivity. The measurable change of the lattice constant in the topmost layer of a solid (typically a few percent) does only affect this layer while the unperturbed bulk electronic states can be found within one lattice constant from the surface. A PES experiment probes several lattice constants perpendicular to the surface and therefore the surface contribution is not a large fraction of the spectrum. Figure 4.7 shows the contribution of the first layer of silicon in its 001-direction to the integral signal assuming a thickness of half a lattice constant. The value for the exponential attenuation constant and its dependence on the kinetic energy was found in the paper of M.P. Seah and W.A. Dench [SD79]. The contribution of the first layer calculated by integration of formula (2.6) to half the lattice

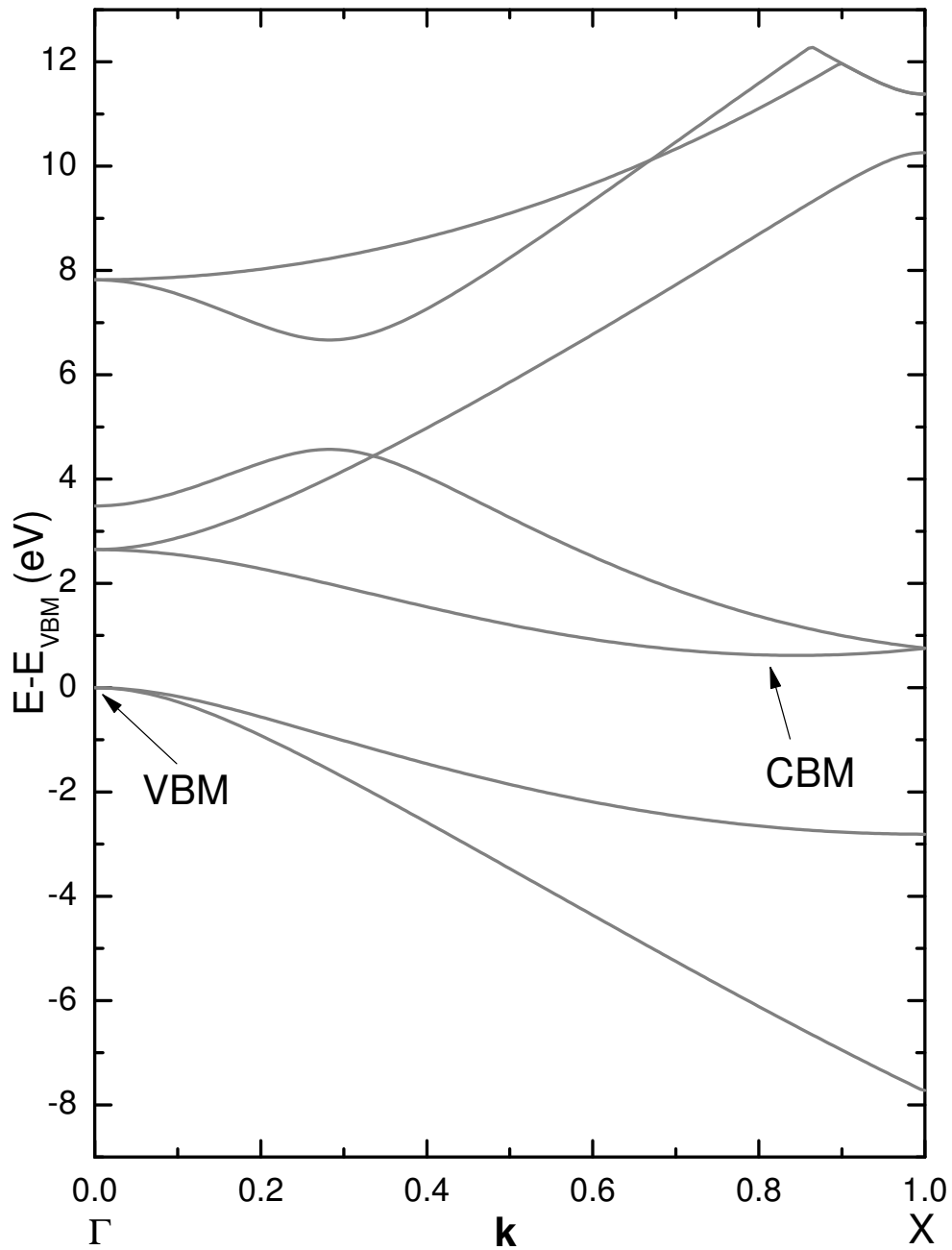


Figure 4.6.: Calculated bandstructure of silicon between  $\Gamma$  and X point. The calculations are LDA based and were conducted with the software MindLab. The energy scale on the y-axis refers to the valence band minimum. It is marked in the graph as VBM and similar to this the conduction band minimum at about  $0.8 \overline{\Gamma X}$  is marked as CBM.

## 4. Determination of the transport levels and their gap

---

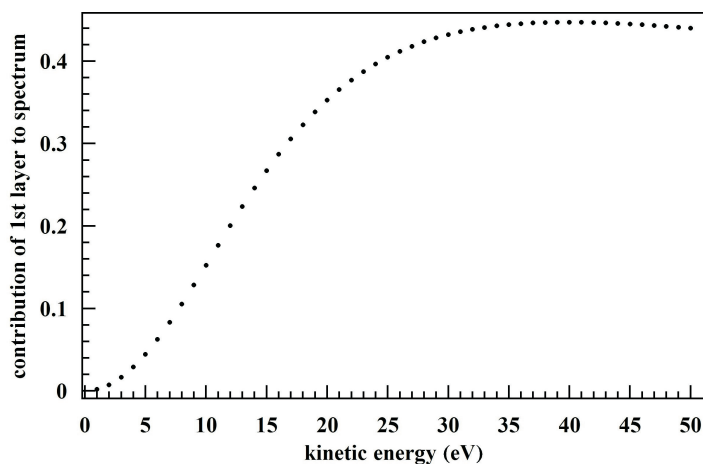


Figure 4.7.: Calculation of the overall contribution of the first layer of Si(001) to the PES spectrum assuming an exponential attenuation of the signal of lower lying layers. This contribution is plotted as a function of the kinetic energy of the photoelectrons using the inelastic mean free path from the paper of M.P. Seah and W.A. Dench [SD79].

constant divided by the integral to infinity. The photoelectrons originating at the valence band maximum excited with a lab source (Ar I=11.83 eV and He I=21.22eV) have about 5-15eV kinetic energy. The first layer hence contributes about 5-25% to the spectrum. Nevertheless, the surface states can appear in the bulk band gap and complicate the identification of the band extrema.

The surface of an inorganic semiconductor is a cut through the crystal that breaks the three dimensional periodicity of it. This affects the surface electronic structure in three ways:

- The Bloch states of the interior of the crystal have to match states that exponentially decay with increasing distance from the surface. This matching condition can either lead to an increase or decrease of the local density of states. If the amplitude of a state significantly increases, it is called a surface resonance or a Shockley state.
- The d-bands experience a weaker potential at the surface than in the bulk, which results in a split-off or Tamm state.
- The cut through the crystal leaves unsaturated bonds at the surface. These "dangling" bonds can saturate with neighboring atoms and form a surface reconstruction with a different crystalline structure as the bulk. These bonds will appear as new surface states in the PES spectrum.

An elaborate review on surface states of inorganic semiconductors can be found in [HU88] and [Him90], as well as the book of S. Hüfner [Hüf95].

Here, Si(001) with 2x1 reconstruction will be utilized as an example to demonstrate the effect of surface states in the spectra. The example focuses on the "dangling" bond surface states, which are especially important for inorganic semiconductors. This reconstruction at the surface and its preparation is described in Section 4.1.1 and leads to new electronic states in the photoelectron spectra. In the late 1980's this kind of surface states was intensively investigated for Si(001) theoretically (e.g., [KP88]) and experimentally (e.g., [HU88], [KGM<sup>+</sup>85], [OH93]) and for other semiconductor surfaces.

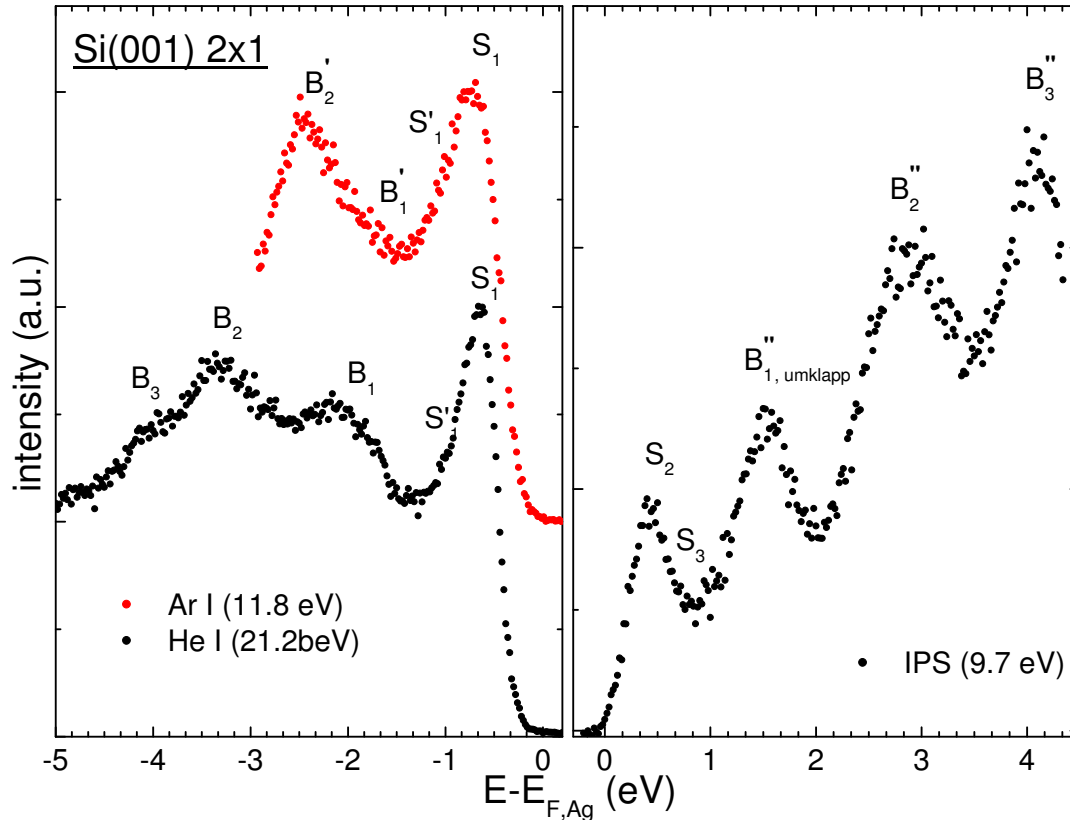


Figure 4.8.: Valence and conduction level spectra of Si(001) 2x1 recorded with two different UV excitation lines and IPS. The surface states in UPS (normal emission) are marked as  $S_1$  and  $S'_1$ , whereas the bulk electronic states are labeled with  $B_1$  to  $B_3$ ,  $B'_1$  and  $B'_2$  (bulk states identified by A.L. Wachs et al. [WMH<sup>+</sup>85] with synchrotron radiation). The IPS surface states are  $S_2$  and  $S_3$  and the bulk states  $B''_1$  to  $B''_3$ , which were identified in the paper of J.E. Ortega and F.J. Himpsel [OH93] with a grating monochromator that allows the use of different photon energies.

Figure 4.8 shows the present experimental results for the valence and conduction levels of the Si(001) 2x1 surface. The surface states  $S_1$  and  $S'_1$  in the UPS spectra can be identified by comparing two spectra at different photon energies, since they do not disperse by changing of the  $k$  component perpendicular to the surface. The states  $B_1$  to  $B_3$ ,  $B'_1$  and  $B'_2$  are bulk states and will be addressed in the next Subsection.

#### 4. Determination of the transport levels and their gap

The assignment of the IPS transitions bases on the publication of J.E. Ortega and F.J. Himpsel [OH93] and identifies two surface states,  $S_2$  and  $S_3$ , as well as the bulk states  $B''_1$  to  $B''_3$ .  $B''_1$  involves an umklapp process with an surface BZ vector, which will also be discussed in the next Subsection.

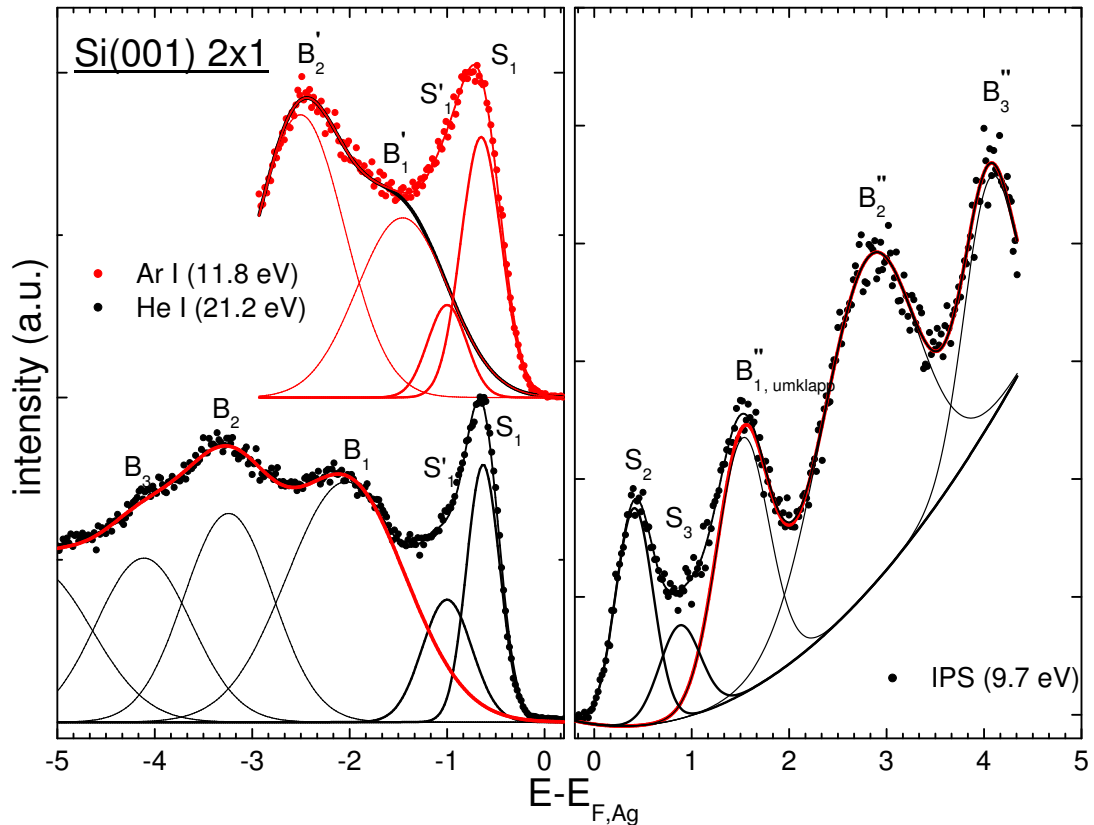


Figure 4.9.: Fit results for the two UPS and one IPS spectrum of Si(001) 2x1. For each spectrum the peaks forming the spectrum are shown and the surface states are marked by bold lines. The black line in the Ar I spectrum as well as the red line for He I and IPS show the spectrum after subtraction of the surface states.

After identification of the surface states, two ways of their elimination in the spectrum will be shown. One way is to saturate the dangling bonds with ,e.g., hydrogen in order to saturate and hence eliminate the surface states. The new surface terminating atoms then form new states which are not in the band gap. The other way is to fit the spectrum with a series of Gaussian peaks and simulate the spectrum without the identified surface states.

Firstly, the results of the fitting method are shown in Figure 4.9. The number of peaks and their position was chosen based on the available literature and in some cases adjusted when necessary. The bulk state identification for the UPS data bases on the synchrotron data of A.L. Wachs et al. [WMH<sup>+</sup>85] who investigated this silicon face and reconstruction with photon energies between 12.0 and 98.4 eV. The only bulk state added



here is the  $B'_1$ , which was necessary for a consistent fit of the experimental data. The positions of the surface states  $S_1$  and  $S'_1$  at  $-0.65$  and  $-1.00$  eV have been held fix for both excitation energies; the widths of these peaks are significantly smaller than for the bulk states. The maximum position of  $S_1$  has been intensively discussed in the literature. The review of G.V. Hansson and R.I.G. Uhrberg [HU88] lists positions between  $-0.4$  and  $-0.9$  eV with a majority at  $-0.7$  eV. Calculations shown in the same publication position  $S_1$  at  $0.3$  eV below the VBM at the  $\Gamma$  point of the surface Brillouin zone. The second component  $S'_1$  used to fit the spectrum does not show up in the calculations on the single domain  $2 \times 1$  reconstruction and might originate from the second domain present at the investigated surface. The superimposition of the valence band maximum and  $S_1$  complicates the identification of the two components in the spectrum measured with Ar I. The black line shows the spectrum after subtraction of the surface states. This is not the case for He I excitation where the surface states are well separated from the bulk states and where they could easily be removed by subtraction of the surface peaks (red line in Fig. 4.9).

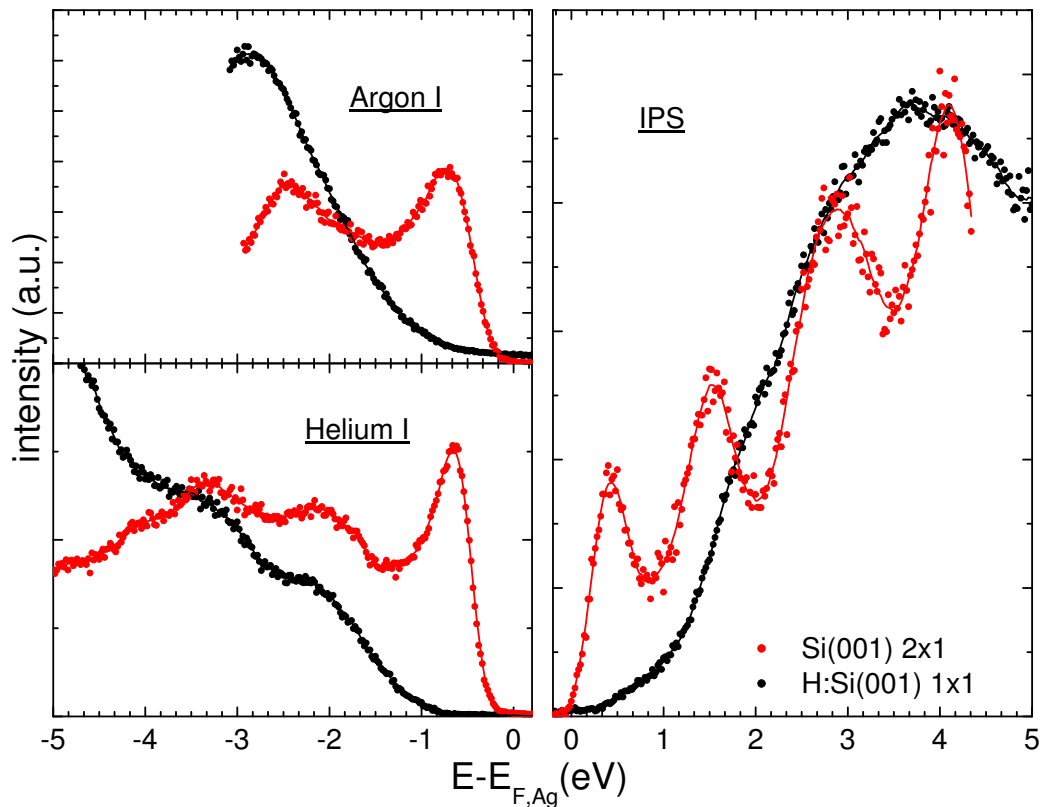


Figure 4.10.: Comparison of valence and conduction level spectra of the Si(001)  $2 \times 1$  and H:Si(001)  $1 \times 1$  surface. It is clearly visible that for all cases the surface states vanish by hydrogen termination. This goes along with a loss of spectral fine structure, which are only visible in the case of He I UPS.

The experimental setup utilized for IPS in this work was not capable to measure

#### 4. Determination of the transport levels and their gap

---

at different photon energies, but there is literature available for this silicon face and reconstruction. J.E. Ortega and F.J. Himpsel [OH93] used a monochromator grating to measure at different points in k-space at once, which allows the identification of surface states as well as the mapping of the band structure. However, the low cross section of the IPS process demands for long integration times, which is faster for the detector utilized in this work - a photon band pass Geiger-Müller counting tube. With the help of their data all peak maxima could be assigned but it was again necessary to add a second surface state component ( $S_3$ ) for a good fit of the data. The small background in the UPS data did not demand for an inclusion in the fit whereas it was necessary for the IPS data. A parabola-shaped background was chosen together with a series of five peaks. Again, the red line shows the spectrum after subtraction of the surface components and leaves only the bulk information.

This result shows that the method is applicable if bulk and surface states are well separated and if all transitions are properly identified to perform a consistent fit. If these conditions are fulfilled the method provides the bulk spectrum of any semiconductor.

The second method to extinguish surface states from the spectrum is the saturation of the "dangling" bonds with a non silicon atom. R.I.G. Uhrberg and G.V. Hansson [UH91] intensively investigated a variety of overlayers on Si(001) 2x1 surface with H, Na, K, Cs, Ga, Cl and As and measured the change in the valence spectrum. They showed that a hydrogen termination completely removes the surface states in UPS and forms new states far away from the VBM at -4.8 and -5.6 eV. The H-termination was done via etching in 5% hydrofluoric acid for 20 s and subsequent dry-blowing with dry nitrogen. After introduction into the UHV chamber system, the sample was heated to 375°C for 5 min delivering a sharp 1x1 reconstruction in LEED and almost no oxygen or carbon signal in XPS (see Fig.4.11). This procedure forms a complete hydrogen termination of the surface and slightly roughens the surface because the (001) face is not as well etched as the (111) face (investigated in detail by P. Dumas, Y.J. Chabal and P. Jakob[DCJ92] with EELS).

The impact on the UPS and IPS spectrum can be seen in Figure 4.10. In all three spectra the surface states vanish completely from the spectrum, but this goes along with a loss of spectral fine structure. Only in the case of He I excitation the hydrogen terminated silicon surface shows the same bulk states as for clean Si(001) without the surface states. Ar I excitation is very close to the  $\Gamma$  point of bulk BZ, but the onset of the new spectrum is below the former surface state position and not about 0.3 eV above it as in the calculations. A possible reason for that could be that the low excitation energy of 11.8 eV the photoelectrons reach no empty final state without 2x1 reconstruction. A possible change in the band bending due to the different surface can be excluded since in the He I spectrum the position of the peaks stays constant. The IPS spectrum shows similar trends as the Ar I spectrum - a nearly featureless curve. Accompanied with the loss of the surface state, a loss of the first bulk feature  $B''_1$  (see Fig. 4.9) is expected since its excitation involves an umklapp process by the 2x1 surface BZ. Indeed, the intensity in these two regions drops drastically, which corroborates this interpretation. The remaining peaks at 2.9 and 4.1 eV are likely to be superimposed by a new state between them. However, no literature is available for IPS on the H-terminated Si(001)

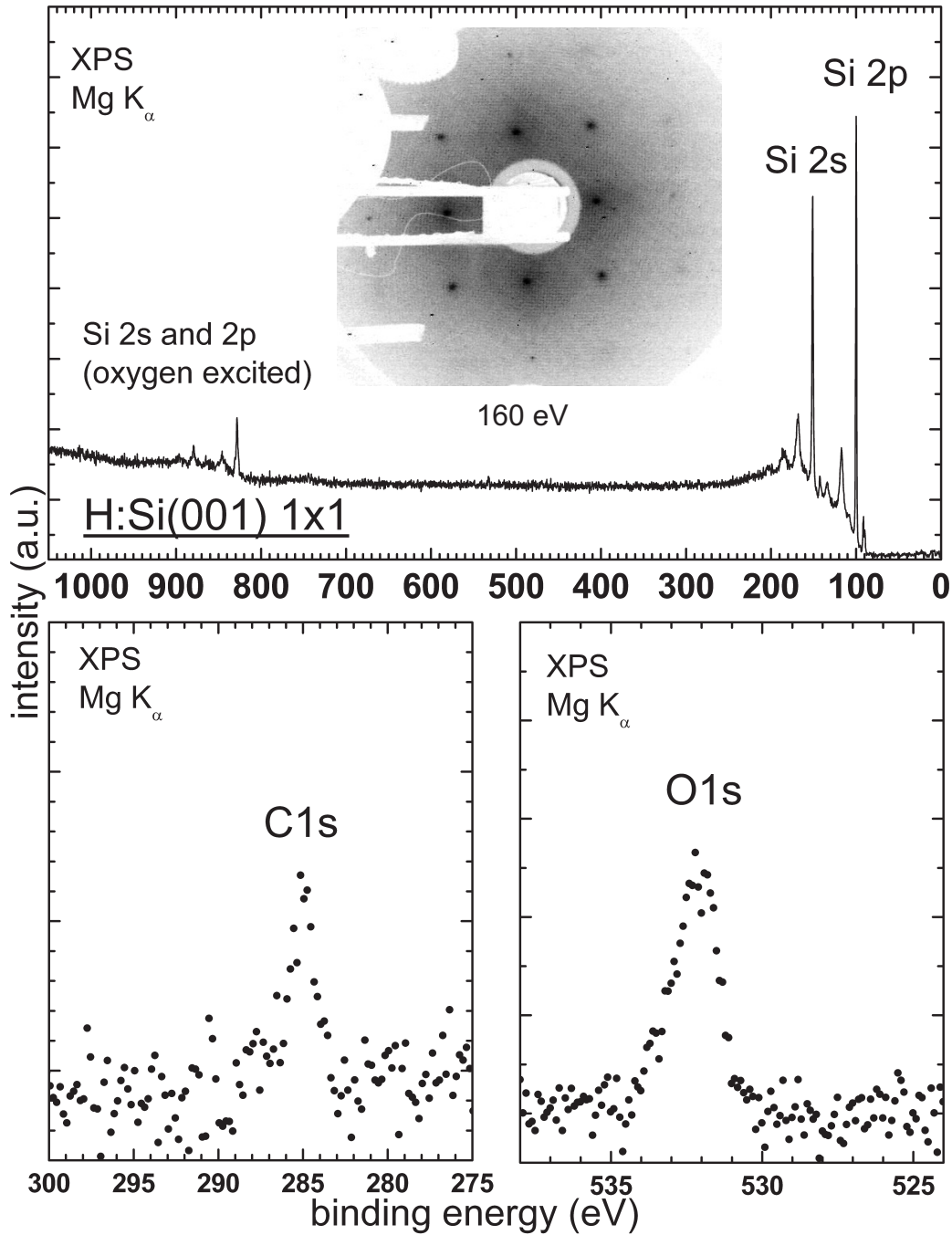


Figure 4.11.: XPS spectra of a silicon (001) surface after etching and subsequent annealing. The upper spectrum shows the survey spectrum which only contains the Si 2s and 2p peaks and their ghost lines (from oxidation of the X-ray anode). Underneath are detailed scans of the O 1s and C 1s peak showing only very low intensities for these lines. The inset in the survey spectrum is a LEED diffractogram of the 1x1 reconstructed surface recorded at 160 eV electron energy.

## 4. Determination of the transport levels and their gap

---

surface. Thus, it is only possible to speculate about the origin of the changes in the bulk region.

In conclusion, these experiments have shown that the method of termination of the dangling bonds at the surface delivers surface state-free band gaps, if the right new bonding partners are chosen. For a more efficient measurement it would be necessary to have a tunable light source like a synchrotron and a wavelength dispersive detector for IPS in order to identify surface states in more detail.

### 4.1.4. Position of the transport levels in the spectrum

The previous two Sections indicate why optical absorption is more favored in the literature to determine the band gap of inorganic semiconductors - it is significantly less complicated. The first investigators who applied the combination of PES and IPS for this matter were F.J. Himpsel and T. Fauster [HF84] in 1984. They investigated silicon without and with silicon-metal compounds at the surface and the ferromagnetic exchange splitting energy of cobalt. Another aim of their work was to use this method for band mapping and to compare the data to theoretical calculations. However, the band gaps were not evaluated and compared with the values of other methods. The comparison to optically determined band gaps was introduced by H. Carstensen et al. [CCMS90] in 1990. On a variety of semiconductor surfaces the UPS and IPS spectra were combined and the difference of the peak maxima determined. It was not distinguished between surface and bulk signals, since it was assumed that the surface sensitivity of the investigation methods delivers only data from the surface Brillouin zone. However, the considerable bulk signal content in the spectrum was demonstrated in Section 4.1.3 showing that the assumption of Carstensen et al. was incorrect.

The work of Carstensen et al. is one example for obtaining band gaps from the peak maxima, a method which is not generally agreed on in literature. Therefore this Section will discuss the position of the transport levels in the photoelectron spectra. As mentioned, some investigators use peak maxima, similar to the approach applied in band dispersion experiments. In the latter type of experiment only the relative peak positions are relevant, since the dispersion data is compared to LDA (local density approximation) calculations. These calculations deliver excellent results for the k-dependent positions of the energy bands relative to each other, but fail in the calculation of the band gap. Therefore the energy axes of the calculated bands are shifted to fit the experimental results. The difference between the use of peak maxima and onsets (which are not easy to determine for peaks within the spectrum) is only small.

A single example, in which the use of peak maxima was compared to and agreed with the data of optical absorption, is the paper of M. Traving et al. [TBK<sup>+</sup>97]. They used the layered system of WSe<sub>2</sub> which is special due to a covalent bond in-plane and a van-der-Waals bond between adjacent planes. WSe<sub>2</sub> is prepared by cleaving the crystal in UHV followed by an investigation with PES and IPS. Although the photoelectron spectroscopy data was determined very carefully to find the maxima in the Brillouin zone, the termination of the surface (W or Se) was not discussed, and no surface states were taken into account. In a subsequent paper [TSK<sup>+</sup>01], the same group investigated

a very similar system,  $\text{HfS}_2$  for which this peak maxima approach failed.

The alternative method of using the peak onsets is widely used in the respective literature concerning band extrema (e.g., [TMDN03], [DKAS98], [GSK<sup>+</sup>03] or [CBW<sup>+</sup>94]), but never a specific reason for using the onsets is given. D. Eich et al. [EOG<sup>+</sup>99] performed PES and IPS measurements on the  $c(2 \times 2)$  reconstructed  $\text{CdTe}(001)$  and  $\text{HgTe}(001)$  surface. By using the variation of photon energy the existence of occupied surface states could be excluded and by the use of Ar I excitation as well as the 9.7 eV IPS band-pass detector, the experiment was close enough to the  $\Gamma$  point of the bulk Brillouin zone. The band gaps of 1.57 eV for  $\text{CdTe}$  and 0 eV for the semi-metal  $\text{HgTe}$  derived from the peak onsets fitted the optical values of 1.54 eV and 0 eV in remarkably good agreement.

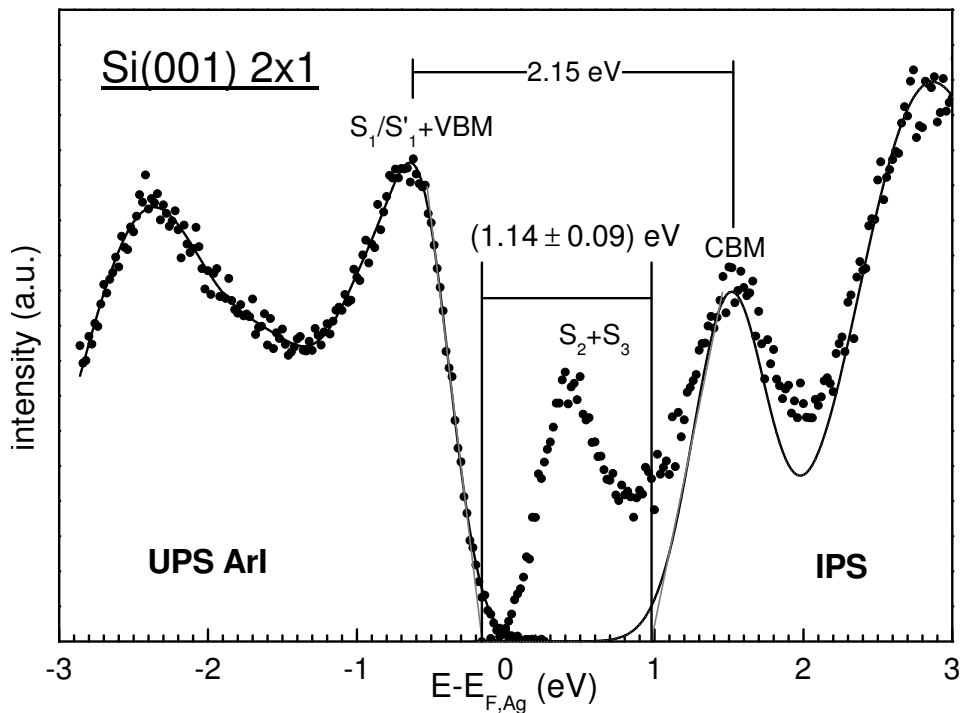


Figure 4.12.: Combined UPS and IPS spectrum of the Si (001) (2x1) reconstructed surface. The UPS spectrum was recorded with a photon energy of 11.83 eV, the IPS with a detector energy of 9.7 eV, both in normal emission/incidence. The black lines through the data points represent the fitted spectra from which in the case of IPS the surface states and the experimental broadening of 400 meV have been removed. The straight gray lines are the peak onset fits, which result in a band gap of 1.14 eV.

Figure 4.12 shows the result of the present silicon measurements including all results of the previous two Sections. In case of the UPS part of this Figure, it was possible to choose an energy that excites electrons close to the  $\Gamma$  point of the silicon BZ. It was not possible to eliminate the surface state in this spectrum, because the VBM is too close to it for a fit of the spectrum and after hydrogen termination of the surface, no final state could be reached close to the VBM. However, the band structure calculations show

## 4. Determination of the transport levels and their gap

---

that the VBM is about 0.3 eV above the surface state. Thus, using the peak onset of the surface state is causing only a minor error. Nevertheless, synchrotron measurements on preferably the hydrogen terminated (111) face of silicon are recommended to obtain better data for this aspect.

In case of the IPS, it was possible to remove the surface state, but the CBM was only reachable with the help of an surface lattice vector - a so-called umklapp process. If the surface reconstruction is removed, this umklapp process does not take place and the IPS setup utilized can not measure at the correct point in the BZ. The fit of the spectrum and the removal of the identified surface states is therefore the better choice. Additionally, it allows to remove the experimental broadening and the result of these two operations can be seen as black line on the IPS side in Fig. 4.12.

The distance between the peak onsets of the band extrema is then 1.14 eV, which is again remarkably close to the optically determined value of 1.11 eV - the peak maxima distance of 2.15 eV is significantly higher. Ironically, the peak maxima distance of the surface states is 1.08 eV, which is also very close to the optical band gap, but can be considered as coincidence. An error of the determined value can not easily be given. The determination of the onset is very reproducible, since it is done by a linear fit through the data points around the inflection point of the peak and, if the peak has a foot, through the first points of the foot. The value is read out at the intersection of these two lines. The error for this method was given by D. Eich et al. with  $\pm 0.06$  eV in total for both onsets, but the fit and subtraction of peaks to obtain the surface state-free spectrum adds a further error, which is estimated to be of the same size resulting in an overall error of  $\pm 0.09$  eV, (i.e., 0.1 eV). However, many assumptions were made to obtain Figure 4.12 and therefore this error bar only marks the lower limit.

In conclusion, the results of D. Eich et al. as well as the results of this work clearly show that it is possible to obtain the same values for the band gap in optical experiments as well as by the combination of UPS and IPS by using the peak onsets. At a first glance it is not obvious (and against intuition) why the onsets should be taken. However, a closer look at the broadening mechanisms, which lead to the asymmetric peaks and which were described in Chapter 3 gives the answer. Asymmetry in this case means that effects broaden the peak only away from the Fermi energy, resulting in the good agreement of the onsets. D. Eich et al. tried to explain this by the phonon interaction (compare Section 3.5) as well as the limited angular resolution (compare Section 3.3). It was shown in Chapter 3, however, that from these peak broadening effects are not sufficient as explanation since the limited angular resolution can be neglected because of the vanishing dispersion near an inflection point, where maxima and minima are located. The vibrational broadening (or in the case of inorganic semiconductors the phonon interaction) is important, but can only be estimated as contributing about 200 to 300 meV to the FWHM, which also does not explain the full width of the electronic states in photoemission.

Later, the list of mechanisms was extended in a subsequent paper by T. Gleim et al. [GHU<sup>+</sup>03] suggesting spatially or temporary incomplete screening. This model is also suggested in Section 3.7. It addresses the very fundamental description of a transport state and where it is likely to be found in a PES spectrum. A charge carrier in the

transport band is a delocalized state. In the language of photoemission, as one extreme the final state hole is fully screened by charge transfer involving surrounding valence electrons, leaving a neutral atom rather than an ion, which is essentially the same as a fully delocalized valence hole as for transport measurements. In the other extreme, the final state is an ionic state which experiences only polarization by neighboring atoms. Thus, in the latter case the produced charge remains at the place where it was produced (localized ionic state, LIS) while in the former case it has experienced all relaxation/screening effects, i.e. it has moved away (fully relaxed state, RIS). The latter case would yield a state close to the Fermi energy similar to a transport state, i.e. at the onset of the measured broad valence peak.

In summary, the data for the II-VI semiconductors HgTe and CdTe as well as the element semiconductor silicon demonstrate that bulk band gap information can be obtained from the combined PES and IPS spectra. However, it is crucial to be aware of surface states and the position in the Brillouin zone in order to find the transport states and the onsets rather than the peak maxima have to be utilized for determination of the gap. This work also explains the fact that peak onsets, although broadened by various effects, are the right choice. The key are the asymmetric broadening effects, which broaden the peaks away from the Fermi energy, and therefore leave the fully relaxed state (= transport state) at the onset.

## 4.2. Organic semiconductors

Thin films of organic semiconductors are in many ways different from their inorganic counterparts. Each molecule is a semiconductor itself. This means that the semiconductor property of a separated valence and conduction level with a gap small enough to excite charge carriers with visible light, is given by the separation of the highest occupied molecular orbital (HOMO) and the lowest unoccupied molecular orbital (LUMO). The molecules are assumed to keep their electronic structure in their solid state and interact by weak forces, e.g. van-der-Waals interaction, with minor overlap of their electronic systems. Therefore the nomenclature for the peaks closest to the Fermi energy is based on the electronic structure of the molecule. Thus the first UPS resonance is named HOMO and the first unoccupied peak LUMO.

After the presentation of the experimental results, this Section will therefore first define the term transport level in these materials. The use of the onsets of inorganic semiconductors is also proposed for thin films of organic semiconductors. The influences on peak positions as well as widths will be discussed to justify this choice. Connected to the transport gap size is the size of the exciton binding energy. Large values have been found in the literature, but the values strongly reduced when using the peak onset approach. The consequences of the smaller binding energies will be discussed in the second Section by a review of experiments concerning the size of the intermolecular interaction.

### 4.2.1. Position of the transport levels in the spectrum

#### Multilayer organic films

Figure 4.13 shows the combined UPS and IPS spectra for all thin films of molecules investigated in this work. All thin films were prepared on a freshly sputter-cleaned and annealed Ag(111) surface under the conditions described in Section 2.2. Despite the band bending in the case of Alq<sub>3</sub> (see Section 2.4.2) a precise determination of the relative positions of the transport levels was possible, while the absolute positions depend on film thickness. For the DIP molecule, the most stable film structure, the high temperature phase, was chosen because it only includes one well-ordered geometric structure resulting in narrower peaks in UPS as well as in IPS (see Section 3.4).

Before the question about the position of the transport levels in spectrum will be addressed, it is necessary to discuss the energy axis of the spectra for the case of organic adsorbates on metal surfaces. The axis is calibrated to the Fermi edge of a gold foil because this has electronic states up to the Fermi level. This level is the same for the silver crystal because Fermi level alignment occurs. Sections 2.3 and 2.4 have shown that for thin films of organic semiconductors the Fermi levels do not align with the silver substrate. Therefore the energy axis show not energy level position relative to the Fermi level of the silver substrate. Most forms of band bending (except for image potential screening, which has not been found for any of the molecules in this work) lead to a shift of the vacuum level, occupied and unoccupied levels in the same direction with increasing distance from the interface. It is therefore necessary to measure a thickness dependent series of UPS and IPS spectra to find out if the positions are stable with thickness or if they shift.

Additionally, the example of DIP on Ag(111) in Section 2.6 shows that the parameter space of the growth conditions needs to be explored and the geometric structure to be investigated. Figure 4.14 shows the influence of the three directly grown geometric structures of Diindenoperylene on the transport levels and their gap. The onset gap varies by about 0.3 eV whereas the absolute position relative to substrate Fermi level can shift by up to 0.5 eV due to changes of the ionization potential. Although DIP is more an exception than the standard case, the growth conditions and thicknesses are important parameters that should be noted for each spectrum for better comparability of different experiments.

Since the question about the position of the transport levels in the spectrum also arises for organic semiconductors, in all spectra the peak maxima as well the onset distances have been marked (Fig. 4.13). The difference between the values determined in both ways is between 1 and 2 eV. The error bar of the peak distance determination is about  $\pm 0.1$  eV and originates mainly from the variation of the peak positions between different preparations and the error of the determination of the peak maxima as well as onsets. The molecular crystal surface is not a cut through an atomic single crystal, all bonds at the surface are already saturated and surface states due to a reconstruction do not occur. Therefore the features closest to the Fermi edge can be attributed to the transport states. In order to discuss the position of a transport state within the



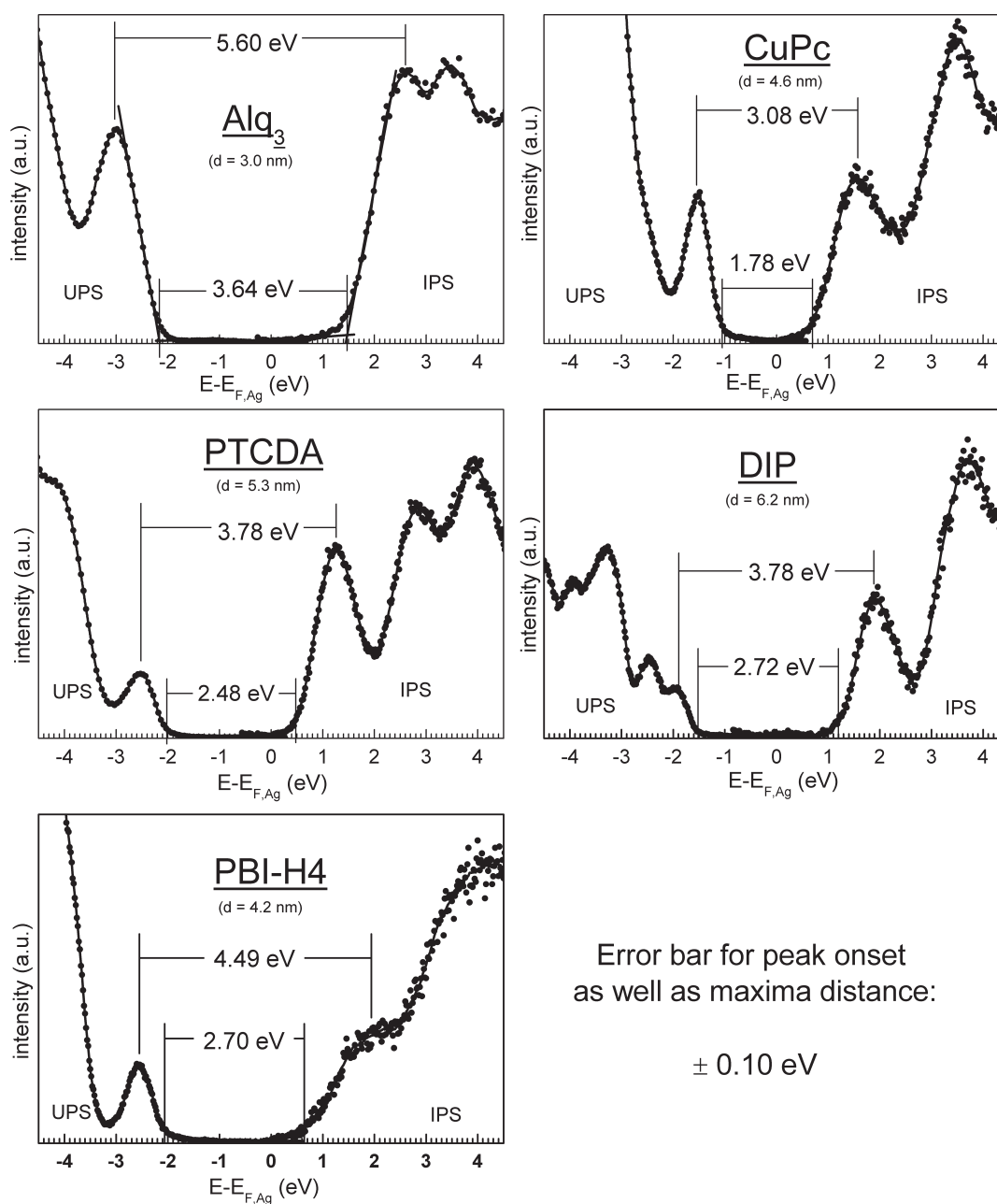


Figure 4.13.: Combined UPS and IPS data for thin films of all molecules investigated in this work on a well prepared Ag(111) surface. In all spectra, the distance of the peak onsets and maxima is indicated by lines and the corresponding energy values are noted. For all molecules (except for Alq<sub>3</sub>) a thickness was chosen at which no further band shift was detectable (compare Section 2.4.2).

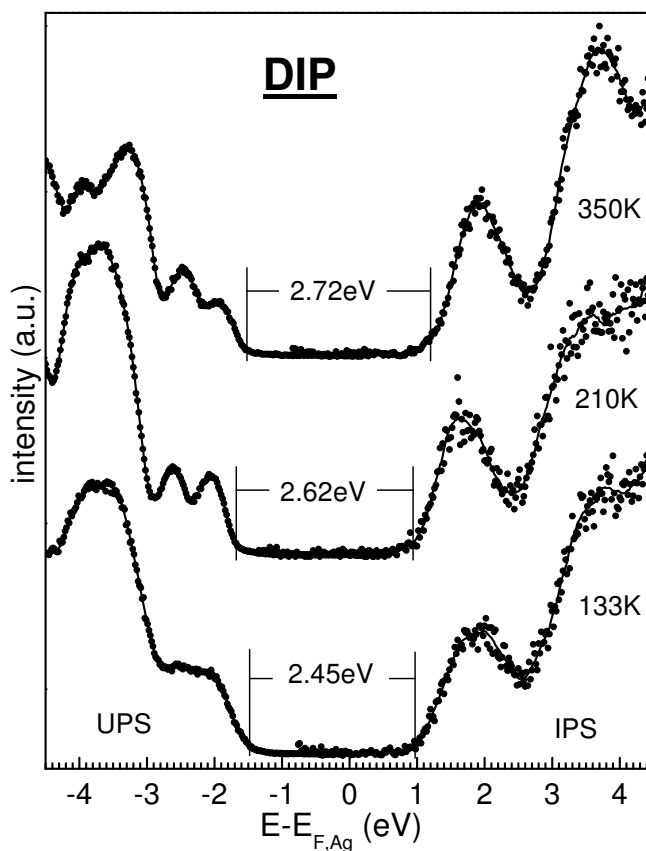


Figure 4.14.: Combined UPS and IPS spectra for the three phases found for DIP on Ag(111).

peak, it first has to be defined for organic semiconductors. Two different concepts for charge transport are discussed depending on the strength of intermolecular interaction. In case of a sufficiently strong interaction, a coherent band-like transport as in inorganic semiconductors is possible. In that case the transport state is a delocalized charge and relaxation effects have only little effect on its binding energy. All possible relaxation effects of the vicinity of this delocalized charge carrier have taken place due to its long lifetime. If the interaction is not sufficient, the charge carrier is localized on a single molecule and has to hop to the adjacent one. The time it remains on one molecule is about  $10^{-14}$  s, which is enough for its vicinity to react to the charge causing some relaxation (screening) effects by polarization. Independent of the contribution of these effects, the transport state is a fully relaxed state.

Similar to inorganic semiconductors, the use of the onset is proposed in this work, based on similar asymmetric peak broadening mechanisms. The effect of limited angular resolution can be considered as less important for the peak widths. The band widths that have been measured so far are fairly small and range between 0.20 and 0.35 eV ([GMK<sup>+</sup>04], [YKO<sup>+</sup>03], [Zou03]) measured on well ordered, single domain organic films. On many surfaces (such as the threefold symmetric Ag(111)) the molecules form

geometric structures with more than one rotational domain, which smears out the dispersion effect in an angle dependent PES experiment and simply broadens all peaks slightly. The peak widths for such a film using good angular resolution (0.60 eV for DiMe-PTCDI HOMO in the work of G.N. Gavrilin et al. [GMK<sup>+</sup>04]) do not differ from the multi-domain, angle integrating measurements (0.55 eV for PTCDA HOMO in this work, Section 3.4), which is a strong indication that this effect can be neglected.

The vibrational broadening needs to be considered. The molecules have a rich spectrum of possible vibrations and the final state of the photoemission process can be an excited as described in Section 3.5. However, this effect explains only a part of the overall peak width and is estimated in the literature [HKSP00] to shift the peak maximum by about 0.1 eV and the width by 0.2 - 0.3 eV (this work). Independent of the exact contribution, the production of a vibration is more probable than its annihilation and the state of lowest energy can therefore be found closer to the peak onset.

The degree of order in thin films of organic semiconductors is often far away from that of a single crystal. Often they consist of micro-crystallites with grain boundaries, several defects, and different orientations. This contributes to the peak width via inhomogeneous broadening, which is based on a different size of the relaxation effects for the final state in PES. As already described in Section 3.4, similar to the additionally proposed effect of dynamic screening fluctuating with time, these effects fluctuate laterally. The state comparable to a transport state is the best screened/relaxed final state close to the peak onset. However, the comparison of the HOMO widths in this work showed that even highly ordered and to this effect insensitive molecules such as C<sub>60</sub> (due to spherical symmetry), show peak widths of about 0.45 eV.

In order to explain the use of the onset, the concept of peak broadening due to dynamic screening of the final states was introduced in Section 3.7. In this model, either the positive charge on the photoionized molecule is compensated by charge transfer from neighbors leading to a complete hole delocalization in the extreme case (= fully screened). In most cases only partial charge transfer will occur and the hole is delocalized over a few molecules. Or the hole remains on the photoionized molecule and polarization screening occurs. In this case the contribution of relaxation screening effects on the final state energy is considered to be fluctuating with time, e.g. by phonon-like molecule movements. Then each photoemission event probes these energies on a time scale faster than the fluctuation. The measured peak therefore is a superposition of all possible final states and the best relaxed state can again be found at the onset.

All these asymmetric broadening mechanisms corroborate the use of the onset as the position of the transport levels in the spectrum, which of course has consequences transport gap and also for strength of the intermolecular interaction, which is the subject of the next Section.

## Polymer P3HT

Before the interaction and exciton binding energies in organic thin films are discussed, the combined UPS and IPS measurements of an intermediate system will be presented. The polymer Poly(3-Hexylthiophene-2,5-Diyl) (P3HT) consists of long molecular chains

#### 4. Determination of the transport levels and their gap

in which the monomers are covalently bound to each other and which interact between the chains by van-der-Waals forces. It is therefore a system in which the charge can easily delocalize in one dimension. Figure 4.15 shows the result for a thin (<10nm) film

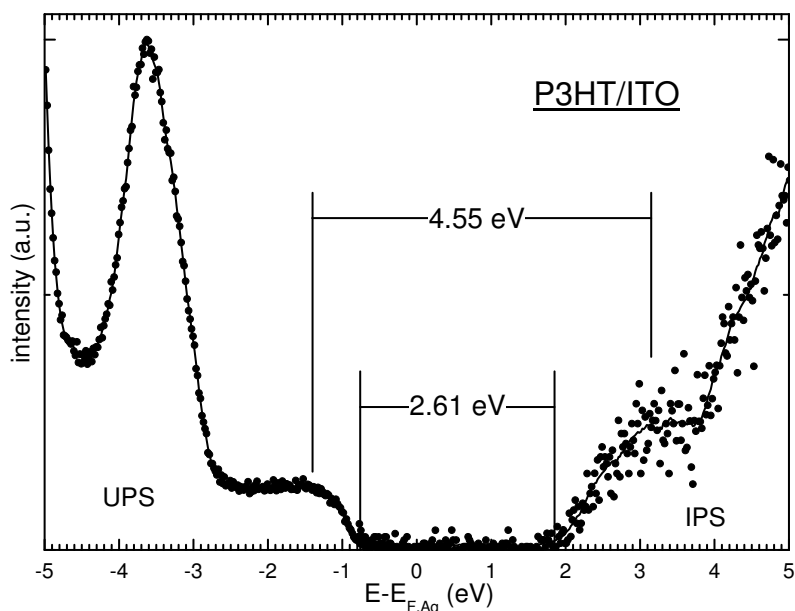


Figure 4.15.: Combined UPS and IPS spectra for the polymer P3HT, which was spin-coated on an ITO substrate.

of P3HT spin-coated on a indium tin oxide (ITO) substrate. The peak maxima are less obvious to identify and the assumed position as well as the one for the onsets is indicated in the spectra. The IPS spectrum is very noisy because the polymer was very sensitive to radiation damage and data could be acquired for only few minutes. The transport gap distance of 2.6 eV is rather close to the optical one. It will be a matter of discussion in the interpretation of the exciton binding energies.

#### Monolayer of PTCDA on Ag(111)

Figure 4.16 shows the first UPS and IPS data for a monolayer of a large organic molecule. This PTCDA monolayer was prepared by annealing of a thick film causing all layers but the interface layer to desorb. This first layer is chemically bound to the silver and was intensively investigated in the past ([TES<sup>+</sup>02b], [Tau07], [TSS<sup>+</sup>00], [Zou03], [ZKS<sup>+</sup>06a]). The focus of these studies was to clarify the nature of the bonding with the help of valence level and vibrational spectra. Figure 4.16 shows the assigned peaks. The chemical bonding to the substrate leads to a partial occupation of the LUMO (F-LUMO, F = filled) and the change in the electron density induces a shift of the HOMO (new HOMO). However, no IPS measurements were performed so far. In order to identify the IPS states the literature was revised for clean Ag(111) spectra and compared to the measurement of Ag(111) of this work, which are presented in Fig. 4.17. Besides an

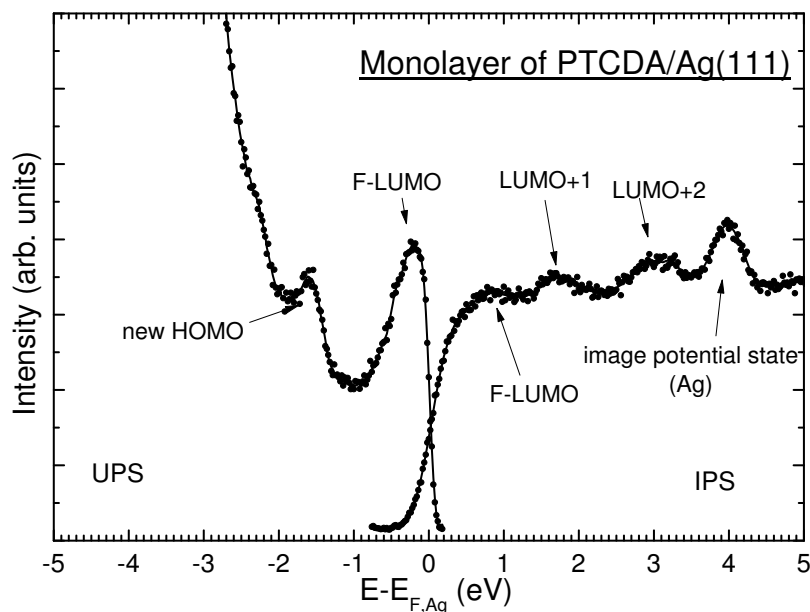


Figure 4.16.: Combined UPS and IPS spectrum of a monolayer PTCDA on Ag(111). The monolayer was prepared by annealing of a multilayer.

intense surface state a signal at around 4 eV is visible, which represents image-potential states. They consist of a series of states which lie near the band edge in the d-band gap of the Ag(111) surface at about 0.6-0.8 eV below the vacuum level ([SW86], [GHH<sup>+</sup>87], [Ste89]). If the angle of incidence is off-normal they disperse strongly and the sp-band edge becomes visible, which was measured by K. Giesen et al. [GHH<sup>+</sup>87] for Ag(111) and in more detail explained for the example of Au(111) by D.P. Woodruff et al. [WRS86]. The fact that the PTCDA monolayer spectra show a state at 4 eV in normal incidence and a step at 15° strongly indicate the presence of a image-potential state. The first peak at 0.8 eV in the bottom spectrum of Figure 4.17 can be related to an interface state, which is the upper part of the partially filled F-LUMO and was also found in two-photon photoemission (2PPE) by C.H. Schwalb et al. [SSM<sup>+</sup>08]. This peak is weak in the IPS spectrum and its position has a larger error bar since it superimposes the underlying Fermi function. In 2PPE a dispersion of this peak of about 0.2 eV for 15° was found, which is again hard to distinguish in the 15° spectrum. The two remaining peaks are attributed to unoccupied states of the molecular layer and are labeled as LUMO+1 and LUMO+2. They only vary in intensity, but their position stays constant.

#### 4.2.2. Determination of exciton binding energies from the comparison to optical absorption

In contrast to the inorganic semiconductors, the question of the size of the exciton binding energies in organic semiconductors is connected to the intermolecular interaction, which in general is assumed to be purely van-der-Waals interaction like in noble gas crystals.

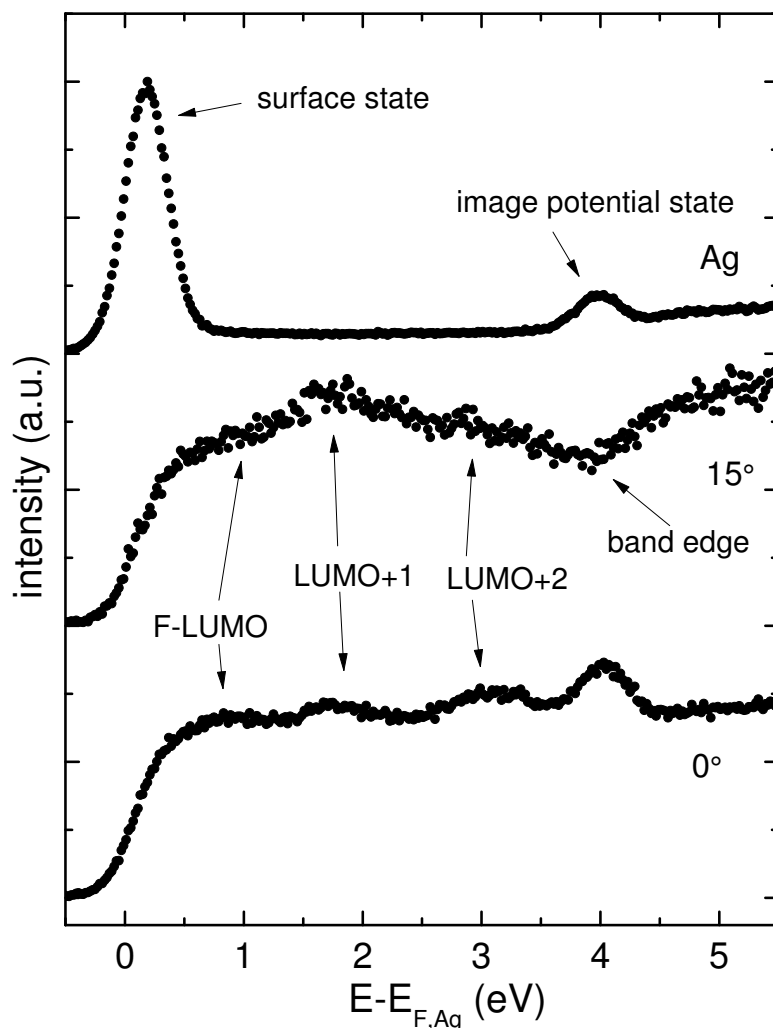


Figure 4.17.: IPS spectra for the clean Ag(111) (top, measured in this work) the PTCDA monolayer on Ag(111) at 15° (middle) and 0° (bottom) angle of electron incidence.

The difference between the gap determined by optical absorption and that by PES and IPS measurements depends on this, and is also expected to be significant because the two methods excite different final states. In optical absorption the lowest energy marks the creation of a bound electron-hole pair - an exciton - by a transition from an occupied into an unoccupied state. In PES/IPS the final state is an unbound hole or electron, which is comparable to a charge carrier. Depending on the strength of intermolecular interaction and the timescale of the photoemission process this charge is confined to a larger (stronger interaction) or smaller volume (weaker interaction).

Table 4.1 shows the results of the evaluation of the spectra in Figures 4.13 and 4.15. Besides the peak maxima and onset distances, literature values for the optical gaps are given in order to determine the exciton binding energies. All values are rounded to the

Table 4.1.: Comparison of the peak maxima ( $\Delta_{PM}$ ) and the peak onset values ( $\Delta_{PO}$ ) for all investigated thin films of molecules as well as a polymer film. These values are compared to literature optical gaps, which are in the case of PTCDA, Alq<sub>3</sub> and CuPc from [HKSP00], DIP from [Dür02], PBI-H<sub>4</sub> from [SSK<sup>+</sup>09] and the P3HT value from [MS02]. The difference between optical gap and peak onset distance is the exciton binding energy ( $E_{B,exciton}$ ).

Molecule	$\Delta_{PM}$ / eV	$\Delta_{PO}$ / eV	$E_{gap,opt}$ / eV	$E_{B,exciton}$ / eV
PTCDA	3.8	2.5	2.2	0.3
CuPc	3.1	1.8	1.7	0.1
DIP (>350K)	3.8	2.7	2.2	0.5
Alq <sub>3</sub>	5.6	3.6	3.2	0.4
PBI-H <sub>4</sub>	4.5	2.7	2.5	0.2
P3HT	4.6	2.6	2.3	0.3

first digit after the comma, because the literature optical gap values were given in this precision and the error bar of the transport gap measurements is about  $\pm 0.1$  eV. The resulting exciton binding energies are significantly smaller than the values of the peak maxima method. I.G. Hill et al. [HKSP00] used the peak maxima to determine the position of the transport levels and corrected these value by the vibrational broadening, which they considered to shift the peak maximum of about 0.1 eV away from the Fermi edge, and by two times 0.3 eV due to the altered polarization screening at the surface and in the bulk during the photoemission and IPS process, respectively. Therefore both transport levels are shifted by 0.4 eV closer to the Fermi energy and the peak maxima derived transport gap reduces by 0.8 eV, which still leads to 0.2 - 1.2 eV higher transport gaps as those derived from the peak onset method. The difference of the polarization contribution of 0.6 eV was shown in Section 2.1.2 to be absent. The resulting exciton binding energies of the peak maxima method are therefore 0.8 - 1.8 eV larger than the ones proposed in this work indicating a very strong confinement of the electron-hole pair. It is not obvious to decide which method has the more reasonable results. Since the volume to which the exciton is confined is a result of intermolecular interaction, a number of experiments will be reviewed that help to estimate this quantity.

One way to measure the strength of this interaction is to determine the dominating channel of charge transfer in the thin films of these molecules. Recent experiments [Kar03] as well as calculations [HS06] point towards the existence of both channels depending on the degree of order in the film as well as the temperature. For highly ordered naphthalene crystals band transport was measured below 50 K. Additionally, the calculations indicate a broad transition temperature region in which both types coexist. The coexistence of both channels shows that the correlation and hence the coherence is reduced for long but not for short distances.

A further experiment that helps to understand the nature of the intermolecular interaction is the comparison of the electronic structure of molecules in the gas phase and in

## 4. Determination of the transport levels and their gap

---

their solid state. Section 2.1.1 discussed this matter already with a focus on polarization effects and concluded that the differences between the two phases cannot be explained by the picture of a molecule separated from but embedded in a polarizable medium, with no direct electronic interaction with its neighbors.

Moreover, a comparison of the exciton binding energies of the archetype van-der-Waals crystal - the noble gas crystal - helps to estimate the expected size of the binding energies. The exciton type expected in the organic molecular crystals is a Frenkel (or charge transfer) exciton, with high binding energies due to the small volume in which it is confined. It can not be simply described by a hydrogen-like picture as its weakly bound Mott-Wannier counterpart. Calculations of excitons in the noble gas crystals show, that not even the ground state of them can be described by a pure Frenkel exciton but a mixture of Frenkel and Mott-Wannier [UKK<sup>+</sup>84]. If the confinement in noble gas crystals is stronger as in molecular crystals as it is generally assumed the observed binding energies of 1.0 eV (Xe) to 1.6 eV (Kr) [Fug78] should give an upper limit for exciton binding energies in molecular crystals, indicating that only the values determined at the onsets are realistic.

All these arguments and the experimental data for P3HT support the use of the peak onsets as the position of the transport states. P3HT is a polymer film in which exciton binding energies of about 0.5 eV are expected since the electron and the hole can at least freely move along the chain to move apart from each other. The measured value of 0.3 eV corroborates the assumption that the two exciton partners in the organic thin films are also able to separate by a few molecular units and that exciton binding energies of less than 1 eV are more reasonable for these systems.

### 4.3. Summary and Conclusions

This chapter started with a well-understood inorganic semiconductor system, for which a broad basis of experimental data and theoretic calculations is available - silicon. Its charge transport mechanism is coherent band transport and charges are therefore very mobile (= delocalized). The final states of photoemission and optical absorption are hence very close in binding energy, because the binding energy between electron and hole produced in an absorption experiment is very small due to the delocalized character of the charge carriers (Mott-Wannier exciton). This fact facilitates the search for the VBM and the CBM (the transport levels) in the (direct or inverse) photoelectron spectrum, since the gap between them should be the same as the optical gap. Nevertheless, it was shown that it is not straight forward to prepare the silicon such that no surface state superimposes the bulk transport states. The application of (I)PES demands an appropriate choice of crystal face, photon energy as well as emission angle to ensure a measurement at the correct point of the bulk Brillouin zone at which the band extrema can be found.

If all these boundary conditions are fulfilled, the transport levels can be found at the peak onsets. Since the peaks are experimentally and lifetime broadened the reason for using this position was not obvious and had to be discussed. Based on the peak broad-



ening discussion in Chapter 3, the discussion can be concentrated on those mechanisms that preferably broaden the peak away from the Fermi energy - the asymmetric peak broadening mechanisms.

The results of the inorganic semiconductors can be transferred to the organic semiconductors. A very crucial fact discussed in Chapter 2 is that the relative position of the electronic energies with respect to the Fermi energy of the metal substrate depends on film thickness and geometric structure. The example of DIP showed that even the gap between the transport level can be affected by geometric structure. Independent of this fact, the position of the transport level was found to be also marked by the peak onsets, which was again discussed on the basis of asymmetric peak broadening. This choice is contrary to the general habit of using the peak maxima. Thus, the present transport gaps using the onsets are significantly smaller. The resulting smaller exciton binding energies can only be explained by a stronger intermolecular interaction, which is discussed in the last part of this chapter utilizing the results of recent publications. A comparison to the intermediate system of a polymer, for which exciton binding energies of about 0.5 eV are expected, yielded 0.3 eV corroborating the choice of the onsets. It is considered intermediate because the charges can freely move along the chain of the polymer resulting in lower exciton binding energies as an electron-hole pair confined on a single molecule.

In conclusion, it was shown that using the peak onsets yields correct transport gaps for inorganic semiconductors and very reasonable transport gaps for organic semiconductors. The method requires for a thorough investigation of thickness and film geometry and their influence on the electronic levels. Since this involves the exploration of a large film preparation parameter space, a single UPS/IPS experiment is only one point within this space and may not represent the general value. The smaller exciton binding energies that are comparable to polymer values, put the picture of weakly van-der-Waals bound crystals up for discussion. That the idea of pure van-der-Waals bonding is rather questionable can be derived from the size of the  $\pi$  orbitals and the distance of adjacent molecules (e.g. 3.2 Å in PTCDA crystal) suggesting appreciable  $\pi$ -overlap and from very recent experiments some of which were discussed in this work.

## 5. Summary

The main goal of this work is to apply a combination of photoelectron and inverse photoelectron spectroscopy to the determination of transport levels and their gaps. This approach is not limited to thin films of organic semiconductors but the focus of this work is on them.

The strategy to accomplish this goal is a three step approach:

- First, gathering of literature information and performing experiments that show which processes influence the **peak positions**.
- Then, gathering literature information and performance of experiments that show which processes influence the **peak widths and shapes**.
- Finally, discussion of the **position of the transport levels in the photoelectron spectrum** considering what a transport level in an organic thin film is in combination with the results of the first two points.

Subsequent to the last point, this work also discusses the size of the exciton binding energies and connected to this basic aspects of the intermolecular interaction in molecular crystals.

Based on this strategy, the first Chapter opens with a discussion about the shift due to the influence of polarizability of organic molecules, which could affect the final state in photoemission. This effect is very often mentioned in the discussion of transport level shifts, but a thorough analysis of the literature and newly published experimental results show that this effect seems to be either not existing or that a photoemission experiment is simply not sensitive to it. Many of the effects that were found to lead to peak shifts depend on the film thickness, which is why the control of the growth mode is considered to be crucial in order to grow flat films with homogeneous thickness. How this can be done by variation of the growth conditions monitored by X-ray photoelectron spectroscopy, is the topic of the subsequent section.

The interface of a metal substrate with an organic overlayer has a huge influence on the position of the energy levels with respect to substrate Fermi level. It was already shown in the literature that most organic thin films exhibit no Fermi level alignment with the substrate even after several hundred nanometer of film thickness. Since the probing depth of a PES experiment is only a few nanometer, a mere vacuum level alignment at the interface shifted by an interface dipole can be observed. This fact makes the determination of the Fermi level of an organic film by UPS impossible. Besides alignment, a thickness dependent shift of the energy levels (band bending) is discussed.

---

The system diindenoperylene on Ag(111) proves to be a perfect candidate to study the effect of changes in the geometric structure of the thin film on the photoemission spectrum. An extensive spot profile analysis low electron energy diffraction (SPALEED) study shows the influence of preparation conditions on the geometric structure. Depending on substrate temperature during film growth, three different structural phases can be distinguished by SPALEED, which range from amorphous films over several coexisting geometric structures to a single crystalline structure with long range order. The changes in the photoelectron spectrum can therefore completely be attributed to these structural differences. High resolution electron energy loss spectroscopy (HREELS) is also applied to these phases in order to detect changes in the intermolecular interaction. The vibration frequencies may be very sensitive to changes of the interaction with neighboring molecules, but the spectra show only slight changes between different phases. This is different for UPS and IPS, which show significant changes of position, relative intensities and even peak widths of the spectra for different phases. Even phase changes were observed for this system, which need a further investigation for a deeper understanding of the processes.

The second step of discussing peak broadening mechanisms starts with the broadening due to structural inhomogeneities in the thin films. This mechanism is very often mentioned as the most important mechanism and affects the final state in photoemission. The measured energy is expected to depend on the surrounding molecules and the geometry with respect to each other. Different geometries result in different screening of the photoinduced charge. The comparison of the average HOMO width of the molecules in thin films reveals that this effect significantly increases the peak width for amorphous films. Nevertheless, even well ordered films of molecules with spherical symmetry, in which this effects should be small, have peak widths of about 450 meV. Vibrational broadening due to excited final states is the effect which is in general assumed to be responsible for the broad peaks in photoemission. It is not possible to measure the size of this effect, but vibration and phonon spectra help to estimate a maximal contribution of 200 - 300 meV. This is not enough to explain the peak widths. Experimental broadening is especially an issue for IPS data, being responsible for a contribution of 400 meV. Surprisingly, the peaks in the IPS spectra are all significantly larger (0.8-1.0 eV) and the deconvolution of these 400 meV has only little effect on the peak widths. The origin of the broader IPS peaks remains unclear and demands for further investigation. Connected to the experimental resolution is the broadening due to limited angular resolution which leads to a significant peak width contribution in the case of strong dispersion of the energy levels. However, organic semiconductors only show small dispersions. Band extrema are inflection points in the Brillouin zone and therefore flat. Since none of the known broadening mechanisms nor their sum can explain the broad peaks in photoemission, another mechanism is introduced at the end of Chapter 3 - dynamic screening. Local variations of screening effects (inhomogeneous broadening) already proved their potential to broaden the peaks and therefore a temporal variation of screening is proposed that accounts for the dynamics of each system even at low temperatures. A crucial aspect of many of these broadening mechanisms is that they preferably increase the measured binding energy and therefore broaden the peak asymmetrically away from the Fermi energy.

## 5. Summary

---

The last step is the identification of the transport states in a PES/IPS spectrum. In the literature contradictory ways have been discussed, which either favor the peak maxima or the onsets of the spectral bulk features closest to the Fermi energy as the position of the transport states. Therefore a well-understood inorganic semiconductor, silicon, is in the focus of the first part of Chapter 4. The use of these investigation methods for band gap determination is not very common and therefore a procedure was established based on available literature. First, the right points in the bulk Brillouin zone need to be found by choosing the appropriate photon energy, emission angle and crystal face. Then, the "dangling" bond induced surface states in the band gap, which superimpose the transport states, need to be eliminated. From the two proposed methods to reach this, hydrogen termination of the surface and the reproduction of the fitted spectrum after subtraction of the identified surface states, only the fitting method proved to be applicable for the experimental setup accessible for this work. The onset derived band gap of  $(1.14 \pm 0.09)$  eV is very close to 1.11 eV of the optical band gap. This fact that a point such as the onset of a peak marks the band extremum, although this onset is influenced by experimental and lifetime broadening, can be discussed based on the asymmetric peak broadening mechanisms of Chapter 3.

Based on the good results for inorganic semiconductors, the use of the onsets is also proposed for thin films of organic semiconductors. The transport states in these films were, independent of the charge transport mechanism, identified as final states for which the surroundings had the time to screen the charge, which is referred to as a relaxed final state. This state resembles the final state in photoemission identified in the peak broadening mechanisms as the one closest to the Fermi energy. The exciton binding energies in thin organic films are expected to be larger than for inorganic semiconductors, since the electron-hole pair is confined to a smaller volume. The lowest energy in optical absorption is a bound electron-hole pair for which a significant binding energy is expected. This binding energy can be measured by comparing the transport and the optical gap. The values found in this work range from 0.1-0.5 eV, which is notably smaller than values derived from peak maxima. The comparison to a polymer showed that the exciton binding energies are in the same order (0.3 eV). These small exciton binding energies point towards a substantial intermolecular interaction in thin films of organic semiconductors, which re-opens the discussion about the bonding of an organic molecular crystal.

## 6. Zusammenfassung

Die vorliegende Arbeit beschäftigt sich mit der kombinierten Anwendung von Photoelektronen- und inverser Photoelektronenspektroskopie (PES und IPS) zur Bestimmung der energetischen Lage der Transportniveaus. Obwohl vor allem organische Dünnschichtsysteme im Fokus der Untersuchung stehen, werden für Vergleichszwecke auch anorganische Halbleiter behandelt.

Das Konzept, mit welchem in dieser Arbeit versucht wird, dieses Ziel zu erreichen, ist dreistufig:

- Zunächst werden anhand der bestehenden Literatur und eigener Experimente die Einflüsse diskutiert, welche die **energetische Lage der elektronischen Niveaus** in der Photoelektronenspektroskopie bestimmen.
- Mit dem gleichen Ansatz werden ebenfalls alle **Signalverbreiterungsmechanismen** diskutiert.
- Unter Berücksichtigung der Ergebnisse der ersten beiden Schritte wird dann diskutiert, wo die **Transportniveaus im Photoelektronenspektrum** zu finden sind.

Aus der Lage der Transportniveaus und ihrer Lücke werden im Anschluss die Exzitonbindungsenergien für die organischen Dünnschichten bestimmt. Die Ergebnisse der Bindungsenergien werden zum Schluss kurz im Hinblick auf ihre Bedeutung für die intermolekulare Wechselwirkung diskutiert.

Dieser Strategie folgend, wird zunächst der mögliche Einfluss der hohen Polarisierbarkeit der organischen Moleküle auf den Endzustand in der Photoemission und die damit verbundenen Verschiebungen der gemessenen Energien diskutiert. Dieser Effekt wird häufig in der Literatur im Zusammenhang mit der Oberflächenempfindlichkeit der Untersuchungsmethode und der unterschiedlichen Bedingungen für Polarisierungseffekte an der Oberfläche und im Volumen genannt. Eine detaillierte Studie in der Literatur und die darin beschriebenen Schlüsselexperimente kombiniert mit teilweise unveröffentlichten Ergebnissen neuerer Studien zeigte jedoch, dass dieser Effekt entweder vernachlässigbar klein bzw. falls unter 0.1 eV die Photoemission nicht empfindlich genug dafür ist. Nachdem viele der Effekte, die in diesem Kapitel beschrieben werden, von der Filmdicke abhängen, wurde die Kontrolle über die Filmmorphologie und die Wachstumsmode als wichtig angesehen. Daher ist diesem Thema ein Unterkapitel gewidmet, in welchem beschrieben wird, wie es mit Hilfe der Variation der Wachstumsparameter und unter der Kontrolle durch Röntgenphotoelektronenspektroskopie (XPS) möglich ist, Filme mit einer sehr homogenen Dicke zu wachsen.

## 6. Zusammenfassung

---

Die Grenzfläche zwischen organischer Dünnschicht und Metallsubstrat hat entscheidenden Einfluss auf die Lage der elektronischen Niveaus der Schicht relativ zur Lage des Substrat-Ferminiveaus. In der diskutierten Literatur konnte für die meisten Moleküle kein Hinweis auf ein Angleichen der Ferminiveaus von Substrat und Schicht gefunden werden und in den wenigen Fällen, in denen dies geschah, war es erst nach einigen hundert Nanometern Schichtdicke der Fall. Organische Schichten scheinen daher aufgrund fehlender freier Ladungsträger lediglich ihr "virtuelles" Vakuumniveau mit dem Substrat anzugleichen, welches um einen Grenzflächendipol verschoben ist. Weil die PES sehr oberflächenempfindlich ist und Aufladungseffekte die maximal untersuchbare Schichtdicke limitieren, ist es daher nicht möglich, mit dieser Methode die Lage des Ferminiveaus innerhalb der organischen Dünnschicht zu bestimmen. Bandverbiegungsmechanismen wurden diskutiert und mit experimentellen Daten belegt.

Ein bisher kaum beachteter Einfluss auf die Lage der elektronischen Niveaus im Spektrum ist die strukturelle Anordnung der Moleküle in einer Schicht, welcher mit Hilfe des Systems DIP auf Ag(111) sehr gut demonstriert werden kann. Dieser wird in dieser Arbeit sehr ausführlich mit hochauflösender Niederenergieelektronenbeugung untersucht, um die Auswirkungen unterschiedlicher Präparationsbedingungen auf die Kristallstruktur herauszufinden. Abhängig von der Substrattemperatur während des Filmwachstums konnten drei unterschiedliche Kristallstrukturen beobachtet werden, welche von amorph über multistrukturell bis langreichweitig, hoch geordnet reichen. Damit bot sich die Möglichkeit, reine Strukturauswirkungen zu untersuchen. Hochauflösende Elektronenenergieverlustspektroskopie wurde ebenfalls angewendet, da die Molekülschwingungen sehr empfindlich auf Änderungen in der intermolekularen Wechselwirkung reagieren können. Mit Hilfe der Strukturdaten und der Schwingungsspektren konnten die deutlichen Unterschiede in den Photoemissionsspektren verschiedenen Effekten zugeordnet werden. Trotz geringer Änderungen in den Schwingungsspektren zwischen den verschiedenen Strukturphasen waren deutliche Unterschiede in den Signalpositionen, den Signalbreiten und ihren relativen Intensitäten in den PES/IPS Spektren messbar. Es wurden sogar Phasenübergänge zwischen den Strukturen beobachtet, die weiterer experimenteller Untersuchung bedürfen.

Im zweiten Schritt wird zunächst die Signalverbreiterung aufgrund von strukturellen Inhomogenitäten untersucht, welche sehr häufig im Zusammenhang mit organischen Dünnschichten für die Signalbreiten verantwortlich gemacht werden. Auf Grund dieser kann der Beitrag von Endzustandseffekten, wie das Abschirmen der Ladung im Photoemissionsprozess, lokal variieren und zu unterschiedlichen Messergebnissen für die Bindungsenergien führen. Deren Überlagerung führt zu breiteren Signalen. Der Vergleich der HOMO Signalbreiten für alle untersuchten Schichten von Molekülen zeigte, dass dieser Effekt einen großen Einfluss auf die Breiten haben kann, dass jedoch auch Signale von hochgeordneten, durch ihre Kugelsymmetrie unempfindliche C<sub>60</sub> Moleküle nicht unter 450 meV Breite kommen. Desweiteren wurde die Schwingungsverbreiterung diskutiert, welche auf schwingungsangeregten Endzuständen beruht und im Allgemeinen (unabhängig vom untersuchten System) für die relativ breiten Signale in UPS und IPS verantwortlich gemacht wird. Es ist leider nicht möglich, den genauen Beitrag dieses Effektes experimentell zu bestimmen, jedoch lässt sich dieser anhand von Schwingungs- und Phononenspektren auf

---

200-300 meV abschätzen, was zu wenig ist, um eine generelle Ursache zu sein. Die experimentelle Verbreiterung beschränkt sich vor allem auf die IPS Spektren, da die 50 meV der UPS Messung kaum ins Gewicht fallen. Überraschenderweise wurde in diesem Zusammenhang festgestellt, dass die IPS Signale im Allgemeinen deutlich breiter sind (0.8-1 eV) und daher die experimentelle Verbreiterung von 400 meV die Signalflanke lediglich um 50 meV verschiebt. Die Ursache der breiten IPS Signale ist bisher ungeklärt und bedarf weiterer Untersuchungen. Ein weiterer auflösungsbedingter Effekt beruht auf dem Umstand, dass eine begrenzte Winkelauflösung zu einer Mittelung über Teile der Brillouinzone führt. Allerdings konnte gezeigt werden, dass dieser Effekt für Bandextrema in anorganischen Halbleitern vernachlässigt werden kann, da die Steigung um Wendepunkte herum allgemein gering ist. In organischen Dünnschichten treten ebenfalls Banddispersionen auf, aber diese sind zu klein und die Überlagerung mehrerer Rotationsdomänen sollte eigentlich zu einer größeren Mittlung über die BZ führen. Jedoch zeigen selbst eindomänige Strukturen bei hoher Winkelauflösung keine signifikant schmalere Signale.

Nachdem also weder einzelne Effekte noch ihre Summe die gesamte Signalbreite erklären können, wird ein weiterer Verbreiterungsmechanismus eingeführt - die dynamischen Abschirmungseffekte. Das Grundprinzip dieses Effektes beruht auf dem der inhomogenen Verbreiterung mit dem Unterschied, dass der Beitrag der Relaxationseffekte nicht mit dem Ort variiert, sondern zeitlich. Ein entscheidender Punkt für viele der hier vorgestellten Verbreiterungsmechanismen ist, dass sie asymmetrisch verbreitern, bevorzugt weg von der Fermienergie.

Nachdem die Lage und Breite der Signale diskutiert sind, ist der letzte Schritt die Bestimmung der Lage der Transportzustände im Spektrum. Diese Lage wird in der Literatur kontrovers diskutiert. Zwei Möglichkeiten der Definition können gefunden werden - die Maxima oder die Flanken der Volumensignale, welche der Fermienergie am nächsten liegen. Um diesen Zwiespalt zu klären, wird im ersten Teil des letzten Kapitels zunächst die Methode auf einen sehr gut verstandenen anorganischen Halbleiter angewandt. Da die Methode zur Bandlückenbestimmung in der Literatur nicht sehr etabliert ist, wird zuerst am Beispiel von Silizium eine Vorgehensweise entwickelt. Diese beginnt mit der richtigen Wahl der Photonenenergie, des Emissionswinkels und der Kristallfläche, um an der richtigen Stelle im k-Raum zu messen, an welcher die Bandextrema gefunden werden können. Danach werden die Oberflächenzustände identifiziert, welche aus ungesättigten Bindungen an der Oberfläche und deren Rekonstruktion stammen. Anschließend wird versucht, diese aus dem Spektrum zu entfernen. Dafür wird einerseits die Sättigung mit Wasserstoff angewandt, welche erfolgreich die Zustände in der Bandlücke entfernt und andererseits die Spektren mit einer Serie von Gausskurven reproduziert. Die Gausskurven der Oberflächenzustände werden abgezogen, so dass das reine Volumenspektrum reproduziert wird. Die letztere Methode erwies sich als besser anwendbar für Silizium und ergab eine Transportlücke von  $(1.14 \pm 0.09)$  eV, die sehr nahe am optischen Wert von 1.11 eV liegt und an der Flanken bestimmt wurde. Die gute Übereinstimmung mit den Signalflanken wird unter Berücksichtigung der asymmetrischen Verbreiterungsmechanismen diskutiert.

Die Ergebnisse des Siliziums werden auf die weniger gut verstandenen organischen Dünnschichten angewandt. Die Verwendung der Signalflanken wird auch für diese vorgeschla-

gen. Um die Lage der Transportzustände zu finden, werden diese zunächst diskutiert. Ein Transportzustand ist unabhängig vom Ladungstransportmechanismus, Band- oder Hüpftransport, ein Endzustand, auf dessen Anwesenheit die umgebenden Moleküle reagieren konnten und der deshalb bereits alle Relaxationseffekte erfahren hat, also ein relaxierter Endzustand. Der Endzustand in der Photoemission, welcher am nächsten zur Fermienergie liegt, ähnelt diesem sehr stark, wie bereits bei den Verbreiterungsmechanismen diskutiert. Aus der so bestimmten Transportlücke können die Exzitonenbindungsenergien durch Vergleich mit der optischen Lücke bestimmt werden, welche jedoch im Gegensatz zu denen der anorganischen Halbleiter als größer angenommen werden können. Dies beruht auf der Annahme, dass sich das Elektron-Loch Paar in einem kleineren Volumen aufhält, da Ladungsträger in organischen Dünnschichten weniger delokalisiert sind. Die gewonnenen Werte von 0.1-0.5 eV sind jedoch deutlich kleiner als bisher veröffentlichte Werte, die aus dem Maximaabstand bestimmt wurden. Die Exzitonenbindungsenergie in dem ebenfalls gemessenen Polymer P3HT ist mit 0.3 eV in derselben Größenordnung. In den Polymeren werden üblicherweise niedrigere Werte erwartet werden als für die Molekülfilme. Die niedrigen Exzitonenbindungsenergien deuten auf eine nennenswerte intermolekulare Wechselwirkung in den organischen Dünnschichten hin, welche die Diskussion über die Natur der Molekülkristalle wieder eröffnet.



# Bibliography

- [AM76] N.W. Ashcroft, and N.D. Mermin. *Solid State Physics*. Cengage Learning / Thomson, 1976. [2.1](#)
- [AU05] M. P. Andersson, and P. Uvdal. New scale factors for harmonic vibrational frequencies using the B3LYP density functional method with the triple- $\xi$  basis set 6-311+G(d,p). *Journal of Physical Chemistry A*, 109(12):2937–2941, 2005. [2.6.1](#), [2.6.1](#), [2.6.6](#)
- [BCH96] J. L. Bredas, J. Cornil, and A. J. Heeger. The exciton binding energy in luminescent conjugated polymers. *Advanced Materials*, 8(5):447, 1996. [1](#)
- [BGM<sup>+</sup>00] M. Brinkmann, G. Gadret, M. Muccini, C. Taliani, N. Masciocchi, and A. Sironi. Correlation between molecular packing and optical properties in different crystalline polymorphs and amorphous thin films of mer-tris(8-hydroxyquinoline)aluminum(III). *Journal of the American Chemical Society*, 122(21):5147–5157, 2000. [2.2.3](#)
- [BKW77] K. Besocke, B. Krahlurban, and H. Wagner. Dipole-Moments Associated with Edge Atoms - Comparative-Study on Stepped Pt, Au and W Surfaces. *Surface Science*, 68(1):39–46, 1977. [2.2](#)
- [BMS72] R. Boschi, J. N. Murrell, and W. Schmidt. Photoelectron Spectra of Polycyclic Aromatic-Hydrocarbons. *Faraday Discussions*, Seiten 116–126, 1972. [2.1.1](#)
- [BN79] O. A. Baschenko, and V. I. Nefedov. Relative intensities in X-ray photo-electron spectra. 4: Effect of elastic-scattering in a solid on the free-path of electrons and their angular-distribution. *Journal of Electron Spectroscopy and Related Phenomena*, 17(6):405–420, 1979. [2.2.1](#)
- [BN80] O. A. Baschenko, and V. I. Nefedov. Relative intensities in X-ray photo-electron spectra. 7: The effect of elastic-scattering in a solid on the angular distribution of photoelectrons escaping from samples covered with thin-films of various thicknesses. *Journal of Electron Spectroscopy and Related Phenomena*, 21(2):153–169, 1980. [2.2.1](#)
- [BN82] O. A. Baschenko, and V. I. Nefedov. Relative intensities in X-ray photo-electron spectra. 9: Estimates for photo-electron mean free paths taking into account elastic collisions in a solid. *Journal of Electron Spectroscopy and Related Phenomena*, 27(2):109–118, 1982. [2.2.1](#)

## Bibliography

---

- [BR96] A. M. Bradshaw, and N. V. Richardson. Symmetry, selection rules and nomenclature in surface spectroscopies. *Pure and Applied Chemistry*, 68(2):457–467, 1996. [2.6.2](#)
- [Buc01] C. Buchberger. *Elektronenspektroskopische Untersuchungen an schwach und stark gebundenen Adsorbaten auf Einkristalloberflächen*. Doktorarbeit, Universität Würzburg, 2001. [2.1.2](#)
- [Cas08] M. B. Casu. Evidence for efficient screening in organic materials. *physica status solidi (RRL) - Rapid Research Letters*, 2(1):40–42, 2008. [2.1.2](#), [4](#)
- [CBW<sup>+</sup>94] M. T. Cuberes, A. Bauer, H. J. Wen, M. Prietsch, and G. Kaindl. Probing the CaF<sub>2</sub> Density-of-States at Au/CaF<sub>2</sub>/N-Si(111) Interfaces with Photoelectron-Spectroscopy and Ballistic-Electron-Emission Microscopy. *Journal of Vacuum Science & Technology B*, 12(4):2646–2652, 1994. [4.1.4](#)
- [CCMS90] H. Carstensen, R. Claessen, R. Manzke, and M. Skibowski. Direct Determination of III-V Semiconductor Surface Band-Gaps. *Physical Review B*, 41(14):9880–9885, 1990. [4.1](#), [4.1.4](#)
- [Che06] Z. Chen.  *$\pi$ -Stacks Based On Self-Assembled Perylene Bisimides: Structural, Optical, And Electronic Properties*. Doktorarbeit, Universität Würzburg, 2006. [2.2.6](#)
- [CHK<sup>+</sup>09] S. Christoph, S. Hansen, I. Kröger, C. Kumpf, and E. Umbach. Tuning intermolecular interaction in long-range-ordered submonolayer organic films. *Nature Physics*, 5:153–158, 2009. [2.5.1](#)
- [CS97] P. J. Cumpson, and M. P. Seah. Elastic scattering corrections in AES and XPS .2. Estimating attenuation lengths and conditions required for their valid use in overlayer/substrate experiments. *Surface and Interface Analysis*, 25(6):430–446, 1997. [2.2.1](#)
- [CSS<sup>+</sup>03] L. Chkoda, M. Schneider, V. Shklover, L. Kilian, M. Sokolowski, C. Heske, and E. Umbach. Temperature-dependent morphology and structure of ordered 3,4,9,10-perylene-tetracarboxylicacid-dianhydride (PTCDA) thin films on Ag(111). *Chemical Physics Letters*, 371(5-6):548–552, 2003. [2.2.2](#)
- [CZK<sup>+</sup>07] M. B. Casu, Y. Zou, S. Kera, D. Batchelor, T. Schmidt, and E. Umbach. Investigation of polarization effects in organic thin films by surface core-level shifts. *Physical Review B*, 76(19):193311, 2007. [2.1.2](#), [2.7](#)
- [DCJ92] P. Dumas, Y. J. Chabal, and P. Jakob. Morphology of hydrogen terminated Si(111) and Si(100) upon etching in HF and buffered-HF solutions. *Surface Science*, 269:867–878, 1992. [4.1.3](#)

- [DDL<sup>+</sup>91] J. Danziger, J. P. Dodelet, P. Lee, K. W. Nebesny, and N. R. Armstrong. Heterojunctions Formed from Phthalocyanine and Perylene Thin-Films - Photoelectrochemical Characterization. *Chemistry of Materials*, 3(5):821–829, 1991. [1](#)
- [Dem05] W. Demtröder. *Experimentalphysik 3 - Atome, Moleküle und Festkörper*. Springer, 3rd. Auflage, 2005. [3.5](#)
- [DH90] L. Daweritz, and R. Hey. Reconstruction and defect structure of vicinal GaAs(001) and Al<sub>x</sub>Ga<sub>1-x</sub>As(001) surfaces during MBE growth. *Surface Science*, 236(1-2):15–22, 1990. [4.1.1](#)
- [DHS<sup>+</sup>08] S. Duhm, G. Heimel, I. Salzmann, H. Glowatzki, R. L. Johnson, A. Vollmer, J. P. Rabe, and N. Koch. Orientation-dependent ionization energies and interface dipoles in ordered molecular assemblies. *Nature Materials*, 7(4):326–332, 2008. [2.6.4](#)
- [DKAS98] L. Diederich, O. Kuttel, P. Aebi, and L. Schlapbach. Electron affinity and work function of differently oriented and doped diamond surfaces determined by photoelectron spectroscopy. *Surface Science*, 418(1):219–239, 1998. [4.1.4](#)
- [DKK<sup>+</sup>03] A. C. Dürr, N. Koch, M. Kelsch, A. Ruhm, J. Ghijsen, R. L. Johnson, J. J. Pireaux, J. Schwartz, F. Schreiber, H. Dosch, and A. Kahn. Interplay between morphology, structure, and electronic properties at diindenoperylene-gold interfaces. *Physical Review B*, 68(11), 2003. [2.5.1](#)
- [DM02] C. D. Dimitrakopoulos, and P. R. L. Malenfant. Organic thin film transistors for large area electronics. *Advanced Materials*, 14(2):99, 2002. [1](#)
- [DMK<sup>+</sup>06] N. Dori, M. Menon, L. Kilian, M. Sokolowski, L. Kronik, and E. Umbach. Valence electronic structure of gas-phase 3,4,9,10-perylene tetracarboxylic acid dianhydride: Experiment and theory. *Physical Review B*, 73(19), 2006. [2.1.1](#), [2.6.1](#), [2.6.3](#), [3](#)
- [DNSF<sup>+</sup>06] A. C. Dürr, B. Nickel, V. Shan-Fia, U. Taffner, and H. Dosch. Observation of competing modes in the growth of diindenoperylene on SiO<sub>2</sub>. *Thin Solid Films*, 503(1-2):127–132, 2006. [2.2.5](#)
- [Dür02] A. C. Dürr. *Growth and Structure of DIP Thin-Films and Au Contacts on DIP Thin-Films*. Doktorarbeit, Universität Stuttgart, 2002. [2.2.5](#), [2.2.5](#), [2.5.1](#), [2.5.1](#), [4.1](#)
- [EOG<sup>+</sup>99] D. Eich, K. Ortner, U. Groh, Z. H. Chen, C. R. Becker, G. Landwehr, R. Fink, and E. Umbach. Band discontinuity and band gap of MBE grown HgTe/CdTe(001) heterointerfaces studied by k-resolved photoemission and inverse photoemission. *Physica Status Solidi a-Applied Research*, 173(1):261–267, 1999. [4.1.4](#)

- [FKS84] S.R. Forrest, M.L. Kaplan, and P.H. Schmidt. Organic-on-inorganic semiconductor contact barrier diodes. I.: Theory with applications to organic thin films prototype devices. *Journal of Applied Physics*, 55:1492–1507, 1984. [1](#)
- [For97] S. R. Forrest. Ultrathin organic films grown by organic molecular beam deposition and related techniques. *Chemical Reviews*, 97(6):1793–1896, 1997. [2.2.2](#)
- [FTS<sup>+</sup>04] M. J. Frisch, G. W. Trucks, H. B. Schlegel, G. E. Scuseria, M. A. Robb, J. R. Cheeseman, J. A. Montgomery, Jr., T. Vreven, K. N. Kudin, J. C. Burant, J. M. Millam, S. S. Iyengar, J. Tomasi, V. Barone, B. Mennucci, M. Cossi, G. Scalmani, N. Rega, G. A. Petersson, H. Nakatsuji, M. Hada, M. Ehara, K. Toyota, R. Fukuda, J. Hasegawa, M. Ishida, T. Nakajima, Y. Honda, O. Kitao, H. Nakai, M. Klene, X. Li, J. E. Knox, H. P. Hratchian, J. B. Cross, V. Bakken, C. Adamo, J. Jaramillo, R. Gomperts, R. E. Stratmann, O. Yazyev, A. J. Austin, R. Cammi, C. Pomelli, J. W. Ochterski, P. Y. Ayala, K. Morokuma, G. A. Voth, P. Salvador, J. J. Dannenberg, V. G. Zakrzewski, S. Dapprich, A. D. Daniels, M. C. Strain, O. Farkas, D. K. Malick, A. D. Rabuck, K. Raghavachari, J. B. Foresman, J. V. Ortiz, Q. Cui, A. G. Baboul, S. Clifford, J. Cioslowski, B. B. Stefanov, G. Liu, A. Liashenko, P. Piskorz, I. Komaromi, R. L. Martin, D. J. Fox, T. Keith, M. A. Al-Laham, C. Y. Peng, A. Nanayakkara, M. Challacombe, P. M. W. Gill, B. Johnson, W. Chen, M. W. Wong, C. Gonzalez, and J. A. Pople. Gaussian 03, Revision C.02. Gaussian, Inc., Wallingford, CT, 2004, 2004. [2.6.1](#)
- [Fug78] I. Y. Fugol. Excitons in Rare-Gas Crystals. *Advances in Physics*, 27(1):1–87, 1978. [4.2.2](#)
- [FYK<sup>+</sup>06] H. Fukagawa, H. Yamane, T. Kataoka, S. Kera, M. Nakamura, K. Kudo, and N. Ueno. Origin of the highest occupied band position in pentacene films from ultraviolet photoelectron spectroscopy: Hole stabilization versus band dispersion. *Physical Review B*, 73(24), 2006. [2.6.4](#)
- [GHH<sup>+</sup>87] K. Giesen, F. Hage, F. J. Himpsel, H. J. Riess, and W. Steinmann. Binding energy of image-potential states: Dependence on crystal structure and material. *Physical Review B*, 35(3):971, 1987. [4.2.1](#)
- [GHU<sup>+</sup>03] T. Gleim, C. Heske, E. Umbach, C. Schumacher, S. Gundel, W. Faschinger, A. Fleszar, C. Ammon, M. Probst, and H. P. Steinrück. Formation of the ZnSe/(Te/)GaAs(100) heterojunction. *Surface Science*, 531:77–85, 2003. [3.6](#), [4.1.4](#)
- [GMD<sup>+</sup>93] M. Gajdardziskajosifovska, M. R. McCartney, W. J. Deruijter, D. J. Smith, J. K. Weiss, and J. M. Zuo. Accurate measurement of mean inner potential of crystal wedges using digital electron holograms. *Ultramicroscopy*, 50(3):285–299, 1993. [4.1.2](#)

- [GMK<sup>+</sup>04] G. N. Gavrilă, H. Mendez, T. U. Kampen, D. R. T. Zahn, D. V. Vyalikh, and W. Braun. Energy band dispersion in well ordered N,N'-dimethyl-3,4,9,10-perylenetetracarboxylic diimide films. *Applied Physics Letters*, 85(20):4657–4659, 2004. [2.1.1](#), [3.3](#), [4.2.1](#)
- [Gra] T. Graber, and et al. to be published. [2.2.1](#), [2.2](#)
- [Gra09] T. Graber. Doktorarbeit, Universität Würzburg, 2009. [2.2.1](#), [2.2](#)
- [GS71] K. H. Gaukler, and Schwarze.R. Improved method for evaluation of mean inner potential from Kikuchi reflection diagrams. *Optik*, 33(2):215, 1971. [4.1.2](#)
- [GS78] O. Gunnarsson, and K. Schönhammer. Co on Cu(100)-Explanation of 3-Peak Structure in X-Ray-Photoemission-Spectroscopy Core Spectrum. *Physical Review Letters*, 41(23):1608–1612, 1978. [3.7](#)
- [GSK<sup>+</sup>03] V. A. Gritsenko, A. V. Shaposhnikov, W. M. Kwok, H. Wong, and G. M. Jidomirov. Valence band offset at silicon/silicon nitride and silicon nitride/silicon oxide interfaces. *Thin Solid Films*, 437(1-2):135–139, 2003. [4.1.4](#)
- [GSS<sup>+</sup>98] K. Glöckler, C. Seidel, A. Soukopp, M. Sokolowski, E. Umbach, M. Bohringer, R. Berndt, and W. D. Schneider. Highly ordered structures and submolecular scanning tunnelling microscopy contrast of PTCDA and DM-PBDCI monolayers on Ag(111) and Ag(110). *Surface Science*, 405(1):1–20, 1998. [2.6.2](#)
- [HC02] L. S. Hung, and C. H. Chen. Recent progress of molecular organic electroluminescent materials and devices. *Materials Science and Engineering: R: Reports*, 39(5-6):143–222, 2002. [1](#)
- [HCH<sup>+</sup>94] Y. Hirose, W. Chen, E.I. Haskal, S.R. Forrest, and A. Kahn. Band lineup at an organic-inorganic semiconductor heterointerface: perylenetetracarboxylic dianhydride/GaAs(100). *Applied Physics Letters*, 64(25):3482–3484, 1994. [1](#)
- [HF84] F. J. Himpsel, and T. Fauster. Probing Valence States with Photoemission and Inverse Photoemission. *Journal of Vacuum Science & Technology a-Vacuum Surfaces and Films*, 2(2):815–821, 1984. [4.1.4](#)
- [HFW01] D. E. Hooks, T. Fritz, and M. D. Ward. Epitaxy and molecular organization on solid substrates. *Advanced Materials*, 13(4):227, 2001. [2.5.1](#)
- [HHF<sup>+</sup>] F. Holch, D. Hübner, R. Fink, A. Schöll, and E. Umbach. Direct spectroscopic evidence for the  $\pi$ - $\pi$  interaction between heteroaromatic molecules. *submitted*. [2.1.1](#), [4](#)
- [HIKK94] A. Hoshino, S. Isoda, H. Kurata, and T. Kobayashi. Scanning Tunneling Microscope Contrast of Perylene-3,4,9,10-Tetracarboxylic-Dianhydride on Graphite and Its Application to the Study of Epitaxy. *Journal of Applied Physics*, 76(7):4113–4120, 1994. [2.5.1](#)

## Bibliography

---

- [Him90] F. J. Himpsel. Inverse Photoemission from Semiconductors. *Surface Science Reports*, 12(1):1–48, 1990. [4.1.3](#)
- [HKSP00] I. G. Hill, A. Kahn, Z. G. Soos, and R. A. Pascal. Charge-separation energy in films of  $\pi$ -conjugated organic molecules. *Chemical Physics Letters*, 327(3-4):181–188, 2000. [1](#), [3.5](#), [4.2.1](#), [4.1](#), [4.2.2](#)
- [HMK00] I. G. Hill, A. J. Makinen, and Z. H. Kafafi. Distinguishing between interface dipoles and band bending at metal/tris-(8-hydroxyquinoline) aluminum interfaces. *Applied Physics Letters*, 77(12):1825–1827, 2000. [1](#), [2.4.1](#)
- [HPT<sup>+</sup>07] M. A. Heinrich, J. Pflaum, A. K. Tripathi, W. Frey, M. L. Steigerwald, and T. Siegrist. Enantiotropic polymorphism in diindenoperylene. *Journal of Physical Chemistry C*, 111(51):18878–18881, 2007. [2.6.6](#)
- [HRKH98] I. G. Hill, A. Rajagopal, A. Kahn, and Y. Hu. Molecular level alignment at organic semiconductor-metal interfaces. *Applied Physics Letters*, 73(5):662–664, 1998. [2.3](#)
- [HS06] M. Hultell, and S. Stafstrom. Polaron dynamics in highly ordered molecular crystals. *Chemical Physics Letters*, 428(4-6):446–450, 2006. [3.6](#), [4.2.2](#)
- [HSF<sup>+</sup>] D. Hübner, V. Shklover, R. Fink, A. Schöll, and E. Umbach. Preparation effects on the vibrational properties in NTCDA multilayer films. *in preparation*. [3.5](#)
- [HU88] G. V. Hansson, and R. I. G. Uhrberg. Photoelectron spectroscopy of surface states on semiconductor surfaces. *Surface Science Reports*, 9(5-6):197–292, 1988. [4.1.1](#), [4.2](#), [4.1.3](#), [4.1.3](#)
- [Hüf95] S. Hüfner. *Photoelectron Spectroscopy*. Springer Verlag, 2nd. Auflage, 1995. [4.3](#), [4.4](#), [4.1.3](#), [4.1.3](#)
- [HWH<sup>+</sup>97] C. Heske, U. Winkler, G. Held, R. Fink, E. Umbach, C. Jung, P.R. Bressler, and C. Hellwig. Surface core-level shifts of the polar semiconductor Cd(Zn)Te(100). *Physical Review B*, 56(4):2070–2078, 1997. [2.1.2](#)
- [IHI<sup>+</sup>04] H. Ishii, N. Hayashi, E. Ito, Y. Washizu, K. Sugi, Y. Kimura, M. Niwano, Y. Ouchi, and K. Seki. Kelvin probe study of band bending at organic semiconductor/metal interfaces: examination of Fermi level alignment. *Physica Status Solidi a-Applied Research*, 201(6):1075–1094, 2004. [1](#), [2.3.1](#), [2.3](#), [2.4](#), [2.4.1](#), [2.4.2](#)
- [IHK<sup>+</sup>07] J. Ivanco, T. Haber, J. R. Krenn, F. P. Netzer, R. Resel, and M. G. Ramsey. Sexithiophene films on ordered and disordered TiO<sub>2</sub>(110) surfaces: Electronic, structural and morphological properties. *Surface Science*, 601(1):178–187, 2007. [2.6.4](#)

- [IKK<sup>+</sup>06] K. Ihm, B. Kim, T. H. Kang, K. J. Kim, M. H. Joo, T. H. Kim, S. S. Yoon, and S. Chung. Molecular orientation dependence of hole-injection barrier in pentacene thin film on the Au surface in organic thin film transistor. *Applied Physics Letters*, 89(3), 2006. [2.6.4](#)
- [IKM<sup>+</sup>03] R. Dennington II, T. Keith, J. Millam, K. Eppinnett, W. L. Hovell, and R. Gilliland. GaussView, Version 3.09. Semichem, Inc., Shawnee Mission, KS, 2003, 2003. [2.6.1](#)
- [INR07] J. Ivanco, F. P. Netzer, and M. G. Ramsey. On validity of the Schottky-Mott rule in organic semiconductors: Sexithiophene on various substrates. *Journal of Applied Physics*, 101(10), 2007. [2.6.4](#)
- [ISIS99] H. Ishii, K. Sugiyama, E. Ito, and K. Seki. Energy level alignment and interfacial electronic structures at organic/metal and organic/organic interfaces (vol 11, pg 605, 1999). *Advanced Materials*, 11(12):972–972, 1999. [2.3.1](#), [2.3.2](#), [2.3](#), [2.4](#)
- [ISS87] H. Inokuchi, K. Seki, and N. Sato. UV photoelectron spectroscopy of organic molecular materials. *Physica Scripta*, T17:93–103, 1987. [2.1.1](#)
- [IWNR03] J. Ivanco, B. Winter, T. R. Netzer, and M. G. Ramsey. Substrate-mediated electronic structure and properties of sexiphenyl films. *Advanced Materials*, 15(21):1812–1815, 2003. [2.6.4](#)
- [JUH88] L. S. O. Johansson, R. I. G. Uhrberg, and G. V. Hansson. Symmetry Properties and Band-Structure of Surface-States on the Single-Domain, Hydrogen-Chemisorbed Si(100)2x1-H Surface. *Physical Review B*, 38(18):13490–13493, 1988. [4.1.1](#)
- [Kar03] N. Karl. Charge carrier transport in organic semiconductors. *Synthetic Metals*, 133:649–657, 2003. [1](#), [3.6](#), [4.2.2](#)
- [KCSU08] S. Krause, M. B. Casu, A. Schöll, and E. Umbach. Determination of transport levels of organic semiconductors by UPS and IPS. *New Journal of Physics*, 10(8):085001, 2008. [1](#)
- [KGM<sup>+</sup>85] P. Koke, A. Goldmann, W. Monch, G. Wolfgarten, and J. Pollmann. Angle-Resolved Photoemission from Si(100) - Identification of Bulk Band Transitions. *Surface Science*, 152:1001–1006, 1985. [4.1.2](#), [4.1.3](#)
- [KGS<sup>+</sup>06] S. Kowarik, A. Gerlach, S. Sellner, F. Schreiber, L. Cavalcanti, and O. Konovalov. Real-time observation of structural and orientational transitions during growth of organic thin films. *Physical Review Letters*, 96(12), 2006. [2.2.5](#), [2.5.1](#), [2.6.4](#)
- [KGS08] S. Kowarik, A. Gerlach, and F. Schreiber. Organic molecular beam deposition: fundamentals, growth dynamics, and in situ studies. *Journal of Physics - Condensed Matter*, 20(18), 2008. [2.2.5](#)

- [KHT<sup>+</sup>08] L. Kilian, A. Hauschild, R. Temirov, S. Soubatch, A. Schöll, A. Bendounan, F. Reinert, T. L. Lee, F. S. Tautz, M. Sokolowski, and E. Umbach. Role of intermolecular interactions on the electronic and geometric structure of a large  $\pi$ -conjugated molecule adsorbed on a metal surface. *Physical Review Letters*, 100, 2008. [2.2.1](#)
- [Kil02] L. Kilian. *Adsorption, Struktur und Morphologie hochgeordneter organischer Adsorbatschichten*. Doktorarbeit, Universität Würzburg, 2002. [2.4](#), [2.1.1](#), [2.1.2](#), [2.2.2](#), [2.5.1](#), [3.4](#), [4](#)
- [KP88] P. Kruger, and J. Pollmann. Scattering-Theoretical Method for Semiconductor Surfaces - Self-Consistent Formulation and Application to Si(001)-(2x1). *Physical Review B*, 38(15):10578–10599, 1988. [4.1.3](#)
- [Krö07] I. Kröger. *Geometrische Struktur von Kupfer-Phthalocyanin Submonolagen auf Ag(111)*. Diplomarbeit, Universität Würzburg, 2007. [2.5.1](#)
- [KU05] S. Kera, and N. Ueno. Deep Insight into a Valence Hole in Organic Semiconductors: High-Resolution Ultraviolet Photoemission Study. *Proc. Int. Symp. Super-Functionality Organic Devices IPAP Conf. Series*, 6:51–56, 2005. [3.5](#), [3.6](#)
- [KUS04] L. Kilian, E. Umbach, and M. Sokolowski. Molecular beam epitaxy of organic films investigated by high resolution low energy electron diffraction (SPA-LEED): 3,4,9,10-perylenetetracarboxylicacid-dianhydride (PTCDA) on Ag(111). *Surface Science*, 573(3):359–378, 2004. [2.2.1](#), [2.2.2](#)
- [KUS06] L. Kilian, E. Umbach, and M. Sokolowski. A refined structural analysis of the PTCDA monolayer on the reconstructed Au(111) surface - "Rigid or distorted carpet?". *Surface Science*, 600(13):2633–2643, 2006. [2.5.1](#)
- [MEP<sup>+</sup>07] K. Manandhar, T. Ellis, K. T. Park, T. Cai, Z. Song, and J. Hrbek. A scanning tunneling microscopy study on the effect of post-deposition annealing of copper phthalocyanine thin films. *Surface Science*, 601(17):3623–3631, 2007. [2.2.4](#)
- [MF04] S. C. B. Mannsfeld, and T. Fritz. Analysis of the substrate influence on the ordering of epitaxial molecular layers: The special case of point-on-line coincidence. *Physical Review B*, 69(7), 2004. [2.5.1](#)
- [MF05] S. C. B. Mannsfeld, and T. Fritz. Understanding organic-inorganic heteroepitaxial growth of molecules on crystalline substrates: Experiment and theory. *Physical Review B*, 71(23), 2005. [2.5.1](#)
- [MGS<sup>+</sup>06] H. Marchetto, U. Groh, T. Schmidt, R. Fink, H.J. Freund, and E. Umbach. Influence of substrate morphology on organic layer growth: PTCDA on Ag(111). *Chemical Physics*, 325(1):178–184, 2006. [2.2.2](#)



- [MS02] R. P. Mikalo, and D. Schmeisser. Electric contacts on conductive polymers: sodium on poly(3-hexylthiophene-2,5-diyl). *Synthetic Metals*, 127(1-3):273–277, 2002. [4.1](#)
- [Mün01] M. Münch. *Strukturelle Beeinflussung der elektrischen Transporteigenschaften dünner organischer Schichten*. Doktorarbeit, Universität Tübingen, 2001. [2.5.1](#), [2.5.1](#), [2.6.1](#)
- [MUW83] E. R. Moog, J. Unguris, and M. B. Webb. Electron-Stimulated Desorption of Xe, Kr, and Ar. *Surface Science*, 134(3):849–864, 1983. [2.1.2](#)
- [MW84] E. R. Moog, and M. B. Webb. Xenon and Krypton Adsorption on Palladium (100). *Surface Science*, 148(2-3):338–370, 1984. [2.1.2](#)
- [NDS<sup>+</sup>98] M. Nagelstrasser, H. Droge, H.-P. Steinruck, F. Fischer, T. Litz, A. Waag, G. Landwehr, A. Fleszar, and W. Hanke. Band structure of BeTe: A combined experimental and theoretical study. *Physical Review B - Condensed Matter and Materials Physics*, 58(16):10394–10400, 1998. [4.1.2](#)
- [Nef95] V. I. Nefedov. Polarization and Extra-Atomic Relaxation on the Surface and in the Bulk of Solids - Influence of the Molecular Shape, Polarizability and Complex Nature of the Adsorbate. *Journal of Electron Spectroscopy and Related Phenomena*, 70(3):207–215, 1995. [2.1.2](#)
- [OH93] J. E. Ortega, and F. J. Himpsel. Inverse-Photoemission Study of Ge(100), Si(100), and GaAs(100) - Bulk Bands and Surface-States. *Physical Review B*, 47(4):2130–2137, 1993. [4.1.3](#), [4.8](#), [4.1.3](#), [4.1.3](#)
- [OLB<sup>+</sup>07] J. H. Oh, S. Liu, Z. Bao, R. Schmidt, and F. Würthner. Air-stable n-channel organic thin-film transistors with high field-effect mobility based on N,N'-bis(heptafluorobutyl)-3,4,9,10-perylene diimide. *Applied Physics Letters*, 91(21):212107, 2007. [2.2.6](#)
- [PJ09] C. J. Powell, and A. Jablonski. Surface sensitivity of X-ray photoelectron spectroscopy. *Nuclear Instruments and Methods in Physics Research Section a-Accelerators Spectrometers Detectors and Associated Equipment*, 601(1-2):54–65, 2009. [2.2.1](#)
- [Sal78] W. R. Salaneck. Intermolecular Relaxation Energies in Anthracene. *Physical Review Letters*, 40(1):60–63, 1978. [2.1.1](#), [2.1.2](#), [2.6](#)
- [SC94] E.A. Silinsh, and Vladislav Capek. *Organic Molecular Crystals*. AIP Press, 1994. [1](#), [2.1](#), [2.1](#), [2.1](#)
- [Sch04] F. Schreiber. Organic molecular beam deposition: Growth studies beyond the first monolayer. *Physica Status Solidi a-Applied Research*, 201(6):1037–1054, 2004. [2.2.5](#)

## Bibliography

---

- [Sch08] M. Scholz. *PES und IPES Untersuchungen an kondensierten baysubstituierten Perylenbisimidfilmen*. Diplomarbeit, Universität Würzburg, 2008. [2.2.6](#)
- [SD79] M.P. Seah, and W.A. Dench. Quantitative electron spectroscopy of surfaces: A standard data base for electron inelastic mean free paths in solids. *Surface and Interface Analysis*, 1(1):2–11, 1979. [2.2.1](#), [4.1.3](#), [4.7](#)
- [SDCF94] P. J. Stephens, F. J. Devlin, C. F. Chabalowski, and M. J. Frisch. Ab-Initio Calculation of Vibrational Absorption and Circular-Dichroism Spectra Using Density-Functional Force-Fields. *Journal of Physical Chemistry*, 98(45):11623–11627, 1994. [2.6.1](#)
- [SDE<sup>+</sup>80] W. R. Salaneck, C. B. Duke, W. Eberhardt, E. W. Plummer, and H. J. Freund. Temperature-Dependent Ultraviolet Photoemission Linewidths of Molecular-Solids - Isopropyl Benzene. *Physical Review Letters*, 45(4):280–283, 1980. [3.5](#)
- [SE84] N. Sheppard, and J. Erkelens. Vibrational-Spectra of Species Adsorbed on Surfaces - Forms of Vibrations and Selection-Rules for Regular Arrays of Adsorbed Species. *Applied Spectroscopy*, 38(4):471–485, 1984. [2.6.2](#)
- [Sil89] E. A. Silinsh. Studies of organic semiconductors for 40 years. *Molecular Crystals and Liquid Crystals*, 171:135–144, 1989. [4](#)
- [SIS<sup>+</sup>82] N. Sato, H. Inokuchi, K. Seki, J. Aoki, and S. Iwashima. Ultraviolet Photoemission Spectroscopic Studies of 6 Nanocyclic Aromatic-Hydrocarbons in the Gaseous and Solid States. *Journal of the Chemical Society-Faraday Transactions Ii*, 78:1929–1936, 1982. [2.1.1](#)
- [SSI81] N. Sato, K. Seki, and H. Inokuchi. Polarization Energies of Organic-Solids Determined by Ultraviolet Photoelectron-Spectroscopy. *Journal of the Chemical Society-Faraday Transactions Ii*, 77:1621–1633, 1981. [2.3](#), [2.1.1](#)
- [SSK<sup>+</sup>09] M. Scholz, R. Schmidt, S. Krause, A. Schöll, F. Reinert, and F. Würthner. Electronic structure of epitaxial thin films of bay-substituted perylene bisimide dyes. *Applied Physics a-Materials Science and Processing*, 95(1):285–290, 2009. [2.2.6](#), [4.1](#)
- [SSM<sup>+</sup>08] C. H. Schwalb, S. Sachs, M. Marks, A. Schöll, F. Reinert, E. Umbach, and U. Höfer. Electron lifetime in a Shockley-type metal-organic interface state. *Physical Review Letters*, 101(14), 2008. [4.2.1](#)
- [Ste89] W. Steinmann. Spectroscopy of image-potential states by 2-photon photoemission. *Applied Physics a-Materials Science and Processing*, 49(4):365–377, 1989. [4.2.1](#)
- [STS<sup>+</sup>00] V. Shklover, F.S. Tautz, R. Scholz, S. Sloboshanin, M. Sokolowski, J.A. Schäfer, and E. Umbach. Differences in vibronic and electronic excitations of PTCDA on Ag(111) and Ag(110). *Surface Science*, 454:60–66, 2000. [2.2.1](#)

- 
- [SW86] N. V. Smith, and D. P. Woodruff. Inverse Photoemission from Metal-Surfaces. *Progress in Surface Science*, 21(4):295–370, 1986. [4.2.1](#)
- [SW07] M. Schwoerer, and H. C. Wolf. *Organic Molecular Solids*. Wiley-VCH, 1st. Auflage, 2007. [3.4](#)
- [SWTT09] S. Soubatch, C. Weiss, R. Temirov, and F. S. Tautz. Site-Specific Polarization Screening in Organic Thin Films. *Physical Review Letters*, 102(17), 2009. [3.4](#)
- [Tau07] F. S. Tautz. Structure and bonding of large aromatic molecules on noble metal surfaces: The example of PTCDA. *Progress in Surface Science*, 82(9-12):479–520, 2007. [2.6.2](#), [2.6.6](#), [4.2.1](#)
- [TBK<sup>+</sup>97] M. Traving, M. Boehme, L. Kipp, M. Skibowski, F. Starrost, E. E. Krasovskii, A. Perlov, and W. Schattke. Electronic structure of WSe<sub>2</sub>: A combined photoemission and inverse photoemission study. *Physical Review B*, 55(16):10392–10399, 1997. [4.1.4](#)
- [TES<sup>+</sup>02a] F.S. Tautz, M. Eremtchenko, J.A. Schäfer, M. Sokolowski, V. Shklover, K. Glöckler, and E. Umbach. A comparison of the chemisorption behaviour of PTCDA on different Ag surfaces. *Surface Science*, 502:176–184, 2002. [2.2.1](#)
- [TES<sup>+</sup>02b] F.S. Tautz, M. Eremtchenko, J.A. Schäfer, M. Sokolowski, V. Shklover, and E. Umbach. Strong electron-phonon coupling at a metal/organic interface: PTCDA/Ag(111). *Physical Review B*, 65(12), 2002. [2.6.2](#), [4.2.1](#)
- [THH<sup>+</sup>97] L. H. Tjeng, R. Hesper, A. C. L. Heessels, A. Heeres, H. T. Jonkman, and G. A. Sawatzky. Development of the electronic structure in a K-doped C-60 monolayer on a Ag(111) surface. *Solid State Communications*, 103(1):31–35, 1997. [3.4](#)
- [TMDN03] K. M. Tracy, W. J. Mecouch, R. F. Davis, and R. J. Nemanich. Preparation and characterization of atomically clean, stoichiometric surfaces of n- and p-type GaN(0001). *Journal of Applied Physics*, 94(5):3163–3172, 2003. [4.1.4](#)
- [TSGK02] E. V. Tsiper, Z. G. Soos, W. Gao, and A. Kahn. Electronic polarization at surfaces and thin films of organic molecular crystals: PTCDA. *Chemical Physics Letters*, 360(1-2):47–52, 2002. [2.1.2](#), [2.1.2](#)
- [TSK<sup>+</sup>01] M. Traving, T. Seydel, L. Kipp, M. Skibowski, F. Starrost, E. E. Krasovskii, A. Perlov, and W. Schattke. Combined photoemission and inverse photoemission study of HfS<sub>2</sub>. *Physical Review B*, 63(3), 2001. [4.1.4](#)
- [TSM<sup>+</sup>92] T. Takahashi, S. Suzuki, T. Morikawa, H. Katayamayoshida, S. Hasegawa, H. Inokuchi, K. Seki, K. Kikuchi, K. Ikemoto, and Y. Achiba. Pseudo-Gap at the Fermi Level in K<sub>3</sub>C<sub>60</sub> Observed by Photoemission and Inverse Photoemission. *Physical Review Letters*, 68(8):1232–1235, 1992. [1](#)

- [TSS<sup>+</sup>00] F.S. Tautz, S. Sloboshanin, V. Shklover, R. Scholz, M. Sokolowski, J.A. Schäfer, and E. Umbach. Substrate influence on the ordering of organic sub-monolayers: a comparative study of PTCDA on Ag(110) and Ag(111) using HREELS. *Applied Surface Science*, 166(1-4):363–369, 2000. [2.6.1](#), [2.6.2](#), [4.2.1](#)
- [UH91] R. I. G. Uhrberg, and G. V. Hansson. Electronic structure of silicon surfaces - clean and with ordered overlayers. *Critical Reviews in Solid State and Materials Sciences*, 17(2):133–185, 1991. [4.1.3](#)
- [UKK<sup>+</sup>84] M. Ueta, H. Kanzaki, K. Kobayashi, Y. Toyozawa, and E. Hanamura. *Excitonic Processes in Solids*. Springer Verlag, 1984. [4.2.2](#)
- [Umb80] E. Umbach. *Mechanismen und Anwendungen der Photoemission an Adsorbaten*. Doktorarbeit, TU München, 1980. [3.7](#)
- [Umb84] E. Umbach. On the Interpretation of XPS Lineshapes of Weakly Chemisorbed N-2 on Transition-Metals. *Solid State Communications*, 51(6):365–369, 1984. [3.7](#)
- [WCLK97] Y. C. Wang, T. M. Chou, M. Libera, and T. F. Kelly. Transmission electron holography of silicon nanospheres with surface oxide layers. *Applied Physics Letters*, 70(10):1296–1298, 1997. [4.1.2](#)
- [Wei05] L. Weinhardt. *Elektronische und chemische Eigenschaften von Grenzflächen und Oberflächen in optimierten Cu(In,Ga)(S,Se)<sub>2</sub> Dünnschichtsolarzellen*. Doktorarbeit, Universität Würzburg, 2005. [3.2](#)
- [WHSK97] C. I. Wu, Y. Hirose, H. Sirringhaus, and A. Kahn. Electron-hole interaction energy in the organic molecular semiconductor PTCDA. *Chemical Physics Letters*, 272(1-2):43–47, 1997. [1](#)
- [WMH<sup>+</sup>85] A. L. Wachs, T. Miller, T. C. Hsieh, A. P. Shapiro, and T. C. Chiang. Angle-resolved photoemission-studies of Ge(111)-c(2x8), Ge(111)-(1x1)H, Si(111)-(7x7), and Si(100)-(2x1). *Physical Review B*, 32(4):2326–2333, 1985. [4.8](#), [4.1.3](#)
- [WMK<sup>+</sup>91] J. H. Weaver, J. L. Martins, T. Komeda, Y. Chen, T. R. Ohno, G. H. Kroll, N. Troullier, R. E. Haufler, and R. E. Smalley. Electronic structure of solid C<sub>60</sub> - experiment and theory. *Physical Review Letters*, 66(13):1741–1744, 1991. [3.4](#)
- [WRS86] D. P. Woodruff, W. A. Royer, and N. V. Smith. Empty surface states, image states, and band edge on Au(111). *Physical Review B*, 34(2):764–767, 1986. [4.2.1](#)
- [WSZT04] L. Wu, M. A. Schofield, Y. Zhu, and J. Taftø. A unique determination of boundary condition in quantitative electron diffraction: Application to accurate measurements of mean inner potentials. *Ultramicroscopy*, 98(2-4):135–143, 2004. [4.1.2](#)

- 
- [YKO<sup>+</sup>03] H. Yamane, S. Kera, K. K. Okudaira, D. Yoshimura, K. Seki, and N. Ueno. Intermolecular energy-band dispersion in PTCDA multilayers. *Physical Review B*, 68(3):033102, 2003. [2.1.1](#), [3.3](#), [4.2.1](#)
- [YKY<sup>+</sup>08] H. Yamane, E. Kawabe, R. Yoshimura, D. Sumii, K. Kanai, Y. Ouchi, and K. Ueno, N. Seki. Intermolecular band dispersion in highly ordered monolayer and multilayer films of pentacene on Cu(110). *Physica Status Solidi B - Basic Solid State Physics*, 245(5):793–798, 2008. [2.1.1](#)
- [YNF<sup>+</sup>05] H. Yamane, S. Nagamatsu, H. Fukagawa, S. Kera, R. Friedlein, K. K. Okudaira, and N. Ueno. Hole-vibration coupling of the highest occupied state in pentacene thin films. *Physical Review B*, 72(15), 2005. [3.1](#)
- [ZGG06] D. R. T. Zahn, G. N. Gavrilu, and M. Gorgoi. The transport gap of organic semiconductors studied using the combination of direct and inverse photoemission. *Chemical Physics*, 325(1):99–112, 2006. [1](#)
- [ZKS<sup>+</sup>06a] Y. Zou, L. Kilian, A. Schöll, T. Schmidt, R. Fink, and E. Umbach. Chemical bonding of PTCDA on Ag surfaces and the formation of interface states. *Surface Science*, 600(6):1240–1251, 2006. [2.2.1](#), [2.6.2](#), [4.2.1](#)
- [ZKS<sup>+</sup>06b] Y. Zou, L. Kilian, A. Schöll, T. Schmidt, R. Fink, and E. Umbach. Chemical bonding of PTCDA on Ag surfaces and the formation of interface states. *Surface Science*, 600(6):1240–1251, 2006. [2.6.2](#)
- [Zou03] Y. Zou. *Electronic properties of organic molecular thin films in condensed and interfacial states with metal substrates*. Doktorarbeit, Universität Würzburg, 2003. [2.1.1](#), [3.3](#), [3.4](#), [4.2.1](#), [4.2.1](#)
- [ZVZ<sup>+</sup>07] F. Zhang, A. Vollmer, J. Zhang, Z. Xu, J. P. Rabe, and N. Koch. Energy level alignment and morphology of interfaces between molecular and polymeric organic semiconductors. *Organic Electronics*, 8:606–614, 2007. [2.6.3](#)

## A. IPS radiation damage for organic semiconductors

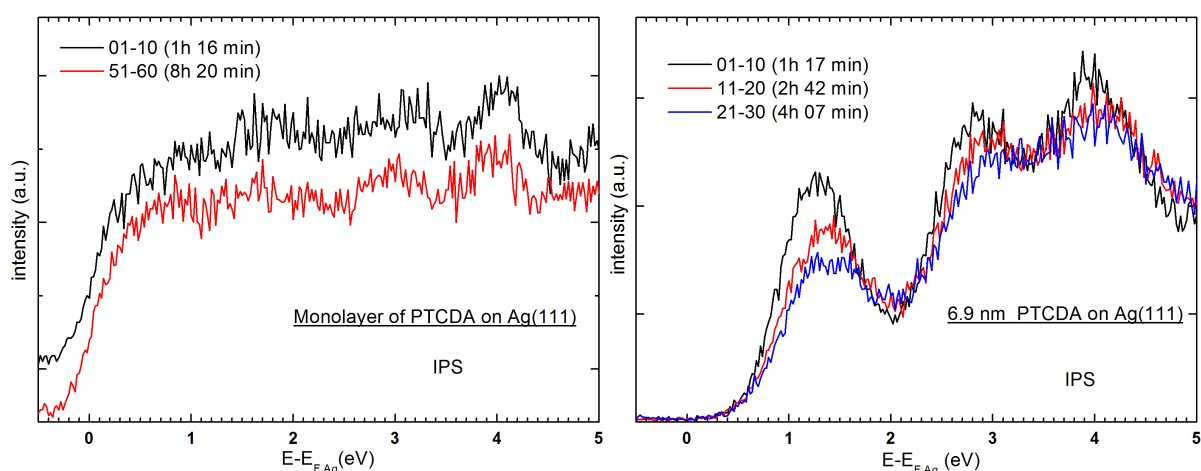


Figure A.1.: IPS spectra of a monolayer PTCDA (left) and of a 6.9 nm thick film (right) on Ag(111). Every spectrum shows the sum of ten scans after different exposure times.

The electron flux in an inverse photoelectron spectroscopy experiment is rather high. It is in the order of several  $\mu\text{A}$  in an area of about half a  $\text{cm}^2$ . The area is so large because of the retraction of the electron source and is about one  $\text{mm}^2$  otherwise. Although thin films of organic semiconductors are comparably good hole conductors, the electron mobilities are in general poor. The ionization weakens the bonds (in particular double or higher ionization) in the molecule and creates radicals. If the charges remain long enough on the molecule due to poor conduction bonds break. This is not only a problem of IPS, but in this work it was often observed for all molecular thin films. Figure A.1 shows how radiation damage alters the shape of the peaks in the spectrum. On the right side is a series of IPS spectra for a 6.9 nm PTCDA on Ag(111) film, which were recorded after different times of electron bombardment on the same spot of the sample. All spectra are the sum of 50 scans (5 Scans per file), which took about one hour to be measured. Which files were added and after which exposure time is indicated in the legend. A clear shift of the peak maxima with time and a broadening of the peaks can be observed, which are clear hints of a growing fraction of destroyed molecules. PTCDA is one of the most stable large organic molecules and it is possible to gain data of one film for about one to one and a half hours. Other molecules, such as  $\text{Alq}_3$ , are less stable and after 30 minutes the spectra significantly changed. The destruction of these molecules was visible by the eye,

---

because they show electro-luminescence, which fades within a few minutes. Note that for these measurements the electron gun was already retracted in order to increase the spot size on the sample without losing the k-resolution. It is therefore crucial to measure as thin films as possible in order to decrease the way the electrons have to travel through the layer. The left series of spectra shows the PTCDA monolayer, which chemically bonds to the silver surface. The good contact to the metal allowed long integration times. Even after eight hours of exposure the spectra still seem to be unaltered.

In order to minimize the effect of radiation damage, only a small number of scans was saved in each file (five scans was the lower limit because of the low statistic of each single scan) and the spot size was increased in the described way. Due to the very low cross section of the IPS process there is a minimum integration time before the spectra are good enough to recognize changes in subsequent files. A small contribution to the spectra can therefore not be excluded, which is unavoidable.

## B. Most intense infrared active modes

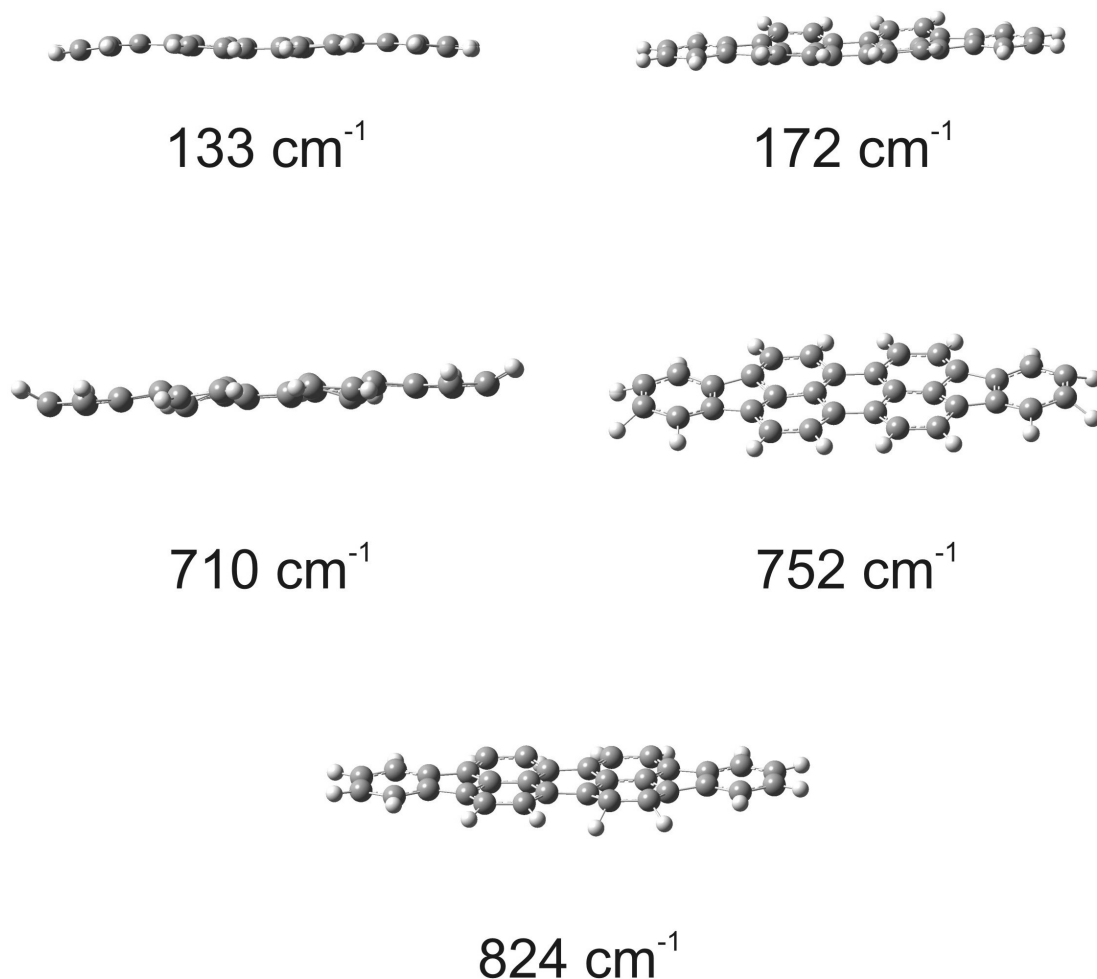
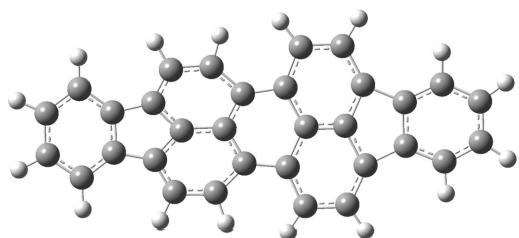


Figure B.1.: Pictures of the five out - of - plane modes at their strongest dislocation. Dislocation is exaggerated for better visibility.

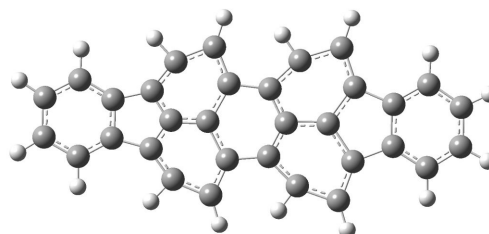
The following figures show the DIP molecule at its strongest dislocation corresponding to the infrared active modes at the given wavenumbers. All vibrations were calculated with the density functional theory method. The B3LYP functional was used in combination with the 6-311G+(d,p) basis set. All dislocations shown are exaggerated for better visibility and are separated in two categories.

First, the out - of - plane modes will be shown followed by the in - plane modes.

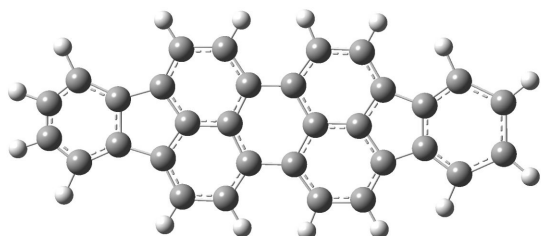




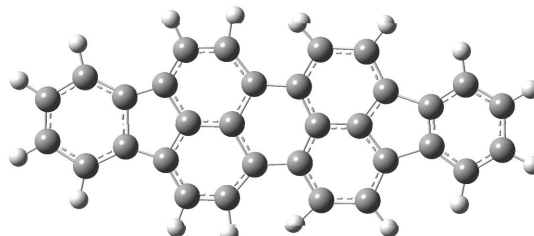
550  $\text{cm}^{-1}$



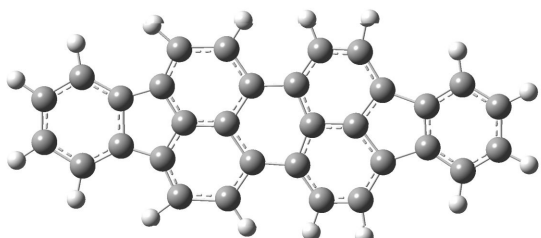
791  $\text{cm}^{-1}$



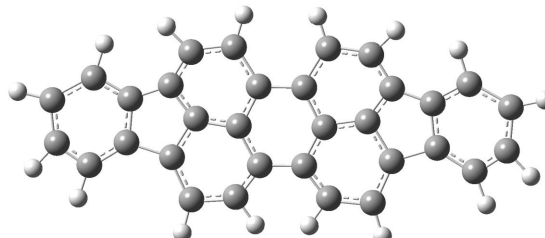
1004  $\text{cm}^{-1}$



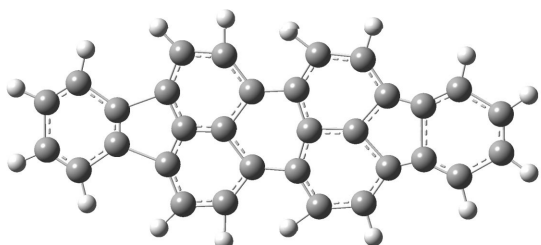
1073  $\text{cm}^{-1}$



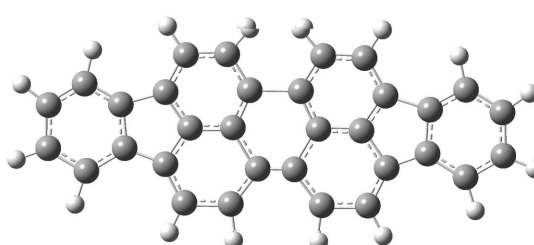
1112  $\text{cm}^{-1}$



1134  $\text{cm}^{-1}$



1234  $\text{cm}^{-1}$



1261  $\text{cm}^{-1}$

Figure B.2.: Part one of the in - plane infrared active modes.

## B. Most intense infrared active modes

---

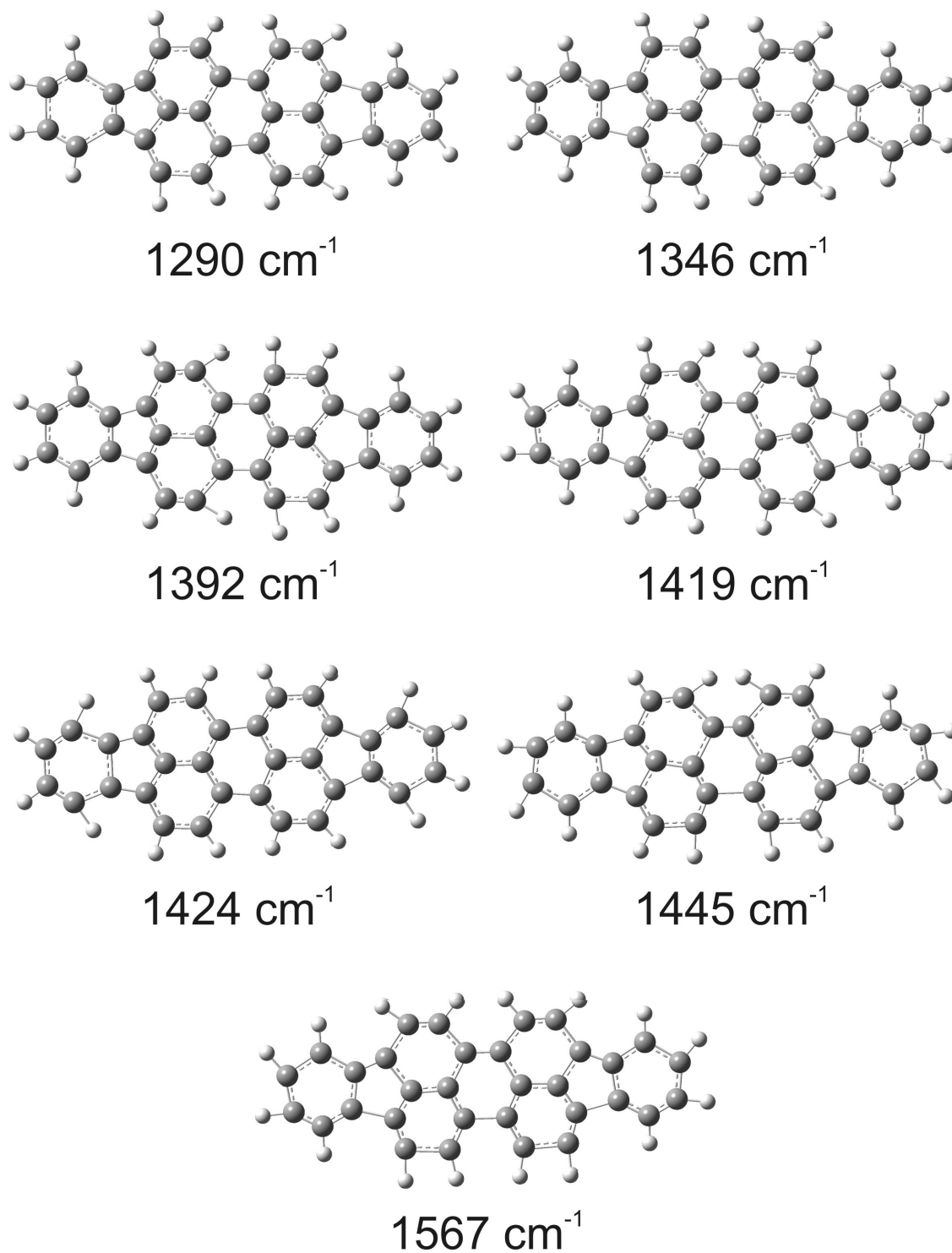


Figure B.3.: Part two of the in - plane infrared active modes.

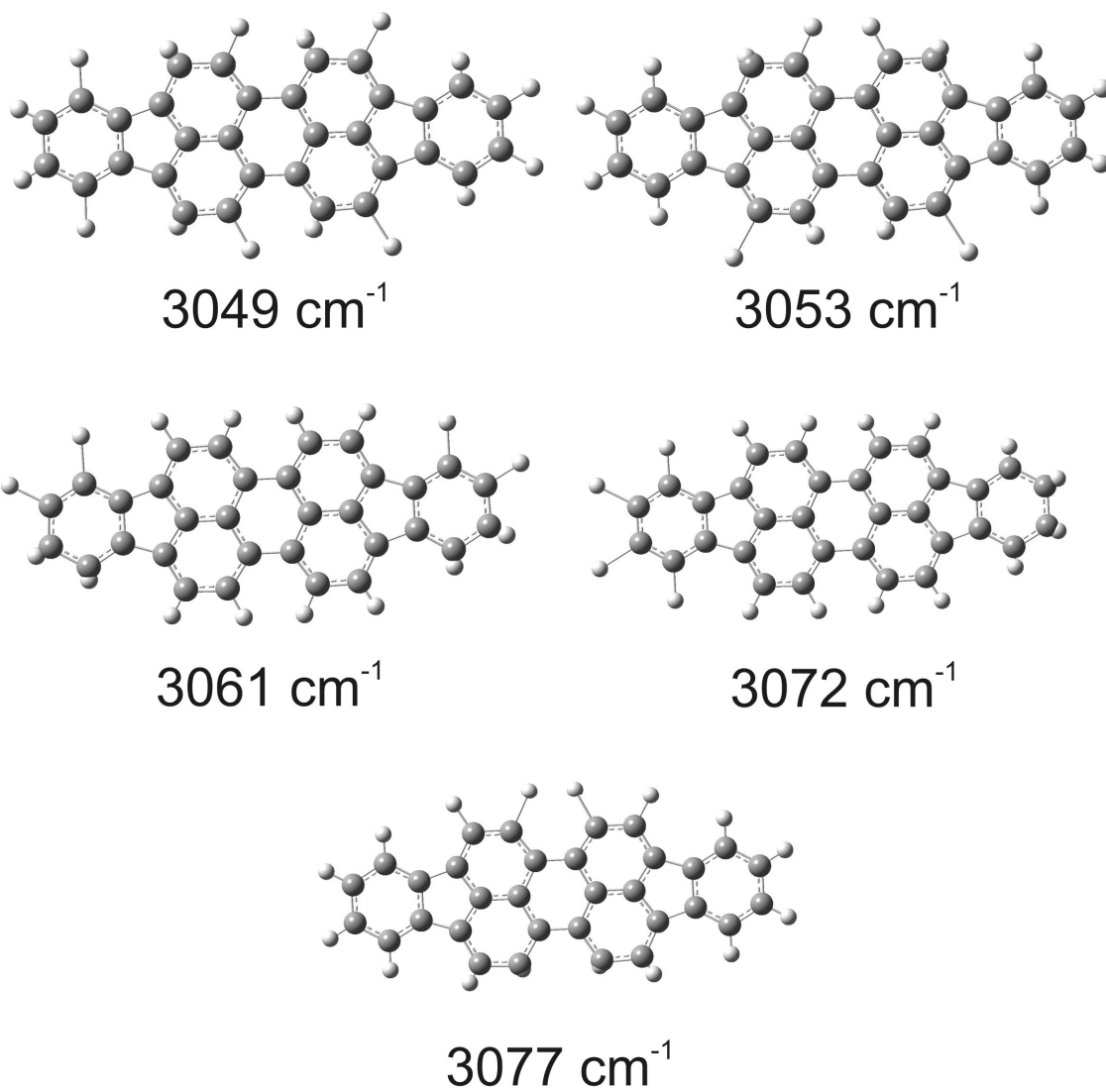


Figure B.4.: Part three of the in - plane infrared active modes.

# Danksagung

An dieser Stelle möchte ich jenen danken, die zum Gelingen dieser Arbeit beigetragen haben:

Mein besonderer Dank gilt Herrn **Prof. Dr. Eberhard Umbach** für die Unterstützung und vielen fruchtbaren Diskussionen, die mir immer sehr geholfen haben. Natürlich bedanke ich mich auch für die Aufnahme in die Arbeitsgruppe und die Stellung des interessanten Themas.

**Prof. Dr. Jens Pflaum** danke ich für die bereitwillige Übernahme des Zweitgutachtens und insbesondere dafür, dass er es in solch kurzer Zeit bearbeiten konnte.

**Prof. Dr. Friedrich Reinert** hat es mit seiner offenen Art und der günstigen Lage unserer Büros einfach gemacht, auch einmal spontane Diskussion zu führen.

Bei **Dr. Achim Schöll** und **Dr. Christian Kumpf** möchte ich mich für die gute Unterstützung während der ganzen Zeit bedanken.

**Ingo Kröger** hat mich in die Geheimnisse der SPALEED und HREELS Maschinen eingeführt. Die Diskussionen, welche gerne auch bei einer Tasse Kaffee geführt wurden, und die bereitwillige, häufige Fehlersuche an der Messapparatur haben mir sehr geholfen.

**Dr. Oliver Fuchs** und **Dr. Lothar Weinhardt** danke ich für die Lösung der vielen Elektronikprobleme und natürlich **Moni Blum**, die mir die erste Zeit in den USA sehr erleichtert hat und ohne die ich die Arbeit gar nicht hätte einreichen können.

Über die Zeit habe ich mein Büro mit **Dr. Florian Pollinger**, **Franziska Niederdraenk**, **Tina Graber** und **Dr. Stefan Schmitt** geteilt und ich möchte mich an dieser Stelle für die schöne Zeit bedanken, welche nicht zuletzt durch die geteilte Kaffeeobsession versüßt wurde.

**Felix Erfuhrt**, **Pavo Vrdoljak** und **Florian Holch** waren in der Arbeitsgruppe jederzeit für spannende Diskussion auch abseits der Physik zu begeistern.

Insbesondere das gute Verhältnis zu den Kollegen und **Freunden** in der **AG Reibach** hat mir über die Jahre viel Freude bereitet.

Natürlich möchte ich meiner Mutter **Karin Krause**, meinem Vater **Frank Krause** und seiner Frau **Ulrike Krause**, sowie meinem Bruder **Christian Krause** einfach dafür danken, dass sie da sind und mich immer unterstützt haben.

Zuletzt danke ich allen, die ich hier nicht namentlich erwähnt habe und die zum Gelingen der Arbeit beigetragen haben.

# Lebenslauf

Name                   Stefan Krause  
Geburtstag           10.04.1978  
Geburtsort           Jena  
Familienstand       ledig  
Wohnort              Las Vegas, NV, U.S.A.

---

08/84 - 07/88       Grund- und Hauptschule Wertheim-Bestenheid  
08/88 - 07/94       Dietrich-Bonhoeffer-Gymnasium Wertheim  
08/94 - 06/97       Wirtschaftsgymnasium Wertheim-Bestenheid  
Juni 1997           Abitur

---

09/97 - 06/98       Grundwehrdienst

---

10/98 - 10/04       Studium der Physik an der Universität Würzburg  
Thema der Diplomarbeit: "Die Tranportlücke in organischen Halbleitern: Eine kombinierte Ultraviolett - und inverse Photoemissionsstudie."  
27.10.2004           Diplom in Physik  
09/01 - 05/02       Integriertes Auslandsstudium and State University of New York (SUNY) at Albany  
19.5.2002           Master of Science  
Seit 12/2004       Promotion am Lehrstuhl Experimentelle Physik II des physikalischen Institutes der Universität Würzburg  
Seit 02/2009       Angestellt am Department of Chemistry der University of Nevada, Las Vegas (UNLV)